PhD Thesis

Development of binder systems based on CAB for powder injection moulding (PIM) and micro powder injection moulding (μ-PIM) of Zircon and Invar powders

Author: Javier Hidalgo García

Supervisors: José Manuel Torralba Castelló and Antonia Jiménez Morales

Tutors: Thierry Barriere and Jean Claude Gelin

Signatures of the Examining Jury:

Signature

President/Presidente:

Board Member/Vocal:

Board Member/Vocal:

Board Member/Vocal:

Secretary/Secretario:

Mark/ Calificación:

Leganés, 27th of January 2012

Universidad Carlos III de Madrid

UNIVERSITÉ DE FRANCHE-COMTÉ

Ph.D Thesis

Development of binder systems based on CAB for powder injection moulding (PIM) and micro powder injection moulding (μ-PIM) of Zircon and Invar powders

Author:
Javier Hidalgo García

Supervisors at UC3M:
José Manuel Torralba Castelló
Antonia Jiménez Morales

Tutors at UFC:
Thierry Barriere
Jean Claude Gelin

Materials Sciences and Engineering Department at Carlos III de Madrid University – Institute Álvaro Alonso Barba
&
Applied Mechanics Department at FEMTO-ST Institute (Besançon)

Leganés, 27th January 2014

Ph.D Thesis

Development of binder systems based on CAB for powder injection moulding (PIM) and micro powder injection moulding (μ-PIM) of Zircon and Invar powders

by Javier Hidalgo García

Supervisors at UC3M:
Professor José Manuel Torralba
Antonia Jiménez

Tutors at UFC:
Thierry Barriere
Jean Claude Gelin

Prepared in co-tutoring at:

- Escuela Politécnica Superior de la Universidad Carlos III de Madrid – Campus de Leganés
- L'U.F.R. des Sciences et Techniques de l'Université de Franche-Comté – FEMTO-ST (Besançon)

In order to obtain the awards of:

- Doctor por la Universidad Carlos III de Madrid en Ciencia e Ingeniería de Materiales
- Docteur de l'Université de Franche-Comté, Sciences pour l'Ingénieur

Defence committee:

Reviewers:

Prof. Y. Bienvenu - Mines Paris Tech (France)

Prof. T. Vieira - Universidade de Coimbra (Portugal)

Examining Jury:

Dr. E. Gordo – Universidad Carlos III de Madrid (Spain)

Prof. E. Carreño-Morelli - University of Applied Sciences Western Switzerland (Switzerland)

Dr. V. Bargues - Guzmán Global S.L., Nules (Spain)

Leganés, the 27th of January of 2014

A mi familia

A mi padre

A Elena

ACKNOWLEDGMENTS
Agradecimientos/ Reconnaissance

Esta Tesis Doctoral es el fruto de cinco intensos años de duro trabajo y esfuerzo personal, pero indudablemente no hubiera sido posible sin la ayuda incondicional, la confianza, la paciencia, el sacrifico y el cariño de un gran número de personas que han estado siempre a mi lado o que he tenido la gran suerte de conocer durante estos últimos años.

Mi primer guiño a esas personas tan especiales va dedicado a mis directores de Tesis, Toñi y José Manuel, con mi más sincero agradecimiento por toda la confianza demostrada y por haberme ofrecido la oportunidad de trabajar y aprender a su lado durante estos años. Siempre habéis estado ahí cuando lo he necesitado, preocupados por tomar siempre las mejores decisiones para mí, anteponiendo en muchas ocasiones mis propios intereses a los vuestros; siempre lo tendré presente y lo valoraré enormemente. Habéis sido más que mis directores, unos amigos que espero mantener toda la vida.

Je veux remercier aussi à Thierry Barriere et Jean Claude Gelin pour l'opportunité de faire la Thèse en cotutelle à l'Institute FEMTO-ST (Besançon) et pour toute l'aide qui ils m'ont donné. Travailler au département de Mécanique Appliqué a été un plaisir et un énorme honneur. Merci beaucoup.

Tampoco puedo dejar de agradecer a todas las personas del Departamento de Ciencia e Ingeniería de Materiales de la Universidad Carlos III de Madrid y en especial al Grupo de Tecnología de Polvos por toda la ayuda y cariño en momentos difíciles. Muchos habéis sido mis profesores a lo largo de mi formación como ingeniero y durante el Master; vuestros conocimientos me han sido de gran utilidad y espero que lo sigan siendo en un futuro. Simplemente decir que sois un grupo humano excepcional y que ha sido un placer formar parte de él.

En particular, tendré siempre presente la camaradería, la ilusión y la simpatía de mis compañeros de trabajo, la mayoría de ellos amigos. A las Doctoras GTP, a los que ya se fueron (Pablo, Luz, Leandro, Raquel, Pepe, se os ha echado de menos en la última parte de mi Tesis), a los nuevos fichajes y a todos los que me han acompañado durante la mayor parte del viaje, *Crazzy Horse* os agradece todos los buenos momentos que hemos pasado juntos. Rober, Dio, Eloy, Nacho, hay que seguir pedaleando fuerte. Fede ya sé que tú eres más de gimnasio, pero igual te digo *rocknrolla*. Mohammed muchas gracias a ti también. A Edwin y las chicas, María V., Paula, Nerea, Rocío, Bea, Amaia, María C., Raquel, y a las que les tengo reservado un parrafito especial, sois unos amores, gracias por todo. A mis compañeros de Máster y con especial cariño a Eva. También a toda la gente de IMDEA Materiales.

También quiero agradecer a todas las personas que me han ayudado durante mis estancias. A Teo Boronat y a Miguel Jorge Reig por acogerme en el campus de Alcoy y permitirme hacer parte del trabajo experimental allí.

Merci beaucoup à Gérard Michel pour la qualité de ses supports techniques au niveau de l'élaboration des microcomposants injectés et de ses aides au niveau de la caractérisation rhéologiques (Ingénieur de recherche à l'ENSMM de Besançon) et à l'ensemble des doctorants de FEMTO-ST pour leurs amabilités et l'ensemble de leurs conseils. A Matthieu, avant je n'imaginai jamais que je pourrais faire de l'escalade.

Je suis aussi très reconnaissant à Françoise Bugnet et à toutes mes amies françaises pour tous les bons moments que nous avons partagés. Si je sais un mot de française est la patiente avec toutes les heures de conversation avec Françoise. Merci pour toutes les fêtes que j'ai participé, à la dégustation des bons vins et les repas associés.

En este párrafo de honor tengo que dejar constancia de toda la ayuda y conocimiento recibido por parte de las chicas MIM. Esta Tesis también es vuestra. Ahora sí que si, Berni, Sofía D., Carol y Alicia, no sé que hubiera hecho sin vosotras. Esta Tesis está escrita pensando en vosotras, en todos esos momentos en los que las máquinas se tomaban unas largas vacaciones, en todos los altibajos que hemos tenido que pasar. Sé que lo vais a hacer genial porque habéis sabido salir adelante frente a múltiples adversidades. Tampoco sé que hubiera hecho sin ti Chema. Gracias por instruirme con todas las máquinas y por todos los conocimientos y consejos valiosos que me has aportado. Siempre has sido un referente y un ejemplo a seguir.

A mis amigos: a Alberto y Miguel, a Cristina y Luis, a Ainhoa y a muchos más esparcidos por todo el mundo…

A mi familia, a mi madre y mi hermano por estar siempre ahí, por apoyarme en todas mis decisiones, por todo el sacrificio y la confianza. No tengo palabras para agradeceros todo lo que os debo. A mi padre; siento no haber podido acabar antes, se que te hubieras sentido muy orgulloso, gracias por dármelo todo y por animarme siempre. Si he llegado hasta aquí ha sido gracias a vosotros. A Santi y a Ela, a Leti y Jorge y a la pequeña Sara.

Por último me gustaría dedicarle este trabajo a la persona más importante de mi vida, Elena, por todo tu amor incondicional y sacrifico estos años en los que has sabido aceptar toda mi dedicación, me has apoyado y animado a seguir adelante. Te has convertido en el motor de mi vida y no puedo estar más feliz por tenerte a mi lado.

CONTENTS

Abstract – Resumen – Résumé III

Preface VII

List of abbreviations and symbols IX

Chapter 1: Introduction to PIM 1

Chapter 2: Motivation and Objectives 43

Chapter 3: Experimental Work 49

Chapter 4: Summary of Results and Discussion 73

Chapter 5: Concluding Remarks 117

Chapter 6: Future Perspectives 123

Appendix 1 127

Paper 1 135

Paper 2 147

Paper 3 167

Paper 4 187

Paper 5 209

Paper 6 221

Paper 7 241

Paper 8 265

Abstract

Powder injection moulding (PIM), in its different versions, is a manufacturing method that in the last decades has been consolidated as an effective and competitive alternative to fabricate small size and complex geometry parts in large batches. Its future expansion to new applications and sectors requires an exhaustive research in new materials and the improvement of the manufacturing process itself. A better understanding between the variables material-processing-properties is still needed to improve the quality and repeatability.

In the last decades, a growing environmental awareness has been observed not only by the costumers but by the own industry. Within the PIM process, there are many possibilities to reduce the energy consumption and the emission of hazardous products. One of those alternatives would consist on using binder systems formulations that do not involve organic solvents, toxic vapours during processing or that allow reducing the fabrication temperatures. The binder systems based on natural derivatives, such as the thermoplastic polysaccharides, offer an interesting alternative to the conventional use of petroleum derivatives that has been scarcely investigated. Their use would suppose a cero balance of CO_2 emissions during the thermal debinding.

This PhD Thesis studied the use of binders based on cellulose acetate butyrate (CAB) and poly(ethylene glycol) (PEG) in different type of materials, including a ceramic, the zirconium silicate, and a metallic alloy, the Invar 36. These materials share their low dimensional stability with temperature with low coefficients of thermal expansion.

The scope of this work is the study and comprehension of the behaviour of the mentioned binder systems when they are employed in different PIM processes and under different conditions and powder-types. With regard to this matter, different formulations were designed with several types of PEG and CAB. These formulations were compared with commercial ones. The intrinsic characteristics of each CAB were linked with the behaviour of the different feedstock also containing PEG and powder particles. The mixtures homogeneity, the optimum and critical solid loading and its flowability were assessed by torque and capillary rheology. Other complementary techniques such as electronic and light microscopy or the measurement of the mixtures densities by pycnometry were carried out to contrast rheology results. The compatibility between the feedstocks' components and their thermal behaviour were analysed by calorimetry and thermogravimetry techniques. These methods were employed by the first time to determine the optimal solid loading.

The optimal compositions were injected by using low or high pressures or by a micro injection moulding process. The debinding and sintering stages were optimised using several atmospheres. Finally, the physical and mechanical properties of the final consolidated parts were measured.

It could be concluded that the studied binder systems based on PEG and CAB presented suitable characteristics for PIM, providing improvements with respect to conventional binder systems and by a more environmental friendly processing. However, that doctoral work was just a first approach to the use of these types of binder systems in PIM. Along this work several issues were detected and some topics regarding the processing should be further investigated to obtain the best of these binder systems.

Resumen

El moldeo por inyección de polvos (PIM), en sus diferentes variantes, es una técnica de fabricación que en las últimas décadas se ha consolidado como una alternativa eficaz y competitiva para la fabricación de piezas de geometría compleja, reducido tamaño y grandes series de producción. Para su futura expansión en nuevos campos de aplicación hace falta una investigación exhaustiva de su aplicabilidad en nuevos materiales y en la mejora del propio proceso productivo. Aún se requiere un mejor entendimiento entre las variables material-procesamiento-propiedades para mejorar la calidad y reproducibilidad de las piezas fabricadas por PIM.

En las últimas décadas se viene apreciando una mayor concienciación medio ambiental tanto por los consumidores como por la propia industria. Dentro de los procesos PIM existen alternativas para reducir el consumo energético y la emisión de productos perniciosos para el medio ambiente. Una de estas alternativas consistiría en utilizar formulaciones del sistema ligante que no conlleven el uso de disolventes orgánicos, la emisión de vapores tóxicos durante el procesamiento o que permitirán reducir las temperaturas de fabricación. Los sistemas ligantes basados en derivados naturales como los polisacáridos termoplásticos ofrecen una alternativa interesante al uso convencional de derivados del petróleo que prácticamente no está estudiada. Su uso supondría una emisión neta cero de CO_2 durante el proceso de eliminación térmica.

Esta Tesis Doctoral estudia la utilización de sistemas ligantes basados en acetato butirato de celulosa (CAB) y poli(etilenglicol) (PEG) en diferentes tipos de materiales, entre los que se incluye un cerámico, el silicato de zirconio y una aleación metálica, el Invar 36. Estos materiales tienen en común su estabilidad dimensional frente a cambios de temperatura con bajos coeficientes de expansión térmica.

El objetivo buscado es el estudio y comprensión del comportamiento de los sistemas ligantes anteriormente mencionados cuando se emplean en diferentes procesos PIM bajo diferentes condiciones y tipos de polvo. Para ello se diseñaron diferentes formulaciones con diferentes tipos de CAB y PEG y se compararon con formulaciones comerciales. Se relacionó las características intrínsecas de cada CAB con el comportamiento de las mezclas con PEG cargadas con diferentes tipos de polvo. La homogeneidad de las mezclas, las cargas óptima y crítica así como su capacidad de fluir se analizaron mediante un estudio reológico exhaustivo combinando reología de "torque" con reología capilar. Otras técnicas como la inspección por microscopía electrónica o microscopía óptica o la medición de la densidad de las mezclas mediante picnometría se utilizaron para contrastar los resultados de reología. La compatibilidad entre los componentes y el comportamiento térmico de las mezclas se analizó mediante técnicas de calorimetría y termogravimetría. Estas técnicas se emplearon por primera vez para determinar la carga óptima de polvo.

Las formulaciones óptimas se inyectaron a baja o a alta presión o mediante un proceso de micro inyección. La eliminación del ligante así como la sinterización fueron optimizadas empleando diferentes atmósferas. Finalmente se midieron diversas propiedades físicas y mecánicas de las piezas finales.

En general, se puede concluir que los sistemas ligantes estudiados basados en PEG y CAB presentan características que les hacen idóneos para el PIM, aportando mejoras con respecto a sistemas ligantes convencionales y mediante un procesamiento más ecológico. Sin embargo,

este trabajo doctoral supone sólo una primera aproximación al empleo de este tipo de sistemas ligantes en PIM. Durante este trabajo se detectaron algunos puntos de mejora y aspectos que podrían ser objeto de futuras investigaciones para obtener lo mejor de estos sistemas ligantes para su empleo en la tecnología PIM.

Résumé

Le moulage par injection de poudres (MIP) et toutes ses variantes sont un procédé de fabrication qui s'est positionné comme une alternative efficiente et compétitive pour l'élaboration en grande série de petites pièces possédant une géométrie complexe. Pour continuer son émergence et voir apparaitre de nouveaux champs d'application, une investigation exhaustive du développement de nouveaux matériaux plus fonctionnels, ainsi que l'amélioration du procédé sont encore nécessaire. Une meilleure compréhension des phénomènes mécaniques et thermo physiques entre les paramètres des différentes étapes du procédé, les nuances des matériaux employées et de leurs interactions, ainsi que les propriétés désirées, est indispensable. De plus, les développements technologiques doivent conduire à l'augmentation de la qualité et de la reproductibilité des pièces élaborées par ce procédé.

Aux cours de la dernière décennie, l'intérêt pour l'environnement est devenu un enjeu international accru aussi bien pour les consommateurs et les industriels. Le procédé MIP a des potentialités avérées et potentielles pour réduire la consommation énergétique et l'émission de produits pernicieux pour l'environnement lors de son utilisation industrielle. Quelques alternatives peuvent être l'emploie de liants qui n'utilise pas dissolvants organiques, qui n'émettent plus de vapeurs toxiques pendant le processus d'élimination thermique au niveau de la phase de déliantage. De plus, la réduction des températures du processus ou de nouvelles investigations pour réduire de manières drastiques les temps de cycle lors des étapes de densification ou déliantage sont des voies à investiguées dans le futur. Les liants basés en matériaux biosourcés comme les polysaccharides thermoplastiques offrent une alternative intéressante à l'utilisation conventionnelle de produits dérivés du pétrole. Cette alternative n'a pratiquement pas été étudiée. L'utilisation de ces éco-matériaux comme liants représenterait zéro émission de CO_2 pendant le déliantage thermique a été développé au cours de cette thèse de doctorat.

Les contributions de cette thèse de doctorat sont focalisées sur les développements de formulations à base de polymères biosourcés et déliantable à l'eau basés sur l'emploi d'acétate butyrate de cellulose (CAB) et de polyéthylène glycol (PEG). Ces nouvelles formulations ont été appliquées sur différentes nuances de poudres métalliques (invar) et céramiques (zircones). Ces matériaux possèdent une bonne stabilité dimensionnelle sous une large gamme de température imposée et possèdent de très bas coefficients d'expansion thermique.
L'objective est l'étude et la compréhension du comportement des liants à base de CAB et PEG quand ils sont utilisés dans les variantes du procédé MIP (étapes de moulage avec ou sans pression, conditions particulières liées à la micro-injection, …) réalisées avec différentes nuances de poudres et différentes granulométries.

Les caractéristiques intrinsèques de chaque CAB, leurs interactions avec le PEG et les poudres, l'influence de la nuance de poudre employée, ainsi que la granulométrie et la morphologie des poudres employées ont été étudiées et analysées en fonction du comportement final de la formulation développé et des taux de charges obtenues. L'homogénéité des mélanges développés, leurs taux de charge critique et maximal, ainsi que

leurs comportements mécaniques, thermiques et rhéologiques ont été analysés et investigués par différentes études mécaniques, thermo et physico-chimiques. De nouvelles analyses chimiques et physiques ont été introduites par accroitre les connaissances sur les formulations développées. Les formulations optimales ont été validées pour différentes applications et avec l'emploi de différentes variantes du procédé MIP conduisant à l'élaboration de composants et de micro-composants PIM obtenus sans défauts et possédant d'excellentes propriétés fonctionnelles. L'étape de déliantage ainsi que l'étape de densification ont été optimisées en termes de cinétique et d'atmosphère aboutissant aux propriétés physiques et mécaniques escomptées pour l'ensemble des nuances de poudres considérées dans cette étude.

En conclusion, les formulations développés des liants basées sur l'emploie de CAB et PEG son exploitable au niveau de la recherche et au niveau industriel dans le procédé MIP. Elles apportent des améliorations par rapport aux liants conventionnels grâce à un procédé plus écologique. Cette première contribution représente une avancée significative dans l'émergence d'un procédé MIP plus écologique mais d'autres travaux futurs sont encore possibles.

Preface

This PhD Thesis is a work that has been performed at the Department of Materials Science and Engineering and Chemical Engineering of the Carlos III University of Madrid (Spain) and the Department of Applied Mechanics of the FEMTO-ST Institute of Besançon (France) which is associated with the Franche-Comté University during the period from October 2010 to November 2013.

This work was performed under a mutual co-tutoring agreement between the above mentioned Universities to confer upon the candidate – if the Examining Board makes such a recommendation – the Doctoral Degree, namely:

for Franche-Comté University: *Docteur de l'Université de Franche-Comté, Sciences pour l'Ingénieur*.
for Carlos III University : *Doctor por la Universidad Carlos III de Madrid en Ciencia e Ingeniería de Materiales*.

Some parts of this doctoral thesis was developed under the frame of the project IPT-2011-0931-020000 granted from the Spanish Ministry of the Economy and Competitiveness and the European Funds for Regional Development (FEDER) in a partnership between Carlos III University of Madrid and the companies GUZMÁN GLOBAL S.L. and ALFA MIMTech.

The thesis consists of an introductory text which reviews the current state-of-art and basic principles of powder injection moulding, a presentation of the experimental work and experimental techniques carried out during this PhD Thesis and a summary of the main results which were reported in detail in the appended papers as shown below:

I. Feedstock development for Powder Injection Molding of Zirconium Silicate
E. Bernardo, J. Hidalgo, A. Jiménez-Morales, J.M. Torralba
Powder Injection Molding International 6 (1) (2012) 75-78

II. Effect of a binder system on the low-pressure powder injection moulding of water-soluble zircon feedstocks.
J. Hidalgo, C. Abajo, A. Jiménez-Morales, J.M. Torralba
Journal of the European Ceramic Society 33 (2013) 3185-3194

III. Torque rheology of zircon feedstocks for powder injection moulding.
J. Hidalgo, A. Jiménez-Morales, J.M. Torralba
Journal of the European Ceramic Society 32 (2012) 4063-4072

IV. Water soluble Invar 36 feedstock development for μ-PIM
J. Hidalgo, A. Jiménez-Morales, T. Barriere, J.C. Gelin, J.M. Torralba
Journal of Materials Processing Technology 214 (2) (2014) 436-444

V. Rheological characterization of zirconium silicate feedstocks based on water soluble binder.
J. Hidalgo, A. Jiménez-Morales, J.M. Torralba
Proceedings of Euro PM2012 Congress and Exhibition on Powder Metallurgy, Basel, Switzerland, 16th-19th September 2012

VI. Thermal stability and degradation kinetics of feedstocks for powder injection moulding – A new way to determine optimal solid loading?
J. Hidalgo, A. Jiménez-Morales, J.M. Torralba
Polymer Degradation and Stability 98 (6) (2013) 1188-1195

VII. Effect of the particle size and solids volume fraction on the thermal degradation behaviour of INVAR 36 feedstocks.
J. Hidalgo, J.P. Fernández- Blázquez, A. Jiménez-Morales, T. Barriere, J.C. Gelin, J.M. Torralba
Polymer Degradation and Stability 98 (12) (2013) 2546-2555

VIII. Mechanical and functional properties of an invar alloy for μ-MIM
J. Hidalgo, A. Jiménez-Morales, T. Barriere, J.C. Gelin, J.M. Torralba
Accepted Manuscript, Powder Metallurgy (2014)

Contribution to the appended papers

I. The candidate supervised the work carried out by E. Bernardo and performed some of the experimental work, like processing the feedstocks and parts based on CAB and PEG and helping with the other formulations. The author contributed to the manuscript writing in close collaboration with E. Bernardo. A. Jiménez-Morales and J.M. Torralba contributed with discussion of the results and supervising the manuscript.
II. The candidate designed the experimental work and performed part of the experimental work in close collaboration with C. Abajo. The candidate wrote the manuscript in full agreement with the rest of the co-authors that extensively contributed in the discussion of the results.
III. The candidate performed all the experimental work and wrote the manuscript in fully agreement of the rest of the co-authors that contributed in the discussion of the results and supervised the manuscript.
IV. The candidate performed all the experimental work and wrote the manuscript in fully agreement of the rest of the co-authors that contributed in the discussion of the results and supervised the manuscript.
V. The candidate performed all the experimental work and wrote the manuscript in fully agreement with the rest of the co-authors that contributed in the discussion of the results and supervised the manuscript.
VI. The candidate performed all the experimental work and wrote the manuscript in fully agreement with the rest of the co-authors that contributed in the discussion of the results and supervised the manuscript.
VII. The candidate performed all the experimental work except all the DSC measurements that were performed by J.P. Fernández- Blázquez. The candidate wrote the manuscript in fully agreement with the rest of the co-authors that contributed in the discussion of the results and supervised the manuscript.
VIII. The candidate performed all the experimental work and wrote the manuscript in fully agreement with the rest of the co-authors that contributed in the discussion of the results and supervised the manuscript.

List of abbreviations and symbols

2C-PIM	Two colour powder injection moulding
CAB	Cellulose acetate butyrate
CIM	Ceramic injection moulding
CPVC	Critical powder volume content
CTE	Coefficient of thermal expansion
DSC	Differential scanning calorimetry
EDX	Energy Dispersive X-ray
FTIR	Fourier transformation infrared spectroscopy
FWO	Flinn-Wall-Ozawa method
HIP	Hot isostatic pressure
HP-PIM	High pressure powder injection moulding
HV	Hardness Vickers
IDT	Initial decomposition temperature
IPDT	Integral procedure decomposition temperatue
KAS	Kissinger-Akahira-Sunose
LDPE	Low density polyethylene
LP-PIM	Low pressure powder injection moulding
LOM	Light optic microscopy
MIM	Metal injection moulding
µPIM	Micro powder injection moulding
PEG	Polyethylene glycol
PIM	Powder injection moulding
PS	Particle size
RSS	Sum of squared residuals
SEM	Scanning electron microscopy
SPD	Severe plastic deformation
SPS	Spark plasma sintering
STA	Simultaneous thermal analysis
TGA	Thermo-gravimetric analysis
TMA	Thermo-mechanical analysis
TTQ	Totalised torque
UTS	Ultimate tensile strength
XRD	X-ray diffraction

a	Carreau-Yasuda coefficient
A	Maron & Pierce coefficient
α	Conversion
α_{SVT}	Moldability Index
β	Heating Rate
C_i	Specific heat of i substance
C_u	Coefficient of uniformity
E_a	Activation energy (flow or degradation)
E_{frict}	Friction energy
E_{sp}	Specific energy of processing
E_t	Work energy
Φ	Solid loading
Φ_{crit}	Critical Solid Loading
$\dot{\gamma}$	Shear Rate
η	Shear Visvosity
η_{app}	Apparent Shear Viscosity
η_{rel}	Relative viscosity
η_∞	Infinite viscosity
η_0	Zero viscosity/reference viscosity
k	Consistency
m	Mass/ Maron & Pierce coefficient
M	Torque
n	Flow index
N	Rotational speed
R	Gas constant
R^2	Multiple correlation coefficient
ρ	Density
S_W	PS distribution parameter
t_{st}	Stabilizing time
T_{curie}	Curie Temperature
T_g	Glass transition temperature
T_m	Melting point
T_{max}	Temperature at maximum decomposition rate
τ	Yield Stress
τ_{app}	Shear Stress
τ_y	Apparent Shear Stress
vol.%	Volume percentage
wt.%	Weight percentage

1 Introduction to PIM

1.1 Introduction to powder injection moulding 3

1.2 The binder system 4

1.3 Development and optimisation of the feedstocks 7

1.3.1 Mixing and torque rheology 8

1.3.2 Rheological characterisation 11

1.3.3 Thermal characterisation 17

1.3.4 Optimising the solid loading and homogeneity evaluation 18

1.4 Injection 21

1.7 Debinding and sintering 23

1.6 Zircon and its processing routes 25

1.7 Invar and its processing routes 27

References 30

1.1 Introduction to powder injection moulding

Powder injection moulding (PIM) is a net- or near net-shape processing technology that is appropriate to the manufacturing of medium-sized to large quantities of durable components of differently complex geometries by use of metals, metals alloys, hard metals or ceramics.

Like powder metallurgy and most of the ceramic consolidation processes, PIM consist in shaping powder particles and subsequently sintering them. PIM make use of the plastic moulding concepts to shape a powder-polymer feedstock into the required geometry. The dimensions of the moulded "green part" are oversized to accommodate shrinkage during sintering. After moulding the polymer is removed to obtain the so-called "brown part" and the particles are densified by high-temperature sintering.

The final product has near full density and performance attributes that are comparable or rival those obtained by other alternative or competitive routes. They are usually superior to that encountered in traditional press-sinter powder metallurgy and investment casting. Moreover, time consuming machining and joint operations can be saved by almost limitless part designs. Faulty green parts could be reused saving material costs. Unfortunately there are limitations in the possible PIM applications. PIM needs post-moulding debinding and sintering steps that require some design considerations such as part weight, cross-sectional thickness and geometries. Furthermore, fine powders with less than 20μm are recommended [1]. In general, and typically in metals, as the powder particle size decreases the price increased. The commonly elevated cost of tooling, especially of mould manufacturing, must be depreciated with large productions. Considering these remarks PIM could be competitive with most of the processing techniques being sometimes the only alternative.

Injection moulding of metals and metals alloys (MIM) leads the global PIM industry with over the 80% of the parts production followed by injection moulding of ceramics (CIM) with around 20% of the market share. There are almost no limits to the materials suitable for PIM applications ever time that they are in the form of fine particles. However, steels capture the major interest in MIM. Around 50% of the applications are made of stainless steels and another 30% are made of other type of steels [2]. Fe-Ni alloys for magnets, Ti [3], Cu, W and superalloys share out almost equitably the rest of the applications [2]. Regarding CIM, dominant materials are zirconia and alumina based engineering materials [4].

Compared to other powder technologies, the PIM is still relatively new. In terms of global incomes PIM would be considered a relatively small industry. The MIM variant is growing at 14% per year. In 2011 MIM products were globally valued at approximately $1 billion. Estimations generally agree that MIM will double yet again to reach $2billion in annual sales by 2017. However there are evidences that PIM is reaching the end of its growth. Rather than innovation most industry R&D efforts have turned to cost reduction, improved quality, improved dimensional control, and improved impurity control. These shorter-term gains will not offset the longer-term needs for new materials, products, and applications as required to sustain MIM toward $2 billion in annual sales [2].

Since the early 1970s PIM has continuously reinvented obtaining a high sophistication level. The powder injection moulding has gained significant credibility over the last 20 years and has become prevalent in markets segments previously impenetrable, including medical implants [5, 6] and aerospace components [7]. Hence, many variants of the technology have been developed to meet the demands of each sector.

New trends are focusing on the growing demand of parts miniaturisation in many fields especially in electronics, micro mechanisms, medicine and bioscience. The MicroPIM variant has demonstrated to be an attractive alternative for micro parts replications [8-14]. Other important trends are the multi-component manufacturing methods including two-component injection moulding (2C-PIM)[15], lost-core technology [16, 17], micro in-mould levelling or sinter joining of metal and ceramics. Special considerations have to be taken into account in all these novel processes. MicroPIM technology needs of submicrometer powders and faces the challenge of developing suitable feedstock and high precision miniaturized mould cavities. 2C-PIM requires compatible coefficient of thermal expansion materials and a tailored study of the shrinkage of different part components.

Both macroscopic and microscopic production increasingly demand effective and realistic simulation tools enabling the modelling and calculation of multi-component material systems for powder injection moulding and allowing the prediction of segregations and sintering deformation [18-21].

It can be concluded that PIM still requires R&D efforts to progress in the comprehensive investigation of the material-parameter-properties interdependences especially demanded in new trends and process simulation. PIM also needs the enlargement of the range of suitable materials for the development of future fields of application.

1.2 The binder system

In the PIM technology, the binder development is considered as the key point. Generally, a binder system has the main commitments of giving the necessary rheological behaviour to the feedstocks for injection moulding and the cohesion to the green part. It is the binder system that transports the powder particles into the mould cavity during the injection stage and holds the required shape during ejection, debinding stages and the beginning of the sintering stage. The binder should provide good flowability to the feedstock in the melted state and rigidity and strength in the solidified state. The binder system is a transitory element of the feedstock that does not remain in the final part and consequently has to be removed. This fact adds extra requirements to the characteristics of binder systems: easy, rapid, clean and defect free elimination process during debinding. Economical and environmental concerns have to be also taken into account when selecting a binder system [4, 22].

Even though during decades a vast variety of binder systems have been developed for PIM processes, to date it could be stated that there is not an ideal solution yet that solve all concerns regarding binder systems. However, this quest to find the philosophers stone of PIM

has created lots of possibilities for components and processes selection. It is a very important but a difficult task to select the appropriate components between the different possibilities as the binder system will determine almost the whole PIM process and its success.

Binder systems are formulated as a mixture of different organic or inorganic substances with several functions within the binder system. A binder system could be composed of any type of polymers, waxes, oils, even water or other substances like lubricant agents and dispersants. Binders can be classified according to the nature of their components, specially the so-called back-bone component that gathers the particles and retain the shape along all the stages before debinding. Another classification considers the subsequent debinding process.

A full thermal debinding commonly is time-consuming due to the slow heating rates necessary; trapped volatiles may build up internal pressures if their diffusion is hindered causing cracks and voids. Several compounds with progressive softening points and elimination temperature ranges are selected in these cases [23]. The green parts can be embedded in a powder bed serving as a wicking media during thermal debinding aiding the extraction by capillary forces [10, 24, 25]. Debinding processes typically combines a first extraction of one or several components by a solvent followed by a thermal elimination of the remaining components. The interconnected channels created during solvent debinding allow a more effective extraction during subsequent thermal step minimising the risk of defects formation. Other sophisticated debinding methods like plasma [26-28] assisted or catalytic debinding [16, 17, 29, 30] outstand for their very fast extraction rates but requires of high investments and/or the use of hazardous chemicals products.

Table 1. 1 Some wax based thermoplastic binder compositions, the powder material and the debinding type.

Binder components in wt.% (* vol.%)	Powder and Application	Ref.
60 paraffin wax, 15 HDPE, 10 PP, 10 PS, 5 stearic acid	Fe-50Ni: trichloroethylene solvent + thermal	[31]
25 paraffin wax, 20 carnauba wax, 20 bees wax, 25 EVA, 5 PP, 5 stearic acid *	316L stainless steel	[32]
50 Paraffin wax, 50 PE	Bronze	[33]
45 LDPE, 55 paraffin wax, 5 stearic acid	316L stainless steel	[34]
59 paraffin wax, 16 microcrystalline wax, 15 EVA, 5 HDPE, 5 stearic acid	17-4 PH steel	[35]
Ultraform® Z2320 (POM based)	Several powder type, catalytic debinding	[29]

Thermoplastic binders are preferred in PIM. The feedstock can be softened and re-solidified several times which is beneficial to reutilise waste material produced during injection and faulty green pieces. Thermoplastic polymers commonly chosen for PIM are polyolefins like polyethylene (PE)[33] and polypropylene (PP) in their different variants [9], polyacetal (POM)[29], polymethyl metacrylate (PMMA)[36], ethylene vinyl acetate (EVA)[32] and polyvinyl butyral (PVB)[37] just to mention some of them. These polymers are commonly

blended with waxes or other low molecular weight polymers like polyethylene glycol (PEG) that act as plasticizers and could have the double mission to be removed by a solvent debinding followed by thermal degradation of remaining components. Some examples of thermoplastic polymers mixed with waxes binder systems are collected in Table 1. 1. Waxes could be used solely as binders, but due to its low viscosity and low molecular weight they fail in drawing together powder particles. Therefore waxes are restricted to low injection moulding pressures (LP-PIM) where the risk of disaggregation between powder and binder is diminished compared to high pressure processes. Furthermore, waxes need hazardous and expensive organic solvents to be removed. Current tendencies are substituting these waxes by PEG since these binders can be subjected to a solvent debinding in more sound and economic water. Table 1. 2 presents some PEG based binders. Examples of commercial water soluble formulations are PolyMIM®, AquaMIM® and Inmafeed®. Auzène et. al. [38] investigated these commercial binder systems. PolyMIM® most likely is based in PP and PEG, AquaMIM® in PE associated with saccharide polyhydric alcohol, cellulosic, glycolic, etc, and Inmafeed in a polyether type PE or polypropylene glycol as deduced from their infrared spectrum [38].

Table 1. 2 Some examples of PEG based binder characterised by a solvent debinding in water step.

Binder components in wt.% (* vol.%)	Powder and Application	Ref.
87 PEG, 11PMMA, 2 stearic acid	Ti6%Al4%V	[36]
65 PEG, 30 PP, 5 stearic acid	Steatite	[39]
60 PEG, 35 PE, 5 stearic acid	316L stainless steel	[40]
PEG/PVB * 2:1 + stearic acid	Alumina, Ti6Al4V	[37, 41]

Thermosets polyesters, polyurethanes, epoxies and other resins binders are scarcely employed due to once they acquire rigidity after a curing process they lose the capacity of being reprocessed. Nevertheless, thermosets present the advantage of obtaining green pieces with a higher green strength and stiffness compared with other binder systems, which in some cases could be necessary. Normally thermosets are more thermally stable than other polymers and require higher temperatures for decomposing them. Therefore the risk of materials contamination with carbon increases in such cases. Examples of thermosets used as binder system could be found in Rodriguez-Senin et. al. [42], Castro et. al. [43] and Levenfeld et. al. [44].

There is a special group of binder systems based on thermogelling substances mixed with water. These substances are frequently polysaccharides like carrageenans [45], starch, cellulose derivatives [46] and the widespread group of agar [6, 47-50]. The injection moulded green parts show a gel type behaviour and are flexible or rubbery until they have been dried. The main advantage of this type of binders is that the thermogelling substance is added in a very low percentage which reduces drastically the organic component compared with other binder systems. In the other hand, these binder systems are restricted to LP-PIM processes because severe shear forces could break the three dimensional gel net and cause water migration within the bulk impeding the flow. Other critical issues for these systems include

the need of careful control of the feedstock's environment, as the water content determines the flow behaviour and solid loading content. These binders are susceptible of bacteria or fungi colonies formation and of rusting metallic powders, consequently a storage problem arises. Feedstocks can be dried for storage and rehydrated at the time of injection process. Antibiotic or antirust substances may be also added.

Aromatic compounds are other alternatives to traditional solvent and thermal debinding. The advantage of aromatics such as naphthalene, anthracene, and pyrene [51] is that they melt at relatively low temperatures and can be completely removed by sublimation under reduced pressure at temperatures below their melting point. However they low molecular weight still makes necessary the use a backbone polymer that anyway shall be thermal degraded at high temperatures. Furthermore, many of these substances are considered carcinogenic with the evident health risk.

To end with this brief binder review just to mention relatively recent binder systems based on thermoplastic polysaccharides. Thermoplastic polysaccharides are long chain polymers that commonly derive from natural raw sources like cellulose or starch. Examples of these thermoplastic polymers are cellulose acetate (CA), cellulose acetate butyrate (CAB) [52-55], cellulose acetate propionate (CAP), thermoplastic starch (TS) [56] and starch acetate, to mention some of them. As the majority of the carbons in their molecules come from fixation of atmospheric CO_2 by vegetables photosynthesis processes, the burn off of these polymers generate an almost 0 net CO_2 emissions. Substitution of these polymers to conventional petroleum derivative polymers is currently investigated for many applications due to its positive effect in the reduction of the global introduction of CO_2 into planet habitats from petroleum sources. They could also introduce positive economical aspects by reduced cost of natural raw materials easily harvested instead of the costly extraction of more and more depleted petroleum deposits which continuously increase the prices of its derivatives. Some examples of polysaccharide based binders can be found in Table 1. 3.

Table 1. 3 Some examples of thermoplastic polysaccharides binder systems.

Binder components in wt.%	Powder and Application	Ref.
41.3 starch, 23.3 glycerol, 28.5 LLDPE, 1.9 citric acid, 5 stearic acid	316L stainless steel: thermal	[56]
65 PEG, 25 PMMA, 10 CAB	316L stainless steel (MicroPIM): solvent in water + thermal	[52, 54]
65-80 CAB, 0-25 PEG, 0-20 glycerine [vol.%]	Catalytic debinding	[55]
2 Agar, 0-2 sucrose, water balanced	Porous NiTi: thermal	[48]

1.3 Development and optimisation of the feedstocks

Once the binder system and the powder are selected for a certain application, mixtures thereof (i.e feedstocks) have to be characterised and optimised. There are many physical properties

that can be characterised from a feedstock that would be used to design the processing conditions or to determine computer simulation parameters. From mixture homogenisation to binder removal, the behaviour of the feedstock has to be understood to obtain the best results possible. One key issue of special interest is to determine the optimal and critical solid loading of a feedstock as well as homogeneity. Elimination of the binder system out of the green body is the bottle neck in MIM processes and a critical and delicate step. It requires tailored optimisation of the time-temperature cycle in order to be economical and effective while avoiding faults like undesirable blistering [57]. These issues will be discussed in this section

1.3.1 Mixing and torque rheology

The torque rheology is a helpful method to characterize the evolution of the mixing of the feedstock components. It is suitable to have an idea of how easy the components are mixed and roughly to determine the homogeneity [58-60]. Moreover, it could be used to estimate the critical and optimal solid loading [61, 62]. Torque rheology mainly consists in monitoring the evolution of torque (M) over the mixing experiment. The torque represents the momentum that has to be exerted upon the rotors to displace the feedstock's components during the blending process. It has the units of Newton per metre [N·m]. Figure 1. 1 shows typical torque vs. time curves of a feedstock with variable solid loadings.

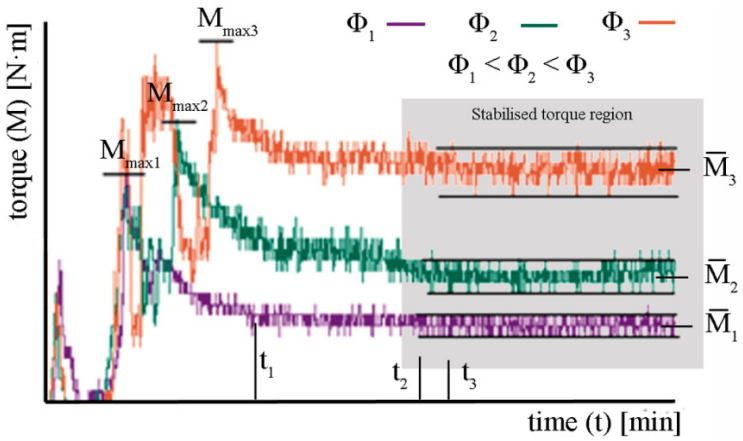

Figure 1. 1 Typical torque vs. time curves of a feedstocks with variable solid loadings (Φ_1, Φ_2, Φ_3 / $\Phi_1 < \Phi_2 < \Phi_3$). The parameters t1, t2 and t3 represent the stabilising times of the different feedstock and thus the optimal mixing times. The maximum and averaged torques are also represented with a upper and a lower limit. The difference between these upper and lower limit is representative of the feedstock homogeneity and the binder capacity to admit powder [58].

The evolution on the feedstock's torque values during the mixing process allows determining when the components are completely mixed and if this mix is homogeneous. Thereby, the optimum mixing time can be assessed. This optimum will be the minimum time to obtain stable values of the torque as observed in the torque vs. time curves or torque rheograms (Figure 1. 1). When stable values of the torque with time are observed, it means that the system presumably is not going to evolve to a different state thus the best mixing state is achieved. To some extent it means that a homogeneous mix is obtained, although what it really means is that the demixing rate (e.g. due to powder-binder separation by shear forces)

is equilibrated with mixing rate[63]. Obviously at this point it is not worth to continue mixing taking the risk of degrade some of the binder components.

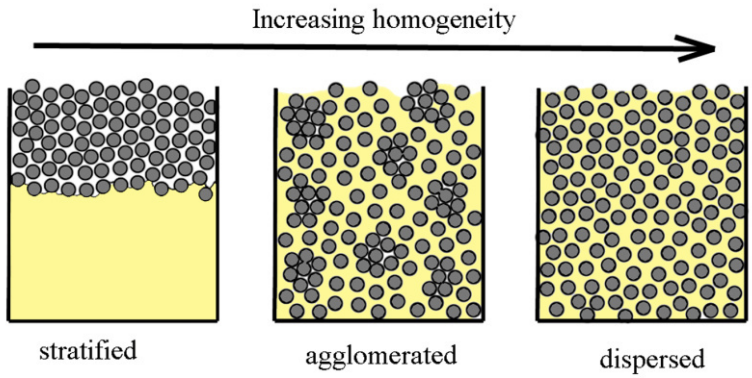

Figure 1. 2 Different levels of homogeneity depending how well the powder is dispersed within the binder.

In the stabilised torque values regions of the Figure 1. 1, variations of the torque values with time are still observed, but the global tendency is that they vary around a constant average value ($\bar{M}$). The differences between the upper and the lower torque values determine the grade of homogeneity of the feedstock (Figure 1. 2) and the facility of the binder to incorporate powder particles [58, 64]. The following explanation is proposed:

> In a completely homogeneous and dispersed feedstock there would not be regions with different composition and the torque value most likely will not vary with time. This is an ideal situation that in practice is impossible since lot of factors like particles and molecules are not equal in size, immiscibility between binder components, different wetability of binder components upon the powders, static forces that produce particle agglomerates, etc. If there are some regions with an excess of binder, consequently there should be other regions with an excess of powder. This is what Figure 1. 2 tries to schematize. The excess of binder would tend to reach the powder-rich areas and the powder would tend to admit this excess to minimise the flow energy. This situation obviously occurs at the first stages of the mixing process when particle clusters (lack of binder) are surrounded by binder reach areas. This also occurs in the stable torque region even though if a good dispersion is achieved. Depending on the feedstock and its components, instabilities in the flow may cause powder-binder segregations creating again powder and binder rich regions. Aggregation and disaggregation of powder particles to the binder would cause the observed torque variations. As there are more incompatibilities between the powders and binder components and/or there is less binder to properly coat the powder particles (thus there would be more competition between particles for the binder) these torque variations would be more pronounced (see Figure 1. 1). That fact could be a signal of the proximity to the critical powder volume content (CPVC) as it will be explained in following sections.

The torque is proportional to the feedstock viscosity, i.e. it is related with the flow capacity of the feedstock. Therefore it is affected by all the parameters affecting viscosity (shear rate

controlled by rotor speed, temperature that can be regulated by heating plates, solid loadings and intrinsic characteristics of the feedstock, to mention some). These parameters also affect to the mixing efficacy. According to Roetenberg [65], increasing the mixing speed increases the mixture homogeneity. The sequence of compounds addition to the mixer chamber [66] and how much this chamber is filled also influence the torque results and the efficacy of mixing.

Torque rheology is not a suitable method to evaluate viscosity [67, 68]. The shear rates are not constant along the volume of the rheometer. It has an intricate geometry copied from that of the industrial mixers or kneaders that are designed to maximize the shear stress and thus the mixing. However a rough estimation of viscosity could be made considering simpler geometries for the calculus [67]. Therefore the torque allows for making comparative measurements between different materials reproducing real mixing conditions. Nevertheless, to carry out these comparative studies it is necessary to measure under the same conditions, i.e. keeping constant the rotors speed, the volume of the sample, the temperature, the geometry of the blades, the incorporation of compounds sequence, etc. Unfortunately torque rheology lacks of a standard. Hence it becomes almost impossible to compare bibliography results.

Table 1. 4 collect some expression to determine mixing energies by torque rheology. The torque is interrelated with the work performed by the mixing equipment to mix all the compounds. This work can be estimated by the totalised torque, which represents the total area under the torque vs. time curve and has units of (J·min) (Eq.1.1). This parameter has been used to estimate the relative network strength in suspensions [69], or the processability of polymer-filler composites [70]. However, to the best of the author knowledge, it has never been used in PIM feedstock studies.

Table 1. 4 Expressions to determine different processing energies with torque results.

Expression	Eq.	Remarks about the expression	Ref.
$E_t = F \cdot d = \\ = 2 \cdot \pi \cdot r \cdot N \cdot \int_{t1}^{t2} \left(\frac{M(t)}{r}\right) \cdot dt = \\ = 2 \cdot \pi \cdot N \cdot TTQ$	Eq.1.1	E_t= work energy supplied to the system by rotors [J]; F=force [N]; d=displacement [m]; r= average blade radius [m]; N= angular speed [rpm]; t= time [min]: TTQ [J·min]	[69, 71]
$E_{sp} = E_t \cdot m_{feed}^{-1}$	Eq.1.2	E_{sp}= specific energy of processing [J·g^{-1}]; m_{feed}= feedstock's mass [g]	[69, 71]
$E_{frict} = c_{feed} \cdot \Delta T_{oh}$	Eq.1.3	$E_{friction}$= energy dissipated by heat due to friction [J·g^{-1}]; c_{feed}= feedstock's specific heat [J·g^{-1}·ºC^{-1}]; ΔT= temperature increment from programmed [ºC]	*

*Proposed by author according to basic thermodynamics

Moreover, few works related with PIM were found that monitored the feedstock's temperature during mixing. Reddy [72] reported that increasing rotor speed makes the temperature rise during mixing due to the amount of energy input by mixing blades was converted into heat during shearing of the mix. By previous experience in the field, the author realised that the temperature of the feedstock increases with respect the programmed temperature during

mixing. This is most likely consequence of friction energy dissipation in form of heat. This energy might be also estimated (Eq.1.3) and balanced with the specific energy of processing (Eq.1.2) to determine the mechanical energy dissipated by particle friction. This would allow, for example, determining the effectiveness of a binder to coat and lubricate powder particles.

1.3.2 Rheological characterisation

The most faithfully way to characterize the flow behaviour of a melted feedstock is studding its viscosity and the dependence of this property with different parameters. Feedstocks in their fluid melted states are complex compared with single phase fluids. They are composed of both a multiple component binder, which remains in a melted state during feedstock elaboration and the injection moulding stage, and a high charge of fine particulate solid powders. Hausnerova [68] compiled a thorough review about feedstock rheology that highlights that interpreting rheological experimental data for PIM feedstocks is not always a simple task. A capillary rheometer is preferred than other types of rheometers to measure feedstock viscosity due to they reproduce more faithfully the conditions experienced by feedstocks in the PIM process. However, because of the measuring method peculiarities some corrections are necessary to obtain real values of the viscosity. In a conventional capillary rheometer a transducer record the pressure at the capillary entrance. Depending on the capillary configuration, this pressure drop is then transformed into a shear stress; with the shear rate controlled by the piston velocity, the viscosity can be obtained as the proportionally constant between the shear stress and the shear rate (see Newton equation in Table 1. 5). Before knowing the real nature of the feedstock a Newtonian behaviour is assumed to assess the shear rates. After the measurements, the shear rate should be corrected considering the real flow behaviour by the Weissenberg-Rabinowitsch correction [73, 74] in the case on non-Newtonian fluids. The Bagley's correction [75] estimates the overpressure at the capillary entrance that is subtracted to the transducer pressure to obtain the pressure inside the capillary. The Mooney analysis [76] takes into account the slip at capillary's wall which introduces errors in the viscosity measurements. These corrections increases the number of experiments thus, for comparative proposes at the same measuring conditions, apparent viscosity is commonly used.

The viscosity of a single phase fluid depends mainly on five parameters: physical-chemical nature of the substance, its temperature, the shear rate, pressure and time [67]. In the case of melted feedstocks, the physical-chemical nature is dependant of the binder viscosity, particle morphology and particle size distribution, interaction between powder surfaces and binder, etc. Moreover, the powder fraction mixed with the binder (the solid loading) plays a noteworthy role in feedstocks' rheology.

a) Feedstocks' components characteristics

Depending on binder system used for feedstock elaboration, the viscosity could vary markedly. For the same polymeric compound, viscosity of blends could fluctuate depending on characteristics like the molecular weight or the level of branched chains and thereby

affecting feedstocks viscosity [77, 78]. It is also important to consider binder-particle interactions. The importance of filler interactions to viscosity of a filled melt decreased as viscosity of polymer component rises. The stress contribution from filler could be considered constant, and therefore as stress contribution from a polymer binder increases, the relative importance of filler is reduced. It is extensively accepted that the viscosity of a binder should be around 1-10 Pa·s considering a posterior notorious viscosity increment when the powder is added. The rule normally says the less the binder viscosity the better, but this consideration should be taken carefully. Low viscosity could lead on a reduction of the shear forces necessary to i.e. disperse the particles or break agglomerates. Separation of the binder from powder during flow could also occur resulting on defects if binder viscosity is low or it doesn't provide suitable interactions with powder.

In addition, Contreras [79] and Sotomayor [80] demonstrated that particle size, particle size distribution and particle morphology are strongly influential factors on the rheology of PIM feedstocks. Senapati [81] obtained a correlation coefficient, $10 \cdot C_u/d_{50}$, that relates particle size characteristics to the viscosity of high filled ash slurries. The coefficient of uniformity, C_u, is defined as the ratio d_{60}/d_{10}. C_u has been demonstrated to be a useful parameter to relate the particle size distribution with the powder packing capacity and, thus, with the properties of the final piece. The higher the value of C_u, the larger the range of the particle sizes in the sample and, hence, the larger the effect on the viscosity of the feedstocks with high solid loading concentrations.

b) Temperature

At temperatures sufficiently far above the softening point of the binder system the relationship between the viscosity and the temperature typically follows an Arrhenius-type behaviour [82] as expressed in Eq.1.4:

$$\eta(T) = B \cdot \exp\left(\frac{E_a}{R \cdot T}\right) \qquad \text{Eq.1.4}$$

where T is the absolute temperature, B refers to the reference viscosity, R is the gas constant and the E_a parameter that represents the flow activation energy.

The study of the viscosity dependence on the temperature is very relevant in PIM. During the injection stage, the feedstock suffers and abrupt change of temperature just at the time it passes from the nozzle to the mould sprue and runners. If the dependence of the viscosity on temperature is noteworthy, a great variation in the viscosity may occur during the mould filling that would induce to faults in the green parts. The E_a is a very suitable indicator of the feedstock's viscosity dependence on the temperature. High values of E_a imply a high viscosity dependence on the temperature and, thereby, they are pernicious for the injection process.

The activation energy can be easily deduced from the linearization of Eq.1.4 by taking the natural logarithm of both sides of the expression. The slope of the resulting straight line

representing $\ln(\eta)$ vs. the inverse of temperature corresponds to E_a. Allaire et al. [83] proposed the activation energy value of 40 kJ/mol as the level above which the probability of defects occurring during injection moulding becomes unacceptable for sub-micrometer zirconia blends.

To end with temperature parameter, just to mention that there are other models that can be used to describe the relationships between viscosity and temperature. The William-Landel-Ferry (WLF) equation (Eq.1.5) [84] models the viscosity behaviour with temperature at all temperature conditions and was especially formulated for polymers and other substances that have a glass transition temperature:

$$\eta(T) = \eta_0 \cdot exp\left[\frac{-C_1 \cdot (T - T^*)}{C_2 + T - T^*}\right] \qquad \text{Eq.1.5}$$

where C_1, C_2, T* and η_0 are empiric parameters (only three of them are independent of each other) and are determined by curve-fitting. Typically, T* is set to match the glass transition temperature.

c) Shear rate

The viscosity of a feedstock is commonly very affected by the shear rate at the typical range of PIM processes. Figure 1. 3left shows different viscous behaviours plotted in a shear rate vs. shear stress curve. A review of the most common mathematical models used to describe viscous behaviours of several types of fluid in made in Table 1. 5.

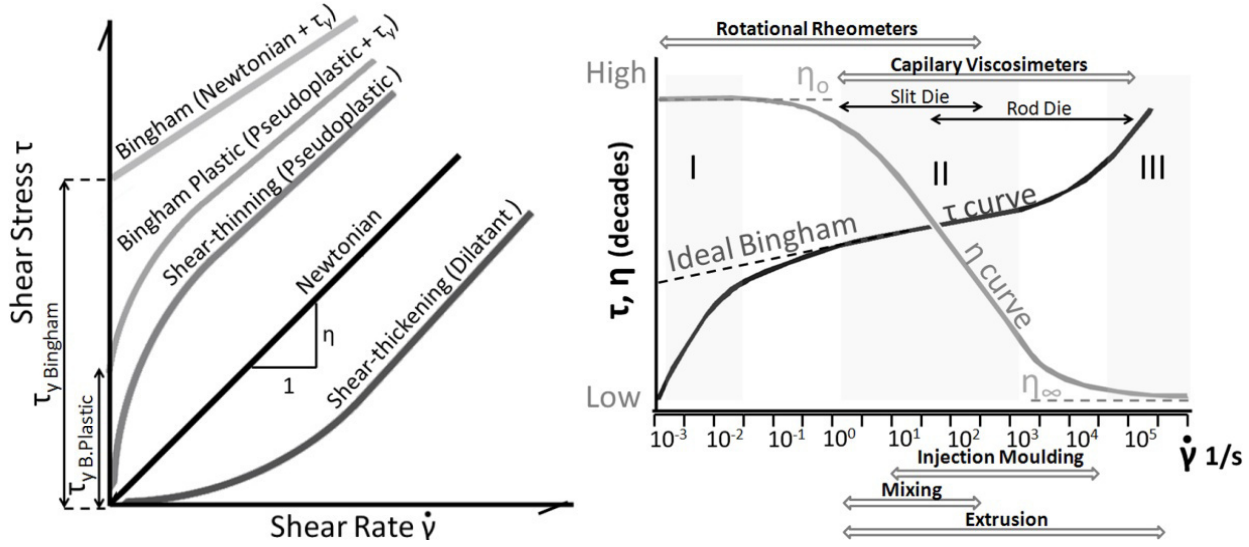

Figure 1. 3 (left) Different fluid behaviours represented by their typical shear stress vs. shear rate curves (based on [67]). (right) Common shear rate ranges for several manufacturing processes and devices for measuring the viscosity; typical feedstocks viscosity vs. shear rate and shear stress vs. shear rate curves showing combined Newtonian and pseudoplastic behaviours along a wide shear rate interval (based on [67]).

For many fluids, including melt polymers and feedstocks, three or more zones can be distinguished in the curve that describes the influence of viscosity with shear rate (Figure 1. 3right). It is worth to note that different rheometer-types are more or less suitable to measure viscosity depending on the shear rate region and that different processing techniques involve different levels of shear rates.

In the low shear rate region, a Newtonian plateau is typically observed which begins to curve at a certain shear rate. Then a pseudoplastic region comes after to end up in a subsequent Newtonian region at high shear rates. The physical explanation of this change of behaviour with shear rate is not well understood jet; however there are many accepted plausible theories that relate them with changes in the internal molecular structure of the fluid, alignment of the polymeric chains and powder particles, segregations of powder and binder, etc.

The Cross [85] and Carreau-Yasuda [86] models are very suitable to explain the three typical stages of the viscosity vs. shear rate curve. The η_0 is the zero shear viscosity, i.e the magnitude of the viscosity at the lower Newtonian plateau at very low shear rates. It is an intrinsic property of the fluids which present such a kind of behaviours. The η_∞ is the infinite shear viscosity. This parameter tells how the fluid is likely to behave in very high shear processing situations.

Table 1. 5 Models linking the viscosity or the shear stress with shear rate.

Model name	Expression	Model name	Expression
Newton	$\tau = \eta \cdot \dot{\gamma}$	Power law [87]	$\tau = k \cdot \dot{\gamma}^n$
Cross [85]	$\eta = \eta_0 + \frac{(\eta_0 - \eta_\infty)}{1 + (k \cdot \dot{\gamma})^{1-n}}$	Carreau-Yasuda [86]	$\eta = \eta_0 + \frac{(\eta_0 - \eta_\infty)}{(1 + (k \cdot \dot{\gamma})^a)^{\frac{1-n}{a}}}$
Sisko [88]	$\tau = \eta_\infty \cdot \dot{\gamma} + k \cdot \dot{\gamma}^n$	Bingham [89]	$\tau = \tau_y + k \cdot \dot{\gamma}$
Herschel-Bulkley [90]	$\tau = \tau_y + k \cdot \dot{\gamma}^n$	Casson [91, 92]	$\tau^{1/2} = \tau_y^{1/2} + (\eta_\infty \cdot \dot{\gamma})^{1/2}$

η=viscosity [Pa·s]; τ=shear stress [Pa]; γ= shear rate [s^{-1}]; n= flow index; η_0=zero viscosity [Pa·s]; η_∞=infinite viscosity [Pa·s]; k=consistency [s]; τ_y= yield stress [Pa]; a =equation coefficient []

The parameter m in the Cross and Carreau-Yasuda models is known as the rate constant. It is dimensionless and is a measure of the degree of dependence of viscosity on shear rate in the shear-thinning region. A value of zero for m indicates Newtonian behaviour with m tending to unity for increasingly shear thinning behaviour. The k parameter is a time constant (sometimes it is referred as consistency) and has dimensions of time. The reciprocal, 1/k, gives us a critical shear rate that proves a useful indicator of the onset shear rate for shear thinning region. The Carreau-Yasuda model is a generalisation of the Carreau model by introducing the a parameter. In Carreau model the a parameter is equal to 2.

If the zero viscosity takes an infinite value and the infinite viscosity takes the value zero, the Cross model is converted in the Ostwald-de-Waele power law [87]. This model is useful

because of its simplicity, but only partially describes the behaviour of real non-Newtonian fluids. For example, if *n* (also known as flow index) were less than one, the power law predicts that the effective viscosity would decrease with increasing shear rate indefinitely, requiring a fluid with infinite viscosity at rest and zero viscosity as the shear rate approaches infinity, but a real fluid has both a minimum and a maximum effective viscosity that depend on the physical chemistry at the molecular level. Therefore, the power law is only a good description of fluid behaviour across the range of shear rates to which the coefficients were fitted.

There is a second set of equations that try to describe mathematically viscoplastic fluids which present a yield point (τ_y): Bingham [89], Casson [92] and Herschel-Bulkley [90]. In PIM feedstocks this feature may be appear depending on the type of dispersed particles and especially on particle size. It is generally accepted that PIM feedstocks has to overcome a threshold values of the shear stress to flow, i.e. a yield point. However the existence of a yield stress is still controversial[68]. Cross and Carreau-Yasuda models can be modified to introduce the occurrence of a yield point [93].

Table 1. 6 Models linking solid loading and relative viscosity

Model name	Expression	Model name	Expression
Eilers [94]	$\eta_{rel} = \left(1 + \frac{1.25 \cdot \phi}{1 - \frac{\phi}{\phi_{crit}}}\right)^2$	Chong et al. [95]	$\eta_{rel} = \left(1 + \frac{0.75 \cdot \frac{\phi}{\phi_{crit}}}{1 - \frac{\phi}{\phi_{crit}}}\right)^2$
Mooney [96]	$\eta_{rel} = \exp\left(\frac{2.5 \cdot \phi}{1 - \frac{\phi}{\phi_{crit}}}\right)$	Mills [97]	$\eta_{rel} = (1 - \phi).\left(1 - \frac{\phi}{\phi_{crit}}\right)^{-2}$
Krieger and Dougherty [98]	$\eta_{rel} = \left(1 - \frac{\phi}{\phi_{crit}}\right)^{-2.5 \cdot \phi_{crit}}$	Quemada [99]	$\eta_{rel} = \left(1 - \frac{\phi}{\phi_{crit}}\right)^{-2}$
Maron & Pierce [100]	$\eta_{rel} = A \cdot \left(1 - \frac{\phi}{\phi_{crit}}\right)^{-m}$	Reddy et al.[101]	$\eta_{rel} = \frac{\phi_{crit}}{\phi_{crit} - \phi}$

η_{rel}= relative viscosity [];ϕ =solid loading [vol.%]; ϕ_{crit}=critical solid loading [vol.%] ; A,m=coefficients

d) Solid loading

At high solid loading the viscosity of a feedstock is very sensitive to solid loading. Viscosity generally increases with addition of powder particles. A large number of works are found in the literature regarding the study of the relationship between viscosity and the solid loading. In Table 1. 6 a brief selection of the most conventional models is compiled. All of the models relate the relative viscosity (η_{rel}), which is the value of the feedstock viscosity divided by the binder viscosity, to the solid loading content (ϕ), reflecting that the binder viscosity is highly related to the global feedstock viscosity. These models also fulfil the condition of an infinite

value for the relative viscosity when solid loading displays the critical value ϕ_{crit} which is consistent with reality. Typical relative viscosity vs. solid loading curves for different PIM feedstocks with different packing factor (PF) powders can be seen in Figure 1. 4. The packing factor influences de critical solid loading ϕ_{crit} that is delimited by the asymptotic red lines.

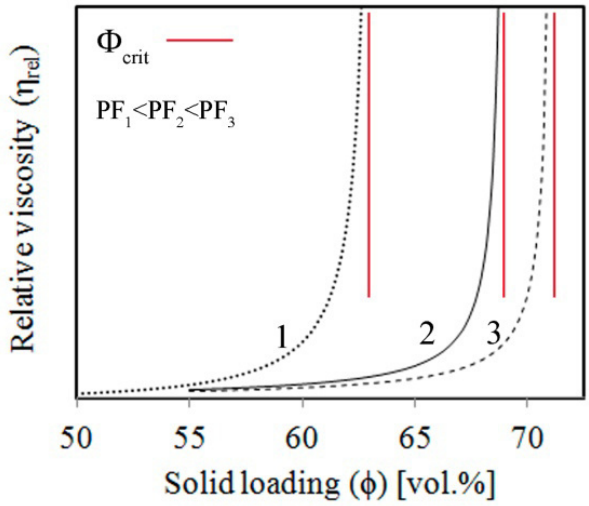

Figure 1. 4 Typical relative viscosity vs. solid loading curves for different PIM feedstocks based on the same binder system but loaded with different packing factor (PF) powders. As it can be seen from figure, the packing factor influences de critical solid loading (Φ_{crit}) that is delimited by the asymptotic red lines.

e) Pressure and time

The fluids' viscosity increases exponentially when an isotropic pressure is applied. The theory of "the free volume" can describe the variations of apparent viscosity with pressure in a polymer melt. As the pressure rises, the free volume decreases hindering the mobility of the macromolecules, thus increasing the viscosity. The pressure effect is more influent at low temperatures, being it almost irrelevant at temperatures far above the glass transition temperature. Generally, in polymer injection moulding this variable has to be considered due to the elevated pressures during this process. In PIM, a high percentage of the feedstock volume is composed of powder which barely is affected by pressures during injection. Hence the variation of viscosity associated to pressure in PIM feedstock is commonly low, especially at high temperatures, and conventionally have been depreciated. However, some authors have begun to consider this underestimated parameter in order to produce more reliable models to simulate feedstock flow behaviour [102-104].

The viscosity of some substances, usually dispersions, depends on the previous shear history, i.e. on the length of time the substance was subjected to continuous shear or was allowed to rest before tested. This can occur due to orientation or molecules or particles, creation of new bonds, etc. with time or under the influence of increasing shear.

1.3.3 Thermal characterisation

Knowing the behaviour of the feedstock with temperature is essential to correctly design some of the key steps and to determine parameters and models for computational methods in PIM technology. The temperature at which feedstock softens (glass transition for amorphous and melting temperature for semicrystalline polymers) and rigidifies (solidification temperature) is relevant for the optimisation of the mixing, the injection and the debinding steps avoiding defects. These temperatures depend on the binder components individual behaviour and can be assessed by a differential scanning calorimeter (DSC). Details of the DSC method can be consulted in Salomon and Fielder [105]. Specific heat is an additional property that can be obtained from thermal analysis. This parameter along with thermal conductivity is of common use for the purpose of PIM feedstock modelling, especially for modelling cooling after moulding [21].

The thermal stability and degradation kinetics of a feedstock determines the processing temperatures. Feedstock should not degrade and decompose during mixing and injection, but have to be successfully eliminated during thermal debinding. Thermogravimetric analyses (TGA) allow measuring the weight loss with time and temperature by isothermal or rate controlled heating.

Thermal stability of feedstocks could be evaluated by determining the initial decomposition temperature (IDT) and the integral procedure decomposition temperature (IPDT). The IDT is determined by the onset weight loss in the TGA curves. The method for calculating the IPDT is proposed by Doyle [106, 107] and converts the area under the TGA curve into a value that approximately represents the characteristic end-of-volatilisation temperature. In Paper 6 and Paper 7 and explanation of how to determine IPDT by TGA curve can be found.

For multi-component binders obtaining optimal thermal debinding cycles is a difficult task that conventionally has been performed by “trial and error”. However recent works propose to investigate the binder decomposition kinetics in order to identify points of rapid weight loss to avoid green parts damage, to speed up the debinding process and lower the overall cost [108-110].

The thermal burn out of organic components during debinding processes of MIM feedstock is intricate. There are several decomposition mechanism involved which are also dependant on several factors. Transport and elementary reactions steps could be rate limiting during debinding. Transport mechanisms would become more influent with increasing sample thickness, whereas in thin specimens such as in micro components, polymer decomposition kinetics would play a predominant role [111].

Regarding the study of the decomposition kinetics, a thorough discussion about the convenience of using model-free isoconversional methods to analyse thermal decomposition of MIM feedstocks instead of conventional isothermal methods could be found in the work of

Salehi [111]. Model-free methods turn out to be the most reliable way to determine kinetic parameters of thermally activated complex processes, because the prior knowledge of the reaction mechanism is not necessary [112]. These methods are based on studying the degree of conversion (the mass loss at a certain time with respect to the total mass loss) with respect to temperature at different heating rates.

In the model free methods decomposition apparent activation energy (E_{ad}) and other kinetic parameters are calculated directly from the TGA curves. The term apparent activation energy comes for the uncertainty of the physical process associated to this activation energy; activation energy most likely takes into account several different processes occurring at the same time. In literature a wide variety of non-isothermal models could be found. Paper 6 and Paper 7 explains the Kissinger-Akahira-Sunose (KAS) [113] and Flynn-Wall-Ozawa (FWO) [114, 115] isoconversional methods in detail. The lack of agreement among kinetic parameters calculated from the same set of experimental data using different methods of mathematical analysis is disturbing. It has been shown that the causes for these differences are due to the intrinsic nature of the methods [116].

1.3.4 Optimising the solid loading and homogeneity evaluation

The optimal solid fraction in the feedstock composition is one of the most important parameters that have to be defined in a PIM process. The solid loading determines all the process stages from mixture to sintering. A suitable solid loading have to allow a good flowability of the feedstock during injection, a rapid and defect-free debinding stage and good tolerances and properties of the final part among other important demands. Therefore defining an optimal solid loading is not always a simple task. The process involves evaluating different features that principally requires developing full PIM processes of different solid loadings feedstock which is time consuming.

Ideally, at critical solid loading the maximum particle packing is achieved. Particles are touching and the free volume left is completely filled by the binder system, therefore there is not mobile binder to contribute in the feedstock flow. At solid loading higher than the critical, there is not enough binder to fill the interparticle free volume, thus voids are created. An excess of binder is also not desirable. All this situations also typically lead on heterogeneities and defects and should be avoided.

Generally, the optimal solid loading is considered between 3% and 5% lower than the critical solid loading. The optimal solid loading is classically defined as the ratio of powder to binder near the critical solid loading level at which the particles are tightly packed but there is still sufficient mobile binder to coat them and allow a good flowability. This situation generally leads to defect-free and good part reproducibility at the end of the sintering stage.

Depending on if there is an excess of powder, and excess of binder, the feedstock has the critical or the optimal powder content, these situations have implications in the way the

feedstocks flow and the properties of the feedstocks which makes possible the estimation of the critical and optimal solid loading by conventional methods with different levels of accuracy. They are briefly summarised below.

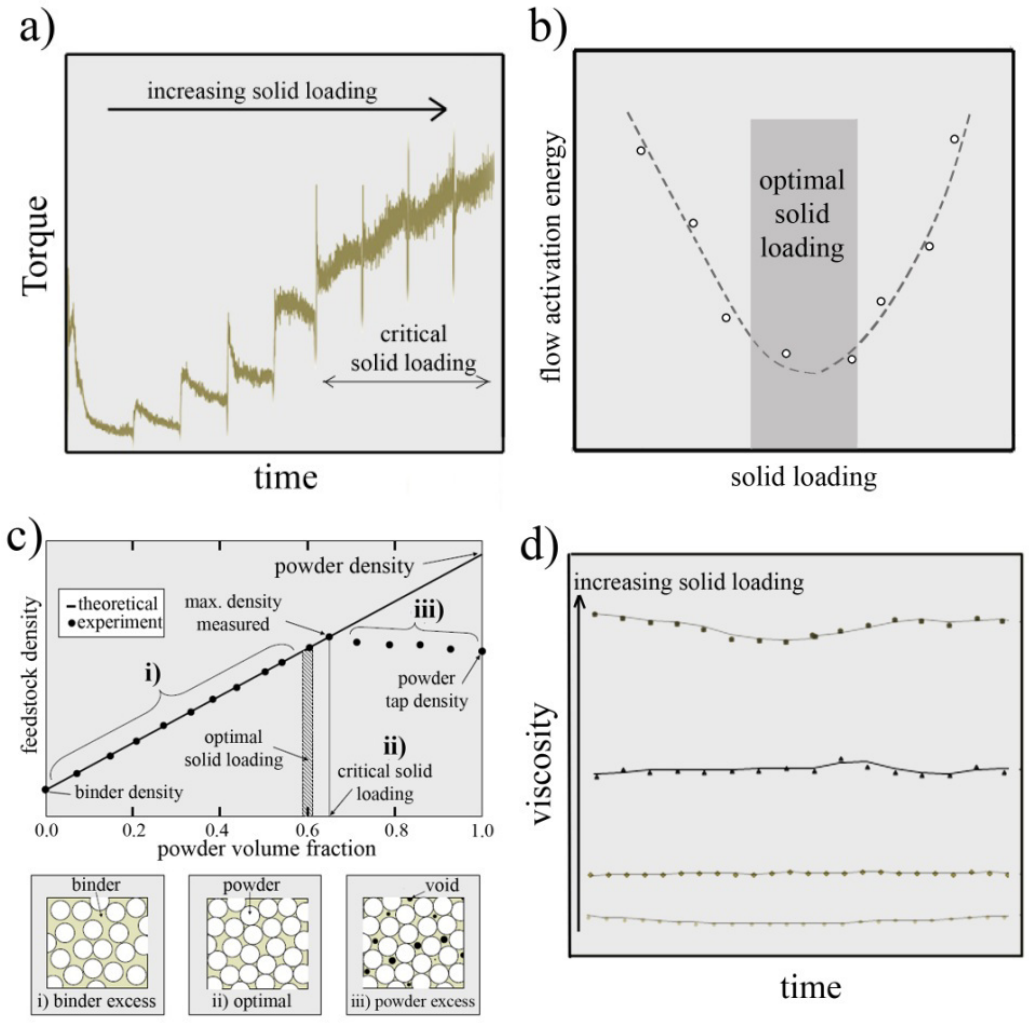

Figure 1. 5 Different methods to determine optimal and critical solid loading and feedstocks homogeneity: (a) by torque evolution with time for different solid loadings, (b) by evolution of flow activation energy with solid loading, (c) by density measurements of different solid loading feedstocks, (d) by measuring the evolution of viscosity with time in capillary rheometer setting the rest of conditions as constants.

The powders tap density can be a preliminary simple rough indicator of the critical solid loading. The tap density is related with the maximum packing factor achievable. Nevertheless, this parameter should be carefully considered. Agglomerates formation reduces the packing capacity of the powders. These agglomerates can be broken by hydrodynamic and erosive effects during mixing increasing the packing capacity of the powders and thus varying the critical volume content. Another straightforward way to evaluate if the critical solid loading was exceeded is by direct visual inspection. A glossy and sticky appearance and easy-to-flow capacity are signals of excess of binder content; a matte and sandy aspect normally is an indication of excess of powders.

Torque and capillary rheology are most employed methods to determine CPVC. A sign of CPVC in torque rheometer is the continuous and erratically increment of the torque values with time with apparently no stabilisation (see Figure 1. 5a). However there are several works that did not observe this behaviour and propose alternative methods [61]. The viscosity of the feedstock tends to infinite in capillary rheometer as the solid loading approach the CPVC value (see Figure 1. 4). A dilatant behaviour, i.e. the viscosity increases with shear rate, is also an indication of CPVC. Many authors have reported that a minimum in the flow activation energy vs. solid loading curve occurred at feedstock's solid loadings around the optimal situation (see Figure 1. 5b) [9, 117, 118]. Other authors assessed the moldability index α_{STV} (Eq.1.6) at different solid loadings [119]. This parameter gathers some parameters related with flow behaviour like a reference viscosity η_0, the flow activation energy E_a and the power law flow index n (R is the gas constant). The higher the α_{STV} is the better the flow features as result of a good viscosity, pseudoplastic behaviour and low viscosity temperature dependence.

$$\alpha_{stv} = \frac{1}{\eta_0} \cdot \frac{1-n}{E_a/R} \qquad \text{Eq.1.6}$$

The CPVC can be determined by measuring the feedstock density [120]. This method considers the voids formation at compositions higher than the CPVC resulting in density deviations with respect the theoretical value calculated by the mixtures rule (see Figure 1. 5c). The packing of the particles and the occurrence of voids can be also determined by scanning electron microscopy (SEM) inspections [121].

Finally, the optimal solid loading could be also determined by measuring the parts distortions after sintering [117]. An excess of binder will cause compact slumping because the power particles settle or migrate during debinding. On the other hand, lowering the binder content near the point at which the viscosity approaches maximum value deteriorates the flowability and homogeneity of feedstocks. All these problems lead to the occurrence of moulding defects and distortions during sintering. Hence, the feedstocks with a solid loading between excess of binder and excess of powder and that produce the less distortion could be considered as optimum.

At the same time a feedstock should be sufficiently homogeneous to allow a good and predictable dimensional control with an even shrinkage during sintering. Heterogeneities could lead on powder-binder separation, defects (e.g. voids and cracks formation) and part distortion [122]. There are several methods to determine feedstock homogeneity. Apart from the discussed torque rheology method (section 1.3.1) the alternative methods are based on characterising different batches of a feedstock and check if there are differences in the properties measured. For example, measuring the density [123] or by thermogravimetry [64] these differences, if they exist, may be appreciated. Another possible method is by registering the feedstock viscosity variations during time in a capillary rheometer maintaining the rest of the conditions (temperature and shear rate)[124] as schematised in Figure 1. 5d. Furthermore,

heterogeneities can be disclosed by controlling the weights of the injected parts or by SEM inspections [121].

1.4 Injection

The key step that differentiates PIM from other processing techniques that use feedstocks (tape casting, slurry casting, rapid prototyping...) is the injection step. This step consists on exerting pressure over a feedstock in a fluid state to force it to fill a mould die cavity. Several different processes arises at this point depending on: low pressure, medium pressure or high pressure is employed, the feedstock is directly transfer to the mould die cavity by a piston or is a screw that previously homogenize feedstock components before pushing it into the mould cavity, a mixture of screw and piston is used, vacuum is made on the mould die cavity dragging the feedstock inside instead of putting pressure directly on the feedstock, etc. Applied pressures between 0.2 to 5 MPa are counted as low pressure process (LPPIM), whereas pressures between 50 to 150 MPa are considered high pressure injection moulding (HPPIM). The intermediate pressure region is denoted as medium pressure.

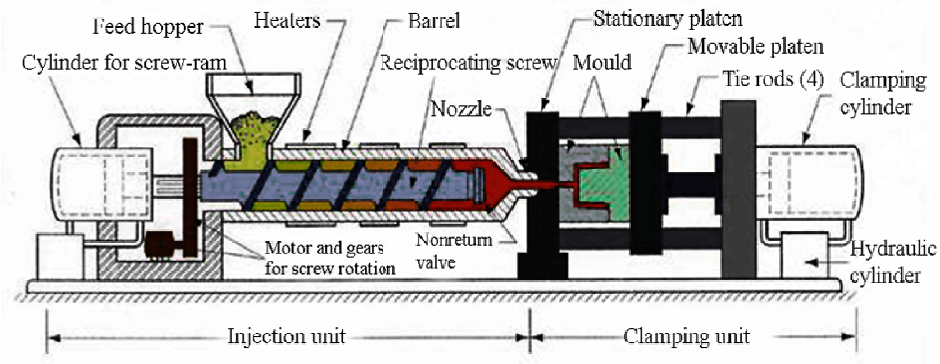

Figure 1. 6 Scheme of the injection and the clamping units of a typical horizontal injection press.

Basically there are two types of injection mould equipments: screw or plunger based. Sometimes a combination of screw and plunger is advisable for small injected volume and accurate parts. Injection could be also assisted by a gas. Plunger equipments have the advantage of easier and less expensive tooling design but have certain disadvantages in comparison with screw machines.

The equipment used for high pressure injection moulding PIM parts is quite similar to the equipment used for the common plastic injection moulding saving some special requirements like the use of special wear resistant materials with or without hard coatings for moulds and injection module components (barrel and screws), and special screw design to homogenise properly the feedstock during softening or melting. A scheme of the injection and clamping units of a typical injection moulding equipment is shown in Figure 1. 6.

In a screw press the feedstock is fed towards the injection chamber by an endless screw in a progressive heated barrel which homogenises and plasticises the feedstock up to the injection

temperature. And important part of the heat comes from the frictional forces between the feedstock trapped between the screw and the cylinder. Typical injection temperatures range from 120 to 200 ºC for thermoplastic moulding compounds.

Once the feedstock is heated up to a semi-fluid state, it is forced into the mould die cavity through and sprue and a gated runner system. In screw machines a check-in barrel mechanism allows the auger to act as a piston, driving the material into the mould. Injection parameters like the injection speed, the holding pressure and the time after injection, the mould and the melt temperatures, the cooling time, among others must be controlled and optimised to avoid defects in the green parts and maximise final part properties. Green parts that at first appear to be of good quality can possess internal stresses, which may in turn lead to cracks during later processing steps such as debinding. Defects which result from the injection moulding process are irreversible and impair the quality of the finished components.

In a plunger press (Figure 1. 7) the heating is produced exclusively by conduction and convection and the feedstock is not homogenised before a piston directly forces the material into the mould die cavity. Therefore it is even more crucial to ensure a high quality feedstock when plunger press is used. Besides, there is a higher risk of a poor degasification of the feedstock prior to the injection compared with the screw-type equipments.

Low-pressure injection moulding (LPPIM) has several advantages for complex shape parts production in comparison to that higher pressure power injection moulding (HPPIM) process [120, 125]. LPPIM is characterized by lower costs, especially for the injection equipment and moulds, and by simplicity in operation. The main advantages of the LPPIM are mainly related to the advantages of low pressure injection equipment in relation to that of high pressure. The use of feedstocks that in a melted or fluidic state has viscosities between 1.5 and 4.0 Pa·s makes possible the transfer inside the mould through compressed air with pressure of the order of 0.8 MPa. This eliminates the need of using hydraulic based units, pistons and spindles with the evident cost savings and simplifications. The consumption of energy is reduced as well as the dimensions of the equipment. Another benefit in comparison with HPPIM is the reduction of the wear of the mould and machine parts, lessening the adhesion of the feedstock to the mould and limiting the contamination of the feedstock with the wear of the spindle and/or piston. This last fact allows employing less restrictive in properties materials that the other way around should provide high wear resistance to the mould and injection machine components. In case of ceramic or hard metal powders PIM, these injection tools most probably would also need an expensive coating made of a hard material. For very low pressures even polymeric or silicon moulds could be employed. Apart from simplifying the production of more inexpensive moulds and injection devices, there are other important benefits that could be obtained with LPPIM. There is a potential reduction of the feedstock components segregation providing an easier control of the flow behaviour and eventually there is a lowering of pressure gradients created in the moulded piece. However, several disadvantages limit the use of LPPIM. Defects typical of HPPIM produced due to low

pressures or post pressures during injection could arise like sinks or air entrapped. With LPPIM less packing of powder particles is obtained which could affect further steps.

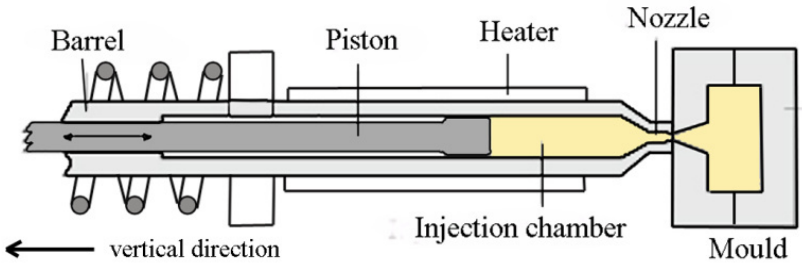

Figure 1. 7 Scheme of the LPPIM vertical plunger type injection unit.

In some devices specially designed for low MicroPIM, the injection unit is especially composed of three stages to achieve the high-precision processing of the very small injection moulding volume. At first the extruder screw pushes the material into the metering sleeve. Then the material is pressed into the nozzle by the pre-dossing piston to conclude with the injection into the mould die cavity carried out by the injection piston. A graphical scheme of the injection unit is shown in Figure 1. 8.

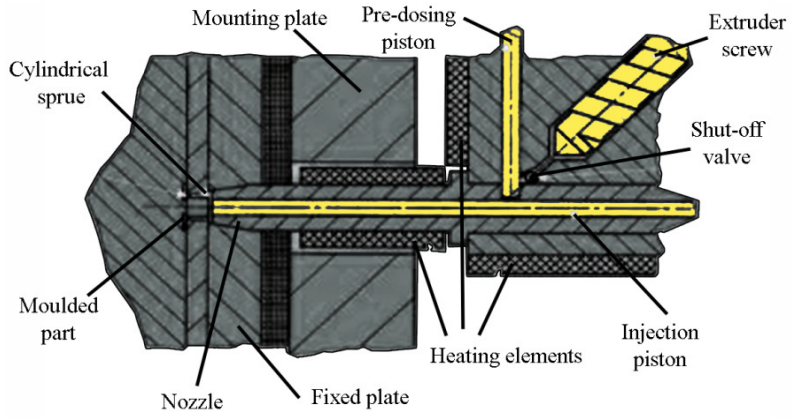

Figure 1. 8 Scheme of the injection and the clamping units of the horizontal micro injection equipment in Battenfeld Microsystem ®.

1.7 Debinding and sintering

These last stages of the PIM process are going to be briefly overviewed.

The main objective of a debinding is to remove as fast as possible the binder system without generating defects. Problems during debinding or incomplete binder elimination may cause components distortion, cracks, blisters or contamination with undesirable elements just to mention some [126]. As described in section 1.2 there are different ways of removing the

organic part of the feedstock before sintering. Only the solvent and the thermal routes will be mentioned as they were chosen as debinding method in this PhD Thesis.

The solvent debinding mechanisms have been widely studied [127-129]. During solvent debinding three stages are commonly identified: (1) an initial stage where the solvent begins to diffuse inside the green part generally producing a swollen gel that makes the sample to expand drastically, (2) a second stage where the solvent continues diffusing until covering all the part volume and the swollen gel gradually disintegrates in a true solution that diffuses towards the surface and (3) finally the part shrinks when the solvent is drained out. The temperature influences the solvent debinding activating the diffusion mechanisms. Temperatures above the softening point of the removable part are recommended to facilitate the extraction and minimise volume variations [130]. The molecular weight of the soluble part also affects the debinding .The backbone polymer should remain changeless during all the solvent process and sustain the part geometry during the volume variations and after the process. If the backbone polymer fails, parts distortions or cracks may appear [130, 131]. The open channels created after solvent debinding will facilitate the subsequent extraction of the backbone polymer by a thermal degradation [126]. Some remarks about thermal debinding were discussed in 1.3.3. The thermal debinding cycles should be designed considering the maximum volatilisation rate temperature ranges to avoid an excess of pressure build-up that will generate defects. The debinding atmospheres should be selected according to their efficacy degrading the backbone polymer but avoiding any influence in the powder (oxidation, contamination with nitrogen or other gases, etc.)

Sintering is the last stage of the PIM process. A detailed review on sintering of metals and ceramics could be found, e.g, in Kang [132], Schatt et al. [133] and Chiang et al. [134]. The powder particles merge generating a dense component with final intrinsic mechanical and physical properties of the material. The sintering mechanisms are activated by temperature, i.e. certain energy should be provided in order to activate the process. The particles joining is produced by individual atoms movement and thus by a mass transfer in a solid, liquid or vapour state. Five different sintering mechanisms are reported: (1) volume diffusion, (2) grain boundary diffusion, (3) surface diffusion, (4) plastic flow and (5) evaporation-condensation. The main sintering driving force in PIM is the large amount of free surface energy of fine particles which tend to a more stable state and a less porous body by merging themselves. The smallest the particle and grain size are the more the sintering is activated; in PIM the particles are particularly small in comparison with other PM processes. The sintering processes could be performed in a solid state but the presence of a transient liquid phase or permanent liquid phase (depending on if the liquid phase involved in the process could dissolve or not in the solid phase), also aid to activate the sintering. Temperature and time determine the efficacy of atoms movements. Sintering temperatures are below the melting point of the main component of the powder (if there are several) but close to this temperature. The sintering atmospheres also play an important role during sintering and can have an oxides reduction purpose, avoid this oxides formation, avoid the elimination of any element in the material composition (e.g carbon), incorporate desirable element to the composition, etc.

1.6 Zircon and its processing routes

Zirconium silicate ($ZrSiO_4$) or zircon is an unusually abundant ceramic-type raw material. Zircon crystallises forming a tetragonal body-centred unit cell (a=6.607Å and c=5.982Å) belonging to the space group $I4_1/amd$. The Zr cations are surrounded by eight oxygen atoms with two different distances, the Si cations coordinate with four oxygen atoms, and the oxygen anions are connected with two Zr-ion and one Si-ion. Hence, zircon crystal comprises an arrangement of SiO_4 tetrahedrons and ZrO_8 dodecahedrons. The density of zircon is 4.6-4.7 cm^3/g.

Table 1. 7 Zircon mechanical and thermal properties in comparison with alumina and zirconia. The properties are not intrinsic of the material but of the resulting porosity and material grades.

	Zircon	**Alumina (α)**	**Zirconia (TZP)**
Bending strength [MPa]	150-320 [135]	210-500 [136, 137]	700-1200 [138]
Fracture Toughness [$MPa \cdot m^{1/2}$]	2.2-3.6 [139]	2.5-6 [136]	7-8 [140]
Hardness [GPa]	6.9-13.7[135, 139]	10-20 [136, 137]	8-12 [141, 142]
CTE [$10^{-6} \cdot ºC^{-1}$]*	4 [143]	5.4 [136, 137]	8 [144]
Thermal conductivity [$W \cdot m^{-1} \cdot K^{-1}$]	3.5-5.1[145]	30-40 [136]	1-3 [146]
Specific Heat [$J \cdot g^{-1} \cdot K^{-1}$]	0.628 [147]	0.775 [136]	0.450-0.585 [146, 147]

*Average from room to 1000 ºC

The interest in zircon as a ceramic and refractory material is due to its excellent thermo-physical properties such as relative low thermal expansion ($4.10^{-6} \cdot ºC^{-1}$), low thermal conductivity, as well as a good corrosion resistance and chemical inertness, for example, against glass melts, slag and liquid metal alloys. The melting point of zircon is around 2200 ºC and it does not show any phase transformation up to 1600 ºC [148]. These temperatures depend on zirconium grades. The mechanical properties of zircon are lower than other engineered ceramics such as tetragonal zirconia polycrystal (TZP) and Si_3N_4. The near fully dense zircon material could compete with alumina in properties. Some of the zircon mechanical and thermal properties are compared with those of the alumina and zirconia in Table 1. 7. Zircon is a brittle material presenting a conchoidal fracture with cleavage indistinct on {110} and {111}. Zircon ceramic posses moderately low flexural strength, hardness, and fracture toughness in the ranges of 200–300MPa; 10–11 GPa; 2–3$MPa \cdot m^{1/2}$ respectively. However, it has been demonstrated that high purity zircon can retain its bending strength up to temperatures as high as 1200-1400 ºC [139, 149, 150]. Accordingly, zircon has a wide range of application as structural material in severe conditions like glass tanks, in iron and steel production, in energy technology, as moulds and cores in precision investment casting or as protective coatings of steel-moulding tools, glass fibre processing tools, etc. Zircon is also a potential candidate for filters in diesel engines due to its high temperature chemical resistance and inertness to some common metallic oxides (PbO, V_2O_5 and CeO_2 from diesel refining, Fe_2O_3 due to the oxidation of metallic particles produced by engine wear, etc.). Zircon inertness is significantly higher than that of other materials; in particular it performs better than cordierite, currently in production as a material for diesel vehicle filter [151]. Zircon is considered for some applications an extremely durable and resistant material with the added

capability of accommodating a large quantity of actinides, which are substituted for zirconium atoms. This feature makes zircon an interesting material in the nuclear industry as one of the new crystalline matrices currently investigated for the disposal of long-lived actinides, e.g. it is being considered for disposal of weapons-grade plutonium [152].

The highly abundant zircon sand is the principal source for zircon material. This sand is commonly micronized by different milling processes before consolidation by sintering. However due to its refractoriness it is difficult to obtain fully dense zircon ceramics. There are also limits in the sintering temperature due to dissociation of $ZrSiO_4$ into $ZrO_2 \cdot SiO_2$ by a solid-state reaction. Dissociation temperature of pure zircon is around 1650 ºC but presence of impurities could lower this temperature in 200 ºC [148, 153]. The fineness of the zircon used also affect the dissociation temperature. The main inconvenience of dissociation is that silica and zirconia may not re-associate during the cooling. During the cooling the tetragonal zirconia resulting from the zircon dissociation might transform into monoclinic zirconia which is the stable phase at room temperature. It is well known the phase transformation is accompanied by a significant volume change which introduces microcracks inside the zirconia particles dispersed into the ceramic matrix [154-156], thus, resulting in a detrimental effect on the mechanical properties. On the other hand, the resulting silica from the zircon dissociation might also decrease both the high temperature mechanical properties and the chemical inertness. The difficult sintering of zircon is the main restriction to employ this material in comparison with other engineering ceramics for many applications.

Additions of some oxides like TiO_2 [157], SiO_2 and Al_2O_3 [158] aids in the densification by liquid phase or solid solution sintering. A number of liquid phase additives have been recognised as allowing a reduction in the required temperature of sintering. However the intergranular phases which are produced by the presence of this kind of additive usually cause some degradation of high temperature mechanical properties of the product. The MgO, TiO_2, Fe_2O_3, and MnO oxides are considered to form a liquid phase of this type. In contrast, the use of solid solution additives, for example Cr_2O_3 or Al_2O_3 can avoid the appearance of an extra phase problem [153]. Natural zircon sand often contains several impurities including the mentioned oxides which influence the final properties. The extent of impurities determines the different grades of zircon.

Instead of addition of sintering aids other methodologies are preferred to increase the densification of the sintered parts avoiding the risk of dissociation and reduction of mechanical properties. Pure zircon could be obtained by combination of ZrO_2-SiO_2 and reaction sintering. The sol–gel routes [159-162], chemical reactions like aerosols [163], reverse micelle process [164] and micro-emulsion process [165] are some alternatives. The method based on combination of amorphous ZrO_2-SiO_2 revealed the incomplete powders crystallization under heat treatment [166, 167] or laser [168]. Spark plasma sintering and microwave sintering emerge as promising alternatives to conventional methods like pressureless sintering (mainly after the slip casting route) [149, 157] or hot-presssing [169, 170]. The use of high energy ball milling (HEBM) mechanochemical activated nano-sized

powders also results an effective method to improve densification with a negligible grain growth which is also positive for mechanical properties [171]. Simultaneously, the resistance of the samples to thermal decomposition increases. Ebadzadeh et. al. [172] performed microwave sintering of previously pressed zircon powders. To reach almost the same densification, microwave heating reduced the sintering time and temperature compared to conventional heating. The results also show that a long microwave heating (higher than 30 min) accelerates the decomposition of zircon forming an extra phase that acts a glassy phase during sintering of the samples. In the works of Rendtorff et. al. [139, 173] spark plasma sintering in combination with pressure and HEBM zircon powders is employed to obtain highly dense parts. Near full dense parts were obtained avoiding dissociation at 1400 ºC with 100 ºC/min heating rates, 100 MPa of pressure and a soaking time of 10 min.

In spite of there is a wide variety of examples of PIM of engineering grades of alumina and zirconia based ceramics there are scarce works regarding PIM of zircon. The only references found are works conducted by Schlechtriemen et al. that performed low pressure injection moulding over mixtures of intermetallic $ZrSi_2$ and ZrO_2 [125, 174]. The reactive sintering of both substances produces pure zircon parts. New applications may arise combining the unique properties of zircon with the freedom of part designs intrinsic of the PIM technology. Apart from structural and refractory engineering applications in competition with conventional PIM ceramics other opportunities may be found in jewellery and watches cases production in the same way as zirconia and alumina [175, 176]. Orthodontics is another potential field due to the opaqueness and the tooth-like colour characteristic of the zircon which combines aesthetics requirements with a strength and abrasive resistant material [177].

1.7 Invar and its processing routes

Low coefficient of thermal expansion (LCTE) Fe_x-Ni_{1-x} alloys, are important materials for many applications requiring high degree of dimensional stability with variations of operation temperature. The abnormal LCTE behaviour within metals, which normally considerably expand with heat and contract with cold, is consequence of the so-called Invar (volume INVARiance) effect. The physical mechanism explaining Invar effect still remains uncertain, but from general standpoint low expansion occurs due to two opposing effects over a specific temperature range. During heating, the alloy naturally expands while simultaneously a ferromagnetic-to-paramagnetic transformation (at temperatures that depend on the alloy but that are around 200-300 ºC in Fe-Ni systems) imposes a magnetostriction that counteracts the expansion [178, 179]. The Invar effect in Fe_x-Ni_{1-x} alloys is observed for $0.50<x<0.73$, where x is expressed in atomic fraction. The minimum CTE in the binary iron-nickel alloying system occurs in the composition $Fe_{0.65}$-$Ni_{0.35}$, the commercial Invar 36, which also has one of the lowest CTE of any alloy from room -70 to about 230ºC, approximately 1.2 $10^{-6}\cdot ºC^{-1}$. The 4.5% cobalt modification (commercially termed as Super Invar) has almost zero expansion but over a limited range [180]. Although exceptional at room temperature, the useful range of Super Invar is limited because the material begins to irreversible transform from austenite to martensite at relatively low temperatures compared to Invar 36. So Invar 36 alloy is still

preferred for cryogenic applications and space craft applications that suffer from very low temperatures during shadow period and high temperatures during exposition to sun radiation [181]. Additions of Co to form Fe-Ni-Co allow commonly broadens the low-expansion temperature range of Fe-Ni invar alloys. On the down side, replacing cobalt for nickel generally increases the CTE of the alloy around ambient temperatures [180].

Microstructure of Fe_x-Ni_{1-x} LCTE alloys commonly consists of a substitutional solid solution of nickel in iron creating an austenitic face centred cubic lattice. The austenitic γ phase, that is present at all temperatures up to the melting point (around 1450 ºC depending on purity and allow composition), shows a high ferromagnetism at temperatures below the Currie temperature, and a paramagnetic behaviour above this temperature. The short range atomic distribution in the Invar lattice could be altered by the presence of 3d transition elements like Mn and Co that substitute Fe and Ni in the FCC lattice or interstitial C, N or H that cause the distortion of the crystalline lattice [182]. Heterogeneities in the cast alloy introduce the possibility of formation of Ni segregation regions within the γ lattice; segregation may be promoted by presence of elements like carbon [183-187]. Therefore low moment (LM) paramagnetic Fe-rich phases could coexist with clusters of Ni-rich high moment (HM) ferromagnetic order phases negatively affecting CTE. Furthermore a martensitic phase could be formed for quenched alloys which also degrade low expansion properties. However, elements like C, N and Ni act as a γ phase stabilizers diminishing the martensitic temperature (Ms). Concentrations below about 33 at.% Ni lead on structural transitions from γ to a body centred cubic phase α which does not show the Invar effect. Carbon presence could stabilize γ phase for concentrations below 33 at.% Ni.

Invar may suffer from aging that become more or less severe depending on the temperature and processing conditions (deformation, annealing, etc.), and elements traces in their composition [188-191]. Aging affects temporal dimensional stability of Invar materials that could expand with time at a constant temperature and with absence of loads. The carbon content of Invar, along with other elements traces and residual stress relief [192] are factors affecting the temporal dimensional stability of Invar. Long term aging occurs as consequence of migrations of the carbon or other elements within the Invar lattice. A proper heat treatment may reduce the temporal growth of the Invar by effectively aging it.

Table 1. 8 shows a comparative between Invar 36 and other invar or austenitic steels properties. The mechanical properties of Invar 36 are comparable to those of austenitic steels but they have less thermal conductivity. All of the alloys in the Fe_x-Ni_{1-x} invar family are very ductile as the austenitic stainless steels if they are compared to other steels. This is presumably due to FCC lattice and the limited content of interstitials (e.g. elemental carbon) or other precipitates like carbides that typically hinders the displacements of slip systems. The FCC lattice has a good number of slip systems and invar alloys also may form annealing twins [193]. The role of twinning in plastic deformation comes not from the strain produced by the twinning (which is almost negligible) but from the fact that orientation changes resulting from twinning may form new slip systems in a favourable orientation with respect to the stress axis

so that the additional slip could take place [193]. Invars could maintain ductility at very low temperatures and the brittle to ductile transition temperature sometimes is not noticeable [194, 195]. However they suffer from creep at high temperatures.

Table 1. 8 Comparative of some mechanical and thermal properties of Invar 36 with Kovar™ and some austenitic stainless steels.

Material Property	Invar 36* [180, 195]	Kovar™** [1]	304 * [196]	316L** [1, 196, 197]
Density [g/cm^3]	8.05	7.8	7.9	7.8
Young's Modulus [GPa]	141	N/A	193	185
Elongation [%]	30	24	45	35-65
Yield Strength [MPa]	241	300	210	180
Ultimate Tensile Strength [MPa]	448-552	450	540-750	520-600
Macro Hardness	66-68 HRB	65 HRB	80 HRB	67 HRB
CTE [$10^{-6}\cdot$ºC^{-1}]	1.2	5.8	16.9	16.2
Thermal Conductivity [W·m^{-1}K^{-1}]	10.4	N/A	16.2	16.3
Specific Heat [W s/kg K]	515	N/A	500	500
Thermal Diffusivity	2.6	N/A	4.1	N/A

* Wrought material, **MIM processed

Due to their ductility invar alloys can be readily cold headed and formed. Stamping from cold-rolled strip is easily accomplished. Parts may be deep drawn from properly annealed strip. However the high ductility along with the low thermal conductivity of Invar would make difficult the posterior machining [198, 199]. Moreover Invar 36, as many nickel alloys, may suffer from work hardening. When machining nickel alloys, and to some Invar alloys, cutting tools will wear relatively quickly and cutting speeds will be slow [199-201], increasing the processing costs. Furthermore the effect of deformation coming from wrought or machined parts, although it may increase mechanical properties, generally causes the deterioration of the Invar properties due to alteration of the short range atomic distribution, thus annealing heat treatments have to be carried out [202, 203]. The formation of precipitates at grain boundaries upon heating of the severely deformed sample can be related to the formation of the $FeNi_3$ intermetallic phase within the FCC solid solution.

Powder metallurgy (PM) of Fe_x-Ni_{1-x} LCTE alloys presents several advantages with respect casting not only in energy and cost savings but also in the reduction of elements segregation risk, thus increasing alloy properties [204]. Furthermore, PM can reduce tedious and time consuming machining steps that are specially complicated and also reduce the needs of joints by welding. Examples of potential PIM application of LCTE Invar 36 alloys are wide in the field of high precision devices like in optoelectronic or light wave communication systems, housing or structural components [205]. For example, since the wavelength of light for optical systems in the visible portion of the spectrum is approximately 0.5μm, and system requirements typically demand that optical elements be held to some tolerance near this value, a structural metal with a low CTE is of extreme value. Some typical applications include lens and mirrors cells, interfacing spacers between optics and other structures [206], metering rods for telescopes [207] and laser cavity structures. Invar alloys are commonly used in ceramic

sealing applications and designed to match the CTE of commercial ceramic and glasses. In that respect, Invar 36 alloys match that of fused silica closely. Another interesting application of invar is the fuel injection system in combustion motors. In some designs, a piezoelectric valve regulates the fuel dosage by electrical impulses. The housing of this piezoelectric requires a good dimensional stability with temperature to accurately control the dosage. Invar 36 alloy is proposed as a suitable material for this application [208].

Currently, there is an increasing demand of miniaturised components for micro devices like micro gears or micro actuators [9, 11, 13, 14] in which micro powder injection moulding (μ-PIM) of low CTE alloys could be an interesting alternative.

References

1. Heaney, D.F., *Powders for metal injection moulding*, in *Handbook of metal injection molding*, D. Heaney, Editor. 2012, Woodhead Publishing Limited: Cambirdge. p. 50-63.
2. German, R.M., *Metal powder injecction molding (MIM): key trends and markets*, in *Handbook of metal injection molding*, D. Heaney, Editor. 2012, Woodhead Publishing in Materials. p. 1-25.
3. German, R.M., *Progress in Titanium Metal Powder Injection Molding.* Materials, 2013. **6**(8): p. 3641-62.
4. Mutsuddy, B.C. and R.G. Ford, *Ceramic injection molding*. Materials Technology Series. 1994: Chapman and Hall.
5. Bidaux, J.E., et al., *Metal injection moulding of low modulus Ti-Nb alloys for biomedical applications.* Powder Metallurgy, 2013. **56**(4): p. 263-266.
6. Barreiros, F.M., et al., *Preparing MIM Feedstocks for Bio-applications using an Agar-based Binder*, in *Advanced Materials Forum Iv*, A.T. Marques, et al., Editors. 2008. p. 385-389.
7. Lenz, J., et al., *Powder Injection Molding of Ceramic Engine Components for Transportation.* Jom, 2012. **64**(3): p. 388-392.
8. Piotter, V., *Micro metal injection moldong (MicroMIM)*, in *Handbook of metal injection molding*, D. Heaney, Editor. 2012, Woodhead Publishing Limited: Cambridge. p. 307-337.
9. Kong, X., T. Barriere, and J.C. Gelin, *Determination of critical and optimal powder loadings for 316L fine stainless steel feedstocks for micro-powder injection molding.* Journal of Materials Processing Technology, 2012. **212**(11): p. 2173-2182.
10. Cha, B., et al., *Micro powder injection molding process using TiH2 powder.* Journal of Ceramic Processing Research, 2012. **13**: p. S22-S25.
11. Quinard, C., et al., *Elaboration of PIM feedstocks with 316L fine stainless steel powders for the processing of micro-components.* Powder Technology, 2011. **208**(2): p. 383-389.
12. Ruh, A., et al., *Studies on size accuracy of microgear wheels produced by powder injection molding of zirconia feedstocks.* International Journal of Advanced Manufacturing Technology, 2012. **58**(9-12): p. 1051-1059.
13. Attia, U.M. and J.R. Alcock, *A review of micro-powder injection moulding as a microfabrication technique.* Journal of Micromechanics and Microengineering, 2011. **21**(4).

14. Piotter, V., et al., *Powder injection moulding of metallic and ceramic micro parts.* Microsystem Technologies-Micro-and Nanosystems-Information Storage and Processing Systems, 2011. **17**(2): p. 251-263.
15. Ruh, A., et al., *The development of two-component micro powder injection moulding and sinter joining.* Microsystem Technologies-Micro-and Nanosystems-Information Storage and Processing Systems, 2011. **17**(10-11): p. 1547-1556.
16. Attia, U.M. and J.R. Alcock, *Fabrication of hollow, 3D, micro-scale metallic structures by micro-powder injection moulding.* Journal of Materials Processing Technology, 2012. **212**(10): p. 2148-2153.
17. Attia, U.M. and J.R. Alcock, *Fabrication of ceramic micro-scale hollow components by micro-powder injection moulding.* Journal of the European Ceramic Society, 2012. **32**(6): p. 1199-1204.
18. Ayad, G., et al., *A fully coupled simulation and optimization scheme for the design of 3D powder injection molding processes*, in *NUMIFORM '07: Materials Processing and Design: Modeling, Simulation and Applications, Pts I and II*, J.M.A. CeasarDeSa and A.D. Santos, Editors. 2007. p. 507-512.
19. Cheng, Z.Q., et al., *The Bi-phasic Numerical Simulation of Metal Co-injection Molding.* International Journal of Material Forming, 2008. **1**: p. 695-698.
20. Mamen, B., et al., *Finite Element Modeling and Numerical Simulation of Sintered Tungsten Components under Hydrogen Atmosphere*, in *11th International Conference on Numerical Methods in Industrial Forming Processes*, S.H. Zhang, et al., Editors. 2013. p. 1092-1099.
21. Kang, T.G., et al., *Modeling and simulation of metal injection molding (MIM)*, in *Handbook of metal injection molding*. 2012, Woodhead Publishing Limited. p. 197-234.
22. Enneti, R.K., V.P. Onbattuvelli, and S.V. Atre, *Powder binder formulation and compund manufacure in MIM*, in *Hanbook of metal injection moldong*, D. Heaney, Editor. 2012, Woodhead publishing limied: Cambridge. p. 64-92.
23. Enneti, R.K., et al., *Review: Thermal Debinding Process in Particulate Materials Processing.* Materials and Manufacturing Processes, 2012. **27**(2): p. 103-118.
24. Gorjan, L., A. Dakskobler, and T. Kosmac, *Partial wick-debinding of low-pressure powder injection-moulded ceramic parts.* Journal of the European Ceramic Society, 2010. **30**(15): p. 3013-3021.
25. Somasundram, I.M., et al., *Phenomenological study and modelling of wick debinding.* Chemical Engineering Science, 2008. **63**(14): p. 3802-3809.
26. de Mello, J.D.B., et al., *Effect of sintering temperature on the tribological behavior of plasma assisted debinded and sintered MIM self lubricating steels*. Proceedings of the Asme 10th Biennial Conference on Engineering Systems Design and Analysis, 2010, Vol 1. 2010. 373-380.
27. Joens, C.J. and S. Banerjee, *Laminar gas flow and plasma reduces cycle time for powder-metal injection-molded parts.* Industrial Heating, 2009. **76**(8): p. 49-53.
28. Schroeder, R., et al., *Plasma Debinding and Sintering of Metal Injection Moulded 17-4PH Stainless Steel.* Materials Research-Ibero-American Journal of Materials, 2011. **14**(4): p. 564-568.
29. Stringari, G.B., et al., *Time-dependent properties of bimodal POM - Application in powder injection molding.* Powder Technology, 2011. **208**(3): p. 590-595.
30. Lamlerttham, J., et al., *Effects of Sintering Time and Atmosphere on Mechanical Properties of Injection Molded Tungsten Alloy*, in *Materials Science and Technology Vii*, J.T.H. Pearce, et al., Editors. 2013. p. 197-208.

31. Ma, J., et al., *Microstructure and magnetic properties of Fe-50%Ni alloy fabricated by powder injection molding.* Journal of Magnetism and Magnetic Materials, 2013. **329**: p. 24-29.
32. Baek, E.R., et al., *Binder system for STS 316 nanopowder feedstocks in micro-metal injection molding.* Journal of Materials Processing Technology, 2007. **187-188**: p. 270-3.
33. Contreras, J.M., A. Jimenez-Morales, and J.M. Torralba, *Fabrication of bronze components by metal injection moulding using powders with different particle characteristics.* Journal of Materials Processing Technology, 2009. **209**(15-16): p. 5618-5625.
34. Setasuwon, P., A. Bunchavimonchet, and S. Danchaivijit, *The effects of binder components in wax/oil systems for metal injection molding.* Journal of Materials Processing Technology, 2008. **196**(1-3): p. 94-100.
35. Li, Y.-m., et al., *Effects of surfactant on properties of MIM feedstock.* Transactions of Nonferrous Metals Society of China, 2007. **17**(1): p. 1-8.
36. Chen, G., et al., *Debinding behaviour of a water soluble PEG/PMMA binder for Ti metal injection moulding.* Materials Chemistry and Physics, 2013. **139**(2-3): p. 557-565.
37. Thavanayagam, G., et al., *A study of polyvinyl butyryl based binder system in titanium based metal Injection moulding*, in *Powder Metallurgy of Titanium: Powder Processing, Consolidation and Metallurgy of Titanium*, M. Qian, Editor. 2012. p. 167-173.
38. Auzène, D., *Investigations into water solule binder systems for Powder Injection Moulding.* Powder Injection Moulding International, 2011. **5**(1): p. 51-54.
39. Urtekin, L., I. Uslan, and B. Tuc, *Investigation of Properties of Powder Injection-Molded Steatites.* Journal of Materials Engineering and Performance, 2012. **21**(3): p. 358-365.
40. Omar, M.A., et al., *Rapid debinding of 316L stainless steel injection moulded component.* Journal of Materials Processing Technology, 2003. **140**: p. 397-400.
41. Fredel, M.C., et al., *A model for PEG removal from alumina injection moulded parts by solvent debinding.* Journal of Materials Processing Technology, 2007. **182**(1-3): p. 268-73.
42. Rodriguez-Senin, E., et al., *Processing of Mn-Zn ferrites using mould casting with acrylic thermosetting binder.* Powder Metallurgy, 2005. **48**(3): p. 249-253.
43. Castro, L., et al., *Mechanical properties and pitting corrosion behaviour of 316L stainless steel parts obtained by a modified metal injection moulding process.* Journal of Materials Processing Technology, 2003. **143**: p. 397-402.
44. Levenfeld, B., et al., *Processing of P/M M2 high speed steels by mould casting using thermosetting binders.* Journal of Materials Processing Technology, 2001. **119**(1-3): p. 1-6.
45. Millan, A.J., M.I. Nieto, and R. Moreno, *Aqueous gel-forming of silicon nitride using carrageenans.* Journal of the American Ceramic Society, 2001. **84**(1): p. 62-64.
46. Huzzard, R.J. and S. Blackburn, *A water-based system for ceramic injection moulding.* Journal of the European Ceramic Society, 1997. **17**(2-3): p. 211-216.
47. Santacruz, I., et al., *Aqueous injection moulding of porcelains.* Journal of the European Ceramic Society, 2003. **23**(12): p. 2053-2060.
48. Chen, G., et al., *Using an agar-based binder to produce porous NiTi alloys by metal injection moulding.* Intermetallics, 2013. **37**: p. 92-99.

49. Olhero, S.M., G. Tari, and J.M.F. Ferreira, *Feedstock formulations for direct consolidation of porcelains with polysaccharides.* Journal of the American Ceramic Society, 2001. **84**(4): p. 719-725.
50. Carreno-Morelli, E., et al., *Metal injection moulding of agar-steel feedstocks.* Powder Metallurgy World Congress & Exhibition (PM2004), 2004: p. 5 pp.-5 pp.
51. Weil, K.S., E.A. Nyberg, and K.L. Simmons, *Use of a naphthalene-based binder in injection molding net-shape titanium components of controlled porosity.* Materials Transactions, 2005. **46**(7): p. 1525-1531.
52. Haw Pei, L. and N. Muhamad, *Rheological analysis of microminiature powder injection molding (muPIM) feedstock.* Applied Mechanics and Materials, 2011. **52-54**: p. 238-243.
53. Park, M.S., et al., *Water-soluble binder of cellulose acetate butyrate/poly(ethylene glycol) blend for powder injection molding.* Journal of Materials Science, 2001. **36**(23): p. 5531-5536.
54. Song, M., et al., *Water-soluble binder with high flexural modulus for powder injection molding.* Journal of Materials Science, 2005. **40**(5): p. 1105-1109.
55. Hidalgo, J., et al. *Rheological behaviour of powder injection moulding (PIM) feedstocks fabricated with a thermoplastic binder system based on polysaccharides*. in *PM2010 World Congress*. 2010. Florence: EPMA.
56. Abolhasani, H. and N. Muhamad, *A new starch-based binder for metal injection molding.* Journal of Materials Processing Technology, 2010. **210**(6-7): p. 961-968.
57. Yun, J.W., et al., *Effect of decomposition kinetics and failure criteria on binder-removal cycles from three-dimensional porous green bodies.* Journal of the American Ceramic Society, 2006. **89**(1): p. 176-183.
58. Supati, R., et al., *Mixing and characterization of feedstock for powder injection molding.* Materials Letters, 2000. **46**(2-3): p. 109-114.
59. Kong, X., et al., *Mixing and Characterisation of stainless steel 316L feedstock.* International Journal of Material Forming, 2009. **2**: p. 709-712.
60. Raman, R., W. Slike, and R.M. German, *Homogeneity of mixed feedstocks in powder injection-molding*, in *Advances in Powder Metallurgy & Particulate Materials - 1993, Vol 5: Powder Injection Molding*, A. Lawley and A. Swanson, Editors. 1993. p. 1-16.
61. Barreiros, F.M. and M.T. Vieira, *PIM of non-conventional particles.* Ceramics International, 2006. **32**(3): p. 297-302.
62. Quinard, C., T. Barriere, and J.C. Gelin, *Development and property identification of 316L stainless steel feedstock for PIM and mu PIM.* Powder Technology, 2009. **190**(1-2): p. 123-128.
63. German, R.M. and A. Bose, *Injection Molding of Metal and Ceramics*. 1997: Metal Powder Industries Federation.
64. Liu, L., et al., *Mixing and characterisation of 316L stainless steel feedstock for micro powder injection molding.* Materials Characterization, 2005. **54**(3): p. 230-238.
65. Roetenberg, K.S., et al., *Optimization of the mixing process for power injection molding*, in *Powder Injection Molding Symposium - 1992*, P.H. Booker, J. Gaspervich, and R.M. German, Editors. 1992. p. 119-130.
66. Wu, R.Y. and W.C.J. Wei, *Torque evolution and effects on alumina feedstocks prepared by various kneading sequences.* Journal of the European Ceramic Society, 2000. **20**(1): p. 67-75.
67. Schramm, G., *A practical approach to Rheology and Rheometry*. 2nd ed. 2004, Karlsruhe: Thermo electron.

68. Hausnerova, B., *Rheological characterization of powder injection molding compounds.* Polimery, 2010. **55**(1): p. 3-11.
69. Abu-Orf, M. and B. Örmeci, *A new tool for measuring biosolids floc strength*. 2004, USA: IWA, Publishing.
70. Escocio, V.A., et al., *Thermal and Dynamic Mechanical Characterization of TPU/Mica Composites Prepared by Torque Rheometer.* Polimeros-Ciencia E Tecnologia, 2011. **21**(3): p. 240-245.
71. Lapa, V.L.D., et al., *Aluminum hydroxide and carbon black filled NBR/PVC composites-vulcanization and processability studies.* Polymer Testing, 2002. **21**(4): p. 443-447.
72. Reddy, J.J., et al., *Loading of solids in a liquid medium: Determination of CBVC by torque rheometry.* Journal of the European Ceramic Society, 1996. **16**(5): p. 567-574.
73. Colbert, G.P. and K.D. Ziegel, *Estimation of end correction in capillary-flow.* Journal of Testing and Evaluation, 1984. **12**(6): p. 400-406.
74. Rabinowitsch, B., Physical Chemistry, 1929. **145A**(1).
75. Bagley, E.B., *End corrections in the capillary flow of polyethylene.* Journal of Applied Physics, 1957. **28**(5): p. 624-627.
76. Mooney, M., *Explicit formulas for slip and fluidity.* Journal of Rheology, 1931. **2**: p. 210-222.
77. Yang, W.W., K.Y. Yang, and M.H. Hon, *Effects of PEG molecular weights on rheological behavior of alumina injection molding feedstocks.* Materials Chemistry and Physics, 2002. **78**(2): p. 416-424.
78. Han, C.D., D.M. Baek, and J.K. Kim, *Effects of molecular-weight and block length ratio on the rheological behavior of low-molecular-weight polyestirene-block-polyisoprene copolymers in the disordered state.* Macromolecules, 1995. **28**(17): p. 5886-5896.
79. Contreras, J.M., A. Jimenez-Morales, and J.M. Torralba, *Improvement of rheological properties of Inconel 718 MIM feedstock using tailored particle size distributions.* Powder Metallurgy, 2008. **51**(2): p. 103-106.
80. Sotomayor, M.E., A. Varez, and B. Levenfeld, *Influence of powder particle size distribution on rheological properties of 316 L powder injection moulding feedstocks.* Powder Technology, 2010. **200**(1-2): p. 30-36.
81. Senapati, P.K., B.K. Mishra, and A. Parida, *Modeling of viscosity for power plant ash slurry at higher concentrations: Effect of solids volume fraction, particle size and hydrodynamic interactions.* Powder Technology, 2010. **197**(1-2): p. 1-8.
82. Baiyun, H., L. Shuquan, and Q. Xuanhui, *The rheology of metal injection molding.* Journal of Materials Processing Technology, 2003. **137**: p. 132-7.
83. Allaire, F., B.R. Marple, and J. Boulanger, *Injection-molding of submicrometer zirconia - Blend formulation and rheology.* Ceramics International, 1994. **20**(5): p. 319-325.
84. Shutilin, Y.F., *On application of Williams-Landel-Ferry and Arrhenius equations to description of relaxational properties of polymers and polymer homologs.* Vysokomolekulyarnye Soedineniya Seriya A, 1991. **33**(1): p. 120-127.
85. Cross, M.M., *Rheology of non-Newtonian fluids - A new flow equation for pseudoplastic systems.* Journal of Colloid Science, 1965. **20**(5): p. 417-&.
86. Pinarbasi, A. and A. Liakopoulos, *Stability of 2-layer Poiseuille flow of Carreau-Yasuda and Binham-like fluids.* Journal of Non-Newtonian Fluid Mechanics, 1995. **57**(2-3): p. 227-241.

87. De Waele, A., *Viscosimetry and plastometry.* Journal of Oil and Colour Chemists' Assiation 1923. **6**(33): p. 33-80.
88. Sisko, A.W., *The flow of lubricating greases.* Industrial and Engineering Chemistry, 1958. **50**(12): p. 1789-1792.
89. Bingham, E.C., *The rheology of the blood. V.* Journal of General Physiology, 1945. **28**(6): p. 605-626.
90. Lapointe, F., S. Turenne, and B. Julien, *Low viscosity feedstocks for powder injection moulding.* Powder Metallurgy, 2009. **52**(4): p. 338-344.
91. Casson, N., *Rheology and the letterpress printing process.* Journal of the Society of Dyers and Colourists, 1953. **69**(13): p. 576-582.
92. Casson, N., *An interpretation of viscosity measurements on suspensions of powdered solid, in terms of the physicl state of the suspended particles.* Journal of the Oil & Colour Chemists Association, 1981. **64**(12): p. 480-489.
93. Suri, P., et al., *Numerical analysis of filling stage during powder injection moulding: effects of feedstock rheology and mixing conditions.* Powder Metallurgy, 2004. **47**(2): p. 137-143.
94. Eilers, H., *The viscosity of the emulsion of highly viscous substances as function of concentration.* Kolloid-Zeitschrift, 1941. **97**(3): p. 313-321.
95. Chong, J.S., Christia.Eb, and A.D. Baer, *Rheology of concentrated suspensions.* Journal of Applied Polymer Science, 1971. **15**(8): p. 2007-&.
96. Mooney, M., *The viscosity of concentrated suspension of spherical particles.* Journal of Colloid Science, 1951. **6**(2): p. 162-170.
97. Mills, P., *Non-Newtonian behavior of flocculated suspensions.* Journal De Physique Lettres, 1985. **46**(7): p. L301-L309.
98. Krieger, I.M. and T.J. Dougherty, *A mechanism for non-Newtonian flow in suspensions of rigid spheres.* Transactions of the Society of Rheology, 1959. **3**: p. 137-152.
99. Quemada, D., *Rheology of concentrated disperse systems and minimum energy-dissipation principle. 1. Viscosity-concentration relationship.* Rheologica Acta, 1977. **16**(1): p. 82-94.
100. Honek, T., B. Hausnerova, and P. Saha, *Relative viscosity models and their application to capillary flow data of highly filled hard-metal carbide powder compounds.* Polymer Composites, 2005. **26**(1): p. 29-36.
101. Reddy, J.J., N. Ravi, and M. Vijayakumar, *A simple model for viscosity of powder injection moulding mixes with binder content above powder critical binder volume concentration.* Journal of the European Ceramic Society, 2000. **20**(12): p. 2183-2190.
102. Hausnerova, B., et al., *The effect of powder characteristics on pressure sensitivity of powder injection moulding compounds.* Powder Technology, 2011. **206**(3): p. 209-213.
103. Hausnerova, B., et al., *Pressure-dependent viscosity of powder injection moulding compounds.* Rheologica Acta, 2006. **45**(3): p. 290-296.
104. Hausnerova, B., T. Sedlacek, and P. Vltavska, *Pressure-affected flow properties of powder injection moulding compounds.* Powder Technology, 2009. **194**(3): p. 192-196.
105. Salomon, A. and K. Fielder, *Practical use of differential calorimetry for plastics*, in *Hadbook of Plastics Analysis*, H. Lobo and J. Bonilla, Editors. 2003, Marcel Dekker: New York. p. 79-109.
106. Jin, F.-L. and S.-J. Park, *Thermal properties of epoxy resin/filler hybrid composites.* Polymer Degradation and Stability, 2012. **97**(11): p. 2148-2153.

107. Doyle, C.D., *Estimating thermal stability of experimental polymers by empirical thermogravimetric analysis.* Analytical Chemistry, 1961. **33**(1): p. 77-&.
108. Liau, L.C.K. and C.C. Chiu, *Optimal heating strategies of polymer binder burnout process using dynamic optimization scheme.* Industrial & Engineering Chemistry Research, 2005. **44**(13): p. 4586-4593.
109. Aggarwal, G., et al., *Master decomposition curve for binders used in powder injection molding.* Metallurgical and Materials Transactions a-Physical Metallurgy and Materials Science, 2007. **38A**(3): p. 606-614.
110. Belgacem, M., T. Barriere, and J.C. Gelin, *Investigations on thermal debinding process for fine 316L stainless steel feedstocks and identification of kinetic parameters from coupling experiments and finite element simulations.* Powder Technology, 2013. **235**: p. 192-202.
111. Salehi, M., et al., *Kinetic analysis of the polymer burnout in ceramic thermoplastic processing of the YSZ thin electrolyte structures using model free method.* Applied Energy, 2012. **95**: p. 147-155.
112. Vyazovkin, S., *Model-free kinetics - Staying free of multiplying entities without necessity.* Journal of Thermal Analysis and Calorimetry, 2006. **83**(1): p. 45-51.
113. Kissinger, H., *Reaction kinetics in differential thermal analysis.* Analytical Chemistry, 1957. **29**: p. 1702-1706.
114. Flynn, J.H. and L.A. Wall, *A quick direct method for determination of activation energy from thermogravimetric data.* Journal of Polymer Science Part B-Polymer Letters, 1966. **4**(5PB): p. 323-&.
115. Ozawa, T., *A new mwthod of analyzing thermogravimetric data.* Bulletin of the Chemical Society of Japan, 1965. **38**(11): p. 1881-&.
116. Vyazovkin, S., et al., *ICTAC Kinetics Committee recommendations for performing kinetic computations on thermal analysis data.* Thermochimica Acta, 2011. **520**(1-2): p. 1-19.
117. Li, Y., L. Li, and K.A. Khalil, *Effect of powder loading on metal injection molding stainless steels.* Journal of Materials Processing Technology, 2007. **183**(2-3): p. 432-439.
118. Contreras, J.M., A. Jimenez-Morales, and J.M. Torralba, *Experimental and theoretical methods for optimal solids loading calculation in MIM feedstocks fabricated from powders with different particle characteristics.* Powder Metallurgy, 2010. **53**(1): p. 34-40.
119. Li, Y., B. Huang, and X. Qu, *Viscosity and melt rheology of metal injection moulding feedstocks.* Powder Metallurgy, 1999. **42**(1): p. 86-90.
120. Rei, M., et al., *Low-pressure injection molding processing of a 316-L stainless steel feedstock.* Materials Letters, 2002. **52**(4-5): p. 360-365.
121. Herranz, G., et al., *Development of new feedstock formulation based on high density polyethylene for MIM of M2 high speed steels.* Powder Metallurgy, 2005. **48**(2): p. 134-138.
122. Zauner, R., et al., *Variability of feedstock viscosity and its correlation with dimensional variability of green powder injection moulded components.* Powder Metallurgy, 2004. **47**(2): p. 151-156.
123. Thian, E.S., et al., *Ti-6Al-4V/HA composite feedstock for injection molding.* Materials Letters, 2002. **56**(4): p. 522-532.
124. Thomas-Vielma, P., et al., *Production of alumina parts by powder injection molding with a binder system based on high density polyethylene.* Journal of the European Ceramic Society, 2008. **28**(4): p. 763-771.

125. Schlechtriemen, N., et al., *Impact of powder morphology on quality of low-pressure injection moulded reaction-bonded net shape oxide ceramics.* Journal of the European Ceramic Society, 2013. **33**(4): p. 709-715.
126. Fan, Y.-L., et al., *Minimum Amount of Binder Removal Required during Solvent Debinding of Powder-Injection-Molded Compacts.* Metallurgical and Materials Transactions a-Physical Metallurgy and Materials Science, 2009. **40A**(4): p. 768-779.
127. Krauss, V.A., et al., *A model for PEG removal from alumina injection moulded parts by solvent debinding.* Journal of Materials Processing Technology, 2006. **182**(1-3): p. 268-273.
128. Yang, W.W., et al., *Solvent debinding mechanism for alumina injection molded compacts with water-soluble binders.* Ceramics International, 2003. **29**(7): p. 745-756.
129. Liu, W., et al., *Debinding Behaviors and Mechanism of Injection Molded ZrO2 Ceramics using Kerosene as Solvents*, in *High-Performance Ceramics Vii, Pts 1 and 2*, W. Pan and J.H. Gong, Editors. 2012. p. 431-434.
130. Yang, W.W. and M.H. Hon, *In situ evaluation of dimensional variations during water extraction from alumina injection-moulded parts.* Journal of the European Ceramic Society, 2000. **20**(7): p. 851-858.
131. Westcot, E.J., C. Binet, and R.M. German, *In situ dimensional change, mass loss and mechanisms for solvent debinding of powder injection moulded components.* Powder Metallurgy, 2003. **46**(1): p. 61-67.
132. Kang, S.J.L., *Sintering: Densification, Grain Growth and Microstructure*. 2005, Oxford: Elsevier Butterworth-Heinemann. 279.
133. Schatt, W. and K. Wieters, *Powder Metallurgy: Processing and Materials*. 1997, Bellstone (UK): European Powder Matallurgy Association.
134. Chiang, Y., D. Birnie III, and W. Kingery, *Physical Ceramics: Principles for Ceramic Science and Engineering*. 1997: John Willey and Sons, Inc.
135. Shi, Y., X.X. Huang, and D.S. Yen, *Fabrication of hot-pressed zircon ceramics: Mechanical properties and microstructure.* Ceramics International, 1997. **23**(5): p. 457-462.
136. Auerkari, P., *Mechanical and physical properties of engineering alumina ceramics*. 1996: Technical Research Centre of Finland 26.
137. Munro, R.G., *Evaluated material properties for a sintered alpha-alumina.* Journal of the American Ceramic Society, 1997. **80**(8): p. 1919-1928.
138. Stawarczyk, B., et al., *The effect of zirconia sintering temperature on flexural strength, grain size, and contrast ratio.* Clinical Oral Investigations, 2013. **17**(1): p. 269-274.
139. Rendtorff, N.M., et al., *Dense zircon (ZrSiO4) ceramics by high energy ball milling and spark plasma sintering.* Ceramics International, 2012. **38**(3): p. 1793-1799.
140. Raigrodski, A.J., *All-ceramic full-coverage restorations: concepts and guidelines for material selection.* Practical procedures & aesthetic dentistry : PPAD, 2005. **17**(4): p. 249-258.
141. Lin, J.D. and J.G. Duh, *Fracture toughness and hardness of ceria- and yttria-doped tetragonal zirconia ceramics.* Materials Chemistry and Physics, 2003. **78**(1): p. 253-261.
142. Din, S.U. and A. Kaleem, *Vickers hardness study of zirconia partially stabilized with lanthanide group oxides.* Materials Chemistry and Physics, 1998. **53**(1): p. 48-54.

143. Li, H., S. Zhou, and S. Zhang, *The relationship between the thermal expansions and structures of ABO(4) oxides.* Journal of Solid State Chemistry, 2007. **180**(2): p. 589-595.
144. Hayashi, H., et al., *Thermal expansion coefficient of yttria stabilized zirconia for various yttria contents.* Solid State Ionics, 2005. **176**(5–6): p. 613-619.
145. Shi, Y., et al., *TEM and HREM characterization of hot-pressed zircon ceramics.* Materials Letters, 1995. **23**(4-6): p. 247-252.
146. Schlichting, K.W., N.P. Padture, and P.G. Klemens, *Thermal conductivity of dense and porous yttria-stabilized zirconia.* Journal of Materials Science, 2001. **36**(12): p. 3003-3010.
147. Victor, A.C. and T.B. Douglas, *Enthalpy and Heat Capacity of Magnesiium Oxide, Zirconium Oxide and Zirconium Silicate from 0° to 900° C*, in *Physical Properties of High Temperature Materials*. 1961, USA National Bureau of Standards. p. 22.
148. Kaiser, A., M. Lobert, and R. Telle, *Thermal stability of zircon (ZrSiO4).* Journal of the European Ceramic Society, 2008. **28**(11): p. 2199-2211.
149. Moreno, R., J.S. Moya, and J. Requena, *Slip casting of zircon by using and organic surfactant.* Ceramics International, 1991. **17**(1): p. 37-40.
150. Rendtorff, N.M., L.B. Garrido, and E.F. Aglietti, *Effect of the addition of mullite-zirconia to the thermal shock behavior of zircon materials.* Materials Science and Engineering a-Structural Materials Properties Microstructure and Processing, 2008. **498**(1-2): p. 208-215.
151. Del Pin, G., et al., *Thermal interaction between some oxides and zircon as a material for diesel engines filter.* Ceramics International, 2004. **30**(2): p. 279-283.
152. Ewing, R.C., *Ceramic matrices for plutonium disposition.* Progress in Nuclear Energy, 2007. **49**(8): p. 635-643.
153. Awaad, M. and S.H. Kenawy, *Sintering of zircon: the role of additives.* British Ceramic Transactions, 2003. **102**(2): p. 69-72.
154. Kelly, P.M. and L.R.F. Rose, *The martensitic transformation in ceramics - its role in transformation toughening.* Progress in Materials Science, 2002. **47**(5): p. 463-557.
155. Chevalier, J., et al., *The Tetragonal-Monoclinic Transformation in Zirconia: Lessons Learned and Future Trends.* Journal of the American Ceramic Society, 2009. **92**(9): p. 1901-1920.
156. Xue-Jun, J., *Martensitic transformation in zirconia containing ceramics and its applications.* Current Opinion in Solid State & Materials Science, 2005. **9**(6): p. 313-18.
157. Badiee, S.H., S. Otroj, and M. Rahmani, *The Effect of Nano-TiO2 Addition on the Properties of Mullite-Zirconia Composites Prepared by Slip Casting.* Science of Sintering, 2012. **44**(3): p. 341-354.
158. K.B. Lee, et al., *Effect of SiO_2, Al_2O_3, and clay additions on the sintering characteristics of zircon.* Korean Journal of Materials Research, 2008. **18**(7): p. 352-356.
159. Shoyama, M., et al., *Sol-gel synthesis of zircon-effect of addition of lithium ions.* Journal of Materials Science, 1998. **33**(19): p. 4821-4828.
160. Mori, T., et al., *Preparation of high-purity $ZrSiO_4$ powder using sol-gel processing and mechanical-properties of the sintered body.* Journal of the American Ceramic Society, 1992. **75**(9): p. 2420-2426.
161. Alarcon, J., *Crystallization behaviour and microstructural development in ZrSiO4 and V-ZrSiO4 solid solutions from colloidal gels.* Journal of the European Ceramic Society, 2000. **20**(11): p. 1749-1758.

162. Alahakoon, W.P.C.M., et al., *Fully densified zircon co-doped with iron and aluminium prepared by sol-gel processing.* Journal of the European Ceramic Society, 2010. **30**(12): p. 2515-2523.
163. Tartaj, P., et al., *Zircon formation from amorphous spherical ZrSiO3 particles obtained by hydrolysis of aerosols.* Journal of Materials Science, 1994. **29**(24): p. 6533-6538.
164. Tartaj, P., *Zircon formation from nanosized powders obtained by a reverse micelle process.* Journal of the American Ceramic Society, 2005. **88**(1): p. 222-224.
165. Tartaj, P. and L.C. De Jonghe, *Preparation of nanospherical amorphous zircon powders by a microemulsion-mediated process.* Journal of Materials Chemistry, 2000. **10**(12): p. 2786-2790.
166. Garvie, R.C., *Improved thermal-shock resistant refractories from plasma-dissociated zircon.* Journal of Materials Science, 1979. **14**(4): p. 817-822.
167. Tartaj, P., et al., *The formation of zircon from amorphous ZrO2 center dot SiO2 powders.* Journal of Materials Science, 1996. **31**(22): p. 6089-6094.
168. Schelz, S., et al., *Recombination of silica and zirconia into zircon by means of laser treatment of plasma-sprayed coatings.* Journal of Materials Science, 2008. **43**(6): p. 1948-1957.
169. Ying, S., H. Xiaoxian, and Y. Dongsheng, *Toughening of hot-pressed ZrSiO 4 ceramics by addition of Y-TZP.* Materials Letters, 1998. **35**(3-4): p. 161-5.
170. Ying, S., et al., *TEM and HREM characterization of hot-pressed zircon ceramics.* Materials Letters, 1995. **23**(4-6): p. 247-52.
171. Antsiferov, V.N., et al., *Application of mechanochemical activation in production of zircon ceramics.* Russian Journal of Non-Ferrous Metals, 2010. **51**(2): p. 182-187.
172. Ebadzadeh, T. and M. Valefi, *Microwave-assisted sintering of zircon.* Journal of Alloys and Compounds, 2008. **448**(1-2): p. 246-249.
173. Rendtorff, N.M., et al., *Zircon-zirconia (ZrSiO4-ZrO2) dense ceramic composites by spark plasma sintering.* Journal of the European Ceramic Society, 2012. **32**(4): p. 787-793.
174. Schlechtriemen, N., et al., *Optimization of feedstock properties for reaction-bonded net-shape zircon ceramics by design of experiments.* Ceramics International, 2010. **36**(1): p. 223-229.
175. Kwak, T.S., *A study of ceramic injection molding of watch case composed of ZrO2 powder*, in *Progress in Powder Metallurgy, Pts 1 and 2*, D.Y. Yoon, et al., Editors. 2007. p. 337-340.
176. Moritz, T. and R. Lenk, *Ceramic injection moulding: a review of developments in production technology, materials and applications.* Powder Injection Moulding International, 2009. **3**(3): p. 23-34.
177. Dewi, F.D., *Posterior crown with zirconium silicate indirect composite restorative system.* E-Journal of Dentistry, 2012. **2**(2): p. 181.
178. Ruban, A.V., et al., *Magnetic state, magnetovolume effects, and atomic order in Fe65Ni35 Invar alloy: A first principles study.* Physical Review B, 2007. **76**(1).
179. Khomenko, O.A., *Origin and specific features of invar anomalies of physical properties: Fe-Ni alloys with an FCC lattice.* Physics of Metals and Metallography, 2007. **104**(2): p. 146-156.
180. Unknown, *Special-Purpose Nickel Alloys*, in *ASM Specialty Hadbook: Nickel, Cobalt and their Alloys*. 2002, ASM International.

181. Sokolowski, W., et al., *DIMENSIONAL STABILITY OF HIGH-PURITY INVAR 36*. Quality and Reliability for Optical Systems, ed. J.W. Bilbro and R.E. Parks. Vol. 1993. 1993. 115-126.
182. Rochegude, P. and J. Foct, *Influence of interstitial nitrogen on the thermal-expansion of Fe64-Ni36 alloys.* Scripta Metallurgica Et Materialia, 1992. **27**(3): p. 325-328.
183. Nadutov, V.M., et al., *Interatomic Interaction and Magnetostriction in Invar Fe-Ni-C-Based Alloys.* Metallofizika I Noveishie Tekhnologii, 2009. **31**(8): p. 1021-1034.
184. Nadutov, V.M., et al., *Magnetic properties of alloyed invar alloys on the base of Fe-Ni-C.* Metallofizika I Noveishie Tekhnologii, 2006. **28**: p. 39-48.
185. Kim, B.S., et al., *Effect of carbon on the coefficient of thermal expansion of As-cast Fe-30wt.%Ni-12.5wt.%Co-xC invar alloys.* Metals and Materials International, 2002. **8**(3): p. 247-252.
186. Wittenauer, J., *Factors affecting the mechanical strength of Fe-36Ni Invar*. Invar Effect: A Centennial Symposium, ed. J. Wittenauer. 1996. 231-238.
187. Hatate, M., H. Sumimoto, and K. Nakamura, *Influence of carbon and nickel on linear thermal-expansion coefficient in low thermal-expansion Fe-Ni-C alloys.* Journal of the Japan Institute of Metals, 1990. **54**(9): p. 1036-1040.
188. Steele, J.M., et al., *Temperature and age effects on the temporal stability of Invar*. Current Developments in Optical Design and Optical Engineering Ii, ed. R.E. Fischer and W.J. Smith. Vol. 1752. 1992. 40-51.
189. Wiedenmann, A., W. Wagner, and H. Wollenberger, *Matastability of Fe-34Ni invar-alloys above 600 degrees C.* Journal of the Less-Common Metals, 1988. **145**(1-2): p. 47-53.
190. Jacobs, S.F., S.C. Johnston, and D.E. Schwab, *Dimensional stability of Invars.* Applied Optics, 1984. **23**(20): p. 3500-3502.
191. Zakharov, A.I., et al., *Time instability of Invar during artificial aging.* Fizika Metallov I Metallovedenie, 1974. **37**(2): p. 442-444.
192. Anishchenko, A.S., *Effect of heat treatment on the properties of deformed alloy 36 N.* Metal Science and Heat Treatment, 1996. **38**(3-4): p. 180-1.
193. Dieter, G., *Mechanical Metallurgy*. SI Edition ed. 1988: McGraw-Hill Book Co. 766.
194. Reed, R.P., *Low-temperature tensile properties of Fe-Ni alloys*, in *Advances in Cryogenic Engineering Materials, Vol 44, Pts a and B*, U.B. Balachandran, et al., Editors. 1998. p. 25-32.
195. Unknown. *36% Nickel-Iron allow for low temperature service*.
196. Unknown, *Stainless Steel: Tables and Technical Properties*. 2nd ed. Materials and Applications. Vol. 5. 2007, Luxembourg: Euro Inox. 24.
197. Heaney, D.F., T.W. Mueller, and P.A. Davies, *Mechanical properties of metal injection moulded 316L stainless steel using both prealloy and master alloy techniques.* Powder Metallurgy, 2004. **47**(4): p. 367-373.
198. Unknown, *Machining nickel alloys*: A Nickel Development Institute (www.nickelinstitute.org).
199. Khidhir, B. and B. Mohamed, *Machining of nickel based alloys using different cemented carbide tools* Journal of Engineering Science and Technology 2010. **5**(3): p. 264 - 271
200. *Guide to machining Carpenter special alloys*. 2002, Carpenter Technology Corporation: Wyomissing (Pennsylvania).
201. Unknown, *Machining*. 9th ed. Metals Handbook. Vol. 16, Metals Park, OH 44073: ASTM International.

202. Bitkulov, I.K., et al., *Effect of severe plastic deformation on the properties of the Fe-36% Ni invar alloy.* Physics of Metals and Metallography, 2006. **102**(1): p. 91-96.
203. Izotov, V.I., et al., *Structure and properties of Fe-36% Ni Invar after intense shear deformation.* Physics of Metals and Metallography, 1996. **82**(3): p. 289-96.
204. Maslyuk, V.A., O.A. Panasyuk, and O.V. Vlasova, *Physical, technological and magnetic properties of powder iron-nickel alloys.* Powder Metallurgy and Metal Ceramics, 2003. **42**(9-10): p. 536-539.
205. Chun-Ting, L., C. Bi-Shiou, and S. Chi, *Cost-effective optoelectronic packages using powder metallurgy.* IEEE Journal of Selected Topics in Quantum Electronics, 2006. **12**(5): p. 970-82.
206. Chen, G.L., *Lens module and digital camera module using the same*, in *USA Patent Application Publication*. 2007, HON HAI Precision Industry Co. LTD.: USA. p. 6.
207. Sokolowski, W., C. Hsieh, and T. O'Donnell. *New HP (high purity) Invar 36*. in *Invar Effect: A Centennial Symposium*. 1996.
208. Kronberger, M., *Housing body*, in *USA Patent Application Publcation*. 2007: USA. p. 6.

2 Motivations and Objectives

2.1 Motivations **45**

2.2 Objectives **46**

References **47**

2.1 Motivations

In the previous chapter a review of the main trends and the future perspectives of PIM were briefly revised. In order to expand PIM opportunities and application fields, research is still needed in many areas such as introduction of novel materials and processes. This requires a comprehensive understanding of the relationships between materials, processes and properties. Optimisation and reproducibility of the processes and costs reduction are the main concerns in today PIM industry. Computational methods begin to be widely employed for such purposes. These methods need a proper modelling of the behaviour and a thorough characterisation of the material properties.

Environmental concerns have become of main importance in modern societies. Regulations affect industry that needs to adapt their processes to reduce energy consumption and hazardous chemicals and global warming gases emissions [1]. The policies of creating sound processes within the industry could be also beneficial to reduce costs and for marketing strategies [2-4]. PM and PIM has still possibilities to improve the efficacy of the process in terms of energy consumption and environmental friendly issues [1, 5].

The polymeric part of a feedstock is just only temporary and has to be removed preferably by a solvent debinding followed by a thermal burn out. Water is a sound and inexpensive solvent that can be employed effectively in PEG based feedstocks. PEG is a non-toxic substance that is commonly combined with petroleum derivative polymers to be part of the feedstock composition. The burn out of these petroleum based polymers produces organic sometimes hazardous volatiles that have to be treated before their emission to atmosphere [6]. Combustion is a rapid oxidation process which results in the destruction of volatiles by converting them to carbon dioxide and water. Using polymers coming from natural vegetable sources instead of petroleum derivatives ensures that all the resulting carbon dioxide was previously fixed directly from the atmosphere gases and is not added from the mineral resources of the earth's mantle. Hence, it could be said, without considering other emissions coming from the intrinsic fabrication and distribution, that for example, cellulose and starch derivative polymers burn out produce a net zero CO_2 emission.

Having these premises in mind, cellulose derivative thermoplastics are proposed in this thesis work as substitutes to conventional petroleum derivative thermoplastics used in PEG based binders. More precisely a cellulose ester family, the cellulose acetate butyrate (CAB) family, was selected for the study due to the following reasons:

- is massively produced as a thermoplastic coming from natural resources
- is accessible and reasonably inexpensive
- is comparatively novel in regard to its applicability to PIM
- is fairly well documented for other applications than PIM

The applicability of such kind of binders to PIM has been very scarcely investigated and it was limited to only few materials [7-9]. CAB properties depend on the percentage of acetyl,

butyryl and hydroxyl side groups in the polymeric chain, the molecular weight and other factors like the polydispersity index [10]. Hence, a wide variety of CABs with different properties are offered [11]. To the best of the author's knowledge there is not any work that deals with the effect of different CAB upon the feedstock behaviour.

Furthermore the binder behaviour is affected by the nature of the powder and its morphological and particle size characteristics. In order to extend the uses of CAB based binders, new materials have to be tested with those binders. Among all the possibilities, a ceramic (zirconium silicate) and a metallic alloy (Invar 36 alloy) were selected. The processability of these materials by PIM route is relatively novel with a lack of examples of pure zirconium silicate and just a few of Invar 36 alloys. Peculiarities of both materials, presented in the Chapter 1, make them interesting subjects of study.

2.2 Objectives

The principal objectives of this thesis work are: a) to investigate the suitability of the use of CAB based binders in the different PIM routes and their applicability to different materials and b) to design and develop a novel competitive feedstock formulation thereof. These objectives are intended to be accomplished by developing two completely different materials PIM processes, using a ceramic irregular shape zirconium silicate powder and different sizes metallic spherical Invar 36 powders.

Furthermore, to fulfill these objectives, partial objectives are contemplated and listed below:

- To study the rheology of different feedstocks formulations both by torque rheology (study of the mixing process) and capillary rheology (study of the viscosity of the materials at different processing conditions). These experimental researches would be helpful to optimise mixing conditions, to determine the suitability of the materials to be injected and to determine the optimal solid loading admissible.

- To study the thermal behaviour of the feedstocks by thermal analysis and calorimetry methods. These experiments will give an idea of the degradation temperature intervals which is very important to design processing temperatures and debinding processes. The degradation kinetics and thermal stability of the feedstocks have to be evaluated.

- Once these preliminary studies are conducted, the feedstocks will be used to perform different full PIM processes. HPPIM, LPPIM and micro-MIM routes will be carried out with the different materials. The processing parameters have to be evaluated and optimised. The resulting sintered parts have to be tested to determine their mechanical and functional properties. These properties have to be compared with those of the wrought material in order to elucidate if the PIM route is suitable to elaborate the selected materials.

- Some of the results obtained from the experimental work could be used in modelling and simulation of different PIM stages. Particularly, rheology results are indispensable to simulate the injection process. This requires adjusting experimental data to different empirical and theoretical models that define the flow behaviour of the feedstocks. Conventional models will be tested and novel models will be proposed if the firsts fails in explaining the flow behaviour of the feedstocks.

References

1. Dale, R.D., *Sustainability Manufacturing within the PM Industry* MPIF, Editor, www.mpif.org. p. 4.
2. Berns, M., et al., *The Business of Sustainability—Imperatives, Advantages, and Actions*. 2009, Boston consulting group: www.bcg.com.
3. Kauffeld, R., A. Malhotra, and S. Higgins, *Green Is a Strategy*, in *Strategy + Business*. 2009: www.strategy-business.com.
4. Lubin, D.A. and D.C. Esty, *The Sustainability Imperative*, in *Harvard Business Review*. 2010: http://hbr.org.
5. Unknown, *Powder Metallurgy—Intrinsically Sustainable*, MPIF, Editor, www.empif.org. p. 8.
6. Unknown, *Control of Volatile Organic Compound Emissions from Manufacture of High-density Polyethylene, Polypropylene and Polystyrene Resins*. 1983, U.S. Environmental Protection Agency.
7. Haw Pei, L. and N. Muhamad, *Rheological analysis of microminiature powder injection molding (muPIM) feedstock.* Applied Mechanics and Materials, 2011. **52-54**: p. 238-243.
8. Song, M., et al., *Water-soluble binder with high flexural modulus for powder injection molding.* Journal of Materials Science, 2005. **40**(5): p. 1105-1109.
9. Park, M.S., et al., *Water-soluble binder of cellulose acetate butyrate/poly(ethylene glycol) blend for powder injection molding.* Journal of Materials Science, 2001. **36**(23): p. 5531-5536.
10. Kamide, K., *Cellulose and Cellulose Derivatives: molecular characteristics and applications*. 1st ed. Polymer Science Library. 2005: Elsevier Science.
11. Unknown, *Eastman™ cellulose-based specialty polymers*, Eastman publications www.eastman.com.

Experimental Work

3

3.1 Scheme of the experimental work..... 51

3.2 Materials..... 52

3.2.1 Binder components selection 52
3.2.2 Powders selection..... 53

3.3 Equipments and methodologies. 57

3.3.1 Thermogravimetrical and calorimetric analyses. 57
3.3.2 Binder and feedstock elaboration and rheological characterization..... 59
3.3.3 Injection moulding..... 60
3.3.4 Debinding setups..... 61
3.3.5 Strategies for sintering optimisation. 63
3.3.6 Dimensional shrinkage and densification evaluation. 65
3.3.7 Microstructural evaluation. 65
3.3.8 X-ray diffraction (XRD) 66
3.3.9 Hardness measurements..... 67
3.3.10 Bending tests..... 68
3.3.11 In situ and ex situ micro tensile tests..... 68
3.3.12 Other properties 68

References..... 69

3.1 Scheme of the experimental work

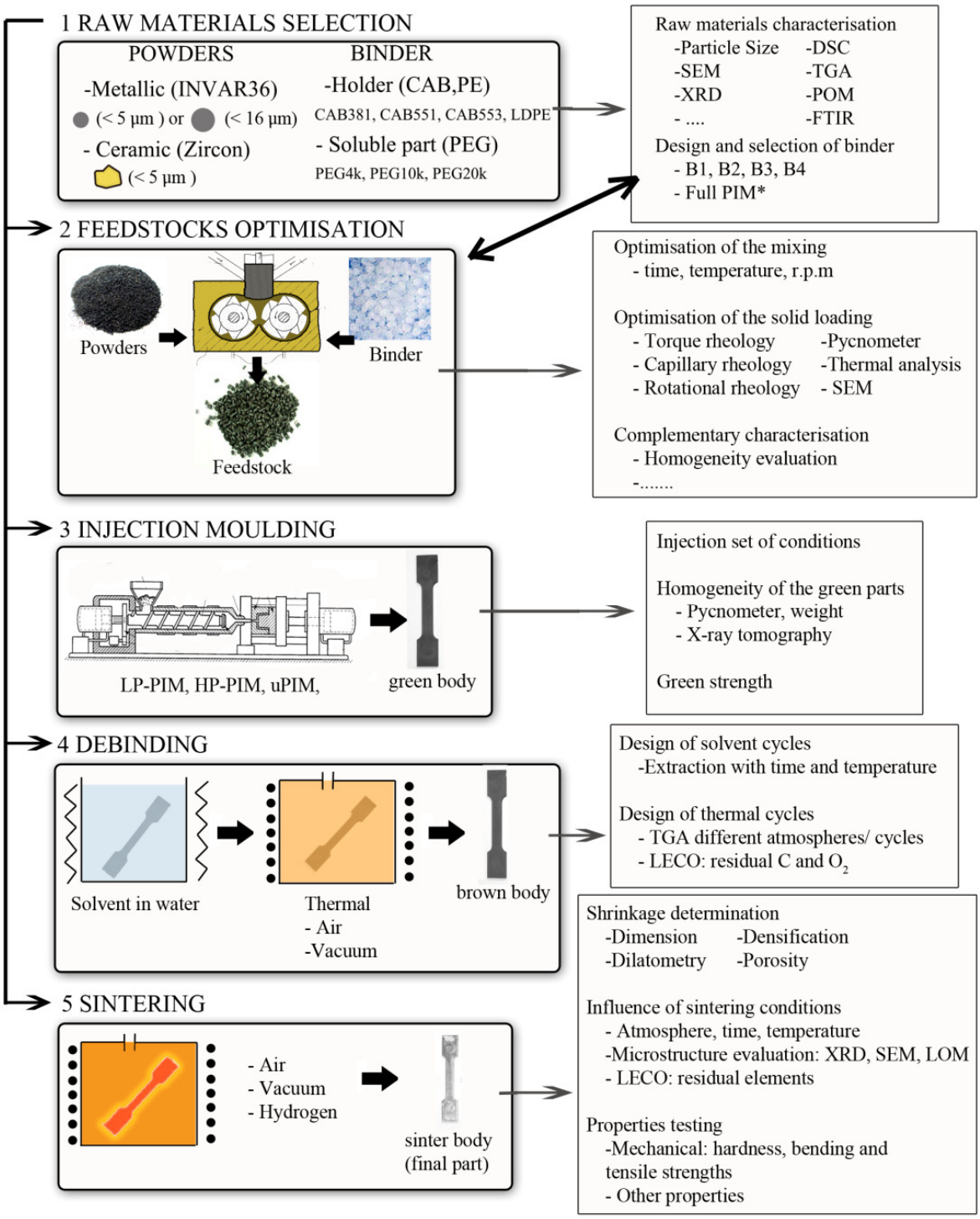

Figure 3. 1 Scheme of the experimental work developed during the thesis.

In this chapter the experimental procedures followed during the experimental part of the thesis are overviewed. The raw materials used and the selection criteria according to their intrinsic properties in relation with the scope of the thesis are also introduced. A review of the typical equipments and methodologies to characterise the materials is presented.

Figure 3. 1 shows the scheme of the experimental work developed during this thesis. First of all the objectives of the experimental work were defined and consequently the raw materials were selected. The raw materials were characterised in order to ensure that they meet the desired specifications.

A study to determine the most suitable binder compounds combinations was carried out. Different types of cellulose acetates butyrate (CABs) and poly(ethylene glycol) (PEG) were evaluated first by developing and characterising single binder systems and then by carrying out a whole PIM process with zirconium silicate powders. After the determination of the advantages and pitfalls using each single component, a binder system was designed and selected to develop and characterise in detail full PIM processes of the zirconium silicate and invar allow powders.

Each stage of the process and the corresponding tasks-to-do needed are shown in detail in Figure 3. 1. It is worth to note that the different stages are developed consecutively and they are very closely related. Therefore, if flaws derived from a previous stage are detected in a subsequent stage, optimisation of the previous stages has to be repeated and changes in the feedstock composition reconsidered.

The determination of the optimal solid loading is one of the main concerns and a critical issue during the design of a PIM process that needs to be carefully considered. The solid fraction added to a binder system will affect all the process stages and the final parts properties. Therefore this work has being mainly oriented to evaluate and determine how solid loading affects the PIM of different types of powders when they are mixed with the binder systems that are the object of study.

Each of the ceramic and metallic materials selected have special features oriented to specific applications. The final parts properties have to be evaluated in order to determine if the materials selected and their processing route result in the required properties.

3.2 Materials.

3.2.1 Binder components selection

Three types of polymer substances were selected to take part of the binder systems. As back-bone polymer, different types of cellulose acetate butyrate (CAB) and low density polyethylene (LDPE) were studied. Several molecular weights polyethylene glycols (PEG) were chosen as the soluble part of the binder systems. The chemical formula of the monomer repetitive unit of CABs is shown in Figure 3. 2a. Cellulose acetate butyrate properties depend on the percentage of acetyl, butyryl and hydroxyl side groups in the polymeric chain, the molecular weight and other factors like the polydispersity index[1]. Hence, a wide variety of CABs with different properties are offered [2]. To that respect, three CABs with similar molecular weights but different percentages of acetyl, butyryl and hydroxyl groups were selected to study the dependence of these side groups in the binder and feedstock

characteristics: CAB381-0.1, CAB551-0.01 and CAB553-0.4 from Eastman (Germany). In order to compare relatively novel CAB formulations with existing polyolefin formulations, a low density polyethylene (LDPE 780E) (Figure 3. 2c) was selected. To complete the binder system formulations, poly(ethylene glycol) (PEG) was chosen (Figure 3. 2b). The PEG's solubility in water [3-5] and other properties like viscosity [6] and thermo-physical [4, 5] properties depends on the molecular weight. A PEG20k having a M_n of 20000 was principally chosen for the binders and feedstocks formulations, although PEGs of lower M_n (PEG10k and PEG4k) were eventually employed to improve feedstocks properties (to reduce their viscosity and improve their solubility in water).

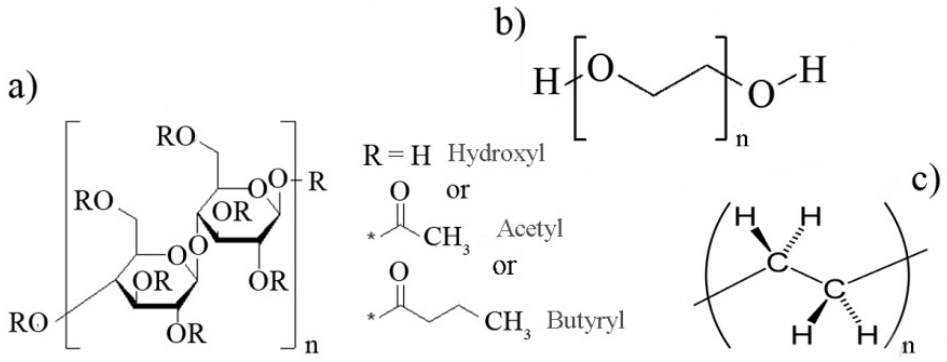

Figure 3. 2 Chemical formula of the monomer repetitive unit of different binder polymers: a) CAB, b) PEG and c) PE

Main polymer compounds characteristics and physical properties are collected in Table 3. 1. Depending on the nature of the back-bone polymers binder were designed as BX with X=1-9. Therefore, nine binders based on polyolefin or CAB and PEG or waxes were compared.

Table 3. 1 Compounds used in binders and their main physical characteristics according to the supplier.

	CAB381-0.1	**CAB551-0.01**	**CAB553-0.4**	**LDPE 780E**	**PEG20k**
Supplier	Eastman	Eastman	Eastman	Dow	Fluka
Butyryl [wt.%]	37	53	46	-	-
Acetyl [wt.%]	13	2	2	-	-
Hydroxyl [wt.%]	1.5	1.5	4.8	-	-
M_n	20000	16000	20000	N/A	20000
ρ [g·cm^3]	1.20	1.16	1.20	0.92	1.22
T_g	123	85	136	N/A	N/A
T_m [°C]	155-165	127-142	150-160	99-121	60-70

3.2.2 Powders selection

Two types of materials were selected to study their influence in the binder system behaviour during the stages of a PIM process: a ceramic zirconium silicate (zircon) and a metal Fe-36Ni alloy (commercially known as Invar 36). Both has in common that they are thermally stable

up to high temperatures with no phases transition registered up to above 1000 ºC, with low coefficients of thermal expansion and relatively very stable to chemicals or corrosion. However their intrinsic nature allows evaluating the suitability of the selected binder systems in different materials-type. Furthermore the powders selected have different morphological features that would influence the process.

Powders were characterised in terms of morphology, particle size distribution and physic-chemical properties. Powders morphology was evaluated by scanning electron microscopy (SEM) introduced in section 3.3.7. The powder particle size distribution parameters were determined by a Malvern Instruments Mastersizer 2000 analyser. The ISO 13320-2009 standard was followed [7]. The measurements were performed in a wet cell using water as dispersion media. A Hydro2000 dispersion unit was used to stir powder-water suspensions previously subjected to a de-agglomeration process with ultrasounds during 15 min. The powders specific surface area was measured using a Micrometrics Gemini VII BET measuring device. LECO type devices were used to determine the carbon and oxygen content of the powders.

The powders real density (ρ_{real}) was measured by a Micrometrics Accupyc helium pycnometer following the MPIF 63 standard [8]. The apparent (ρ_{app}) and the tap (ρ_{tap}) densities are properties that give an idea of how easy powder particles can be packed to leave apart the least free volume possible, i.e. a rough estimation of the critical an optimal solid loadings (as discussed in Chapter 1). These densities are dependent of the powder nature, the particle size distribution, the powder morphology and the powder capacity to form agglomerates. The ASTM B527-06 [9] and ASTM B212-13 [10] standards were followed to determine the tap and apparent densities respectively.

Zircon powders

Zircon was supplied by GUZMAN GLOBAL S.L (Nules, Spain). The powder comes from natural zircon raw sand that was milled and fragmented to the desired particle size distribution by a continuous rotating balls mill. Powders are not totally pure and contain certain traces of other compounds, predominantly metallic oxides listed in Table 3. 2. These impurities may favour the sintering processes of the zircon parts but they could also promote the dissociation of the zircon (Zr_2SiO_4) into zirconia (ZrO_2) and silica (SiO_2) [11, 12].

Table 3. 2 Chemical composition of the zircon powder. The wt.% of ZrO_2 and SiO_2 corresponds to the stoichiometric formula of the zircon (Zr_2SiO_4)

	ZrO_2	SiO_2	Al_2O_3	TiO_2	Fe_2O_3
wt.%	66	33.59	0.25	0.11	0.05

A summary of the main zircon powder characteristics can be found in Table 3. 3. These powders exhibit an irregularly shaped morphology, as shown in Figure 3. 3, which also shows the particle size distribution curves for the zircon powder. The irregular morphology of these

powders contrasts with the spherical or round powders that are conventionally used for PIM. The particle sizes parameters, the D_{50} and D_{90}, of the powders are 1.604 and 4.650 µm, respectively, which are relatively low values for PIM. However the particle size distribution is reasonably wide with a S_w of 2.69 which in theory is a positive aspect [13-16]. The powders have a specific surface area of 5.04 m²/g.

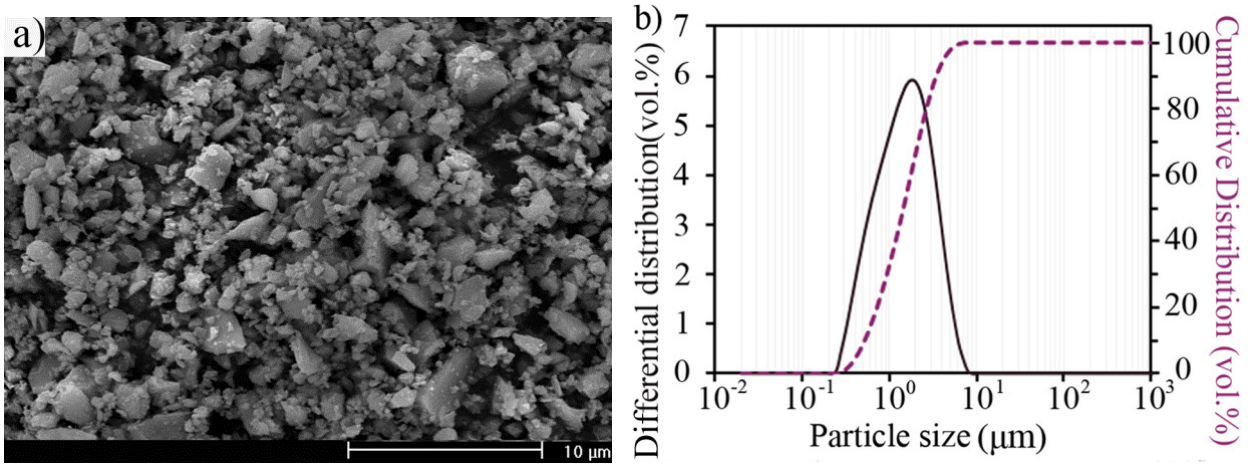

Figure 3. 3 a) Secondary electron scan SEM image of the zircon particles; b) particle size distribution of the zircon powders.

The low tap and apparent densities, 32.45% and 21.07% of the material density (4.58 g·cm^{-3}), respectively, reflect the low-packing capacity of the powders and their tendency to form agglomerates, which are both direct consequences of the shape and particle size of the powder.

Table 3. 3 Summary of the zircon powder characteristics

Characteristics of zircon powder				
Morphology	Angular			
Density [g·cm^{-3}]	4.58±0.01			
Apparent density [%real]	21.07±1.01			
Tap density [%real]	32.45±2.11			
Specific surface [m^2·g^{-1}]	5.04			
Particle size distribution	**d_{10} [µm]**	**d_{50} [µm]**	**d_{90} [µm]**	**S_w**
	0.521	1.604	4.650	2.69

These unattractive characteristics of powders would normally make the powder unsuitable for a PIM process [13, 17, 18]. PIM has generally been limited to high performance and dimensionally precise components, associated with the use of expensive raw materials with tailored characteristics. The use of non-conventional PIM powders such as natural raw materials or waste products from other processes has been investigated and shown to be possible [19-21]. These previous works lead to consider the use of as-supplied natural zircon mineral sand as a possible and interesting raw material for the end objective of this thesis work: study the suitability of CAB based binders employed in PIM processes. The zircon

powder allows evaluating the mentioned binder systems in very unfavourable conditions and therefore their real potential in PIM applications.

Invar 36 powders

Two different particle sizes of gas atomised INVAR 36 alloy powders were used in this PhD Thesis. The INVAR 36 alloy consists of 36 wt% of Ni and Fe balanced with other trace elements. The chemical composition of both powders as reported by the supplier is shown in Table 3. 4. The powders were supplied by Sandvik Osprey Ltd. (UK). The coarsest powder, with a D_{90} of around 12 μm, is referred as INV1 and the finest, with a D_{90} of around 5 μm is referred as INV2. A summary of the main characteristics of the INVAR 36 powder can be found in Table 3. 5. Both powders have a spherical morphology, as seen in the scanning electron microscopy (SEM) images presented in Figure 3. 4. Particle size distribution curves are presented in Figure 3. 5.

Table 3. 4 Chemical composition of the INVAR 36 alloy powders

Composition	Ni	Mn	Si	C	O	Fe
[wt.%]	36.50	0.20	0.02	0.01	0.13	Balanced

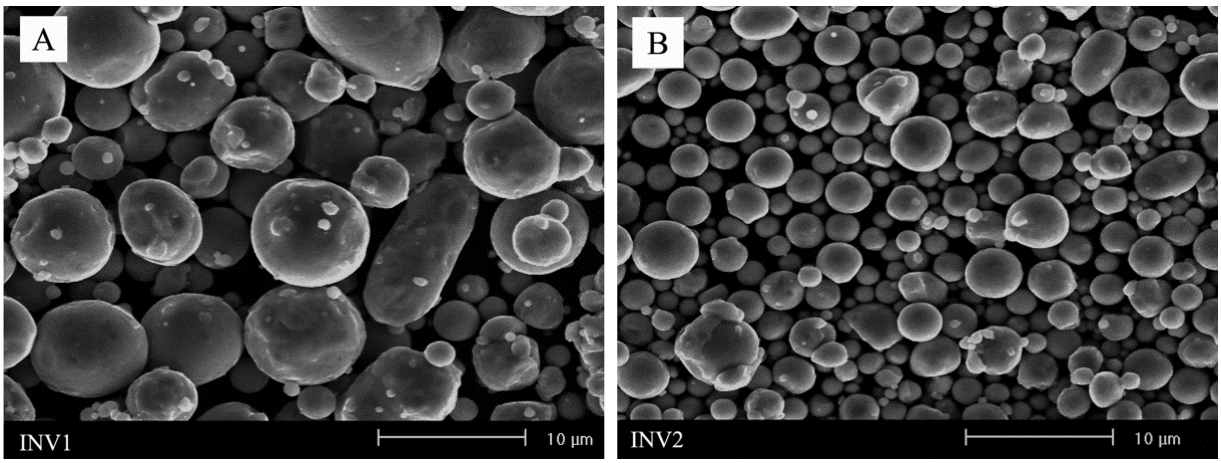

Figure 3. 4 Particle morphology evaluated by SEM: a) INV1 powders, b) INV2 powders.

The INV1 and INV2 powders composition and morphology was specially formulated for MIM with originally very low carbon content and very rounded shape. The differences in the particles sizes allow assessing the influence of this parameter in the rheological and decomposition behaviour of the feedstocks. However, according to the S_w parameter the particle size distribution of the powders is very narrow. This parameter takes big values for narrow and small values for wide particle size distributions. According with the current experience in PIM field, it is generally accepted that the easiest moulding is performed with powders having S_w around 2 (very wide distribution) and some of the knotty ones uses powders with S_w ranging from 4 to 5. Values of S_w over 7 represent particle size distribution complicated to be moulded [13, 18]. To this concern should be summed the risk of contamination with pernicious carbon, oxygen or nitrogen elements during MIM process.

These elements can diffuse and occupy interstitial positions or form oxides, carbides and nitrides that may ruin mechanical and physical properties of the Invar36 alloy, especially its noteworthy low coefficient of thermal expansion.

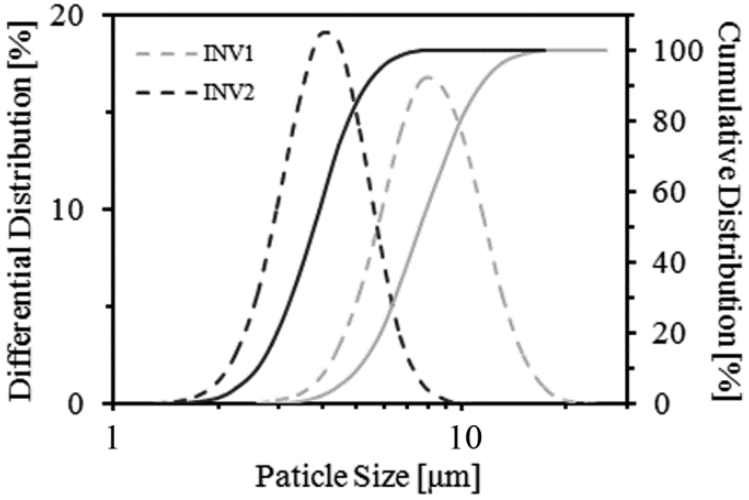

Figure 3. 5 Invar 36 powders INV1 and INV2 particle size distribution curves.

The small particle size of the INV2 powders was also selected thinking on the development of MicroMIM processes. It is advisable to keep a minimum of 10 particles in the thinnest section of the part in order to avoid monocrystalline microstructures and meet with other requirements like obtaining a true-to-detail design and surface roughness [22-25]. A small grain size promoted by small particles is also desirable to improve the Invar 36 mechanical and physical properties[26].

Table 3. 5 Summary of the INAVR 36 powders characteristics

Characteristics of INV36 powders								
	INV1				INV2			
Morphology	Spherical				Spherical			
ρ_{REAL} [g·cm^{-3}]	8.11±0.01				8.09±0.02			
ρ_{APP} [%real]	32.05±1.14				27.12±1.31			
ρ_{TAP} [%real]	55.24±2.24				49.56±1.86			
BET [m^2·g^{-1}]	0.138				0.243			
PSD	d_{10} [µm]	d_{50} [µm]	d_{90} [µm]	S_w	d_{10} [µm]	d_{50} [µm]	d_{90} [µm]	S_w
	5.05	7.69	11.44	7.21	2.60	3.81	5.29	8.30

3.3 Equipments and methodologies.

3.3.1 Thermogravimetrical and calorimetric analyses.

Thermogravimetrical and calorimetric analyses were conducted mainly to evaluate thermal behaviour of single polymeric compounds, the binder systems and the feedstocks, but also of the sintered parts and raw powders.

Simultaneous thermal analysis method was employed in the majority of the situations. This method allows for the simultaneous evaluation of losses and gains of mass (Thermo gravimetrical analysis, TGA) and the specific interchange of heat (Differential scanning calorimetry, DSC) associated to these processes (or other processes of constant mass) in isothermal or controlled heating rates thermal cycles. A Perkin Elmer STA 6000 simultaneous thermal analyser was employed for such purposes. The TGA signal could detect mass changes associated to decomposition, vaporisation and sublimation, desorption and absorption, oxidation and other chemical reactions. For a better comprehension of thermal analysis and calorimetry the author refers the reader to Haines [27] or Salomon and Fielder [28]. In this Thesis work, the thermogravimetric study focuses on the evaluation of the thermal degradation of the binder systems at different atmospheres (mainly nitrogen and air), temperature ranges, and how this degradation is affected depending on powder characteristics. The DSC signal gives information of the temperature intervals at which physical transformations occurs. Phase transitions like melting points (T_m), glass transitions (T_g) or crystallization processes (T_c) of the material could be assessed as well as the energy transfer associated with this transitions.

The configuration of the STA 6000 for measuring simultaneously the TGA and the DSC curves is out of the conventional DSC or TGA devices and has limitations in the accuracy of both results. An alumina sample pan is placed directly over a platinum reference pan (with thermocouple sensors) that at the same time is mounted over a weighting scale. Heaters concentrically and homogeneously transfer the heat over the sample and the reference pan. A temperature difference between sample and the reference pan is measured in reality, thus a differential thermal analyser (DTA) signal. However the temperature and the enthalpy were calibrated using indium as a standard in order to obtain a DSC signal. A blank, measured previous to the sample test, should be subtracted to remove the influence of the alumina pan to the measurement. Moreover, during the test the observed baseline is not a desired horizontal straight line. This makes losing precision in the measurements and lateral resolution.

A TA Instruments Q200 differential scanning calorimeter (DSC) equipped with a refrigerated cooling system was also employed to contrast STA results. The base line was calibrated in scanning the temperature domain with an empty pan. The temperature and the enthalpy were calibrated using indium as a standard. All the experiments were carried out with an aluminium pan. These experiments allow data acquisition at lower temperatures ranges with a better resolution than with combined STA technique. Typical heating-cooling-heating cycles were programmed to delete the thermal history of the feedstocks and to evaluate the melting and crystallization temperatures.

Variations on the DSC peaks and TGA curves may reveal compatibilities between feedstock components. These studies were supported by Fourier transform infrared spectroscopy (FT-IR) using a Perkin Elmer Spectrum GX device. TGA analysis is also helpful to determine binder thermal stability by the IPDT temperature and degradation kinetics by isothermal or isoconversional methods as explained in section 1.1.3.

3.3.2 Binder and feedstock elaboration and rheological characterization

A Rheomix 600 Haake torque rheometer coupled with a Haake Rheocord 252p module and twin sigma rotors was used for the mixing of all the binder and feedstock components. At the same time torque and temperature of the blend evolution with time were monitored. A temperature of 150º C was used for all the batches, and the mixing chamber was filled with feedstock to 72% of the total volume (the chamber volume is 69 cm^3). A rotor speed of 50 rpm was employed to mix the feedstock and the binder for 60 min to ensure complete homogenisation. All the feedstock components were added at the same time. All the mixer components are coated by a titanium nitride layer that protects from the wear and erosive effect of the metallic and ceramic powders.

For capillary rheology measurements, a Rosand RH2000 double piston capillary rheometer was used. Two capillaries, both with a diameter of 1 mm, were used. Their L/D ratio (length divided by diameter) were L/D≈30 and L/D<1. The pressure drop values at the capillary entrance were acquired for different shear rates, temperature and solid loading by a pressure transducer with a maximum pressure registration of 70 MPa. Those values were then converted into shear viscosity and elongational viscosity values. The apparent shear rate range studied covers shear rates from 10 to 10000 s^{-1}. Several temperatures were evaluated depending in the feedstock type, at least three temperatures per feedstock to determine the viscosity dependence with the temperature. The feedstock's viscous flow behaviour was tried to be adjusted to different mathematical or empirical models.

Experimental data model fitting

For the non-linear regression of the experimental set of points and adjustments of the models, optimisation algorithms based on the generalised reduced gradient method GRG [29, 30] were used. These algorithms also allow one to solve non-linear regression problems. For such purposes, a minimisation problem is commonly proposed for the sum of the squared residuals (RSS) expressed in Eq.3.1. A residual is the difference between the model's predicted value (η_{est}) and the real measured value (η_{mes}). The predicted model values depend on the variation of the model equation coefficients. The coefficients are varied in an iterative process until the RSS value is minimised. In this work, a minimisation problem for a modified RSS (RSS_p) was established (Eq.3.2). The RSS_p is an RSS value for which the residuals are adjusted by dividing them by the measured value. The values of viscosity or shear stress can differ by several magnitude orders with variations in the shear rate. The RSS alone would only properly adjust the highest values of viscosity, i.e., the ones that might contribute more extensively to the sum of squares. The RSS_p attempts to equilibrate the adjustment process for all the points concerned.

$$RSS = \sum_{i=1}^{m}(\eta_{mes} - \eta_{est})^2 \qquad \text{Eq.3.1}$$

$$RSS_P = \sum_{i=1}^{m}\frac{(\eta_{mes}-\eta_{est})^2}{\eta_{mes}} \qquad \text{Eq.3.2}$$

In this Thesis work, the value of the acquired points, m, varies in each experiment at different measurement conditions. The number of parameters that must be adjusted, p, also differs depending on the mathematical model. Considering these issues and to allow a comparison between obtained RSS_P values for different models and experiments, a normalised parameter, RSS'_P, is proposed in Eq.3.3:

$$RSS'_P = 100 \cdot \frac{RSS_P}{m-p} \qquad \text{Eq.3.3}$$

The multiple regression coefficient (R^2) was also used to validate the model adjustments and is presented in Eq.3.4:

$$R^2 = \frac{\sum(\eta_{mes}-\overline{\eta_{mes}})\cdot(\eta_{est}-\overline{\eta_{est}})}{\sqrt{\sum(\eta_{mes}-\overline{\eta_{mes}})^2\cdot\sum(\eta_{est}-\overline{\eta_{est}})^2}} \qquad \text{Eq.3.4}$$

3.3.3 Injection moulding

Hydraulic Arburg 220-S injection equipment was used to perform high pressure powder injection moulding (HPPIM) of zircon feedstocks. The main technical data are shown in Table 3. 6.

Table 3. 6 Technical specifications of Arburg 220-S injection equipment

Clamping force (max.)	20 kN
Injection volume	3 to 12 cm^3
Screw diameter	15 mm
Screw length	600 mm
Injection speed (max.)	366 mm/s
Injection temperature (max.)	400 ºC
Injection pressure (max.)	250 MPa
Injection flow (max.)	22 cm^3/s

Injection temperatures were varied from 160 ºC to 170 ºC to optimise the injection temperatures without reaching degradation temperatures. Injection pressure, injection post-pressures and injection flow were also optimised by assessing the as-moulded pieces quality in terms of weight and absence of defects. The characteristic mould cavity geometry and mould dimensions used are shown in Figure 3. 6a. This mould size was specially designed for PIM in the mentioned Arburg equipment. Four different parts type were injected at a time: two different sizes tensile test specimens and two different sizes bending test specimens.

A Bimba model from AB (Canada) plunger type injection moulding unit allowed the LP-PIM of zircon feedstocks. It has a pneumatic control with pressurized air. In this case only injection pressure, injection time (including post-`pressure time), mould clamping force and injection and mould temperatures could be regulated. The maximum pressure is 1 MPa. A mould with

the geometry of a bending test sample was used to fabricate green parts (60x8x4 mm). Mould and injection temperatures were varied until the complete filling of the mould was achieved.

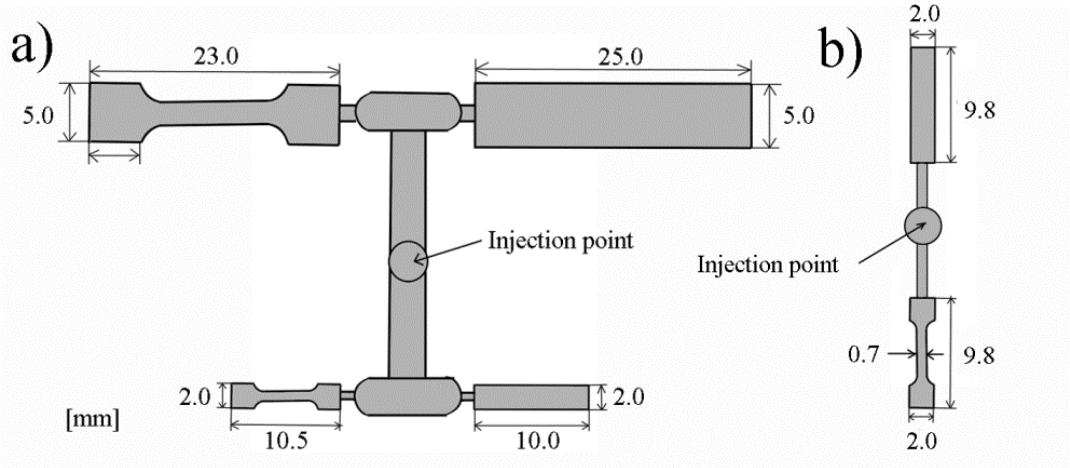

Figure 3. 6 a) Scheme of the mould used with the Arburg 220-S horizontal hydraulic press injection equipment and b) scheme of the mould used with the Battenfeld Microsystem 50.

A micro-injection Battenfeld Microsystem 50 has been used to perform μ-MIM of Invar 36 feedstocks. The injection unit is especially composed of three stages to achieve the high-precision processing of the very small injection moulding volume: a 14 mm diameter extruder screw, a 5 mm piston for pre-dosing with a accuracy of 0.001 cm^3 and an injection piston with a diameter of 5 mm. The main technical data is shown in Table 3. 7. The characteristic mould geometry and mould cavity dimensions used are shown in Figure 3. 6b. This mould was specifically designed for Battenfeld Mricosystem equipment.

Table 3. 7 Technical specifications of Battenfeld Microsystem 50 injection equipment.

Clamping force (max.)	50 kN
Injection volume	0.025-1.1 cm^3
Injector plunger diameter	6mm
Screw diameter	14 mm
Ejection force	1.2 kN
Injection speed* (max.)	760 mm/s
Injection pressure (max.)	250 MPa

* electrically driven

3.3.4 Debinding setups

All the binder systems used in this work are multi-component and mainly consists of combination of a non-water soluble backbone polymer and water soluble PEG. All of the binder components are susceptible to be eliminated by a thermal degradation of their molecules. However a previous solvent debinding in water of the PEG compounds may be preferable. Considering all these factors, in this work the thermal via or the solvent via were studied and optimised.

a) Solvent debinding

Although PEG could also be removed by other solvents like ethanol [3], water was chosen due to it is an inexpensive abundant substance and it is not harmful or toxic. This is positive for economical, health and environmental concerns. CAB compounds selected are likely not strong affected by water and are not soluble in this medium according to supplier specifications.

The solvent debinding, as any other thermally activated process, would depend on the process temperature chosen. The temperature, however, is limited by the solvent boiling point. In the case of water, and depending on the room's pressure, the temperature is limited to approximately 100 ºC. This temperature is above the PEGs melting point (50-70 ºC). The PEG is going to be removed more straightforwardly if it remains in a molten state [4]. Nevertheless the softening point of the CABs (< 85 ºC), that are going to act as holders after PEG removal, also has to be considered to avoid any possible distortion or swelling. Several temperatures were evaluated from room temperature to 60º C.

The dimensions of the parts are also going to affect the extraction process. The water will advance from the surface to the part's inner core by diffusive phenomena. The PEG is going to be extracted from the surface to more internal regions of the part by an osmotic effect and diffusion mechanisms. The optimization of the necessary time to extract the majority of the soluble part was carried out by using several parts types of different dimensions. Parts were immersed in a temperature regulated bath of stirred water during a certain time. Then the parts were extracted and after the excess of superficial water was removed they were weighted and sized to evaluate the percentage of absorbed water and the swelling. Subsequently, parts were dried at 70 ºC in a furnace during 12 hour to eliminate all the absorbed water and possible remaining moisture and were reweighted. PEG extraction vs. time (Eq.3.5) and absorbed water vs. time (Eq.3.6) curves were plotted applying the following equations to different immersion time parts:

$$\%\mathrm{PEG}_{\mathrm{eliminated}} = \frac{W_i - W_d}{W_{PEG}} \qquad \text{Eq.3.5}$$

$$\%\mathrm{Water}_{\mathrm{absorbed}} = \frac{V_{water}}{V_{PEG}} \qquad \text{Eq.3.6}$$

where W_i is the sample weight before the immersion, W_d is the weight of the dried sample, W_{PEG} is the total removable weight of PEG, V_{water} is the volume of water absorbed and V_{PEG} is the total removable weight of PEG.

b) Thermal debinding

Thermal debinding cycles were designed considering TGA analysis results. Several different debinding atmospheres including air, nitrogen or vacuum media were tried. Thermal debinding was carried out alone or in combination with a previous solvent debinding in water.

Imperfections after sintering like blisters of superficial cracks were searched by visual inspection of the green parts. Internal defects were evaluated after sintering. Residual carbon and oxygen after thermal debinding were evaluated by LECO type devices and by Thermo Fischer Scientific Flash 2000 CHNS/O elementary analyser.

3.3.5 Strategies for sintering optimisation.

The sintering conditions were selected depending on the material assisted by the literature consulted and the predictions based on thermodynamic modelling software Thermocalc®.

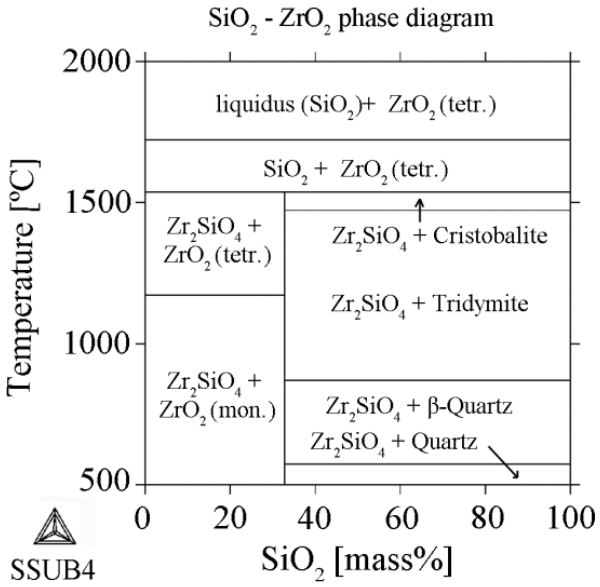

Figure 3. 7 Silica-Zirconia equilibrium phase diagram calculated using Thermocal® SSUB4 database.

As discussed in Section 1.6, zircon is a very thermal stable material that maintains the same phase structure up to high temperatures. That complicates the sintering process of zircon powders. In the silica-zirconia phase diagram generated by Thermocal® (Figure 3. 7) it could be seen that approximately at 36 mass% of SiO_2, zircon is formed exclusively and that it disaggregates into silica and zirconia above 1500 ºC. Disaggregation of zircon at high temperatures is an issue that also limits the sintering temperature. If this disaggregation occurs and during the pull down the silica and zirconia do not recombine, then common phase transitions of both components would lead to a volume change that may generate internal stresses and cracks worsening the properties.

Sometimes the consolidation of zircon powders is aided by employing microwaves, pressure (in HIP processes) or a spark plasma sintering. In this PhD Thesis work conventional sintering processes were carried out. Regarding sintering atmospheres, in theory there should not be any problem by using air atmospheres. Actually, air is the atmosphere mainly used in the publications consulted. Nevertheless low vacuum atmospheres were also used up to 1450 ºC for comparative purposes. The optimal sintering temperature of zircon should be somewhere

between 1400 ºC to 1600 ºC. The 1400 ºC should be enough for achieving the sintering thermal activation; however temperatures above 1500 ºC are preferred in literature. Disaggregation into silica and zirconia may occur in the cited temperature range and would depend on the percentage of impurities present in zircon powders. To evaluate the effect of temperature and time in the sinterablity of PIM zircon powers different temperatures, in the range of 1200-1500 ºC, and sintering times, in the range of 15 min - 3 h, were evaluated. The use of air or low vacuum atmosphere was also evaluated. The heating rates selected were 5 ºC/min. The cooling rates were lowered to 5 ºC/min to avoid generating internal thermal stresses that derive in crack formation. The vacuum furnace has limitations with temperature (up to 1450 ºC) in comparison with the high temperature muffle furnace (up to 1800 ºC).

The Invar 36 powders are more prone to elements contamination than the zircon powders, thus sintering condition were designed more carefully, especially in the selection of sintering atmospheres. The Invar 36 maintains an austenitic FCC structure up to the melting temperature, which depending on impurities should be around 1455 ºC according to the Fe-Ni binary phase diagram [31] and Thermocalc® software predictions (Figure 3. 8a). However, as discussed in Section 1.7, contamination of Invar 36 with interstitial elements such as carbon, nitrogen or hydrogen coming from the intrinsic PIM process may ruin its structural and functional properties. These elements could also considerably vary the melting point. Figure 3. 8b shows Thermocal® predictions of the system Fe-36Ni at different carbon contents. Small amounts of carbon could lower the apparition of a liquid phase to around 1200 ºC.

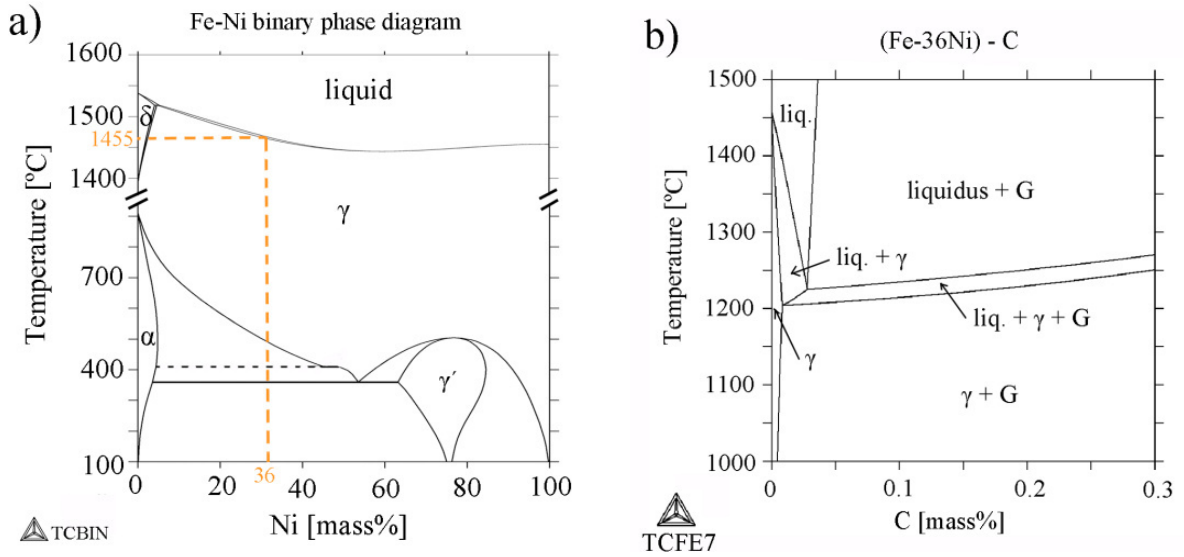

Figure 3. 8 a) Fe-Ni equilibrium phase diagram calculated using Thermocalc® TCBIN database, b) (Fe-36Ni)-C equilibrium phase diagram calculated using TCFE7 Thermocalc® database . G =graphite; γ, γ´= FeNi(FCC); α, δ =FeNi(BCC).

A study was proposed considering different debinding and sintering atmospheres. Levels of carbon and oxygen can be tailored regulating thermal debinding conditions. A vacuum or oxygen thermal debinding up to 400 ºC created different levels of residual oxygen and carbon before sintering stage. Subsequent hydrogen or vacuum sintering atmospheres allowed

evaluating the reductive power of the different conditions upon the oxides created and the post-sintering carbon and other elements content. Sintering temperatures ranging the 1000 ºC to 1150 ºC were evaluated as well as different heating rates. The 1150 ºC maximum was chosen trying to avoid a possible liquid phase formation that in one hand would help on the sintering process, but in the other may introduce dimensional stability concerns. Moreover, 1120 ºC is a very common industrial furnace sintering temperature. All the samples were maintained during one hour at selected sintering temperature. A cooling rate of 10 ºC/min was chosen trying to avoid the formation of undesirable α BCC or γ´ FCC that are predicted in the equilibrium phase diagram (Figure 3. 8a).

3.3.6 Dimensional shrinkage and densification evaluation.

The shrinkage evolution during sintering of zircon parts was evaluated in situ with a Netzsch402ES dilatometer using different conditions similar to the real sintering processes in tubular of muffle furnaces. These studies were not possible with the Invar 36 micro parts due to the reduced size that falls for instrumental errors.

For all the materials and conditions, sintered parts were carefully sized and compared with the corresponding green part dimensions to evaluate the total shrinkage from moulding to final geometry. This is an important issue to evaluate in order to properly design the mould cavities in further applications.

When there was enough material, pycnometer density was evaluated with a lacquered part to seal superficial porosity and determine the close porosity. Comparing this density with the real material density, the part densification (in %) can be determined. Other possible methodology consists on employing the Archimedes' method weighting the lacquered parts before and after an immersion in a known density liquid. Water at room temperature was selected as immersion media with a density of 1.000 g/cm^3.

To complete densification studies Fiji image analysis open software was used to analyse the porosity in light optic microscope (LOM) and scanning electron microscope (SEM) images. The relation between total pore area and material area as observed in the microscope images can give an idea of the part densification.

3.3.7 Microstructural evaluation.

Light optical microscopy (LOM) was used for the microstructure evaluation of the polymeric, metallic and ceramic materials evaluated in this PhD Thesis work. LOM was performed by an Olympus GX71 light microscope

In the case of the binder evaluation, PEG crystallises forming spherulites that could be easily identified by using special polarised light filters. Depending on the cooling conditions and the binder components the nucleation of the spherulites may vary. Miscibility of compounds could also be detected with this technique. A thin translucent layer on around 0.5 mm was created by

facing two microscope slides and pressing the sample in its melting state. Samples were melted at 160º C during 30 minutes. Then they were air quenched at same cooling rates for comparison purposes.

Microstructure and porosity features can be evaluated with LOM in case of zircon and Invar 36 consolidated specimens. Samples have to be previously grinded and polished with special sandpapers and polishing media depending on the material characteristics. Special care was taken to ensure that the porosity of the sintered pars was properly opened. To reveal austenitic phase in the Invar 36 alloy an etching with *aqua regia* was carried out. This etching consists in a solution of concentrated nitric acid and concentrated hydrochloric acid in a volumetric proportion of one part for each three.

A Philips XL-30 with tungsten filament scanning electron microscope was also employed for the microstructure evaluation. An electron beam bombarded the sample at vacuum conditions scanning its surface. Different types of signals are created due to the interaction between the electron beam and the material. These signals are collected by different detectors to create a magnified image. Backscattering electrons are directional, i.e. reveals sample details that are aligned with the detector system. Their number increases with the atomic number allowing a compositional contrast [32]. Backscattering electron detector allows distinguishing different phases within the materials, e.g. oxides or precipitates. This mode also facilitates the observation of the particle distribution within the binder matrix in the feedstocks sample. The secondary electrons are not directional and allow distinguishing topographic detail. A 3D appearance image is created which is very useful for fractography surfaces analysis and particle morphology evaluation. Finally, semi-quantitative elements analysis of the phases observed was carried out by a Philips EDAX-DX_4 energy disperse spectroscopy (EDS) detector.

Poor electrical conductivity samples (feedstocks and zircon) have to be coated with a conductive layer to allow their characterisation by SEM. Gold or carbon thin layers were deposited by PVD over the sample surface. Carbon is preferred in zircon samples since gold and zirconium have similar emission energies.

3.3.8 X-ray diffraction (XRD)

For the complementary characterization of the microstructures and to contrast and confirm the crystalline phases observed during the microstructural evaluation, the x-ray diffraction technique was employed. A Philips X'Pert x-ray diffractometer was used for such purposes. The software HighScore allowed the acquisition and treatment of the data. An x-ray beam with a wave length corresponding to the K_α excitation line of Cu (λ=1.542Å) was generated by and x-ray tube with an anode of Cu and a W filament excited with a current of 40 mA. The potential to accelerate the electrons was 40 kV. The samples were scanned varying the $2\cdot\theta$ angle from 30º to 110º in steps of 0.02º. The diffractograms obtained were compared with

patterns contained in the database PCPDFWIN and thereby the characteristic peaks of each phase were identified.

Additionally, the x-ray technique allows assessing the lattice parameters and the extent of the crystalline domains. Random positioning and alignment of the samples and the systematic errors during the measurement may introduce distortions in the determination of the interlayer distance. Hence, the Cohen's method was used to determine the lattice parameter. The extrapolation of the data employing this method eliminates the systematic measurements errors and minimizes the random errors during the positioning of the samples.

3.3.9 Hardness measurements

For the evaluation of the hardness, microhardness Vickers standard (HVS) was selected. One of the standards that specify these types of test is the ASTM E384 [33]. Microhardness was obtained by a Time Technology Europe digital microhardness tester HVS-1000. In both cases, the Invar 36 and the zircon sintered parts, a measurement of the hardness of one specific phase was not searched because the microstructures were basically composed of one single phase. However, the small sizes of the Invar 36 parts and the brittle behaviour of the zircon made necessary to perform the experiments in a scale lower than conventional Vickers measurements. The procedure for testing is very similar to that of the standard Vickers hardness test, except that it is done on a microscopic scale with higher precision instruments. The Vickers test is often easier to use than other hardness tests since the required calculations are independent of the size of the indenter, and the indenter can be used for all materials irrespective of hardness.

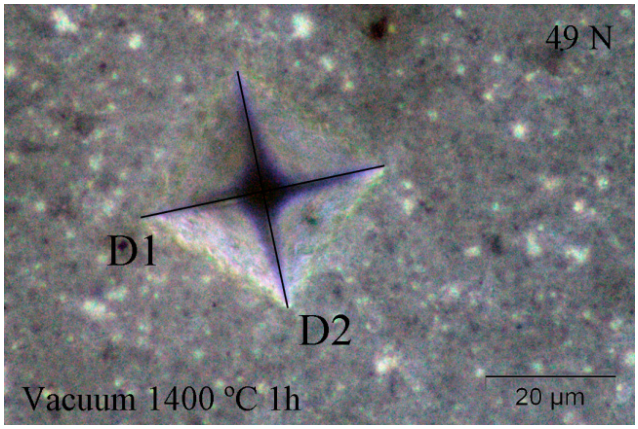

Figure 3. 9 Example of Vickers square footprint with the diagonals D1and D2. This particular case corresponds to a zircon sample sintered in vacuum at 1400 ºc during 1h. The load applied was 4.9 N.

A load of 9.8 N applied during 20 seconds was selected for the Invar 36 micro parts whereas a load of 4.9 N was selected for the zircon samples. The footprint area can be calculated by Eq.3.7 and the hardness Vickers (HV) by Eq.3.8, where D_1 and D_2 are the diagonals of the square footprint in millimetres, F is the force applied in Newton, thus the hardness HV is in MPa.

$$A_{footprint} = \frac{D_1 \cdot D_2}{2 \cdot \sin(68°)} \cong \frac{D_1 \cdot D_2}{1.8544} \quad \text{Eq.3.7}$$

$$HV = \frac{F}{A_{footprint}} = \frac{1.8544 \cdot F}{D_1 \cdot D_2} \quad \text{Eq.3.8}$$

3.3.10 Bending tests

To compare the bending strength of the green and sintered parts fabricated from different feedstocks, three point bending tests were carried out. The bending test can be performed following the recommendations of MPIF 41 or ASTM C1161 standards [34]. A Shimadzu AG-1 universal mechanical testing equipment with an electromechanical control and a load cell of 1 kN was used. A crosshead speed of 1 mm/min was chosen for the tests. The distance between the support pins was 40 mm. The bending strength (BS) [N/mm^2] was calculated using the following expression:

$$BS = \frac{3 \cdot F \cdot L}{2 \cdot t^2 \cdot w} \quad \text{Eq.3.9}$$

where F is the load at the fracture point and is expressed in [N], L is the length of the support pins span [mm], t is the thickness of the sample [mm] and w is the width [mm].

3.3.11 In situ and ex situ micro tensile tests

A Kammrath and Weiss micro-mechanical testing stage with a load cell of 1 kN was used to perform Invar 36 micro parts micro tensile tests at room temperature. Zhao et al. [35] discussed the limitations and issues in correctly interpreting micro tensile experiments. The micro test experimental studies assumes errors in strain measurements as the data were collected directly from the cross head displacement without any extensometers, digital image correlation or laser interferometry. Thus, only engineering results are presented in this thesis. However, as the tests were performed on the same device, the results are considered valid for comparative purposes.

Some of the experiments were conducted inside a Zeiss EVO MA15 scanning electron microscope to in situ evaluate the microstructure changes during the micro mechanical tests. SEM images of the fracture surfaces were also performed to have an idea of the strain mechanism involved and the fracture type.

3.3.12 Other properties

Determination of Curie's Temperature

In the case of Fe-Ni Invar alloys it is important to know their ferromagnetic to paramagnetic transition temperature or Curie's temperature (T_{curie}). This change in the magnetic properties is also associated with the end of the temperature range at which these alloy maintain a very low

and almost constant coefficient of thermal expansion. This temperature is very sensible to the presence of interstitials elements like carbon nitrogen or oxygen, most likely present as a result of the PIM. It is also sensible to Ni segregations or development of other phases different to the typical austenite.

The ferromagnetic to paramagnetic transition in Fe-Ni36 alloy is not associated to a phase transition but to a change in the lattice parameters. Therefore this change is difficult to be detected with calorimetric analysis. However the T_{curie} can be assessed in a thermogravimeter analyser coupling a magnet to the normal measurement mode. During the experiment, the magnet is placed near the sample attracting it in the ferromagnetic state. After the transition to the paramagnetic state the sample will not be attracted any longer by the magnet causing a sudden abrupt variation in the weight registered by the thermo balance. The T_{curie} is calculated by taking the maximum/minimum of the TGA curve derivative peak.

A TA Instruments Q50 thermogravimeter was employed for the determination of the T_{curie}. The magnet was placed always at the same position to keep the same magnetic field affecting the samples. The samples were heated from 100 to 400 ºC at 10 ºC/min since the typical T_{curie} of the invar alloys is around 200 ºC.

Determination of the coefficient of thermal expansion

For the determination of the linear coefficient of thermal expansion a TMA Q400 of TA Instruments thermo mechanical analyser was employed with a special expansion probe for dilatometry tests. A creep and stress relaxation mode was employed were the input stress was held constant and the resulting strain was monitored as a function of temperature. The experiments were performed from 25 to 350 ºC in a nitrogen atmosphere.

References

1. Kamide, K., *Cellulose and Cellulose Derivatives: molecular characteristics and applications*. 1st ed. Polymer Science Library. 2005: Elsevier Science.
2. Unknown, *Eastman™ cellulose-based specialty polymers*, Eastman publications www.eastman.com.
3. Haglund, B.O. and R. Svensson, *A thermoanalytic method for the study of the solubility of polyethylene glycols in ethanol and water.* Journal of Thermal Analysis, 1989. **35**(2): p. 391-395.
4. Yang, W.W. and M.H. Hon, *In situ evaluation of dimensional variations during water extraction from alumina injection-moulded parts.* Journal of the European Ceramic Society, 2000. **20**(7): p. 851-858.
5. Yang, W.W., et al., *Solvent debinding mechanism for alumina injection molded compacts with water-soluble binders.* Ceramics International, 2003. **29**(7): p. 745-756.

6. Yang, W.W., K.Y. Yang, and M.H. Hon, *Effects of PEG molecular weights on rheological behavior of alumina injection molding feedstocks.* Materials Chemistry and Physics, 2002. **78**(2): p. 416-424.
7. ISO, *Laser diffraction methods*, in *Particle size analysis*. 2009: . p. 51.
8. MPIF-63, *Density Determination of Metal Injection Molded (MIM) Components (Gas Pycnometer)* 2008.
9. ASTM-B527-06, *Standard Test Method for Determination of Tap Density of Metallic Powders and Compounds*. 2000.
10. ASTM-B212-13, *Standard Test Method for Apparent Density of Free-Flowing Metal Powders Using the Hall Flowmeter Funnel*. 2012.
11. Awaad, M. and S.H. Kenawy, *Sintering of zircon: the role of additives.* British Ceramic Transactions, 2003. **102**(2): p. 69-72.
12. Kaiser, A., M. Lobert, and R. Telle, *Thermal stability of zircon (ZrSiO4).* Journal of the European Ceramic Society, 2008. **28**(11): p. 2199-2211.
13. German, R.M. and A. Bose, eds. *Injection Molding of Metals and ceramics*. 1997, Metal Powders Industry Federation.
14. Contreras, J.M., A. Jimenez-Morales, and J.M. Torralba, *Influence of the morphology and particle size on the processing of bronze 90/10 powders by metal injection moulding (MIM)*, in *Progress in Powder Metallurgy, Pts 1 and 2*, D.Y. Yoon, et al., Editors. 2007. p. 365-368.
15. Contreras, J.M., A. Jimenez-Morales, and J.M. Torralba, *Improvement of rheological properties of Inconel 718 MIM feedstock using tailored particle size distributions.* Powder Metallurgy, 2008. **51**(2): p. 103-106.
16. Sotomayor, M.E., A. Varez, and B. Levenfeld, *Influence of powder particle size distribution on rheological properties of 316 L powder injection moulding feedstocks.* Powder Technology, 2010. **200**(1-2): p. 30-36.
17. Heaney, D.F., *Handbook of metal injection molding*, ed. D.F. Heaney. 2012: Woodhead Publishing in Materials.
18. German, R.M., *Powder Injection Molding*, in *ASM Handbook*. 1998. p. 355-364.
19. Agote, I., et al., *Rheological study of waste porcelain feedstocks for injection moulding.* Journal of the European Ceramic Society, 2001. **21**(16): p. 2843-2853.
20. Barreiros, F.M. and M.T. Vieira, *PIM of non-conventional particles.* Ceramics International, 2006. **32**(3): p. 297-302.
21. Suri, P., et al., *Effect of mixing on the rheology and particle characteristics of tungsten-based powder injection molding feedstock.* Materials Science and Engineering a-Structural Materials Properties Microstructure and Processing, 2003. **356**(1-2): p. 337-344.
22. Piotter, V., et al., *Powder injection moulding of metallic and ceramic micro parts.* Microsystem Technologies-Micro-and Nanosystems-Information Storage and Processing Systems, 2011. **17**(2): p. 251-263.
23. Kong, X., T. Barriere, and J.C. Gelin, *Capabilities of Micro Powder Injection Molding for Microparts Manufacturing.* AIP Conference Proceedings, 2011. **1315**: p. 9-14.
24. Attia, U.M. and J.R. Alcock, *A review of micro-powder injection moulding as a microfabrication technique.* Journal of Micromechanics and Microengineering, 2011. **21**(4).
25. Piotter, V., *Micro metal injection moldong (MicroMIM)*, in *Handbook of metal injection molding*, D. Heaney, Editor. 2012, Woodhead Publishing Limited: Cambridge. p. 307-337.

26. Izotov, V.I., et al., *Structure and properties of Fe-36% Ni Invar after intense shear deformation.* Physics of Metals and Metallography, 1996. **82**(3): p. 289-96.
27. Haines, P.J., *Principles of Thermal Analysis and Calorimetry*. 2002: Royal Society of Chemistry.
28. Salomon, A. and K. Fielder, *Practical use of differential calorimetry for plastics*, in *Hadbook of Plastics Analysis*, H. Lobo and J. Bonilla, Editors. 2003, Marcel Dekker: New York. p. 79-109.
29. Lasdon, L.S., S.K. Mitter, and A.D. Waren, *Conjugate gradient method for optimal control problems.* Ieee Transactions on Automatic Control, 1967. **AC12**(2): p. 132-&.
30. Waren, A.D., M.S. Hung, and L.S. Lasdon, *The status of nonlinear-programming software - An update.* Operations Research, 1987. **35**(4): p. 489-503.
31. Swartzendruber, L.J., V.P. Itkin, and C.B. Alcock, *The Fe-Ni (iron-nickel) system.* Journal of Phase Equilibria, 1991. **12**(3): p. 288-312.
32. Goldstein, G.I., et al., *Scanning electron microscopy and x-ray microanalysis*. 1981, New York: Plenum Press.
33. ASTM-E384-11e1, *Standard Test Method for Knoop and Vickers Hardness of Materials*. 2011.
34. ASTM-C1161-13, *Standard Test Method for Flexural Strength of Advanced Ceramics at Ambient Temperature*. 2008.
35. Zhao, Y.H., et al., *Influence of specimen dimensions and strain measurement methods on tensile stress-strain curves.* Materials Science and Engineering a-Structural Materials Properties Microstructure and Processing, 2009. **525**(1-2): p. 68-77.

Summary of Results and Discussion

4

4.1 Introduction to the experimental results 75

4.2 Rheological studies of the feedstocks. 76

4.2.1 Mixtures studies by torque rheology 76

4.2.2 Capillary rheology 80

4.3 Thermal stability and degradation kinetics of the feedstocks 87

4.4 Mechanical and physical properties of the sintered parts 95

4.4.1 Zircon 95

4.4.1 Invar 36 100

4.5 Modelling the rheological behaviour 102

4.5.1 Feedstocks' dependence on shear rate 103

4.5.3 Feedstocks' viscosity dependence on temperature 106

4.5.4 Feedstocks' viscosity dependence on solid loading 108

4.5.5 Particle size dependence 110

4.5.6 Global viscosity model 111

References 114

4.1 Introduction to the experimental results

This chapter will summarise and compare the experimental results which are reported in detail in the appended papers and will also include other experimental works performed during this Thesis.

Multiple binder compositions were tried. A first set of binders based on literature review were selected and compared to study the influence of different back-bone polymers on PIM. Some of these preliminary works are included in Paper 1. When the efficacy of cellulose acetate butyrate (CAB) based binders in comparison to conventional polyolefin based binders was confirmed, a more conscious study was proposed and presented in Paper 2. This work tried to elucidate and identify key parameters on the vast possibilities that CABs' family offers regarding compositional issues. Finally and based on the findings with Paper 1 and Paper 2 compositions, two more binders were proposed. It could be said that a systematic evaluation of different issues was performed to achieve an optimal binder composition. A thorough characterisation of the mixtures of the best binders with specific features powders was performed.

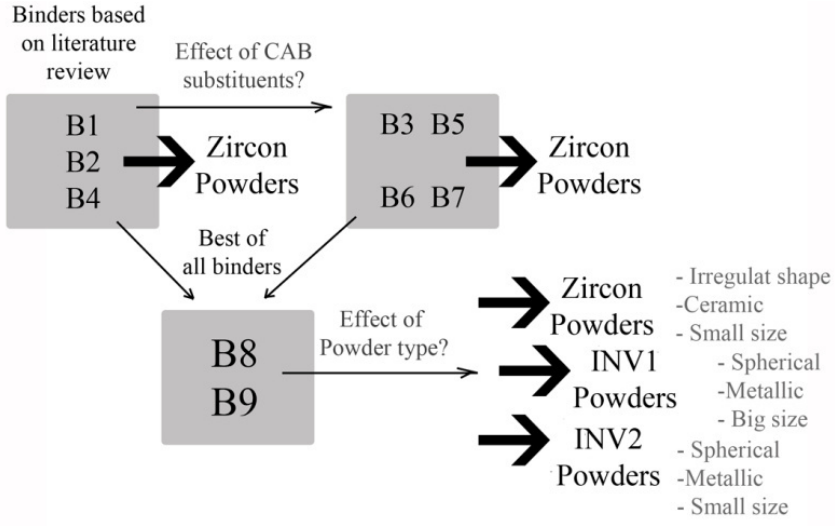

Figure 4. 1 Scheme of the steps followed to study and to optimise the different binder compositions.

Table 4. 1 Summary of the different binder systems compositions and designations.

Binder composition [vol.%]	Powders	Tag
47 LDPE, 48 paraffin wax, 5 stearic acid	Zircon	B1
55 HDPE, 40 PEG20k, 5 stearic acid	Zircon	B2
30 LDPE, 70 PEG20k	Zircon	B3
30 CAB551-0.01, 60 PEG20k, 5 PEG10k, 5 PEG4k	Zircon	B4
30 CAB381-0.1, 70 PEG20k	Zircon	B5
30 CAB551-0.01, 70 PEG20k	Zircon	B6
30 CAB553-0.4, 70 PEG20k	Zircon	B7
30 CAB551-0.01, 10 CAB381-0.1, 55 PEG 20k, 5 PEG4k	Zircon	B8
30 CAB381-0.1, 10 CAB551-0.01, 55 PEG 20k, 5 PEG10k	INV1 and INV2	B9

The main binder compositions studied during this Thesis are presented next; they are to some extent classified in different groups. B1, B2 and B3 are polyolefin based binders whereas B4, B5, B6 and B7 are based in CAB polymers with different acetyl, butyryl and hydroxyl groups as described in section 3.2.1. B1 and B2 are based in conventional PIM formulations. B3, B5, B6 and B7 have the same amount of PEG 20k. B4 is comparable with B6 but B4 incorporated a certain percentage of lower molecular weight PEG. B8 and B9 are based in mixtures of different CABs and PEGs and were proposed after the rest of the binders were compared. In Table 4. 1 the different binder compositions are described.

Apart from the different binder compositions, two completely different materials PIM processes were developed. Three types of powders were studied to test the CAB based binders upon different conditions: an irregular zircon powder, and two different particle sizes gas atomised Invar 36 alloy powders. These powders are described in 3.2.2. In Figure 4. 1 an scheme of the steps followed to study and to optimise the binder compositions and the effect of different powder types can be seen.

This chapter is divided in four sections that will give insights about different topics that have to be considered when new feedstocks for PIM are designed:

1. An study of the rheological behaviour of the different binders and feedstocks is carried out focusing on the mixing process and the resulting feedstock viscous features.
   → **Paper 1 to Paper 5**
2. The thermal behaviour of the different systems is analysed to determine processing temperatures and degradation kinetics.
   → **Paper 2, Paper 6 and Paper 7**
3. The suitability of different feedstock will be evaluated by performing full PIM processes and determining the final parts properties.
   → **Paper 1 to Paper 4 and Paper 8**
4. Modelling of the rheological results will be accomplished and a global viscosity model will be proposed. This model may be used in process simulations of injection processes of different mould cavities geometries with CAB based feedstocks.
   → **To be published**

4.2 Rheological studies of the feedstocks.

4.2.1 Mixtures studies by torque rheology

This section is about how well the different binder systems behave when they are mixed with different types of powders. They are going to be compared in terms of torque rheology parameters which will give an idea of, e.g. how well the feedstocks are homogenised or the admissible solid loading.

In Paper 1 it was concluded that B4, apart from admitting and homogenising zircon powders in a better way, reduces markedly the feedstocks' torque and allowed a higher solid loading keeping a good rheological features compared to B1 and B2. These facts were associated with a possible better compatibility between CAB-based feedstocks and zircon powders than polyolefin-based feedstocks. However this assumption was not clear enough since the formulations were composed of different percentages of back-bone-acting polymers and lubricant-acting compounds that may be affecting on the results. Paper 2 reformulated the study with B3, B5, B6 and B7 maintaining the percentage and molecular sieze of PEG constant. Thereby, different types of CABs were compared with a LDPE.

The results of Paper 2 were in the same sense of Paper 1. Table 4. 2 shows an extended version of the torque results presented in Paper 2. B3 composed of LDPE not only gave the highest torque values with the longest stabilising times and variability in the torque; it showed the greatest deviations from programmed temperature and the highest mixing and friction dissipated by heat energies values. These results suggested a poorer homogenisation and lubricating effect of the polyolefin in comparison with CABs.

Table 4. 2 Torque rheology parameters of zircon feedstocks using different binder systems after 60 min of mixing. The mixing temperature and rotors speed was in all cases 150 ºC and 50 r.p.m. Φ = solid loading, $\bar{M}$=average torque values at stabilised region, ΔM= deviations of torque values at stabilised region, T= temperature, Esp = specific mixing process energy, E_{frict} = energy dissipated by heat due to friction

			B5					B6		
Φ [vol.%]	**$\bar{M}$ [N·m]**	**ΔM [N·m]**	**T [ºC]**	E_{sp} [J/g]	E_{frict} [J/g]	**$\bar{M}$ [N·m]**	**ΔM [N·m]**	**T [ºC]**	E_{sp} [J/g]	E_{frict} [J/g]
52.5	-	-	-	-	-	-	-	-	-	-
55	6.7	0.8	159.8	972.3	12.2	-	-	-	-	-
57.5	7.0	0.9	160.7	1120.6	13.0	1.2	0.3	155.2	507.3	6.3
60	11.6	1.2	164.0	1737.7	16.5	2.0	0.3	155.4	631.9	6.4
62.5	37.5	5.5	184.1	4152.8	34.1	3.6	0.9	156.1	779.4	7.0
65	-	-	-	-	-	15.0	1.7	161.6	1473.5	12.7
			B7					**B3**		
52.5	-	-	-	-	-	7.6	0.5	160.7	1142.9	14.5
55	-	-	-	-	-	8.7	0.8	161.4	1337.8	15.0
57.5	3.7	0.7	156.9	645.2	8.4	12.2	1.0	164.2	1985.9	18.2
60	6.5	0.8	158.9	973.8	10.5	17.3	1.3	170.2	2478.2	25.0
62.5	11.3	1.5	163.7	1659.1	15.6	-	-	-	-	-
65	47.0	4.0	187.9	4589.5	42.1	-	-	-	-	-

* Cp calculated by the mixing rule considering C_{ZIRCON} = 0.628 J/g·ºC [1], C_{CAB} = 1.55 J/g·ºC, C_{LDPE}=2.1 J/g·ºC and C_{PEG} = 2.2 J/g·ºC

Among the different CABs, B6 composed of CAB551-0.01resulted in the best torque rheology results. It looked like B6 would admit higher solid loading without compromising the rheology. CAB551-0.01 has the highest percentage of butyryl groups. Butyryl groups are more voluminous and likely reduce the viscosity more effectively than acetyl or hydroxyl groups do also lowering the glass transition and melting temperatures. This most probably would explain the lowest torque values. Nevertheless it would not totally explain why higher solid loadings

seem to be possible. In all situations the powder is the same and thus it should have the same packing capacity unless agglomerates are present. Powder packing capacity is related with the maximum solid loading admissible in a feedstock. Agglomerates may reduce the packing capacity and thus the maximum solid loading admissible. In the case of B6 it could be also a better interaction between feedstock's compounds that resulted in a better homogenisation, avoiding the formation of agglomerates and with a better lubrication of the particles. The same concept may be generalised to CABs systems in comparison with LDPE. However it is not possible to make this assumption by only torque rheology.

Apart from torque rheology, the work developed in Paper 1 and Paper 2 gave other type of information that resulted in the proposal of B8 and B9. These binders are very similar and are based in a combination of different CABs. It was concluded that higher percentages of CABs and addition of some fractions of low molecular weights PEG might aid to reduce some defects formed during the process. These new formulations were applied to a zircon (B8) powder in Paper 3 and to an INV2 powder (B9) in Paper 4. The resulting feedstocks were evaluated by torque rheology in both cases. Additionally, INV1 powders were mixed with B9. Therefore the effect of the particle size and particle geometry on torque rheology was evaluated. Figure 4. 2 compares torque values of the different feedstocks at several solid loadings. There is a clear effect of the particles characteristics on the torque rheology. In one hand it is the packing capacity of the powder and in the other it is the specific surface of the powders that affects rheology. Irregular zircon powders even though they were mixed with B8 (with a higher content of CAB551-0.01 to reduce expected high feedstock viscosity) showed the highest torque values and the poorer packing capacity.

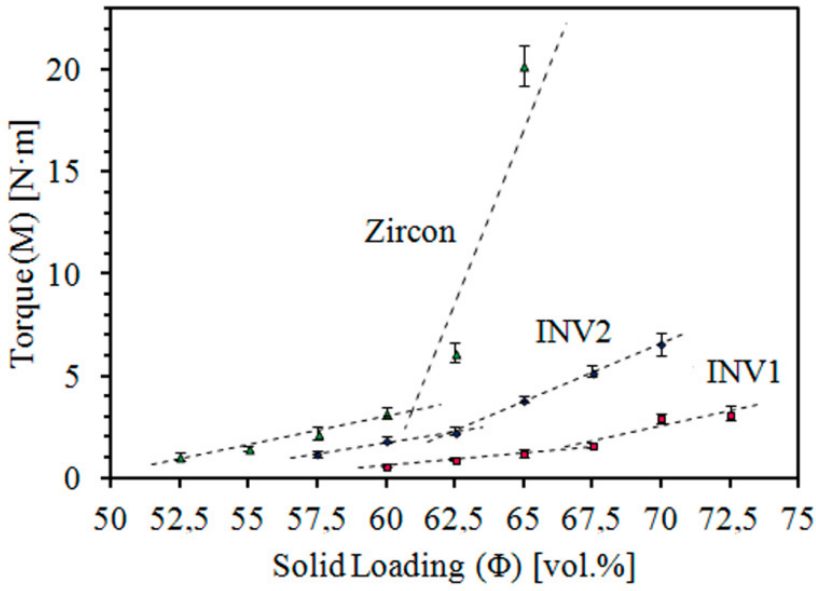

Figure 4. 2 Values of the averaged torque after 50 min of mixing with standard deviation error bars (the last minute acquired data were used for the statistics). The dashed lines represent the fitting of the experimental data to a linear curve.

Barreiros et al. [2] and some other authors proposed that the optimal solid volume fraction could be assessed from torque vs. solid loading data by fitting the experimental points to different linear behaviours. The point where these linear behaviours intersect at high solid loading could be considered as the optimal solid loading. According to these authors and for B8 and B9 binders, the optimal solid loading would be between 58 vol.% to 61 vol.% in the case of zircon powders, between 62 vol.% to 63 vol.% in case of INV2 powders and between 67 vol.% and 68 vol.% in case of INV1 powders.

Table 4. 3 Mixing parameters at the stabilised region: Φ= solid loading, M = averaged torque with standard deviation, t_{st} = stabilising time, T = temperature. If the torque was not stabilised after 50 min it is denoted by a "N/A".

	Zircon			INV1			INV2		
Φ [%]	M [N·m]	t_{st} [min]	T [ºC]	M [N·m]	t_{st} [min]	T [ºC]	M [N·m]	test [min]	T [ºC]
52.5	1.06±0.18	18	154.8	-	-	-	-	-	-
55	1.44±0.14	29	155.2	-	-	-	-	-	-
57.5	2.20±0.30	42	156.0	-	-	-	1.17±0.09	40	153.8
60	3.18±0.26	53	157.4	0.58±0.07	25	152.5	1.83±0.11	46	154.9
62.5	6.15±0.48	N/A	160.8	0.92±0.07	29	153.8	2.24±0.16	50	155.2
65	20.20±0.98	N/A	169.3	1.19±0.06	32	154.2	3.81±0.12	52	155.9
67.5	-	-	-	1.59±0.08	35	154.7	5.17±0.18	56	157.3
70	-	-	-	2.93±0.15	40	155.1	6.53±0.27	N/A	159.1
72.5	-	-	-	3.10±0.13	46	155.4	-	-	-

Table 4. 4 Totalised torque (TTQ), specific energy of processing E_{sp} and specific energy dissipated by friction in form of heat E_{frict} calculated from torque vs. curves at 50 min of mixing for different feedstocks.

	Zircon				INV1				INV2		
Φ [%]	C_{feed}* [J/g·C]	TTQ [J·min]	E_{sp} [J/g]	E_{frict} [J/g]	C_{feed}* [J/g·C]	TTQ [J·min]	E_{sp} [J/g]	E_{frict} [J/g]	TTQ [J·min]	E_{sp} [J/g]	E_{frict} [J/g]
52.5	1.25	99.7	213.0	6.0	1.19	-	-	-	-	-	-
55	1.22	129.7	269.5	6.3	1.16	-	-	-	-	-	-
57.5	1.19	202.1	408.9	7.1	1.12	-	-	-	148.4	179.8	4.6
60	1,15	376.7	742.4	8.5	1.08	56.8	66.6	2.7	190.2	223.0	5.3
62.5	1.12	579.9	1114.1	12.1	1.05	88.1	100.0	4.0	205.8	233.8	5.5
65	1.09	738.3	1383.6	21.0	1.01	110.0	121.2	4.2	247.7	275.9	6.0
67.5	1.05	-	-	-	0.98	139.1	148.8	4.6	348.1	372.2	7.1
70	1.02	-	-	-	0.94	199.4	207.1	4.8	469.3	487.5	8.5
72.5	0.99	-	-	-	0.91	201.5	203.6	4.9	-	-	-

* Theoretical specific heat calculated by the mixing rule at room conditions considering C_{Zircon}= 0.628J/g·ºC [1], $C_{Invar36}$ = 0.515 J/g·ºC, C_{CAB} = 1.55 J/g·ºC and C_{PEG} = 2.2 J/g·ºC

Table 4. 3 collects some torque rheology parameters of the different feedstocks and Table 4. 4 focuses on energy assessments derived from torque rheology. Although B8 has a back-bone-acting polymer percentage of 40 vol.% instead of the 30 vol.% of B5 and B6, torque rheology results are somewhere in between these last formulations. Zircon sharpen irregular

morphology, however is most likely responsible of the highest torque among all the materials, so it is of the highest energy values. Irregular zircon surfaces create more contact points in contrast to rounded shaped INV1 and INV2 particles. Hence friction forces would be presumably more intense in zircon powders for the same volume fraction. That is what was reflected in the feedstock's temperature and friction energy dissipated by heat results. The lower optimal solid loading was also consequence of the lower packing factor of irregular powders combined most probably with agglomerates formation.

Comparing INV1 and INV2 powders, smaller INV2 powders with higher specific surface and more prone to agglomerate, predictably resulted in worsened torque rheology features. A higher specific surface implies more particle contact points for the same volume fraction and thus higher friction energy. This is reflected in the increased torque and friction energy values of INV2 with respect INV1. INV1 and INV2 powders have similar particle size distribution and hence they would be having similar packing factors, therefore the higher tendency to agglomerate of INV2 would be probably causing a lower optimum solid loading compared to INV1 powders.

To end up with torque rheology just to mention that energy parameters, assessed by totalised torque or by monitoring the feedstocks temperature, resulted very helpful to explain and to compare different feedstock behaviour. Although they are rough estimations, they allowed to link torque results with friction between particles and the capacity of the different binders to lubricate them. They could be used as a powerful tool to compare different feedstocks keeping in mind that the same mixing conditions should be maintained in all the experiments.

4.2.2 Capillary rheology

This section is going to study the flow behaviour of different feedstocks in a melted state. This flow behaviour was evaluated by measuring the apparent viscosity at different shear rates, temperatures and solid loadings in a capillary rheometer. Different flow parameters like the apparent flow activation energy (Ea) and the moldability index (α_{stv}) were assessed and discussed. Experimental or theoretical mathematical models suitability for explaining the collected data will be evaluated in subsequent sections.

Paper 2 present a brief description of the viscosity dependence with shear rate of B3, B5, B6 and B7 at 150 ºC and at 57.5 vol.%. All the feedstocks presented a shear thinning behaviour, i.e. the viscosity decreases with increasing shear rate. The decreasing rate is more pronounced in B3 which could be said that is the most pseudoplastic of all four. According to it, B6 is the least pseudoplastic and the one that gave the lowest viscosity values at low shear rates. This suited with the torque rheology results. All of them maintained a viscosity below 10^3 Pa·s in the shear rate range from 10^1 to 10^4 s^{-1}. That would make all them acceptable to be injected at high pressures at this temperature but the injection at low pressures would be difficult since it requires lower viscosities [3].

A more thorough and complete capillary rheology was performed with B8- and B9-based feedstocks mixed with zircon and Invar 36 powders respectively. Paper 3, Paper 4 and Paper 5 point out the capillary rheology works carried out with these feedstocks. Binders' flow behaviour was also evaluated since it strongly affects the feedstocks' flow behaviour.

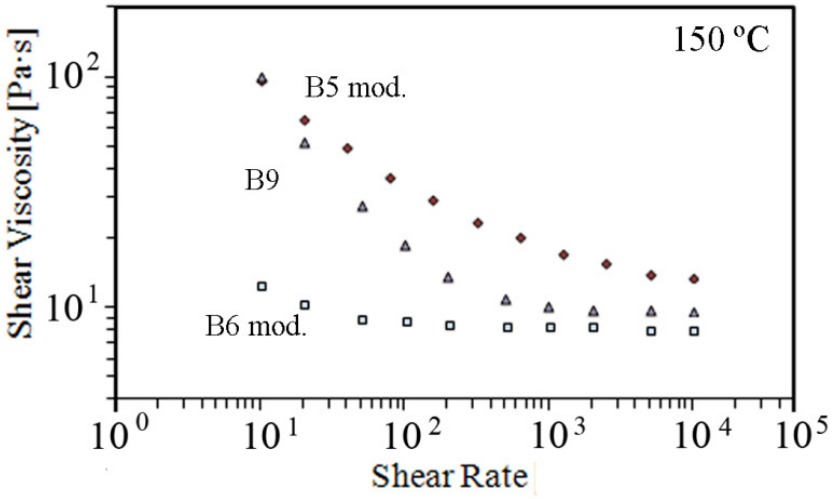

Figure 4. 3 Binder B9 flow behaviour with shear rate at 150 ºC. It was compared with a B5 modified and a B6 modified, both with 40 vol.% of their representative CAB and with some low molecular weight PEG according to B9 formulation.

Figure 4. 3 shows the flow behaviour of binder B9 compared with a B5 modified binder and a B6 modified binder (both with 40 vol.% of CAB381-0.1 and CAB551-0.01 respectively an some amount of low molecular weight PEG according to B9 formulation). The B6 modified showed the lowest viscosity as it was predictable since it contains CAB551-0.01 that is less viscous than CAB385-0.1. CAB551-0.01 has a higher percentage of butyryl groups affecting viscosity and other parameters like glass transition temperature and melting temperature. As expected, the B9 (containing a mixture of CAB551-0.01 and CAB381-0.1) showed and intermediate behaviour between B5 modified and B6 modified.

Focusing on the low shear rate region of the studied shear rate interval, when apparent shear rate was increased the apparent shear rate decreased. This indicates a non-Newtonian shear thinning or also referred as pseudoplastic behaviour. This behaviour is typically explained by binder molecules orientation and ordering with flow. Although CAB/PEG blends had demonstrated certain affinity, the extent of miscibility between these polymers is still uncertain. Anyhow, the effect of stress when the blend passes through the capillary may case separation of a priori miscible phases. Then, sheets or fibres of CAB dispersed phase may be formed within the PEG matrix. Fibrillation can occur in immiscible polymer blends if they are subjected to an elongation flow, which is exactly the flow at capillary. The effect of shear rate on the shape and size of the disperse phase is multiple. Shear rate acts on the deformation of the dispersed phase and can affect viscoelasticity of polymer blends during the melting process [4]. As shear stresses increase due to an increase of the shear rate, the deformation of the disperse phase intensifies and sheets or fibres of the disperse phase may be formed. These

sheets of fibres may also coalesce depending on the shear rate. Li et al. [5] pointed out that factors like mixing ratio, shear rate or draw ratio also influence the shape and size of nanofibres of immiscible CAB/PTT fibrillar composites.

At high shear rates the apparent shear viscosity is less affected by an increment of shear rate and the flow turns into Newtonian. The reason explaining this fact is uncertain. Barnes pointed out that this Newtonian plateau after a pseudoplastic region may result from two distinct, but widely spaced shear-thinning mechanisms if e.g. one of the phases has a relative high shear rate departure from Newtonian behaviour [6]. Barnes also related this behaviour with a possible wall slip phenomenon [7]. The viscosity ratio between the dispersed phase and the matrix plays an important role on the deformation of dispersed phase. Plate et al. [8] studied 13 different pairs of polymers and indicated that good fibrillation can be achieved when viscosity ratio is in the range of 0.1 < viscosity dispersed phase/viscosity matrix < 10. Xue et al. [9] demonstrated that the viscosity ratio of immiscible CAB/iPP blends is an important factor that determines the morphology of the polymer blend and the formation of fibres when this blend is drawn with an extruder. The change of viscous behaviour occurred at a lower shear rate in B6 modified (≈400 s^{-1}) compared to B9 (≈1000 s^{-1}) and B5 modified (>5000 s^{-1}). This may occur due to differences in viscosities ratios between the dispersed phases (CAB551-0.01, CAB381-0.1 or a mixture thereof) and the matrix (PEGs). More viscous CAB381-0.1 would need higher shear rates to deform and straighten into sheets or fibres affecting the flow behaviour. However another factor may be influencing the viscous behaviour. Although the nature of the CABs is similar, their compositional differences may change their interfacial tension with melted PEG which is another important factor in determining formation of different blend morphologies.

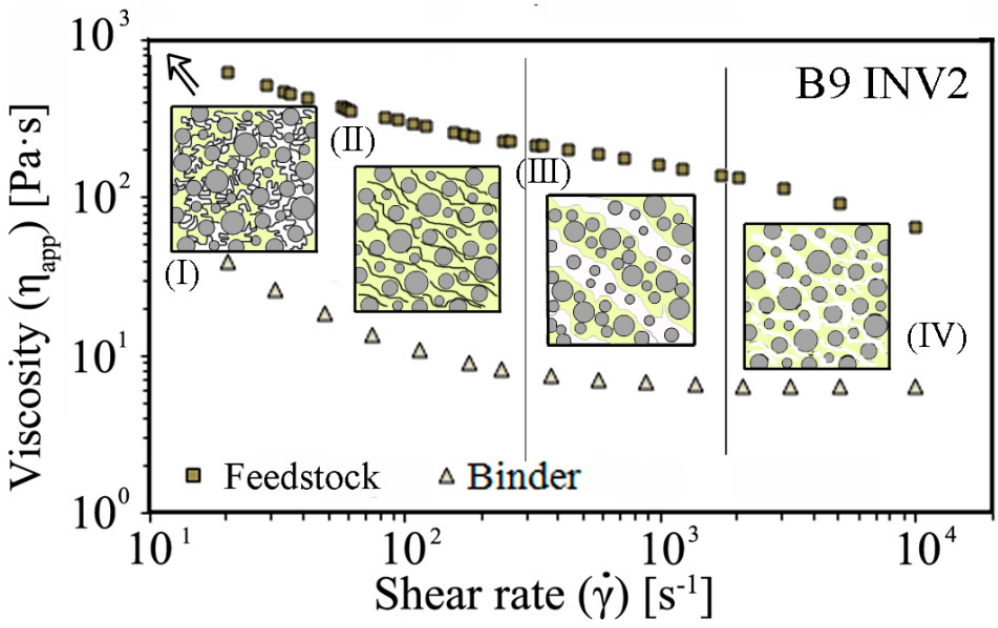

Figure 4. 4 Binder B9 and a INV2 feedstock based on B9 viscosity dependence with shear rate and sketches of hypothetical possible situations at the different regions of the feedstock's curve. Each sketch visually tries to show feedstock's features at three different curve stages. The curves correspond to 160 ºC and solid loading of 60 vol.% experiments.

Figure 4. 4 shows the flow behaviour of B9 at 160 ºC and a INV2 feedstock at 160 ºC and 60 vol.%. This behaviour is somewhat reproduced in other B8 and B9 based feedstocks. Focusing on the feedstocks behaviour, three stages are typically observed in their viscosity vs. shear rate curves. This behaviour may be explained as follows:

(i) At low shear rates a pseudoplastic behaviour is observed both for the binder and the feedstock. It seems that viscosity would be very high at values near 0 s^{-1} according with the observed trend which suggest the possibility of the occurrence of a threshold shear stress that has to be surpassed in order to the feedstock began to flow. In this region, a network structure was assumed for the binder system. In case of the feedstock, a similar structure may be formed (see schematic explanation in Figure 4. 4(I)) but with the particularity of a more rigid structure due to the presence of a high number of particles and interactions between the binder and powder particles. These particles are likely homogeneously distributed within the binder matrix, but the presence of certain heterogeneities in the particle distribution or the formation of agglomerates is not dismissed. Some authors relate the observation of a yield stress with the occurrence of this particle network structure within the melt [10, 11]. Confirmation of a yield stress would require a more thorough investigation in the low shear rate range by rotational rheology because according to Barnes a double sigmoid is not dismissed with a Newtonian plateau at very low shear rates.

(ii) This theorised network structure, which is relatively stable at very low shear rates, is destroyed as the shear rate increases. Then, the viscosity is dominated by hydrodynamic interactions, which results in shear thinning as particles and polymer orientate and order (Figure 4. 4(II)) in the flow direction to allow inter-particle motion as discussed by Husband [12]. Then, the shear thinning rate of the feedstock lowers approximately following the Newtonian behaviour of the binder in the intermediate shear rate region (around 200-300 s^{-1}). This Newtonian behaviour may be explained by segregation of the binder phases. The effect of high shear stresses would pull aside the PEG from CAB. The most viscous phase (in this case CAB) would contain a higher portion of particles since they would be more effectively retained when a high shear is applied. These are the bases of slip band theory that in the case of binders systems containing PEG is well explained and argued by Chuankrerkkul [13]. Hence low particle content PEG regions will be formed (Figure 4. 4(III)). The flow is favoured at these low viscosity regions, but in contrast is reduced in the CAB high particle and high viscosity regions reducing the shear thinning effectiveness with shear rate.

(iii) Until the end of this intermediate region, it could be said that the rheological behaviour of the feedstock is, to some extent, dominated by the binder behaviour. Thereafter other factors begin to dominate. Instabilities in the viscosity measurements begin to be observed. A possible explanation of the pseudoplastic behaviour at high shear rates would be the rupture of the slip bands hypothetically formed. Some authors relate a shear thinning behaviour to the breakage of agglomerates as reported by Hausnerova [10]. This could be also a plausible explanation of the shear thinning since the viscosity would be reduced by disruption of CAB highly particles concentration regions (see Figure 4. 4(IV)).

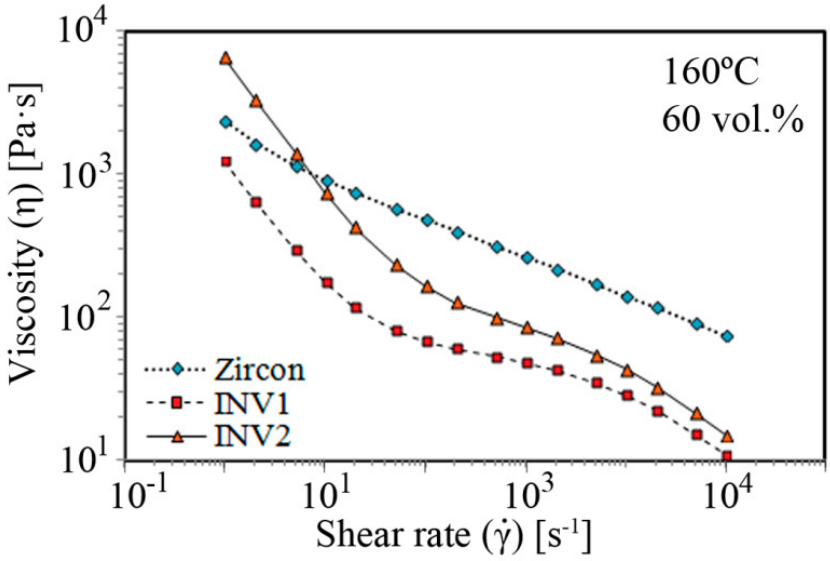

Figure 4. 5 Comparative of the apparent shear viscosity vs. the shear rate for 60 vol.% feedstocks of zircon, INV1 and INV2 powders measured at 160 ºC.

Figure 4. 5 compares the apparent viscosity vs. shear rate curves of different B8 and B9 feedstocks with zircon, INV1 and INV2 powders at 160º C and 60 vol.%. These figure is somewhat reproduced at different temperature and solid loading conditions. Excluding some points at low shear rates, the viscosity of these compositions sorts as follows: $\eta_{ZIRCON}>\eta_{INV2}>\eta_{INV1}$. This is consistent with the torque rheology results and the results obtained for B5 and B6. B9 containing more CAB381-0.1 is more pseudoplastic than B8 containing more CAB551-0.01. This fact also agrees the binder systems viscosity measurements where CAB551-0.01 based binders showed a more Newtonian behaviour (especially at low shear rates) compared to other binders.

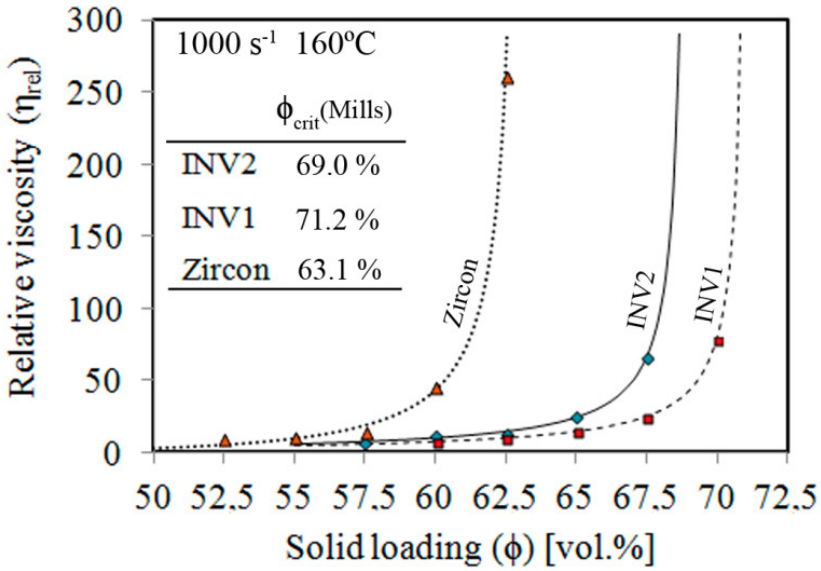

Figure 4. 6 Comparative of the relative shear viscosity vs. the solid loading curves for Zircon, INV1 and INV2 feedstocks. Markers represent experimental data whereas dashed and straight lines represent data fitting to a Mills modified model. According to this model and considering a shear rate of 1000 s^{-1} and a temperature of 160 ºC, the assessed critical powder volume contents are showed.

A comparative between different feedstocks relative viscosities at different solid loadings can be found in Figure 4. 6. All the curves show a horizontal-like line at low solid loadings were the relative viscosity increases a little or almost remain constant with solid loading. This occurred until a point where an inflection of this tendency was observed and the relative viscosity grows abruptly with the solid loading. Then the relative viscosity asymptotically grew to infinite at a certain solid loading considered the critical.

Following the criteria of the infinite asymptote of relative viscosity vs. solid loading curves, the critical solid loading of zircon feedstock would be somewhere around 63 vol.%, around 71 vol.% for INV1 and around 69 vol.% for INV2. These results follow the same discussion done with torque rheology. Irregular shape and a higher specific surface increase the contact between particles and thus the viscosity, while the powders packing capacity affects to the optimal and critical powder volume fractions.

The apparent flow activation energy (E_a) was assessed by comparing viscosity results at different temperatures as described in 1.3.2 . Figure 4. 7a plots the E_a of different feedstocks at several solid loadings. The E_a gives an idea of how the temperature affects the feedstocks flow. The higher the E_a is the more the temperature affects feedstocks' rheology. All the feedstocks showed a minimum in the E_a vs. solid loading curves.

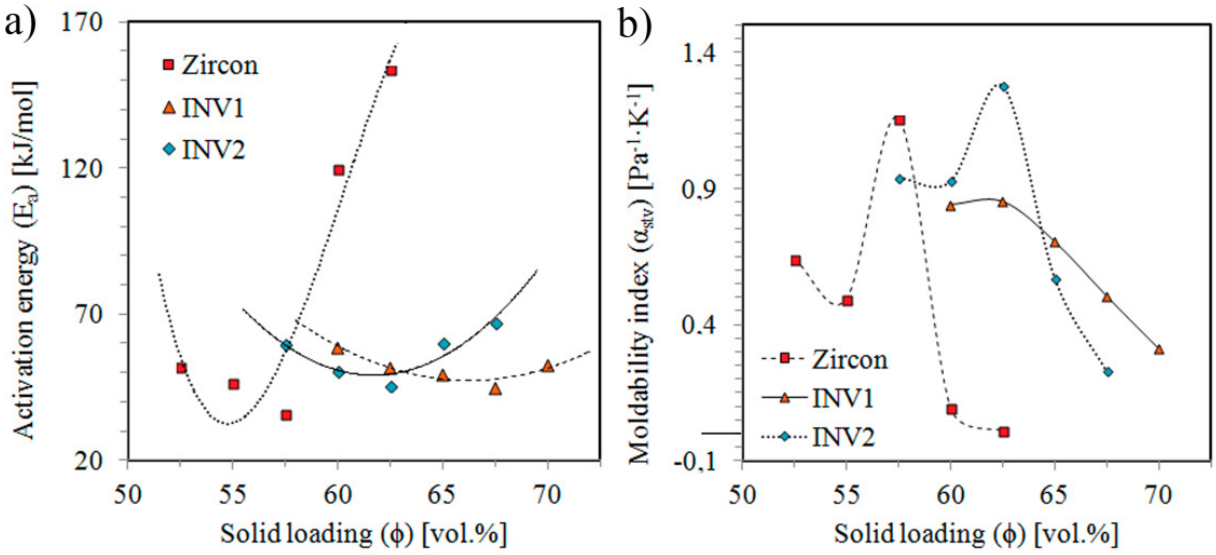

Figure 4. 7 a) Flow activation energy vs. solid loading for zircon, INV1 and INV2 feedstocks calculated at 2000 s^{-1}. Markers represent experimental point and lines a polynomial fit to the data. b) Moldability indexes vs. solid loading for zircon, INV1 and INV2 feedstocks at the reference conditions of 2000 s^{-1} and 160 ºC.

This minimum was reported by several authors [14-16] and may be explained as follows: the effect of the powder particles starts to dominate over the binder viscosity at high volume fractions were the contacts between particles are more probable; hence the temperature has less influence on the feedstock viscosity than the inherent effect of the friction between particles and thus the E_a decreases. As the particle packing reaches a maximum at solid loading near the critical point, the binder gap between particle decreases as well as the

lubricating efficacy. Then the temperature becomes again relevant. Differences in the coefficients of thermal expansion between the powder and the binder make that small changes of temperature significantly increase the binder volume while maintaining the powder volume approximately constant. In the critical region, these relative volume variations make a difference and strongly affect the feedstocks viscosity.

Hence, this minimum would be related with the optimal solid loading due to: 1) this composition is the less affected by temperature variations which is very positive during injection 2) this minimum reveals an optimal binder packing with sufficient binder content coating the particles. Regarding this last, optimal solid loading of zircon feedstocks would be 57.5 vol.%, 62.5 vol.% for INV2 and 67.5 vol.% for INV1 (see Figure 4. 7a).

E_a is more affected by the solid loading in the case of zircon feedstocks than in the Invar 36 feedstocks, especially at solid loadings near the critical point. According with the explanation of the minimum value this behaviour is predictable since the irregular powders would be more affected by reduction of the binder content; as the particle contacts presumably occur by layers instead of by single points, the lubrication is more critical. Nevertheless, many of the activation energies calculated for different feedstocks independently of the powder type and solid loading are around 50 kJ/mol, which could be considered a reasonable good value. Allaire et al. [17] proposed a value of 40 kJ/mol as the level above the defects occurring during injection moulding become unacceptable for sub-micrometer zirconia blends. The minimum E_a value for each powder-type feedstocks is bellow or close to 40 kJ/mol. In the other hand, this reference value was obtained for a very specific system and CAB based feedstocks of zircon and Invar 36 powders may behave in a different way.

The moldability index α_{svt} summarises different rheological parameters like the reference viscosity, η_0 (at a certain temperature and shear rate), the activation energy, E_a, and the flow index n. The flow index is conventionally the power law exponent which determines the shear thinning ratio in the pseudoplastic region. The higher the moldability index is, the better a feedstock is in terms of its ability to be moulded, i.e: it is more pseudoplastic or/and is less dependent on temperature (low E_a) or/and its viscosity is lower at a certain temperature. Considering that last, it is obvious that the zircon feedstocks are worse than Invar 36 feedstocks as it is deduced from Figure 4. 7b, which plots the moldability indexes of the feedstocks at different solid loadings. It was also observed that α_{svt} got to a maximum value at a certain solid loading. Except for the INV2 feedstocks, where this maximum is less evident and occurred at a solid loading lower than the estimated by other methods, this maximum could be associated with the previously determined optimum solid loading.

It is worth to note that although in Figure 4. 7 auxiliary dashed lines are used to better follow the data evolution with the desired variables, they do not represent a polynomial or other mathematical model fit.

4.3 Thermal stability and degradation kinetics of the feedstocks

This section is going to summarise the thermal analysis studies of different feedstocks which will give an idea of the working temperatures and the thermal degradation intervals. The thermogravimetry and calorimetry results are presented extensively in Paper 2, Paper 7 and Paper 8, whereby the influence of the binder components and the different powder particles on the degradation of the feedstocks was investigated. These studies were also useful to determine the compatibility between the different compounds.

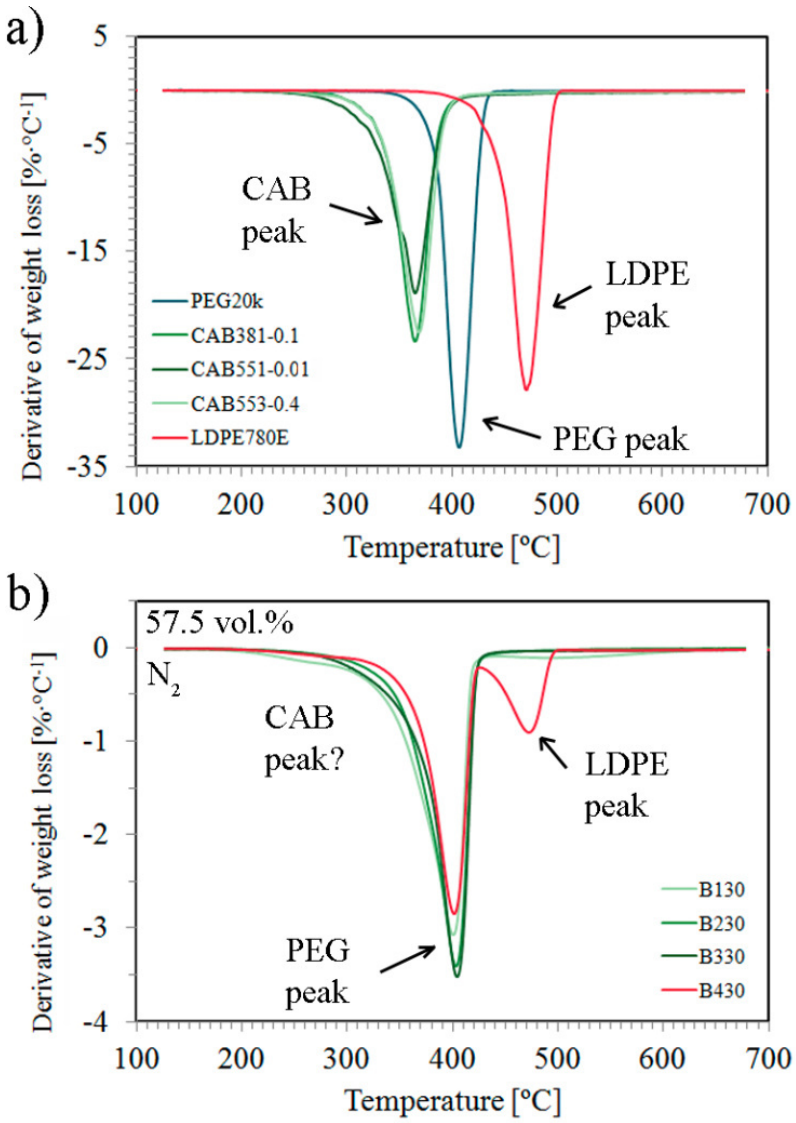

Figure 4. 8 DTG curves of a) different binder components and b) zircon feedstocks elaborated with different binders systems and with a solid loading of 57.5 vol.%. In both cases the heating rate was 10 ºC/min and a nitrogen atmosphere (40 ml/min) was used. The measurements were performed in a Perkin Elmer STA6000 device.

The thermal degradation analysis by TGA suggested a better compatibility between CABs and PEG than LDPE (see Paper 2). The derivative of the TGA curves with respect the temperatures (DTG) of the different components in N_2 atmosphere are plotted in Figure 4. 8a.

A characteristic peak for each single substance occurring at different temperature ranges is observed. CABs have similar decomposition behaviour and are the first to volatilise, followed by PEG20k and LDPE 780E thereafter. Figure 4. 8b represents the different feedstocks DTG curves at the same measuring conditions. In the case of LDPE-based feedstocks the peaks appears at the same temperatures than the plain LDPE 780E and PEG20k whereas in the case of CABs-based binders the CABs' corresponding peaks are displaced with tendency to merge with the PEG's peak. This fact may be related with a better compatibility between CABs and PEG or with an effect of the zircon particles. The retarded degradation of CAB may be a consequence of interactions between polymer chains or particle surfaces. These results were reproduced in Paper 7 and Paper 8 were additional FTIR and DSC analyses confirmed that the interactions between CAB and PEG molecules exists but also between the binder components and the powder particles, both for zircon and Invar 36 powders. These interactions presumably occurred between the polymers or at the particle surface -OH groups and polymer C-O-C or C=O groups.

Other interesting conclusions can be drawn comparing the thermogravimetric analysis at different atmospheres. At nitrogen inert atmosphere, although CABs decomposition interval mainly is below LDPE range, they do not completely degrade up to around 600-700 ºC leaving an organic residue. This fact may be reducing the clear advantage of CABs over LDPE that apparently need lower debinding temperatures. The lower CAB degradation temperatures allow for the reduction in energy consumption in comparison to LDPE. However the organic residue is a dangerous carbon source that may be introduced in the material composition at high temperatures if it is not eliminated. Therefore, atmospheres containing oxygen (that could be pernicious in powders susceptible to be oxidised) or hydrogen (that would increase the process cost) should be used.

When air is used as debinding atmosphere, the combustion oxidative reactions with the polymer compounds move ahead the onset degradation temperature but the end-of-degradation point is the same than in the nitrogen experiments. This broadening of the degradation range may be positive to attain a more progressive elimination. What is really interesting is that a complete elimination of the organic compounds is achieved. Using air as debinding atmosphere commonly is not a problem in ceramics, but at the debinding temperature ranges may cause the oxidation of some metals and metal alloys.

There is another disturbing fact in the degradation of CABs and PEG in nitrogen atmosphere. The multi-component binder systems are normally designed to have different thermal elimination steps to facilitate the subsequent compound volatilisations without compromising the integrity of the brown part. The coincidental PEG's and CABs' degradation intervals in presence of zircon powders would hinder a possible full thermal removal. It is not only that the degradation intervals coincide, but that the degradation window would be very narrow to progressively remove degradation volatiles at an acceptable heating rate. Nevertheless, there is the possibility a solvent debinding process in water.

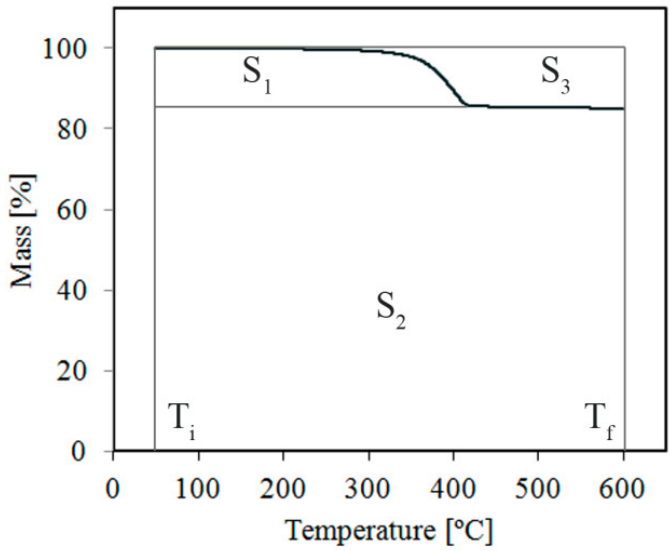

Figure 4. 9 Scheme representing the different areas used to calculate the IPDT.

When different powder-types were compared, the effect of the nature and characteristics of the powders on the degradation kinetics was evidenced. Table 4. 5 collects some measured characteristics degradation parameters of the different evaluated feedstocks. It may be noticed that the integral procedure decomposition temperatures (IPDTs) have values between 4000 to 17000 ºC. These surprisingly high values have not a real physical meaning and they are consequence of the used method. This method compares different areas of the resulting TGA curve, S_1, S_2 and S_3 delimited by an initial (T_i) and a final temperature (T_f) (see Figure 4. 9). These areas are related in the following expressions, $A^*=(S_1+S_2)/(S_1+S_2+S_3)$ and $K^*=(S_1+S_2)/S_1$, from which the IPDT can be worked out:

$$IPDT[^oC] = A^* \cdot K^* \cdot (T_f - T_i) + T_i \qquad \text{Eq.4.1}$$

Table 4. 5 Typical decomposition parameters comparative between different feedstocks. The values correspond to a heating rate of 10 ºC/min and nitrogen atmosphere. IDT = initial decomposition temperature, IPDT = integral procedure decomposition temperature, T_{max} = temperature for the maximum decomposition rate, Re = organic residue.

	Zircon				INV1				INV2			
Φ [%]	IDT [ºC]	IPDT [ºC]	T_{max} [ºC]	Re [%]	IDT [ºC]	IPDT [ºC]	T_{max} [ºC]	Re [%]	IDT [ºC]	IPDT [ºC]	T_{max} [ºC]	Re [%]
52.5	287.4	3859	388.3	4.6	-	-	-	-	-	-	-	-
55	285.6	4436	390.1	6.1	-	-	-	-	-	-	-	-
57.5	283.1	4695	398.1	5.4	-	-	-	-	261.2	8714	407.5	5.4
60	248.7	4976	404.1	4.6	265.7	9260	408.1	3.0	259.9	9839	407.2	5.7
62.5	242.7	5516	404.6	2.9	261.4	10388	408.3	3.4	257.8	10955	407.1	6.4
65	260.9	6244	399.7	3.2	259.3	11513	408.3	3.7	256.3	12263	407.8	6.8
67.5	-	-	-	-	257.9	12655	407.8	3.5	248.1	13527	407.7	6.3
70	-	-	-	-	243.4	14776	407.7	4.7	241.1	14774	407.1	7.0
72.5	-	-	-	-	246.0	16689	407.2	4.6	-	-	-	-

The high IPDT values are then explained considering that the zircon and Invar 36 powders are very thermally stable and are an important mass fraction of the feedstocks. As consequence S_2 is going to be always much bigger than S_1 and S_3. This parameter was first proposed in polymer systems that leaves an organic residue [18] and has demonstrated its utility to estimate thermal stability of loaded polymers [19, 20]. The meaning of the IPDT would be the temperature at which the sample completely volatilises considering the programmed heating rate, but this temperature is only estimative [18].

Figure 4. 10 plots the initial decomposition temperature of different feedstock at different solid loadings. This parameter represents the temperature at which the 2 wt.% of the binder was removed out of the feedstock at a constant heating rate TGA analysis. IDT remained approximately constant at low solid loadings and at a certain solid loading it began to fall as the solid loading is increased.

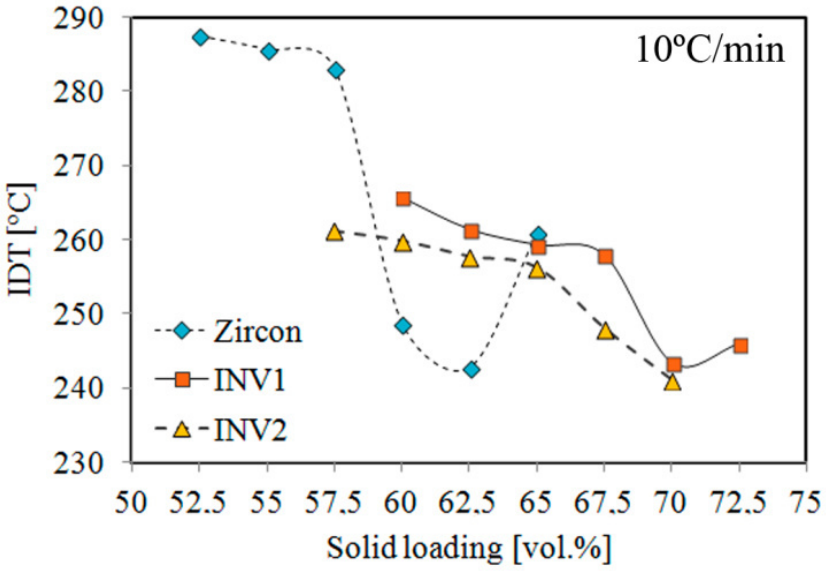

Figure 4. 10 Initial decomposition temperature vs. solid loading for zircon, INV1 and INV2 feedstocks assessed considering the 2 wt.% of the binder in a TGA cycle with a heating rate of 10 ºC/min and nitrogen atmosphere.

This change of behaviour is in concordance with the estimated optimal solid loading assessed by rheological methods. Differences were also observed when all the materials were compared. At solid loadings between 52.5 vol.% to 57.5 vol.%, zircon powders seemed to retard the beginning of the binder degradation compared to Invar 36 powders. However, from then on the IDT values were lower or similar to Invar 36 feedstocks. Invar 36 feedstocks (INV1 and INV2) had similar behaviour except for the point at which IDT values felt abruptly.

Figure 4. 11 represent the IPDT values of the different materials at different solid loadings. The normalised IPDT value with respect the density of the feedstock was represented due to the IPDT parameter is very influenced by the residual weight percentage during the TGA

experiment. At same powder volume fraction, zircon powder weight is approximately two thirds of the Invar 36 powder. The normalised IPDT value is proposed in order to compare different materials with different densities.

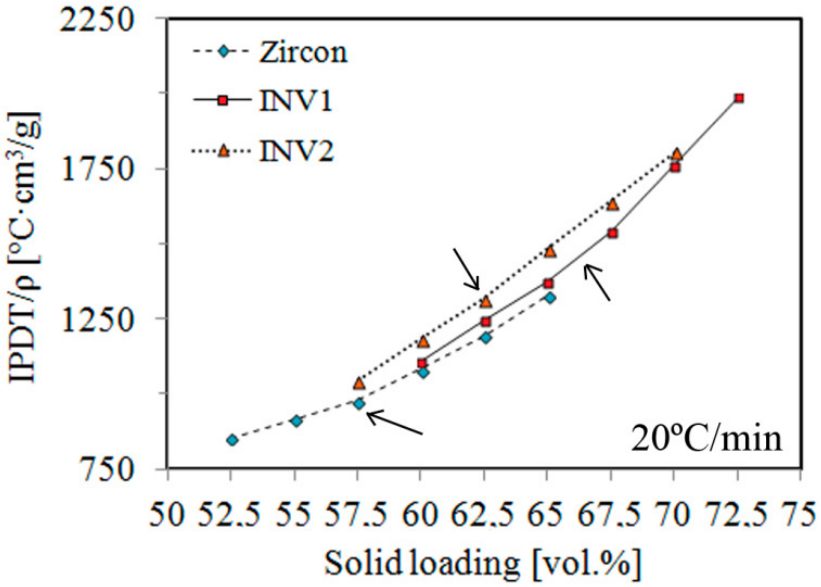

Figure 4. 11 IPDT values normalised with the density of the different materials. A heating rate of 20 ºC/min was employed. Several results for different solid loading are shown. The arrows indicate a change in the slope of the linear tendency of the IPDT variation with solid loading.

With the solid loading, the IDPT value grew following a linear trend. A change of the curve's slope was observed at a certain solid loading depending on the material (marked with an arrow in Figure 4. 11). This solid loading again coincided with the optimal solid loading determined with rheological methods. Considering that the higher the IPDT is the better the thermal stability, above 57.5 vol.% Invar 36 feedstocks could be considered more stable than zircon feedstocks. In contrast, if the Invar 36 feedstocks' trend line is extended to solid loading bellow 57.5 vol.%, it looks like zircon feedstocks would be more stable, but it could not be assured since there is a lack of experimental points.

The degradation activation energy was also assessed by using isoconversional FWO and KAS methods. Figure 4. 12 shows the evolution of the activation energy with the conversion rate of different feedstocks. The behaviour is approximately the same in all the materials. At low conversion values the activation energy progressively increases with conversion. Some authors relate this behaviour with concurrent competitive reactions. Then, up to around 0.5 the activation energy values stabilise of smoothly decrease. The activation energies were lower with zircon powders, particularly at high conversion rates. The INV1 powders showed the highest activation energy values at all conversion rates. At low conversion the feedstocks' activation energies were lower than those for the binder or binder compounds suggesting a catalytic or other type of effect derived from the powders (see Paper 7). At high conversion rates the E_a of the feedstocks is higher than the E_a of all the single binder components, but similar or slightly lower (in the case of zircon feedstock) than the Ea of the binder system.

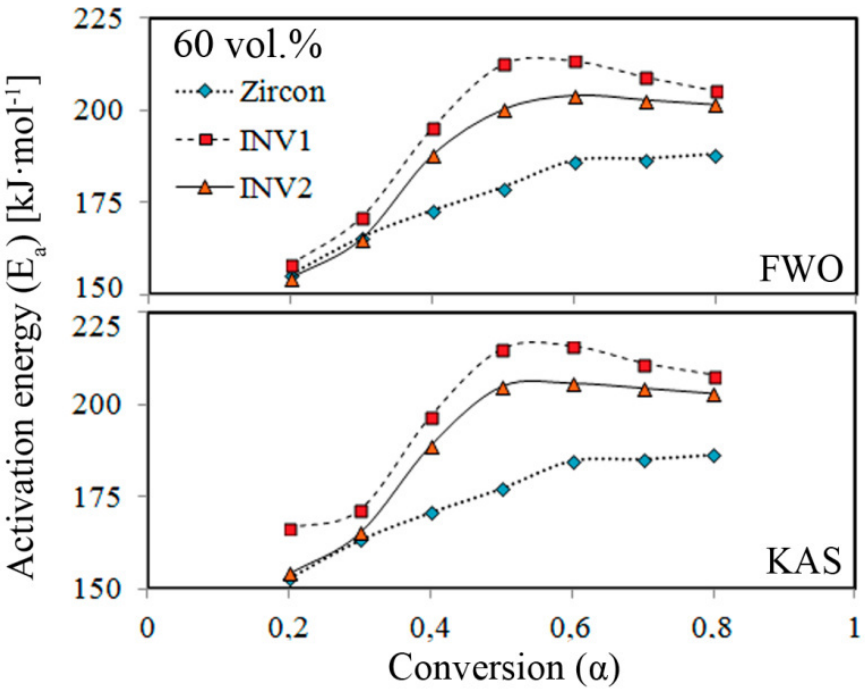

Figure 4. 12 Evolution of the decomposition activation energy of 60 vol.% zircon, INV1 and INV2 feedstocks assessed according to the FWO or the KAS isoconversional methods.

Figure 4. 13 compares different decomposition activation energy results of different materials and solid loadings. A minimum is observed for all the materials in the E_a vs solid loading curves. This minimum again matched with the optimal solid loading assessed by rheological methods.

The analysis of the thermal stability and degradation kinetics with solid loadings disclosed several signs of occurrence of an optimal solid loading: a sudden drop of the IDT values, a change in the slope of the IPDT linear trend with solid loading or a minimum in the values of the degradation activation energy, all presumably occurring at this solid loading.

To properly theorise about the nature of these behaviours, the following issues should be first considered:

1. Binder components are interacting: this fact was revealed by displacements of the PEG's crystallisation peaks in presence of CAB, by light microscopy, by a merging trend of the corresponding PEG's and CAB's peaks of the derivative of TG curves of the binders and feedstocks and by an increment of the degradation apparent activation energies of the binder in comparison with those of the single binder compounds.
2. Powders and binders are interacting: this affirmation was evidenced by DSC and FTIR experiments. The powders may also impair a catalytic effect on the thermal degradation of the binders. Aggarwal et al. [21] analysed 316 L stainless steel feedstocks thermal debinding and propose this catalytic effect to explain the thermal behaviour. This catalytic effect is also proposed in Atre et al. [22] and Enneti [23]. This would explain some of the results in the kinetic studies.

3. Powder particles are tightly packed within the feedstock and this packing in more severe at solid loading near the critical point. Powder may hinder the evacuation of volatiles and thus affect the degradation kinetics.
4. CABs do not completely degrades and form a thermally stable organic residue in presence of nitrogen atmosphere. This organic residue may accumulate and obstruct the volatiles evacuation pathways created between particles. This organic residue is going to be referred as char.

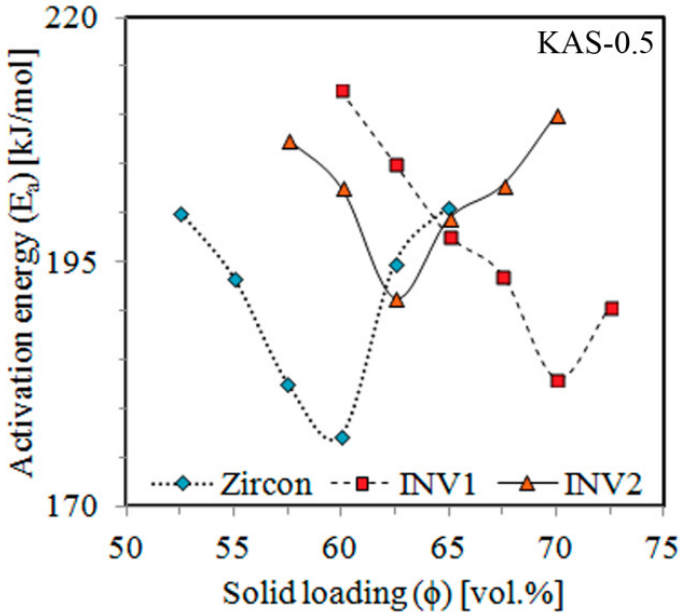

Figure 4. 13 Comparative of degradation activation energies vs. solid loading

Rigorously TGA device measures the weight lost associated with volatilisation of break-down by-products. These by-products should have a certain low molecular weight in order to volatilise. Hence, although the binder degradation began at lower temperatures it is only going to be detected when the polymer chain achieve a suitable low molecular weight as consequence of scission.

As discussed in Senapati [24] the effect of mechanical mixing favours the formation of links between polymer chains. The presence of powders also favours the mechanical mixing by an increment of the shear stresses that are applied more locally within the feedstock's bulk. This could be one reason explaining why the PEGs and CABs corresponding peaks in the derivative of TG curves are closer in the experiments with feedstocks than in the experiments with binders. Senapati work mentioned the formation of "weak links". He argued that these weak links would further act as chain scission points during thermal degradation facilitating the process. However the nature of these links in the study case is not clear at all. Stable links favoured by temperature could be formed by cross-linking or grafting in the case of CAB and PEG. This fact would explain the higher activation energies of the binder system compared with those of the CAB and PEG. Although the investigation of the nature of these interactions would be very interesting it would require time and more sophisticated methods and it was out

of the scope of this Thesis work. Interactions presumably occur between –OH groups present in both binder and powder surface and C-O-C and –C=O groups. These type of interactions were reported by Tanaka [25] who studied the immobilization of PEG chains by reaction with active OH on metal oxides surfaces and by Derosa [26] who studied the interactions between PEG and silica and alumina. However, other types of interactions were not discarded.

At this point is worth to remember that the IDT values decreased with solid loading. This could be linked with a catalytic effect of the powders that would be favoured as the available powder surface increase with solid loading. But this effect alone would not explain the sudden decrease of the IDT values from a certain solid loading. When the particle packing approaches the maximum value, friction between particles begin to predominate over the lubricant effect of the binder. The binder system is subjected to higher shear forces and also to higher temperatures due to friction; this may cause that the polymer chains began to split in lower molecular weight chains during mixing. The optimal point would set the beginning of these severe mixing conditions due to a lack of binder to effectively lubricate the particles accelerating its decomposition. This could be also linked with a rapid increment of the torque values from the optimal solid loading on. This theory is consistent with a more severe fall of the IDT values in zircon feedstocks as the friction forces are more intense in the case of irregular shape powders.

The effect detected with the change of the IPDT vs. solid loading curve's slope may be also explained by the occurrence of maximum packing. IPDT take into account the entire of the decomposition process not only the initial stages as it does the IDT parameter. Formation of a thermally stable char is assumed due to incomplete degradation detected with TGA analyses. At packing factors close to the maximum, this char would hinder more severely the volatiles removal affecting the weight loss rates and retarding the elimination of break-down products, thus affecting the IPDT.

Both catalytic effect of the powder and degradation during mixing would favour the degradation reducing the activation energy up to a point where the particles are so tightly packed that this effect begins to be masked by the effect of the powder particles and the char formation. This theory would explain the minimum of the degradation activation energy with temperature.

Degradation kinetic studies have demonstrated that it depends on many factors. It is difficult to evaluate if the powders really have a catalytic effect and at which extent. It seemed that the Invar 36 has a more effective catalytic effect than zircon as it could be deduced from the lower IDT and IPDT values at low solid. However the lower degradation activation energies of the zircon feedstock make doubt of the last statement.

4.4 Mechanical and physical properties of the sintered parts

This section contains information about the mechanical and physical properties of zircon and Invar 36 parts manufactured by PIM and how these properties are affected by the processing conditions.

4.4.1 Zircon

Paper 1 and Paper 2 show bending tests results of zircon parts elaborated with different binder systems and processing conditions. The influence of the binder system on the flexural strength was highlighted. Feedstocks containing CAB resulted in better properties than polyolefin-based feedstocks. This fact was associated with improved feedstock's features like a better homogeneity or flow capacity. These improved feedstock's features, as discussed in previous sections, are presumably consequence of a better affinity between feedstock's components. Hence, a proper particle distribution and moulding might result in an enhanced sintered part. Large LDPE fibres were observed between zircon particles clusters. They were responsible of big empty spaces after thermal removal. Hence big pores were observed after sintering. Moreover, heterogeneities of the polyolefin based feedstocks generally resulted in part bending during sintering. That was not the case of CAB, almost indistinguishable from PEG and embedding the particles more evenly; that resulted in less or at least in finer and better distributed porosity and a better shape retention after sintering. However, injection and debinding stages could involve the formation of macro defects like cracks, delamination, blistering or macro voids regardless binder or processing conditions. That also conditioned mechanical test results and is an issue that should be mitigated or eliminated.

High molecular weight PEG20k was selected to avoid binder-particle segregations commonly appreciated when low molecular weight PEG is used [27]. However, high molecular weight PEG is more difficult to be extracted and melts at higher temperatures [28, 29]. Cracks and delamination occurring during PEG removal in solvent debinding were consequence of PEG swelling after water diffuses inside the part and a gel is formed. To mitigate swelling effect PEG molecular weight could be reduced. This concept was incorporated to formulations B8 and B9 after the good results observed with B4 that included low molecular weight PEGs.

B4 produced the best bending test results comparing Paper 1 and Paper 2, but it is worth to note that: (i) the feedstock contained 60 vol.% of zircon instead of 57.5 vol.% or lower, (ii) the parts were sintered at 1500 ºC in air during 3h instead of 1450 ºC in vacuum during just one hour in some cases and (iii) less macro-defects were observed after solvent debinding probably due to low molecular weight PEGs. B6, pretty similar to B4, tended to trap macro air bubbles. This fact was almost inappreciable in B4 parts and most likely is affecting negatively B6 parts' properties. Although B7 showed good flexural strength and the lowest porosity when it was compared to B3, B5 or B6, the results were more erratic and less reproducible as consequence of macro defects. B6 also showed good results with a reduced swelling using PEG20k and less macro defects.

The aim of Paper 1 and Paper 2 was just comparing different binder systems. A proper zircon sintering study was not made. The last part of this section will deal with the effect of sintering conditions of B8 feedstocks on the part shrinkage and final properties.

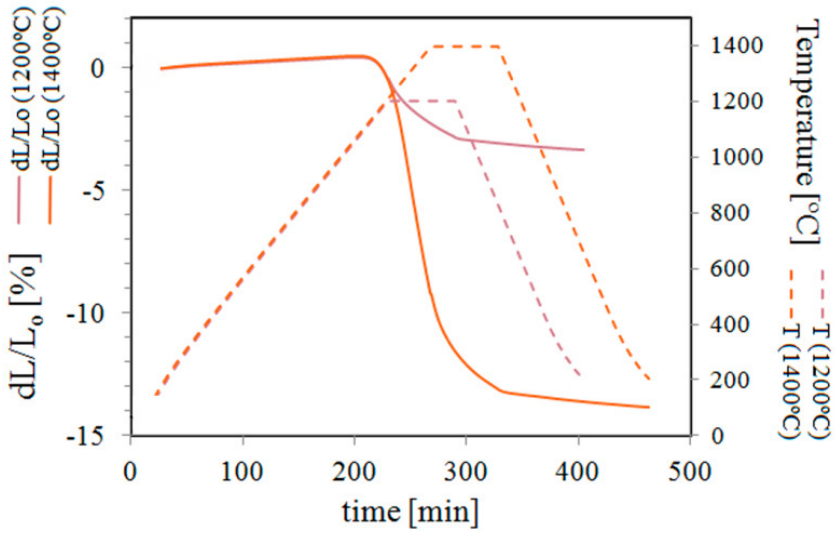

Figure 4. 14 Dilatometry test curves of brown zircon parts with 57.5 vol.% of solid loading for several heating cycles: (i) Heating up to 1200 ºC at 5 ºC/min – holding the temperature 1h – pulling down the part to room temperature at 5 ºC/min. (ii) Heating up to 1400 ºC at 5 ºC/min – holding the temperature 1h – pulling down the part to room temperature at 5 ºC/min. In both cases argon atmosphere was used and the parts were pre-sintered at 1000 ºC during 1h to avoid the parts crumbling during the positioning in the dilatometer.

Figure 4. 14 shows the dilatometry test curves of brown zircon parts subjected to two different sintering cycles at argon atmosphere. The part expands during heating until approximately 1150 ºC corresponding to normal zircon expansion with temperature variation. Then the tendency is inverted and the part begins to shrink. That can be associated with the activation of the atoms diffusion mechanisms and the beginning of the sintering stage, making the particles to coalesce. As expected, the sintering temperature has a dominating effect over the sintering time. When the part is pulled down the typical dimensional variation of the part due to temperature variation can be observed; the shrinkage is no longer related with the sintering mechanisms.

The averaged coefficient of thermal expansion from 200 ºC to 1000 ºC (calculated from the cooling stage of the dilatometry curves) resulted $4.31 \cdot 10^{-6}$ ºC^{-1} in the 1200 ºC thermal cycle and $4.85 \cdot 10^{-6}$ ºC^{-1} in the 1400 ºC thermal cycle. These values were comparable with some data base and literature of zirconium silicate properties that report values between $4.1 \cdot 10^{-6}$ ºC^{-1} - $4.2 \cdot 10^{-6}$ ºC^{-1} from room temperature to 1400 ºC [30, 31]. The total linear shrinking (just considering sintering) was 12.6 % for the 1400 ºC and 1h sintering cycle and 2.9 % for the 1200 ºC and 1h sintering cycle.

Table 4. 6 gathers some shrinkage, flexural strength and micro-hardness Vickers results of zircon parts at different sintering conditions. Two atmospheres were compared. For the vacuum experiments there was a physical limitation of the furnace temperature and parts were

only sintered up to 1400 ºC. Three temperatures were tested at this atmosphere, 1200 ºC, 1300 ºC and 1400 ºC holding them during 3h. A fourth experiment was performed at 1400 ºC during 15 min. In the case of sintering in air, two temperatures were tested (1400 ºC and 1500 ºC) holding them during 3h.

Table 4. 6 Volumetric shrinkage and mechanical properties of zircon parts as a function of the processing conditions and temperatures. The parts were fabricated with B8 feedstocks at 57.5 vol.%. The heating and cooling rates were 5 ºC/min.

T_{SINT} [ºC]	t_{SINT} [h]	Atmosphere	Shrinkage [vol.%]	Flexural Strength [MPa]	Micro-hardness Vickers* [GPa]
1400 ºC	15 min	Vacuum	20.6±1.74	34.4±7.8	6.1±0.5 - 3.4±0.3
1200 ºC	3h	Vacuum	7.3±0.2	8.7±1.9	1.5±0.2 - 0.8±0.1
1300 ºC	3h	Vacuum	14.9±0.6	30.1±7.9	5.6±0.4 - 3.9±0.3
1400 ºC	3h	Vacuum	27.2±1.0	59.2±8.8	11.1±0.6 - 7.7±0.4
1400 ºC	3h	Air	32.4±1.2	64.0±5.2	13.6±0.5 - 8.4±0.4
1500 ºC	3h	Air	36.6±1.74	68.6±7.3	12.3±0.6 - 9.1±0.5

* First value corresponds to a load of 4.9 N and second value corresponds to a load of 9.8 N

Since maximum strength generally occurs at maximum density, the latter is considered of high importance in evaluating sintering. Sintering time also affects densification. This could be seen by comparing shrinkage values of parts sintered in vacuum at 1400 ºC during 15 min or 3 h. As expected, the 1200 ºC cycle has an insignificant effect on the part densification. The 1300 ºC cycle produced less shrinkage than the 1400 ºC – 15 min cycle evidencing that the sintering mechanisms are more activated by temperature than by time, at least in this temperature interval.

Air atmosphere seemed to improve sintering as it is deduced from the better shrinkage results. No references were found mentioning the effect of oxygen in the sintering of zirconium silicate. An explanation based on the presence of impurities is proposed. Raw zircon powder contains certain impurities like Al_2O_3, TiO_2 or Fe_2O_3. Moreover, contamination with different elements (specially iron coming from steel) may occur during PIM process due to a wearing effect of hard zircon particles over tools. Air atmosphere is more prone to maintain or form new metallic oxides at high temperatures than vacuum. At very low oxygen partial pressures and high temperatures some metal oxides including iron oxides would be reduced according with Ellingham- Richardson diagram [32, 33]. The conditions during sintering in vacuum could be enough to avoid the formation of oxides of elements coming-from-wearing or reduce the oxides in the raw powder.

It is reported that metal oxides could improve the sintering behaviour of zircon by formation of a permanent liquid phase, a transient liquid phase or by solid solution [34-36]. Fe_2O_3 and TiO_2 are considered liquid phase formers. Al_2O_3 is a solid solution former although aluminium could react with zircon to form mullite. Particularly, Awaad [37] reported that Fe_2O_3 and Al_2O_3 reduce the temperature at which minimum porosity is achieved (1450 ºC – 1500 ºC respectively) in comparison to other metal oxides. However Fe_2O_3 produced lower levels of

porosity than Al_2O_3. Fe_2O_3 is beneficial for part densification, but may form a glassy phase that could be responsible of formation of micro cracks that lowers the toughness of zircon and may reduce its properties at high temperature. At air atmosphere presumably more oxides were available during sintering to form a possible liquid phase than in vacuum improving the sintering. This would be in accordance with better shrinkage values.

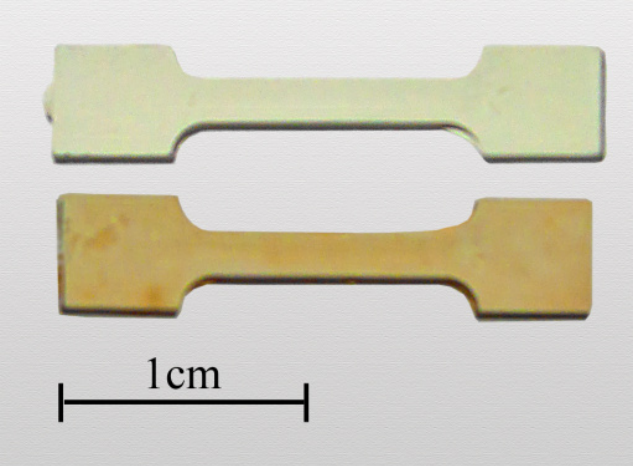

Figure 4. 15 Examples of zircon sintered parts at 1400 ºC during 3h in vacuum (top) and in air (bottom). These tensile specimens were injected at high pressures and were not mechanically tested.

It is worth to note that parts sintered at vacuum showed a bright white colour whereas the parts sintered in air developed a pale creamy colour that tends to reddish (see Figure 4. 15). This would be important if zircon applications of aesthetic requirements. Solid solutions of different elements in zircon lattice have been reported to be responsible of zircon pigmentation. For example, it has been reported that V^{4+} in solid solution turn the zircon into blue [38]. Another alternative is using inclusion pigments. The colour is not developed by introduction of coloured ions into matrix lattices or by the formation of solid solutions, but by the inclusion of small coloured crystals into the matrix during the sintering process. That is the case e.g. of hematite-zircon pigments also known as coral pink [39]. In any case, the source of studied zircon pigmentation in air could come from its impurities. No pigmentation due to Fe_2O_3 inclusion was observed in vacuum atmosphere, assuming this is the mechanism for the observed pigmentation in air atmosphere. Therefore it apparently seems that iron oxides or other impurities are playing an important role during sintering at air, fact probably do not occur or occur at less extent at vacuum.

Zircon parts densification has an important effect on the mechanical properties (see Table 4. 6). The higher the shrinkage was, the better were the flexural strength and the micro hardness results. It is relevant that none of the conditions led to flexural strengths above 100 MPa. These are considered poor values compared to typical zircon (~ 150-300 MPa)[40] or other possible competing ceramics like α-alumina (150-450 MPa) [41, 42] or zirconia (>600 MPa). B4 parts at the above mentioned condition were the only that exceeded 100 MPa values. B8 parts did not achieve these values even though some parts were sintered with same B4 conditions. The main difference was the solid loading. A higher solid loading means less

shrinkage to achieve the same densification values, there is a less risk of defect formation or residual stresses after sintering. Particles were presumably closer packed which also facilitates the sintering. For the future works with zircon, one crucial objective might be to achieve higher solid loadings and contrast this effect upon mechanical properties.

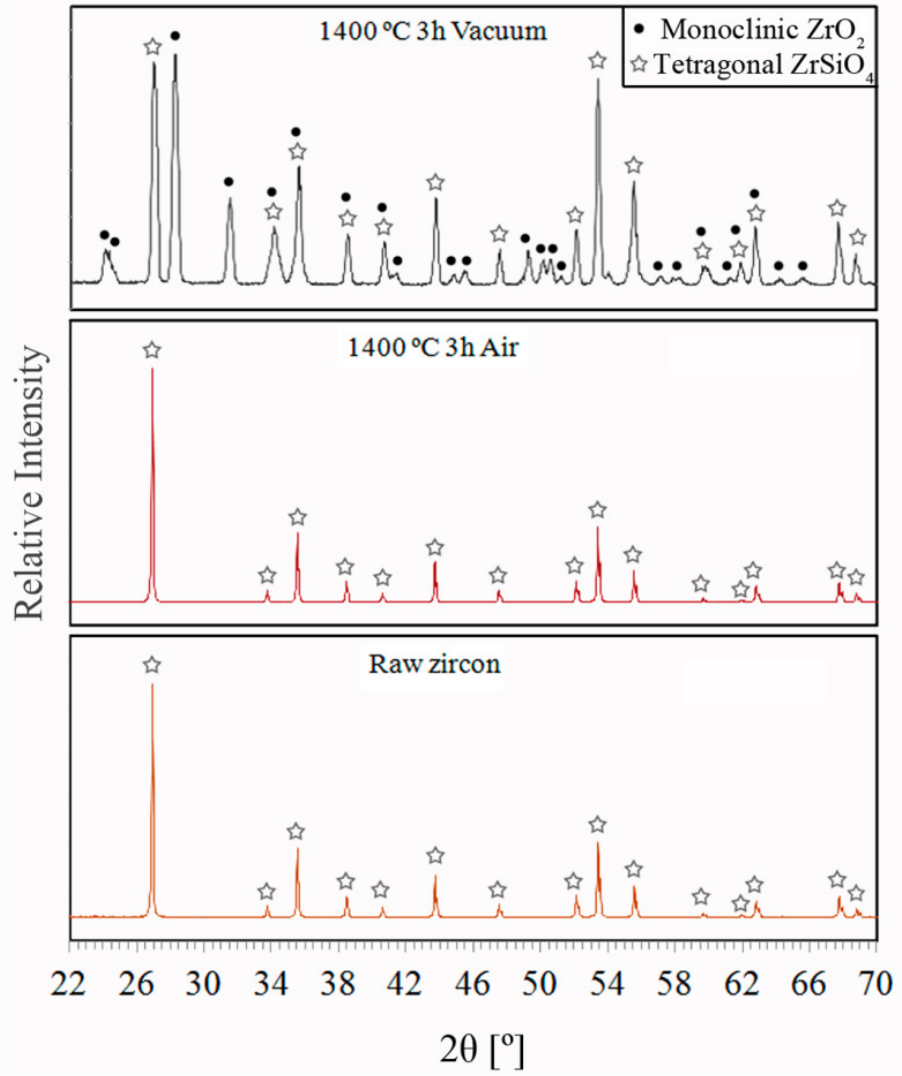

Figure 4. 16 DRX diffractograms of raw zircon powder and some parts sintered at different conditions.

Regarding the micro hardness results, they were similar to those reported by N.M. Rendtorff et. al. [43] who used spark plasma sintering (SPS). By using SPS at 1200 ºC, 1300 ºC, 1400 ºC and 1500 ºc this authors obtained slightly higher values than the measured in this work but with only 10 min of dwell. They achieved 13.9 GPa by using 1300 ºC during 1h which was equivalent to the parts sintering in air at 1400 ºC during 3h.

An important issue is to determine if under the sintering conditions zircon dissociation occurred. Figure 4. 16 shows DRX diffractograms of raw zircon powder and some parts sintered at different conditions. Dissociation occurred at 1400 ºC during 3h and vacuum condition. This was deduced from the identified zirconia peaks alternating with zircon peaks. The presence of silica, which should also result from the zircon dissociation (see Figure 3. 7),

was not clearly observed from the diffractograms. In contrast, the same conditions but using air instead of vacuum seemed to not produce dissociation; the identified peaks corresponded to tetragonal zircon and coincided with original zircon powders peaks. The mechanisms explaining dissociation in vacuum and not in air are unclear. Moreover, a slight bulging of the diffractograms baseline at low angles was observed at 3h, 1500 ºC in air condition. This may indicate the presence of a glassy phase, but this affirmation is also uncertain due to the low magnification of this phenomena. No dissociation was observed at 1200 ºC in vacuum.

Dissociation and shrinkage may explain differences between sintered in vacuum or sintered in air parts' mechanical properties. The occurrence of a possible glassy phase at 1500 ºC in air would explain why the differences between the sintered at 1400 ºC parts mechanical properties are not that obvious, despite of a better shrinkage values.

4.4.1 Invar 36

The main concern with Invar 36 was the possible contamination with carbon or other elements during the MIM process. This would affect the properties of the alloy as explained in 1.7. This concern was based on the organic residual left by the incomplete pyrolysis of CAB in an inert atmosphere like nitrogen. Nitrogen could be also introduced in the Invar 36 lattice at debinding or sintering temperatures and have an effect on the properties [44]. Air atmosphere has shown to be effective in the thermal elimination of CAB. Labrador et al. [45] performed oxidation analysis of wrought Invar in air. They observed an insignificant mass gain of the evaluated specimens below 580 ºC when they were heated at 3 ºC/min. Insignificant in this case means values close to 0.1 g/cm^2 or less. However, the high specific surface of the powder make that this depreciable value could have a real effect on it. Considering the alternative of thermal debinding in air and assuming certain oxidation of the powders, still there is the alternative of using a reductive hydrogen atmosphere during sintering. Other possibility is ignoring the carbon residue left during debinding in an inert atmosphere and expecting that using atmospheres like vacuum or hydrogen had a positive effect in the carbon elimination during the sintering. This was the proposal of Paper 8 that develops an study of the debinding and sintering atmospheres on the physical and mechanical properties of Invar 36 micro parts. Four different debinding-sintering atmospheres combinations were studied: vacuum-vacuum (V-V), air-vacuum (A-V), vacuum-hydrogen (V-H) and air-hydrogen (A-H). Moreover, different temperatures and heating rates were tried. Paper 4 also studies the influence of the solid loading in the mechanical properties. The main conclusion drawn after these works are detailed next.

- Effect of the processing atmospheres on densification and microstructure:

All the debinding and sintering conditions can produce parts with more than 90 % of the Invar 36 density. The parts sintered in hydrogen, independently of the debinding atmosphere, showed densifications of around 98 %. Good results were also obtained in parts with the V-V combination that reached values of around 97 % of densification. The A-V condition turned out to be the most unfavourable condition. These parts show thick oxide layers surrounding

original particles that did not take part on the sintering. These oxides were formed most likely during debinding. The assessment of the oxygen by elemental analysis revealed a 0.57 wt.% of oxygen in contrast with the debinding in vacuum that resulted in just only 0.15 wt.% (very close to the 0.13 wt.% of the raw powders). In V-V conditions some original particles surrounded by oxides were also observed and sporadically occurred in parts sintered in hydrogen. The oxide layer was very thin and sometimes discontinuous in all the conditions except A-V. This fact was associated with the poorer densification and higher porosities observed in A-V compared to the rest of the conditions. The effective and prompt oxides reduction in V-H condition allowed initiating the sintering mechanisms earlier than other conditions, which was reflected in bigger austenite grains. The lowest grain sizes corresponded to A-V condition; the grain growth was limited by the presence of oxides.

- Effect of the solid loading on densification:

Significant differences were observed in the pore quantity and the pore net distribution depending on the solid loading. In the case of the parts loaded with 57.5 vol.%, the pore density was high and heterogeneous with small pores in the range of particle size or bellow, but also with large areas of bigger pores. The pores were sometimes interconnected forming clusters. As long as the solid loading was increased, the pores were smaller, more homogeneously distributed and their density was reduced. Large pores at low solid loading may occur because of the low packing of the particles and the larger voids left after the binder removal in comparison to higher solid loading parts. This is also linked with the higher shrinkage values observed at low solid loadings. These green parts need to reduce more their volumes to obtain densifications close to the high loaded parts. The small rounded pores observed in all the conditions are associated with the final stages of the sintering [46]. At the very early stages of the sintering, the pores have irregular shapes that tend to form spheres due to this geometry is energetically more favourable, i.e. the surface energy is minimised. The pores sizes are consistent with the small and spherical powder particles.

- Effect of the temperature and heating rates:

As expected, the temperature and heating rates have an important effect on the parts densification. This was reflected on the shrinkage values and the residual porosity. The parts sintered at 1000 ºC showed poorer densification and shrinkage in comparison with the parts sintered at 1100 ºC or 1150 ºC. The influence of heating rates was not that evident in the studied parts. Sometimes faster heating rates favoured the sintering and sometimes not. The differences were so small in many cases that they probably felt in the measuring error. Hence, not a clear conclusion could be drawn. The parts processed under A-V conditions had a significant influence on temperature and heating rates in contrast with the rest of the parts. The sintering in this case was hindered by the presence of thick oxide layers surrounding the particles. The low diffusivity trough oxides in comparison with the metal alloy is probably making that temperature and heating rate variations had a noteworthy influence on the sintering.

- Mechanical properties:

The mechanical properties were influenced by the densification but also by the presence of interstitial elements. In Paper 4 a comparison of micro tensile strength of V-V parts at different solid loadings was performed. As the solid loading was increased and thus the densification, the parts showed better ultimate strength results. This occurred until 65 vol.%. The 67.5 vol.% despite of presenting better micro-porosity, they also showed some macro defects that worsen the properties. The densification was not the only responsible of the mechanical properties of Invar 36 micro parts. Interstitial elements like hydrogen or the presence of oxides, may be responsible of the mechanical properties worsening as it is discussed extensively in Paper 8. This was specially evidenced in the reduction of parts elongation in the V-H and A-H conditions most likely due to the hindering effect of interstitial hydrogen on the slip bands movements. An embrittlement effect was also observed in these parts that produced the highest hardness values and less ductile appearance fracture surfaces. The presence of oxides also interferes in the deformation mechanism lowering the parts' elongation.

- Curie's temperatures and coefficients of thermal expansion (CTEs)

The linear CTE values measured vary from 1.5-5 $10^{-6}\cdot ºC^{-1}$ below 150 ºC depending of the processing conditions. Considering the limitations with the accuracy of the measurements (due to small parts and single rod dilatometry measurements) these values coincides to some extent with the low CTE expected for an Invar 36 alloy (1.2 $10^{-6}\cdot ºC^{-1}$ below Curie temperature [47]) . The lowest CTEs along a temperature range from room to 350 ºC were always obtained in the A-V condition. The explanation of this fact is uncertain. It is reasonable to admit that the worsening on the CTE values observed in the sintered in hydrogen parts is consequence of interstitial hydrogen. The presence of interstitial C in the parts processed by V-V combination will not explain the higher CTE values measured in comparison to A-V condition because both resulted in similar levels of carbon after sintering. A combination of smaller grains sizes (that may have a positive effect on producing low CTE [48]) and the iron oxides that have an approximately constant CTE of 10 $10^{-6}\cdot ºC^{-1}$ below 400 ºC [49] may explain the better behaviour of the A-V condition in comparison to V-V in the evaluated temperature range. Both showed similar CTE values until 120 ºC but from then on A-V conditions differentiates from the others. The A-V combination also showed the highest Curie's temperature (≈213 ºC) followed by the V-V condition (199 ºC) and then the A-H (187 ºC) and V-H (186 ºC). These values are far below the 230 ºC Curie point typical of Invar 36 alloy.

4.5 Modelling the rheological behaviour

In this section the capillary rheology results are going to be analysed in detail and the experimental data are going to be related with different viscosity models. These models would typify viscosity variation with processing parameters like shear rate, temperature, solid loading or powder particles characteristics. Commonly, the models relate viscosity with a

single parameter, or maximum two parameters. Therefore, they could not be used alone to completely describe the feedstocks behaviour when e.g. temperature, solid loading and particle size dependence want to be analysed altogether. In this Thesis work a generalised model is proposed and discussed. This global viscosity model takes into account some of the most influencing parameters in feedstocks viscous behaviour. This novel model would be relevant to improve the accuracy and flexibility of currently existing models used in process simulation. It would be probably the first time that so many parameters are tried to be included in a single equation like the one proposed.

To accomplish this objective, this section mainly is going to focus on the Invar 36 and B9 feedstocks rheology, first of all analysing the viscosity dependence with single parameters and then gathering all the results to propose the mentioned model. To validate the models, a non-linear regression methodology, described in 3.3.2, was employed to correlate the model with the experimental points for both INV1 and INV2 feedstocks at different conditions.

4.5.1 Feedstocks' dependence on shear rate

After modelling the flow behaviour with shear rate by different viscosity models, all the feedstocks' behaviours showed a good match when using Cross or Carreau-Yasuda models in the shear rate range between 100 to 10000 s^{-1}. More precisely, the feedstocks better fitted to Cross (Eq.4.2) or Carreau-Yasuda (Eq.4.3) modified models which considered the occurrence of a yield point at low shear rates.

Apparent viscosity results were always compared. In Appendix 1 some attempts of Bagley and Weissenberg-Rabinowitsch corrections were performed for some INV2 feedstocks. Although viscosity and shear rate values were perceptively altered after corrections, the global viscosity behaviour was slightly modified. Hence it was considered that despite real viscosity values would lead to more accurate results, the deviations produced by using apparent viscosity are not sufficiently high to take the time and resources for further corrections. The main objective in any case was evaluating the suitability of different models. These corrections are recommended however if the results are intended to be employed in a real process simulation.

An example of experimental points curve fitting can be seen in Figure 4. 17. In Appendix 1 the Table A1.1 collects the entire Cross and Carreau-Yasuda modified models coefficients resulting from viscosity vs. shear rate experimental data curve fitting of INV1 and INV2 B9 based feedstocks. In all cases three temperatures and five solid loadings were evaluated. The different coefficients were extensively explained in section 1.3.2. As can be deduced from the model fitting evaluation parameter RSS'p and Figure A1.1, Cross and Carreau-Yasuda modified models showed an excellent match in the shear rate interval between 10 to 10000 s^{-1}. This occurred for the majority of the points and conditions evaluated.

$$\boldsymbol{\eta} = \tau_y \cdot \dot{\gamma}^{-1} + \frac{\eta_0}{1+(k_{II}\cdot\dot{\gamma})^{1-n}} \qquad \text{Eq.4.2}$$

$$\eta = \tau_y \cdot \dot{\gamma}^{-1} + \frac{\eta_0}{(1+(\lambda\cdot\dot{\gamma})^{a})^{\frac{1-n}{a}}} \qquad \text{Eq.4.3}$$

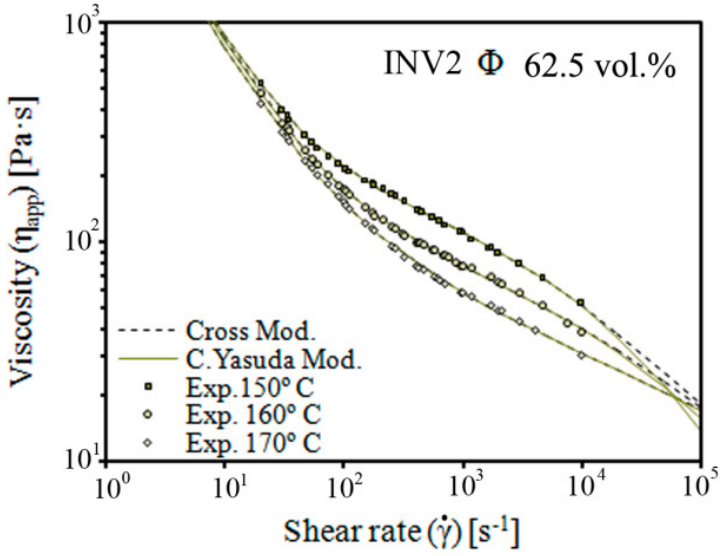

Figure 4. 17 Example of experimental points curve fitting for INV2 and B9 feedstocks at 62.5 vol.% and three different temperatures. The dashed line corresponds to the Cross modified model while the solid line corresponds to a Carreau-Yasuda modified model.

For lower shear rates, plate-plate rheology was performed. However the resulting curves did not follow the behaviour of capillary rheology curves (see Figure 4. 18). These curves were displaced in the viscosity axe to lower values of the viscosity. Moreover they tended to lower or none threshold value compared with the predictions carried out with capillary rheology data. That made doubt of the real existence of a yield point which is a controversial issue between different authors.

Obviously, both viscosity measuring techniques develop different flow modes and measure the viscosity based on different principles. These facts would be responsible of these differences. In high loaded complex binder systems, there is a great part of the bulk that won't suffer from deformation during flow behaviour investigations. The gliding effect linked with the migration of one of the components may be more severe in these systems. If this occurs, the instrument would evaluate the binder component viscous behaviour instead of the whole feedstock behaviour. This would affect more negatively to instruments that uses high areas as plate-plate rotational devices. Furthermore, there is the possible effect of particles agglomeration at the capillary entrance. This effect may explain erratic pressure drops measurements at high shear rates but it may also explain the observation of a yield stress at very low shear rates. The yield point would be the minimum shear stress that is needed to break the collapse at the capillary entrance due to particle agglomeration and to initiate the flow.

Capillary rheology is an inappropriate technique to measure viscosity at low shear rates. Understanding this limitation, in this Thesis work the occurrence of a yield stress is going to be assumed according with the prediction of capillary rheology curves, omitting the plate-plate rheometer results. Some authors believe that capillary rheology results are more reliable than rotational rheology since they reproduce the conditions during injection in a better way.

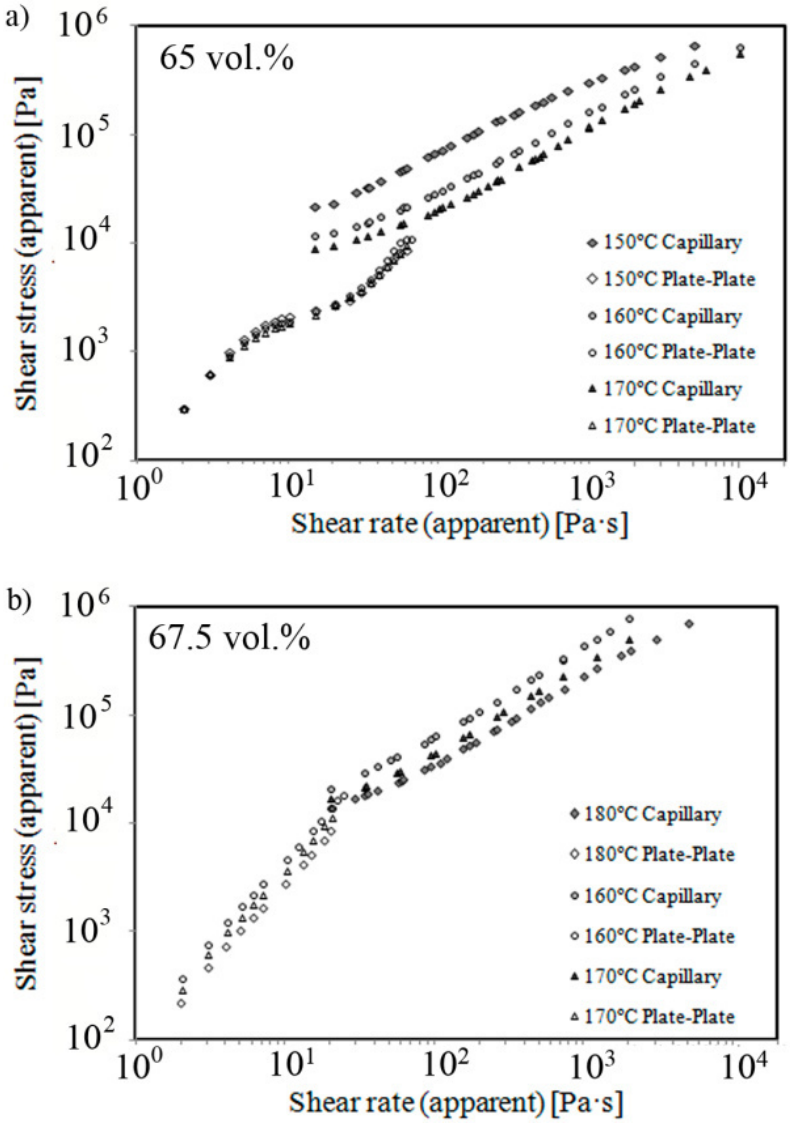

Figure 4. 18 Comparative between capillary rheometer and rotational rheometer measurements for: a) INV2 65 vol.% and b) INV2 67.5 vol.%

Evaluating the Cross (Eq.4.2) and Carreau-Yasuda (Eq.4.3) equations coefficients, they were not completely independent of processing conditions like temperature, solid loading or particle size:

- The yield stress (τ_y) was strongly affected by the solid loading but slightly by the temperature. In a capillary rheometer the yield stress may be related with the accumulation and an obstruction of the powder particles in the capillary entrance which is a narrowing point of the feedstock flow. This issue would explain the solid loading and particle size effect that are dominating over temperature and why this threshold value is not clearly observed in plate-plate rotational rheology.
- The η_o coefficient depends on the solid loading and the particle characteristics, but in this case it is strongly affected by temperature. The η_o has to do with the Newtonian part of the models. This is consistent with the observation of a high temperature

dependence of the viscosity in the middle shear rate range, where the curve shows Newtonian behaviour, but in less extent in the low and high shear rate range.

- The rest of the coefficients behave erratically, and there is not a clear relationship with the parameters T, Φ and PS. Although the curve fitting for both the Cross modified and Carreau-Yasuda modified models resulted in a strong correlation for all the points, it seems that there was a lack of registered points in the high shear rate region. This is apparently the region in which the shift to an abrupt shear thinning behaviour takes place for the studied feedstocks. All the parameters that are related to this shift in the curve behaviour are the ones that present relatively incoherent evolution with different conditions, i.e., they are the coefficients that the algorithm predicts poorly. Sensitivity analysis of the non-linear regression algorithm employed revealed that variations of an adjusting coefficient have a strong influence in all the coefficients except η_0 and $\tau_{y,}$ especially in the case of the Carreau-Yasuda modified model.

After comparing how well all the models matches with experimental data, and saving the controversy of the real existence of a yield point, Cross modified model was selected over Carreau-Yasuda modified model. It has less adjusting coefficients and converged more easily to an optimal solution. Moreover, when working with the Carreau-Yasuda modified model sometimes the algorithm converged to multiple optimal solutions with totally different parameters, leading to the uncertainty of which of the solutions was the most suitable.

4.5.3 Feedstocks' viscosity dependence on temperature

Figure 4. 19 shows an example of the ln (η) versus 1/T plot for INV2 60 vol.% and presents the corresponding lines obtained by the linear regression of the data points. Some representative values of the assessed E_a for different conditions of the shear rate and solid loading are included in Table 4. 7. The multiple correlation coefficients, R^2, reveal a suitable adjustment of the experimental data to the Arrhenius relation in most of the cases.

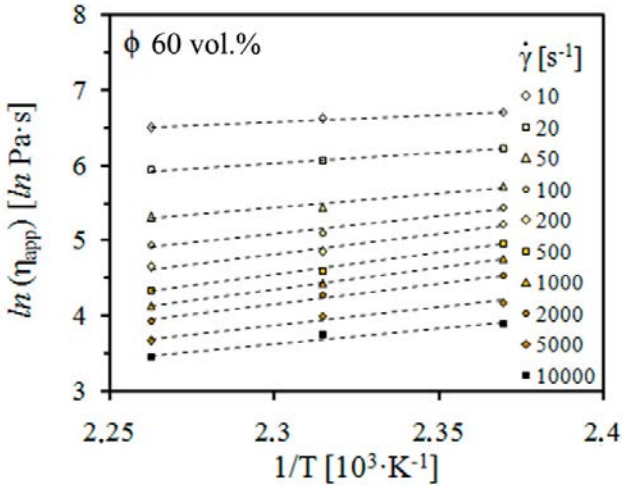

Figure 4. 19 Example of linearization viscosity dependence on temperature for INV2 60 vol.%

Table 4. 7 Values of activation energies for INV1 and INV2 at several conditions

		57.5 vol.%		60 vol.%		62.5 vol.%		65 vol.%		67.5 vol.%	
	$\dot{\gamma}$	E_a	R^2	E_a	R^2	E_a	R^2	E_a	R^2	E_a	R^2
INV2	100	49.0	1.00	29.4	0.98	39.3	0.97	94.5	0.97	48.5	0.99
	1000	60.6	0.99	48.7	0.99	48.1	1.00	73.7	0.98	51.8	0.99
	10000	52.9	0.99	38.0	1.00	34.6	0.96	34.9	0.99	91.2	1.00
INV1	100			50.0	0.99	46.3	0.99	41.6	0.99	78.31	1.00
	1000	-		53.5	1.00	52.1	0.99	51.9	1.00	52.6	0.98
	10000			40.6	0.98	34.2	0.99	32.6	0.99	41.26	1.00

$\dot{\gamma}$ [s^{-1}]; E_a [kJ/mol]

All of the studied feedstocks, independently of solid loading (except INV1 and INV2 for 67.5 vol.% values of activation energy), follow a particular behaviour over the shear rate range from 10 to 10000 s^{-1}. The value of the activation energy is not constant and is dependent on both the shear rate and solid loading parameters. This behaviour is visually described in Figure 4. 20 that uses INV2 feedstocks as a representative example of what occurred with the rest of the feedstocks. It seems that the activation energy values follow a convex curve with a maximum at a certain shear rate.

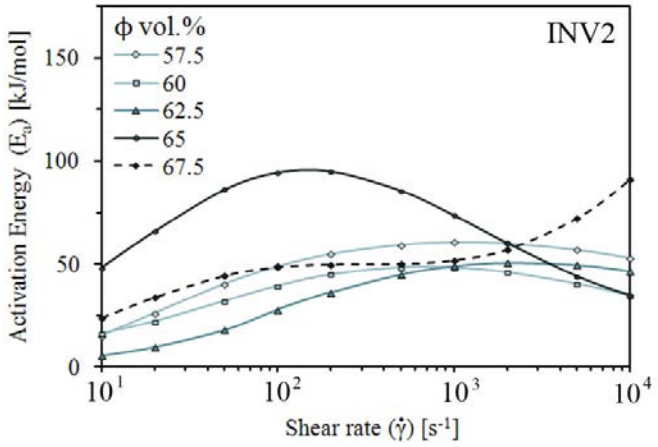

Figure 4. 20 Comparative activation energies for different values of solid loading and shear rates for INV2 feedstocks. Activation Energy is not constant within the shear rate range.

In the low shear rates region, when the shear rate increased the dependence of the viscosity on temperature (activation energy) increased too. Once a maximum is overcome, the value of the activation energy decreases with increasing shear rates. This could be indicative of a change in the viscous behaviour of the melted feedstocks in which the flow is favoured as the shear rate increases, leading to a drop in the activation energy. The reduction of viscosity, which is caused by the pseudoplastic behaviour of these materials at high shear rates, appears to dominate the changes in the viscosity related to the temperature.

For INV2 loaded at 67.5 vol.% feedstocks the value of the activation energy always tends to increase evidencing that they are in a situation close to the critical solid loading.

4.5.4 Feedstocks' viscosity dependence on solid loading

In this section the viscosity dependence on solid loading is analysed. Three different models, which describe relative viscosity (η_{rel}) behaviour with solid loading, are going to be evaluated: 1) Maron and Pierce (M.&P.) (Eq.4.4), Chong modified (Eq.4.5) and Mills modified (Eq.4.6). The ϕ is the solid loading parameter and ϕ_{crit} the critical solid loading coefficient. The rest of the coefficients (A, C, m) are equation coefficients with not clear physical meaning. They regulate the occurrence of the curve inflection or its displacement in the y-axis, i.e., the curve shape. The ϕ_{crit} coefficient determines the vertical asymptote of the curves.

The dependence of the relative viscosity on solid loading of INV and INV2 feedstocks at 160ºC and 1000 s^{-1} is presented in Figure 4. 21. These graphs include the correlation curves of the experimental points adjusted to the different proposed models. These behaviours are representative of what occurs for the rest of the temperatures and shear rate analysed. A summary of some of the non-linear regression coefficients for the different models and conditions investigated and their corresponding evaluating statistics can found in Table 4. 8. An extension of Table 4. 7 can be found in Appendix 1, Table A1.2.

$$\eta_{rel} = A \cdot \left(1 - \frac{\phi}{\phi_{crit}}\right)^{-m} \qquad \text{Eq.4.4}$$

$$\eta_{rel} = A \cdot \left(1 + \frac{C \cdot \frac{\phi}{\phi_{crit}}}{1 - \frac{\phi}{\phi_{crit}}}\right)^{m} \qquad \text{Eq.4.6}$$

$$\eta_{rel} = A \cdot (1 - \phi) \cdot \left(1 - \frac{\phi}{\phi_{crit}}\right)^{-m} \qquad \text{Eq.4.6}$$

It could be said that all the studied models (M.&P., Chong and Mills modified) can properly describe the relationship between relative viscosity and solid loading. Nevertheless, the Maron and Pierce (M.&P.) and Chong modified models produce similar results with a better correlation compared with the results of the Mills modified model considering the statistics employed to evaluate the adjustment (residuals squared sum, RSS, and squared correlation coefficient, R^2).

It should also be noted that these models differ in their predictions of the critical solid loading. The Mills modified model seems to predict more reliable values for the critical solid loading. The Maroon-Pierce (M.&P.) and Chong models tend to predict a ϕ_{crit} close to the highest value of the solid loading measured. For example, in the case of the INV2 150ºC measurements for which no data for 67.5 vol.% were available (because of the limitations of the pressure transducer used), the M.&P. and Chong models predict values for the critical solid loading near 65 vol.%, which was the maximum solid loading measured. This was not the case with the Mills modified model, which predicts critical solid loadings near the 67 vol.% at 150ºC. At 160 ºC and 170 ºC all models predicted a critical solid loading around 68 vol.%. In that cases a maximum of 67.5 vol,% was evaluated. The 68 vol.% value is more

coherent with the 67.5 vol.% estimated by other than capillary rheology methodologies carried out to determine critical solid loading. Hence, independently of temperature, it looked like 68 vol.% is a good estimation of the critical solid loading for INV2 feedstocks.

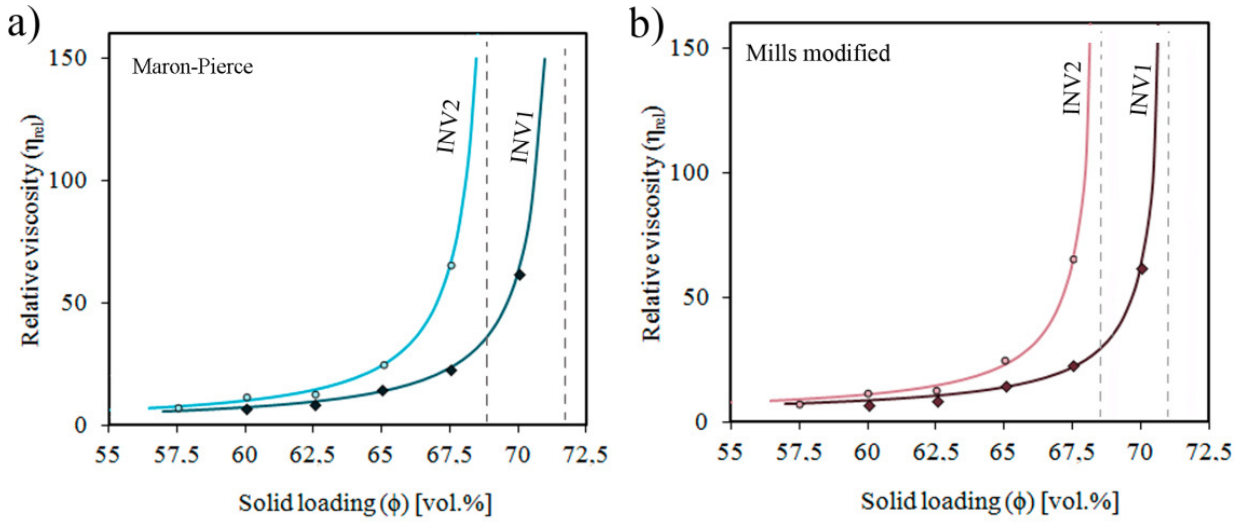

Figure 4. 21 Examples of relative viscosity vs. solid loading non-linear regression adjust to different models: a) Maron-Pierce, b) Mills modified. The experimental data points correspond to 160 ºC, 1000 s^{-1} measurement conditions.

Table 4. 8 The resulting coefficients and corresponding model evaluating statistics of the adjusted models

160 ºC			**1000 s^{-1}**					**10000 s^{-1}**				
Mills	**A**	**m**	**Φ_{crit}**	**R^2**	**RSS**	**A**	**m**	**Φ_{crit}**	**R^2**	**RSS**		
INV1	2.13	0.59	71.2	**0.99**	**6.89**	6.37	4.84	70.6	**1.00**	**1.21**		
INV2	0.07	0.019	68.7	**0.99**	**9.90**	6.04	5.14	68.1	**1.00**	**0.91**		
Chong	**A**	**k**	**m**	**Φ_{crit}**	**R^2**	**RSS**	**A**	**k**	**m**	**Φ_{crit}**	**R^2**	**RSS**
INV1	1.29	0.81	1.09	71.7	**1.00**	**2.09**	1.11	0.52	0.89	70.6	**0.99**	**2.41**
INV2	2.54	0.10	1.20	69.4	**0.99**	**6.00**	1.41	1.64	0.51	67.6	**1.00**	**0.63**
M&P	**A**	**m**	**Φ_{crit}**	**R^2**	**RSS**	**A**	**m**	**Φ_{crit}**	**R^2**	**RSS**		
INV1	0.93	1.15	71.8	**1.00**	**1.72**	1.68	0.55	70.2	**1.00**	**0.44**		
INV2	0.95	1.17	69.4	**0.99**	**6.01**	1.40	0.60	67.8	**1.00**	**0.64**		

The model fitting was recalculated for all models, but in this case avoiding the 67.5 vol.% result at 160ºC and 170ºC. This was made to evaluate the sensitivity of the models to the experimental data used, i.e., if the models still generate reproducible predictions of the critical solid loading after limiting the number of points at solid loading far from the critical point. The results showed that all of the models are sensible of these experimental data elimination. The modification of the points selected had a drastic effect in the M.&P. and Chong modified models, which predicted critical solid loading values quite close to 65 vol% in comparison with the 67.4 vol% obtained with the Mills modified model. Therefore it was concluded that for an accurate prediction of the critical solid loading with a non-linear regression of the

proposed models, an increase in the number of experiments is needed, at least for values near or below the expected critical point.

Regarding the other equation coefficients, the Mills modified models exhibit a relatively abrupt variation in both the m and A parameters with temperature and shear rate compared to the M.&P. model. Nevertheless, these dependences exist in all studied models. It difficult to relate the M.&P., Chong or Mills coefficients with other variables like temperature, shear rate or particle size. The A coefficient might merge the influences of temperature and shear rate on the relative viscosity; thus, this coefficient may be expressed as a sum of other relations that takes into account all the factors. However, the m exponent seems to have neither a simple nor a direct relationship with the other variables influencing viscosity.

The M.&P. properly reproduces the INV1 and INV2 feedstocks behaviours, has less coefficients than e. g. Chong modified model and estimate consistent and reliable values of all equation coefficients. Hence, is going to be chosen as the best model.

4.5.5 Particle size dependence

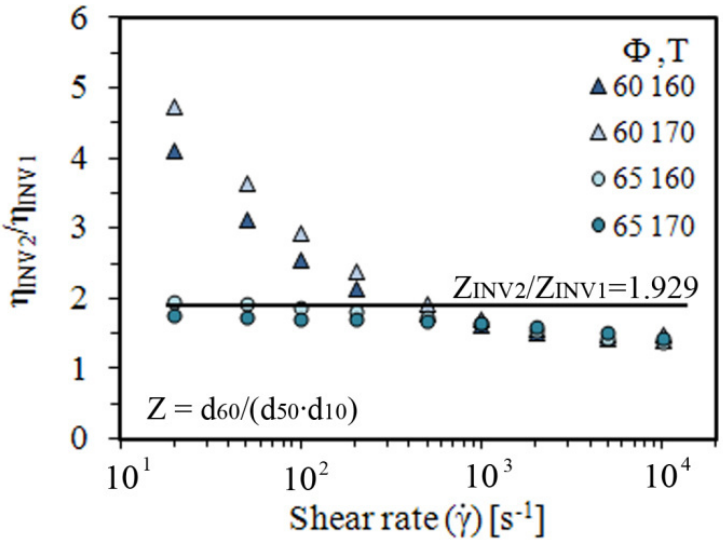

Figure 4. 22 Comparison between INV2 and INV1 feedstock viscosities for 60 vol.% and 65 vol.% and different temperatures. Relationship between INV2 and INV1 particle size distributions is plotted as a straight line.

The particle size has a strong influence on the shear viscosity value. Studying the ratio of the INV2/INV1 viscosities, a relatively constant average factor of 1.69±0.3 was obtained for 160ºC to 170ºC and 65 vol.% conditions, which is very close to the 1.93 value obtained for the ratio of the $D_{60}/D_{10}\cdot D_{50}$ values of both powders. However, for 60 vol.% and for other solid loadings under lower temperature conditions, this result is only valid for the high shear rates region, as can be observed in Figure 4. 22. This result could be explained by considering that at low shear rates, as has been discussed previously, the binder dominates the feedstock viscous behaviour. This dominance is more evident as the solid loading decreases and, thus,

the binder content increases. However, this result also evidence that at high shear rates and high solid loadings, powder particles exert the primary influence on the viscous behaviour.

4.5.6 Global viscosity model

During the rheological study of Invar 36 feedstocks based on CAB and PEG binders, relationships between feedstock's viscosity, shear rate, temperature, solid loading and particle size distribution were established using different models that relate these variables separately. The Cross modified model that introduces yield stress at low shear rates, the Arrhenius model and, i.e., and the M.&P. modified model were demonstrated to be effective for properly linking the shear rate, temperature and solid loading with viscosity respectively.

The works of Lapointe [50] and Senapati [24] propose statistically optimal models utilising a combination of two or three of these parameters for PIM feedstocks. These models assume that the equation coefficients remain essentially constant regardless of temperature, shear rate, solid loading or particle size variation; thus, average values of these coefficients are normally employed. In Kang et al. [51] a combination of Cross and WLF models is proposed to be used in simulations of injection moulding stage. Hence shear rate and temperature viscosity dependence are combined in one model. To the best of the author knowledge, there is not any viscosity model that has successfully included all the viscosity dependant parameters in a single expression. This is the aim of this section: to propose a global viscosity model that could be used as a tool for predicting feedstock's viscous behaviour aiding in the design of PIM processes by computational methods reducing the need of time consuming and costly experimental work.

Through this rheological study, it was also concluded that some of the evaluated coefficients, e.g., the Arrhenius E_a, Cross n, Mills m, etc., are not constant and depend substantially on the temperature, solid loading, shear rate or particle size parameters under certain conditions. However, considering the critical solid loading coefficient, for example, an average value of 68.6 vol.% could be adopted as a good estimation of this coefficient, regardless of shear rate, temperature or particle size. For INV1 and INV2, the E_a coefficient can be considered to be relatively constant in the solid loading range from 60 vol.% to 65 vol.% (around the E_a minimum value) and for the shear rate range above 500 1/s. In this interval, an average value of 42.3 $kJ \cdot mol^{-1} \cdot K^{-1}$ is estimated for both INV1 and INV2. However, the modelled viscosity dependence on shear rate (Cross and Carreau-Yasuda modified models) exhibits coefficients that vary with temperature or solid loading; the relationships with these variables are unclear.

For the feedstocks studied, a global viscosity model resulting from a combination of Cross, Arrhenius and M.&P. models is proposed:

$$\eta(\dot{\gamma}, T, \phi, PS) = \frac{C_u}{D_{50}} \cdot \exp\left(\frac{E_a}{R \cdot T}\right) \cdot \left(\frac{\tau_y}{\dot{\gamma}} + \left(\frac{\eta_0}{(1+k \cdot \dot{\gamma}^n)}\right)\right) \cdot \left(\frac{\phi_{crit}}{\phi_{crit} - \phi}\right)^m \quad \text{Eq.4.7}$$

The coefficients τ_y, η_0, k and n come from the Cross modified viscosity model and represent the yield stress, the cero viscosity and the flow index, respectively. The remaining Eq.4.7 coefficients and variable have been already introduced within this section.

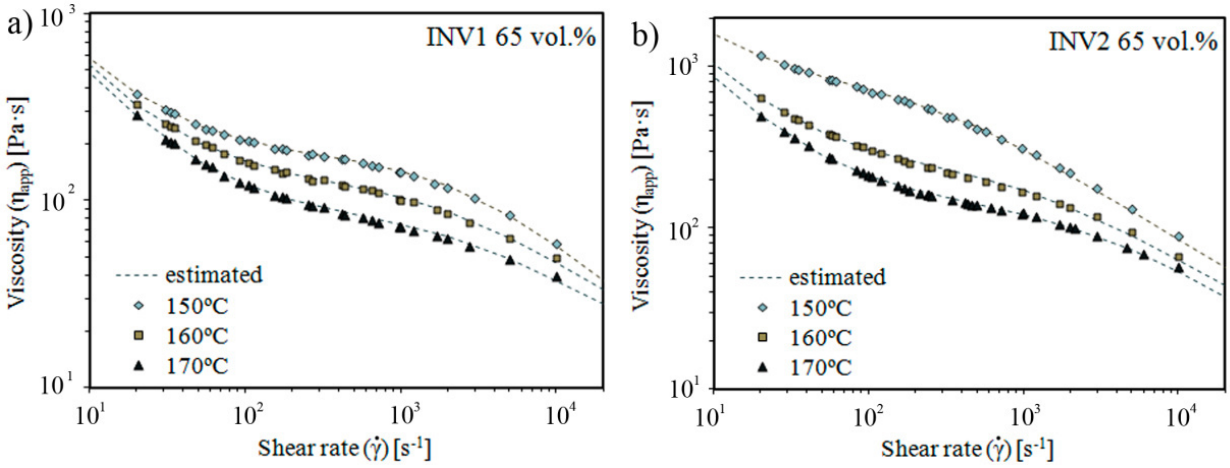

Figure 4. 23 Curves fitting the experimental points for the model described by Eq.4.6. a) INV1 65 vol.% b) INV2 65 vol.%. Markers and dashed lines represent experimental points and the resulting model fitting curves, respectively.

The coefficients τ_y, η_0, n, k and m were defined as variable coefficients, whereas Φ_{crit} and E_a were fixed at constant values. Some representative results are presented in Figure 4. 23 and Table 4. 9 for INV1 and INV2 65 vol.%. As can be observed from Figure 4. 23 and Table 4. 9, the predicted curves exhibit good correlation with the experimental points. Table 4. 10 includes the average values obtained for η_0, m and n for INV2 and different solid loadings at the three studied temperatures.

Table 4. 9 The resulting coefficients after curve fitting with the model described in Eq.4.6 of the experimental points at different temperatures. Φ=65 vol.%, Φcrit=68.6 vol.%, Ea=42.3 kJ/(mol·K).

	C_u/d_{50}	T [K]	η_o [Pa]	n	m	k [s]	τ_y [Pa]	RSS´p	R^2
INV2	**0.41**	**423**	105.49	0.59	0.98	$4.37 \cdot 10^3$	1060.0	0.22	1.00
INV1	**0.21**	**423**	45.55	0.77	0.97	$3.22 \cdot 10^4$	1059.8	0.02	1.00
INV2	**0.41**	**433**	31.35	0.56	0.98	$9.78 \cdot 10^4$	1059.5	0.18	1.00
INV1	**0.21**	**433**	32.68	0.56	0.97	$4.95 \cdot 10^4$	1059.4	0.06	1.00
INV2	**0.41**	**443**	20.71	0.59	0.95	$4.28 \cdot 10^4$	1060.0	0.06	1.00
INV1	**0.21**	**443**	21.76	0.50	0.97	$3.96 \cdot 10^4$	1059.9	0.05	1.00

The coefficients most compliant and sensible to other coefficients variation were η_0 and k. The influence of different variables on Eq.4.6 coefficients is described below:

- The coefficient k has the most erratic and inconsistent behaviour.
- Predicted values of η_0 vary considerably with temperature but appear to be relatively similar regardless of the powder content and type under given conditions. The

dependence of η_0 on temperature in this intermediate shear rate region may be explained by a dominating influence of the binder on the feedstock viscosity. In fact, the values obtained for η_0 are equivalent to those obtained for the binder in this shear rate range; thus, this coefficient may be related to the binder viscosity. Additionally, there is also a relationship of this coefficient with solid loading, as is reflected in Table 4. 10.

- The coefficient m appears to be very stable with regard to temperature and particle size but varies with solid loading. This coefficient does not influence the shape of the curve but does influence the displacement along the viscosity axis.
- The coefficient n is another coefficient that appears to vary slightly with temperature and particle size; however, this variation only occurs at high solid loadings. The n coefficient determines the pseudo-plasticity, i.e., the shear thinning, of the feedstocks; on average, the pseudo-plasticity increases with solid loading.
- Regarding τ_y, this coefficient remains constant under all of the conditions evaluated, with a value of approximately 1060 Pa. This coefficient could be considered as a reference threshold value of the shear stress that must be exceeded if feedstock flow is to occur. This coefficient influences the curve behaviour in the low shear rate region.

Table 4. 10 Average values of ηo, m and n at different solid loading values for INV2

Φ [vol.%]	**η_o [Pa]**	**m**	**n**
57.5	63.8	0.60	0.27
60	21.0	1.30	0.31
62.5	26.0	1.10	0.34
65	52.3	0.97	0.58

It could be concluded that the proposed global viscosity model is suitable to describe the viscous behaviour of CAB and PEG based feedstocks considering several variables at the same time. This kind of model might be also suitable to predict the flow behaviour of other feedstocks if the appropriate coefficients are selected. These coefficients could be obtained by experimental data curve fitting by a non-linear regression. Unfortunately some of these coefficients have shown a markedly dependence on other equation variables. The relationships of all these coefficients with the standard variables ($\dot{\gamma}$,T, Φ,PS) should be further investigated, although these relationships could increase the complexity of the model.

The proposed model has to be validated it in other feedstocks composed of different binders systems or materials. It would be a very interesting and necessary future work to widen its applicability to describe PIM feedstocks' viscous behaviour.

References

1. Victor, A.C. and T.B. Douglas, *Enthalpy and Heat Capacity of Magnesium Oxyde, Zirconium Oxyde and Zirconium Silicate from 0 ºC to 900 ºC*, in *Physical Properties of High Temperature Materials*. 1961, National Bureau of Standards. p. 16.
2. Barreiros, F.M. and M.T. Vieira, *PIM of non-conventional particles.* Ceramics International, 2006. **32**(3): p. 297-302.
3. German, R.M. and A. Bose, *Injection Molding of Metal and Ceramics*. 1997: Metal Powder Industries Federation.
4. Ghodgaonkar, P.G. and U. Sundararaj, *Prediction of dispersed phase drop diameter in polymer blends: The effect of elasticity.* Polymer Engineering and Science, 1996. **36**(12): p. 1656-1665.
5. Li, M.F., R. Xiao, and G. Sun, *Morphology development and size control of poly(trimethylene terephthalate) nanofibers prepared from poly(trimethylene terephthalate)/cellulose acetate butyrate in situ fibrillar composites.* Journal of Materials Science, 2011. **46**(13): p. 4524-4531.
6. Barnes, H.A., *The yield stress - a review or 'pi alpha nu tau alpha rho epsilon iota' - everything flows?* Journal of Non-Newtonian Fluid Mechanics, 1999. **81**(1-2): p. 133-178.
7. Barnes, H.A., *A review of the slip (wall depletion) of polymer-solutions, emulsions and particle suspensions in viscometers - Its cause, character and cure.* Journal of Non-Newtonian Fluid Mechanics, 1995. **56**(3): p. 221-251.
8. Plate, N.A., V.G. Kulichikhin, and R.V. Talroze, *Mesophase polymers in the coming decade - Problems and trends.* Pure and Applied Chemistry, 1991. **63**(7): p. 925-940.
9. Xue, C.-H., et al., *Morphological development of polypropylene in immiscible blends with cellulose acetate butyrate.* Journal of Polymer Research, 2011. **18**(6): p. 1947-1953.
10. Hausnerova, B., *Rheological characterization of powder injection molding compounds.* Polimery, 2010. **55**(1): p. 3-11.
11. Metzner, A.B., *Rheology of suspensions in polymeric liquids.* Journal of Rheology, 1985. **29**(6): p. 739-775.
12. Husband, D.M., N. Aksel, and W. Gleissle, *The existence of static yield stresses in suspensions containing noncolloidal particles.* Journal of Rheology, 1993. **37**(2): p. 215-235.
13. Chuankrerkkul, N., P.F. Messer, and H.A. Davies, *Flow and void formation in powder injection moulding feedstocks made with PEG/PMMA binders Part 1 - Experimental observations.* Powder Metallurgy, 2008. **51**(1): p. 66-71.
14. Kong, X., T. Barriere, and J.C. Gelin, *Determination of critical and optimal powder loadings for 316L fine stainless steel feedstocks for micro-powder injection molding.* Journal of Materials Processing Technology, 2012. **212**(11): p. 2173-2182.
15. Li, Y., L. Li, and K.A. Khalil, *Effect of powder loading on metal injection molding stainless steels.* Journal of Materials Processing Technology, 2007. **183**(2-3): p. 432-439.
16. Contreras, J.M., A. Jimenez-Morales, and J.M. Torralba, *Experimental and theoretical methods for optimal solids loading calculation in MIM feedstocks fabricated from powders with different particle characteristics.* Powder Metallurgy, 2010. **53**(1): p. 34-40.

17. Allaire, F., B.R. Marple, and J. Boulanger, *Injection-molding of submicrometer zirconia - Blend formulation and rheology.* Ceramics International, 1994. **20**(5): p. 319-325.
18. Doyle, C.D., *Estimating thermal stability of experimental polymers by empirical thermogravimetric analysis.* Analytical Chemistry, 1961. **33**(1): p. 77-&.
19. Jin, F.-L. and S.-J. Park, *Thermal properties of epoxy resin/filler hybrid composites.* Polymer Degradation and Stability, 2012. **97**(11): p. 2148-2153.
20. Tarrio-Saaavedra, J., et al., *Effect of silica content on thermal stability of fumed silica/epoxy composites.* Polymer Degradation and Stability, 2008. **93**(12): p. 2133-2137.
21. Aggarwal, G., et al., *Master decomposition curve for binders used in powder injection molding.* Metallurgical and Materials Transactions a-Physical Metallurgy and Materials Science, 2007. **38A**(3): p. 606-614.
22. Atre, S.V., et al., *Master decomposition curve analysis of ethylene vinyl acetate pyrolysis: influence of metal powders.* Powder Metallurgy, 2008. **51**(4): p. 368-375.
23. Enneti, R.K., et al., *Review: Thermal Debinding Process in Particulate Materials Processing.* Materials and Manufacturing Processes, 2012. **27**(2): p. 103-118.
24. Senapati, P.K., B.K. Mishra, and A. Parida, *Modeling of viscosity for power plant ash slurry at higher concentrations: Effect of solids volume fraction, particle size and hydrodynamic interactions.* Powder Technology, 2010. **197**(1-2): p. 1-8.
25. Tanaka, Y., et al., *Active hydroxyl groups on surface oxide film of titanium, 316L stainless steel, and cobalt-chromium-molybdenum alloy and its effect on the immobilization of poly(ethylene glycol).* Materials Transactions, 2008. **49**(4): p. 805-811.
26. Derosa, R.L. and J.A. Trapasso, *Poly(ethylene glycol) interactions with alumina and silica powders determined via DRIFT.* Journal of Materials Science, 2002. **37**(6): p. 1079-1082.
27. Yang, W.W., K.Y. Yang, and M.H. Hon, *Effects of PEG molecular weights on rheological behavior of alumina injection molding feedstocks.* Materials Chemistry and Physics, 2002. **78**(2): p. 416-424.
28. Yang, W.W. and M.H. Hon, *In situ evaluation of dimensional variations during water extraction from alumina injection-moulded parts.* Journal of the European Ceramic Society, 2000. **20**(7): p. 851-858.
29. Yang, W.W., et al., *Solvent debinding mechanism for alumina injection molded compacts with water-soluble binders.* Ceramics International, 2003. **29**(7): p. 745-756.
30. Shi, Y., et al., *TEM and HREM characterization of hot-pressed zircon ceramics.* Materials Letters, 1995. **23**(4-6): p. 247-252.
31. *Zirconium Silicate (ALUKA)*. http://www.kanasindustries.com/, Kanas Industries: Ceramic and glass chemicals catalog.
32. German, R.M., *Sintering theory and practice*. 1996: Willey-Interscience.
33. Ellingham, H.J.T., *Reducibility of oxides and sulfides in metallurgical processes.* Journal of the Society of Chemical Industry (London), 1944. **63**: p. 125-133.
34. Melo, M.F., et al., *Multicomponent toughened ceramic materials obtained by reaction sintering. 3. ZrO_2-Al_2O_3-SiO_2-TiO_2 system.* Journal of Materials Science, 1985. **20**(8): p. 2711-2718.
35. Miranzo, P., et al., *Multicomponent toughened ceramic materials obtained by reaction sintering. 2. ZrO_2-Al_2O_3-SiO_2-MgO system.* Journal of Materials Science, 1985. **20**(8): p. 2702-2710.

36. Pena, P., et al., *Multicomponent toughened ceramic materials obtained by reaction sintering. 1. ZrO_2-Al_2O_3-SiO_2-CaO system.* Journal of Materials Science, 1985. **20**(6): p. 2011-2022.
37. Awaad, M. and S.H. Kenawy, *Sintering of zircon: the role of additives.* British Ceramic Transactions, 2003. **102**(2): p. 69-72.
38. Akdemir, S., E. Ozel, and E. Suvaci, *Stability of zircon pigments in water and diethylene glycol media: The case of turquoise V-ZrSiO4.* Ceramics International, 2013. **39**(2): p. 1909-1915.
39. Cannio, M. and F. Bondioli, *Mechanical activation of raw materials in the synthesis of Fe2O3-ZrSiO4 inclusion pigment.* Journal of the European Ceramic Society, 2012. **32**(3): p. 643-647.
40. Shi, Y., X.X. Huang, and D.S. Yen, *Fabrication of hot-pressed zircon ceramics: Mechanical properties and microstructure.* Ceramics International, 1997. **23**(5): p. 457-462.
41. Munro, R.G., *Evaluated material properties for a sintered alpha-alumina.* Journal of the American Ceramic Society, 1997. **80**(8): p. 1919-1928.
42. Auerkari, P., *Mechanical and physical properties of engineering alumina ceramics*, K. Tirronen, Editor. 1996, Technical Research Centre of Finland.
43. Rendtorff, N.M., et al., *Dense zircon (ZrSiO4) ceramics by high energy ball milling and spark plasma sintering.* Ceramics International, 2012. **38**(3): p. 1793-1799.
44. Rochegude, P. and J. Foct, *Influence of interstitial nitrogen on the thermal-expansion of Fe64-Ni36 alloys.* Scripta Metallurgica Et Materialia, 1992. **27**(3): p. 325-328.
45. Labrador, N. and P. Lefort, *Invar alloy oxidation in air.* Journal De Chimie Physique Et De Physico-Chimie Biologique, 1999. **96**(5): p. 810-829.
46. German, R.M., *Powder Metallurgy of Iron and Steel*. 1998: Wiley-Interscience.
47. Unknown, *Special-Purpose Nickel Alloys*, in *ASM Specialty Hadbook: Nickel, Cobalt and their Alloys*. 2002, ASM International.
48. Bitkulov, I.K., et al., *Effect of severe plastic deformation on the properties of the Fe-36% Ni invar alloy.* Physics of Metals and Metallography, 2006. **102**(1): p. 91-96.
49. Takeda, M., et al., *Physical Properties of Iron-Oxide Scales on Si-Containing Steels at High Temperature.* Materials Transactions, 2009. **50**(9): p. 2242-2246.
50. Lapointe, F., S. Turenne, and B. Julien, *Low viscosity feedstocks for powder injection moulding.* Powder Metallurgy, 2009. **52**(4): p. 338-344.
51. Kang, T.G., et al., *Modeling and simulation of metal injection molding (MIM)*, in *Handbook of metal injection molding*. 2012, Woodhead Publishing Limited. p. 197-234.

Concluding Remarks

5

5.1 Concluding remarks 119

5.1 Concluding remarks

The main conclusions that can be drawn from the whole results obtained during this PhD Thesis work are the following:

Regarding binder system selection and optimization:

- It was possible to satisfactorily manufacture, by the powder injection moulding (PIM) route, zircon and Invar 36 components using novel binder systems based on cellulose acetate butyrate (CAB) and polyethylene glycol (PEG). These binder systems showed improved characteristics when compared to classical polyolefin based binders, most likely due to a better compatibility of all feedstock components and thus due to a better processability.
- The influence of the butyryl, acetyl and hydroxyl groups on different issues of the PIM process was analysed and an optimal formulation proposed. This formulation consisted of a 40 vol.% of different CABs and of different molecular weight PEGs. To that respect it can be concluded that:
  - The higher the butyryl content on CAB was, the lower the viscosity of the resulting binders and feedstocks and the higher the powder solid loading admissible. On the contrary, the capacity to maintain the component geometry during solvent extraction due to swelling was lesser than other CAB types.
  - The higher the acetyl content on CAB was, the highest the viscosity of the resulting binder and feedstocks. Acceptable values of viscosities were obtained however that allowed for the injection of the feedstocks even though employing low pressure. Moreover these types of CAB retained the part geometry during solvent extraction in a better way than other CAB types.
  - A high hydroxyl content probably make the binder more compatible with the powders but this group of CABs showed other drawbacks during the injection process. In particular, it is worth to remark the long time required to rigidify the component during the cooling stage of the injection. This commonly resulted on component distortion during extraction.
  - A small content of low molecular weight PEG not only aided to reduce feedstocks viscosity, improving the injection process, but also allowed for a better solvent debinding reducing the swelling and the defects resulting from the process.

Regarding evaluation of feedstocks' characteristics

- A thorough rheology study was carried out for all the feedstocks analysing their viscous behaviour as a function of shear rate, temperature, solid loading and powder characteristics. The resulting viscosity curves were interpreted from a physical standpoint and adjusted to different existing models. Finally a novel viscosity model that incorporates the multiple variables affecting feedstock viscosity was proposed and its efficacy to reproduce feedstocks' viscous behaviour experimentally demonstrated.

- The optimal solid loading, the critical solid loading and the homogeneity of the selected feedstocks were evaluated by torque and capillary rheology and contrasted by other methods like pycnometer density and scanning electron microscope (SEM) inspections. To that respect it can be concluded that:
  - As expected, the powder characteristics (the intrinsic nature of the powder, it morphology, its particle size distribution, etc.) affected the optimal and critical solid loading due to the different packing capacities, specific surface or particle-particle contact points.
  - The CAB based feedstocks were quite homogeneous at compositions near the optimal independently of the powder types. A better homogeneity compared to polyolefin based feedstock lead to a better final specimen properties.
  - High optimal solid loadings were obtained with all the powders and the optimised CAB based compositions: a meritorious 57.5 vol.% for the irregular shape zircon powders, a remarkable 65 vol.% for small and spherical Invar 36 powders special for micro powder injection moulding, and around 70 vol.% for conventional PIM-size spherical Invar 36 powders.
- A novel method was proposed to evaluate the efficacy and the energy involved during the mixing process of PIM feedstocks. It consisted on monitoring the evolution of the feedstock's temperature and totalized torque during mixing. Thereby the inter-particle friction and the processing energy can be roughly estimated as well as the capacity of the binder to incorporate and lubricate the powders. This method resulted very helpful to compare different feedstocks and added an extra value to the torque rheology results.

Regarding injection processes optimization

- Different injection processes (low pressure, high pressure and micro injection moulding) using optimised CAB based feedstocks were evaluated. The most adequate injection parameters were determined in each case. The injected components showed good mould cavity shape reproducibility and green strength with apparently a flawless appearance even tough for the micro components.

Regarding solvent and thermal debinding studies

- Solvent extraction in water of the PEG was evaluated at different temperatures. Swelling was detected in all binder systems and feedstock independently of the debinding temperature; sometimes swelling led to delamination and cracks formation. Adding 40 vol.% of CABs (instead of 30 vol.%), selecting preferentially high acetyl content CAB and incorporating low molecular weight PEGs mitigated the effects of swelling during solvent debinding.
- Thermo-gravimetric studies were conducted to determine processing temperatures, thermal stability and degradation kinetics of different binders and feedstocks. From these studies it can be concluded that:

- CABs are less thermally stable than PEG or polyolefin. However they need an oxidising atmosphere to completely degrade before temperatures at which there is a risk of carbon contamination.
- There is a certain affinity between the CABs and PEG and between these compounds and the powders.
- The powders may be exerting a catalytic effect on the thermal degradation of the binder.
- A relationship between some thermal stability and degradation kinetics parameters and the occurrence of the optimal compositions was demonstrated for the first time. This finding might be very helpful since it would mean a novel method that could substitute (or be used together with) conventional methodologies to determine the optimal powder volume fraction.

Regarding final components' properties

- Zircon brown components were subjected to different sintering cycles where temperature, time and sintering atmosphere were varied. Mechanical properties were then tested:
  - The CAB based sintered components showed good shape retention in contrast to polyolefin based components that distorted because of feedstocks heterogeneities.
  - Zircon specimens showed lower flexural strength values compared to the typical reported in literature independently of the sintering process conditions. Not completely full-dense parts were obtained and in some cases zircon disaggregation into zirconia and silica was detected. These facts would explain the bending test results.
  - The best properties were obtained in parts sintered in air at 1500 ºC during 3h and by using a high butyryl CAB based feedstock loaded with 60 vol.% of zircon powder. Low feedstock viscosity probably helped to obtain improved properties of the green component compared to other systems. Moreover, higher solid loadings produced less component shrinkage during sintering. Altogether would explain these good results.
- A study of the effect of different thermal debinding and sintering atmospheres combination and the effect of temperature and heating rate on the densification and the physical and mechanical properties of Invar 36 components was carried out:
  - In general typical mechanical and physical properties of an Invar 36 alloy were somewhat reproduced by using PIM route.
  - All the atmospheres combination produced similar levels of carbon content on the sintered component. This carbon content was higher than the measured in the raw powders but still low enough to be within the acceptable levels for an Invar 36 alloy.
  - Hydrogen sintered atmosphere demonstrated to be an effective media to reduce oxides originally present in the Invar 36 powders or formed during thermal debinding in air. However, contamination with hydrogen most probably occurred as

deduced from the reduction of mechanical properties and from the increase of the coefficient of thermal expansion.

- A combination of vacuum debinding and sintering atmospheres and sintering temperatures of 1100 or 1150 ºC has demonstrated to be effective to produce high dense parts with acceptable physical and mechanical properties.

Final general conclusions

During this PhD Thesis work the feasibility of using a cellulose derivative thermoplastic polymer, the CAB, in feedstocks compositions of different materials and in different PIM processes was confirmed. These feedstocks have demonstrated to be a novel, attractive and competitive alternative to conventional polyolefin based feedstocks. They incorporate an environmental friendly perspective in the burn out of the CAB that, to some extent, it could be considered to generate a net zero CO_2 emissions to the atmosphere. CAB was successfully combined with PEG, which can be removed by a solvent debinding in sound and inexpensive water media. This polymers combination has also demonstrated to have a good affinity by ceramic zircon powders and metallic Invar 36 powders, which resulted in a better homogeneity of the feedstock, a better processability and thus in a better final properties.

Future Perspectives

6

6.1 Future perspectives 125

6.1 Future perspectives

During this PhD Thesis a thorough work was carried out and many interesting results were obtained. However, some of the results brought up new challenges and questions that make thinking on continuing researching. The author proposes the following topics and tasks that would be interesting to be considered after the current works:

- Although the use of the selected binder systems resulted in good processability and final par properties, there are still some aspects in the binder formulation that are susceptible of being investigated and improved. This work has mainly focused on determining the effect of side groups in CAB polymers and according with these results a binder formulation was designed. The effect of the molecular weight, both in the case of the CABs and PEG, was scarcely or not at all investigated. Furthermore, injection temperatures were close to the onset decomposition temperature of the feedstock. The use of antioxidant or degradation retardant agents must be studied. It is expected that the addition of these substances would allow for increasing the injection temperature avoiding the degradation of the feedstocks' properties and thus improving their recyclability. To the date some works are being carried out regarding these concerns.

- The family of thermoplastic polysaccharides and of sound polymers derived from natural sources is not limited to the CAB family. Following the main argument of this thesis work of creating more sound binder systems, other polymers within the thermoplastic polysaccharides, like thermoplastic starch or other cellulose esters or cellulose derivatives might be evaluated.

- Many of the results obtained during this thesis work are valuable to conduct computer simulation trials of different PIM process stages of the studied feedstocks. Capillary rheology data could be used to simulate mixing and injection processes complementing or improving the optimisation carried out with the experimental work. Studies of the decomposition kinetics could be implemented to determine master decomposition curves that might be used along with shrinkage results to simulate the degradation at different conditions and of different geometry parts. Solvent debinding and sintering results are also susceptible to be used in process simulation. Therefore, it would be interesting to make the most of the current results and implement them in computational modelling and simulation. Nevertheless, to accomplish this objective further experimental work has to be performed, e.g. determining the heat capacity or thermal conductivity of the feedstocks. These studies are currently planned and have begun to be developed.

- The proposed rheological model was suitable to describe several CAB based Invar 36 feedstocks viscous behaviour. Nevertheless it would be interesting to test this model

in other feedstocks type using different binder systems or materials to validate the model and widen its applicability.

- The major effort of this thesis work was oriented to study the feedstocks characteristics. Although sintering studies were conducted and final part properties were evaluated there are still possibilities in studying, e.g. other sintering conditions and atmospheres. Microwave assisted or spark plasma sintering methods probably would reduce remaining porosity of zircon parts increasing their mechanical properties. Invar green parts could be subjected to different debinding and sintering cycles in order to improve the low coefficient of thermal expansion results and mechanical properties. For example a process involving a thermal debinding in hydrogen rich atmospheres like argon-hydrogen followed by a sintering in vacuum would get rid of the carbon and oxygen problem, minimising the pernicious effect of hydrogen in the Invar 36 properties.

- It would be also interesting to study the viability of performing a two colours injection moulding of invar and zircon as they presumably have similar coefficients of thermal expansion. The current rheological studies can be taken into advantage for optimising the injection. The differences in the shrinkage of both types of feedstocks may be solved by regulating the solid loading content. Wettability tests and interfaces evaluation should be performed to study the compatibility between zircon and invar materials.

Appendix 1

A1

Rheological models and data fitting 129

Corrections of the apparent shear stress and viscosity values 131

References 134

Rheological models and data fitting

Table A1.1 Some model fitting parameters after modelling of the shear viscosity dependence on shear rate data of Invar 36 feedstocks. Two models are compared: Cross and Carreau-Yasuda modified.

Carreau-Yasuda Modified												
T	**η_0**	**τ_y**	**k**	**a**	**1-n**	**RSS'$_P$**	**η_0**	**τ_y**	**k**	**a**	**1-n**	**RSS'$_P$**
	INV1 57.5 vol.%						**INV2 57.5 vol.%**					
150	-	-	-	-	-	-	138	917	$1.2\cdot10^{-2}$	0.32	0.50	0.52
160	-	-	-	-	-	-	76	1225	$4.8\cdot10^{-3}$	0.37	0.65	0.69
170	-	-	-	-	-	-	91	1218	$8.5\cdot10^{-2}$	0.21	0.35	0.13
	INV1 60 vol.%						**INV2 60 vol.%**					
150	88	1282	$6.1\cdot10^{-6}$	1.09	0.33	0.90	243	6159	$3.4\cdot10^{-3}$	0.43	0.61	0.78
160	66	1093	$1.1\cdot10^{-3}$	0.41	1.35	0.14	111	6407	$3.2\cdot10^{-4}$	0.67	0.41	0.56
170	45	969	$4.5\cdot10^{-4}$	0.72	0.30	0.15	164	5573	$2.7\cdot10^{-2}$	0.25	0.62	0.45
	INV1 62.5 vol.%						**INV2 62.5 vol.%**					
150	95	2133	$2.1\cdot10^{-4}$	0.86	0.76	0.23	222	6952	$1.9\cdot10^{-3}$	0.30	0.53	0.88
160	83	2209	$1.5\cdot10^{-5}$	0.96	0.63	0.36	200	7000	$5.0\cdot10^{-3}$	0.20	0.58	0.66
170	78	1998	$5.7\cdot10^{-6}$	0.57	0.71	0.40	341	6482	$0.2\cdot10^{0}$	0.25	0.67	0.90
	INV1 65 vol.%						**INV2 65 vol.%**					
150	177	4056	$1.2\cdot10^{-5}$	0.83	0.91	0.54	815	8279	$2.2\cdot10^{-5}$	0.88	0.58	2.17
160	131	4056	$9.4\cdot10^{-5}$	0.70	0.68	0.56	288	7849	$1.1\cdot10^{-3}$	0.47	0.87	2.23
170	88	4014	$1.8\cdot10^{-4}$	0.60	0.99	0.36	157	6938	$2.3\cdot10^{-4}$	0.60	0.79	1.44
	INV1 67.5 vol.%						**INV2 67.5 vol.%***					
150	324	6850	$1.4\cdot10^{-4}$	0.67	0.59	0.64	1300	8800	$1.2\cdot10^{-1}$	0.17	0.22	1.61
160	195	1798	$5.5\cdot10^{-6}$	0.83	1.25	1.82	415	9634	$6.7\cdot10^{-4}$	0.50	0.45	1.15
170	119	1233	$1.7\cdot10^{-6}$	0.89	1.85	0.54	287	8847	$1.9\cdot10^{-5}$	0.70	1.44	2.49

Cross Modified										
T	**η_0**	**τ_y**	**k**	**1-n**	**RSS'$_P$**	**η_0**	**τ_y**	**k**	**1-n**	**RSS'$_P$**
	INV1 57.5 vol.%						**INV2 57.5 vol.%**			
150	-	-	-	-	-	-	1099	$4.1\cdot10^{-4}$	0.47	0.34
160	-	-	-	-	-	-	1272	$2.4\cdot10^{-4}$	0.47	0.73
170	-	-	-	-	-	-	1229	$2.6\cdot10^{-4}$	0.30	0.11
	INV1 60 vol.%						**INV2 60 vol.%**			
150	92	1324	$2.1\cdot10^{-4}$	0.64	1.03	218	6218	$9.5\cdot10^{-4}$	0.55	0.45
160	60	1173	$1.2\cdot10^{-4}$	0.60	0.06	110	6468	$2.2\cdot10^{-4}$	0.59	0.76
170	46	980	$1.5\cdot10^{-4}$	0.53	0.17	119	5650	$1.2\cdot10^{-3}$	0.42	0.38
	INV1 62.5 vol.%						**INV2 62.5 vol.%**			
150	93	2210	$3.2\cdot10^{-4}$	0.75	0.56	182	7065	$6.1\cdot10^{-4}$	0.53	0.57
160	87	2023	$2.7\cdot10^{-4}$	0.64	0.72	128	7394	$6.3\cdot10^{-4}$	0.44	0.52
170	74	1925	$2.3\cdot10^{-4}$	0.81	0.24	342	6483	$0.6\cdot10^{0}$	0.27	0.91
	INV1 65 vol.%						**INV2 65 vol.%**			
150	176	4020	$2.3\cdot10^{-4}$	0.86	0.46	879	7958	$2.6\cdot10^{-3}$	0.69	1.79
160	131	4036	$2.2\cdot10^{-4}$	0.71	0.55	252	7996	$4.6\cdot10^{-4}$	0.69	2.12
170	87	4033	$1.5\cdot10^{-4}$	0.67	0.33	146	7183	$2.0\cdot10^{-4}$	0.76	1.27
	INV1 67.5 vol.%						**INV2 67.5 vol.%***			
150	331	6742	$4.7\cdot10^{-4}$	0.62	0.68	1264	8732	$2.9\cdot10^{-2}$	0.19	1.60
160	191	1793	$1.9\cdot10^{-4}$	1.05	0.46	410	9663	$1.5\cdot10^{-4}$	0.52	1.18
170	117	1222	$1.2\cdot10^{-4}$	1.05	0.33	280	8990	$1.9\cdot10^{-4}$	0.84	2.26

T → [ºC]; η_0 → [Pa·s]; τ_y → [Pa]; k_{II}, λ → [s]; * → measured at 160, 170 and 180 ºC

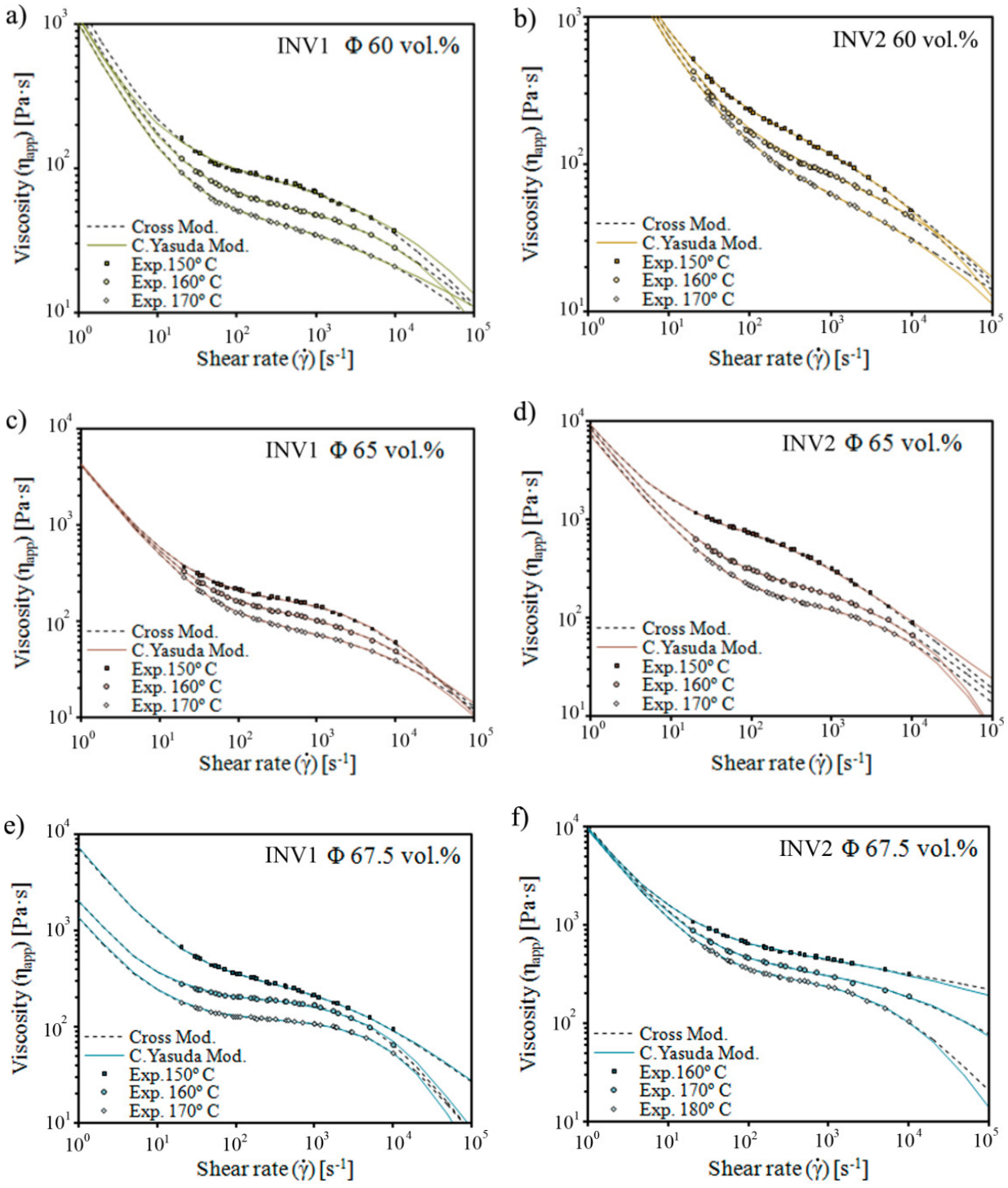

Figure A1. 1 Viscosity vs. shear rate curves of different feedstock and at different solid loadings and temperatures. The markers correspond to experimental data while the lines correspond to fitting model curves to the experimental data. (a) INV1 60 vol.%, (b) INV2 60 vol.%, (c) INV1 65 vol.%, (d) INV2 65 vol.%, (e) INV1 67.5 vol.%, (f) INV2 67.5 vol.%.

Table A1 2 Some model fitting parameters after modelling of the relative viscosity dependence with solid loading data of Invar 36 feedstocks. Three models are compared: Mills modified, Chong modified and Maron and Pierce (M.&P.).

INV1			**1000 s^{-1}**					**10000 s^{-1}**				
Mills	**A**		**m**	**Φ_{crit}**	**R^2**	**RSS**	**A**		**m**	**Φ_{crit}**	**R^2**	**RSS**
150	0.53		0.16	71.1	**0.99**	**3.08**	3.05		2.44	70.6	**1.00**	**0.05**
160	2.12		0.59	71.2	**0.99**	**6.89**	6.37		4.84	70.6	**1.00**	**1.21**
170	2.14		0.54	71.3	**0.99**	**6.67**	6.21		4.55	70.9	**0.99**	**6.81**
Chong	**A**	**k**	**m**	**Φ_{crit}**	**R^2**	**RSS**	**A**	**k**	**m**	**Φ_{crit}**	**R^2**	**RSS**
150	1.44	0.88	1.13	71.2	**1.00**	**1.91**	2.06	0.01	1.41	70.1	**1.00**	**0.08**
160	1.29	0.81	1.09	71.7	**1.00**	**2.09**	1.11	0.52	0.88	70.6	**0.99**	**2.41**
170	1.33	1.00	1.02	71.7	**1.00**	**1.95**	3.05	0.10	1.30	70.9	**1.00**	**1.38**
M&P	**A**		**m**	**Φ_{crit}**	**R^2**	**RSS**	**A**		**m**	**Φ_{crit}**	**R^2**	**RSS**
150	1.14		099	71.3	**1.00**	**1.72**	0.91		0.91	70.3	**1.00**	**0.01**
160	0.93		1.15	71.9	**1.00**	**1.72**	1.69		0.55	70.2	**0.99**	**0.44**
170	1.05		1.14	71.9	**1.00**	**1.46**	1.72		0.61	70.3	**0.99**	**0.88**
INV2			**1000 s^{-1}**					**10000 s^{-1}**				
Mills	**A**		**m**	**Φ_{crit}**	**R^2**	**RSS**	**A**		**m**	**Φ_{crit}**	**R^2**	**RSS**
150	0.02		0.003	66.8	**0.99**	**6.95**	19.45		14.00	67.1	**0.98**	**1.34**
160	0.07		0.019	68.7	**0.99**	**9.90**	6.04		5.14	68.1	**1.00**	**0.91**
170	0.01		0.004	68.8	**0.99**	**14.86**	5.22		3.28	68.4	**0.99**	**2.10**
Chong	**A**	**k**	**m**	**Φ_{crit}**	**R^2**	**RSS**	**A**	**k**	**m**	**Φ_{crit}**	**R^2**	**RSS**
150	4.17	1.35	0.58	65.7	**0.99**	**2.61**	4.37	2.80	0.23	65.3	**0.99**	**0.60**
160	2.54	0.10	1.20	69.4	**0.99**	**6.00**	1.41	1.64	0.51	67.6	**1.00**	**0.63**
170	0.73	1.42	1.17	69.5	**0.99**	**9.33**	0.96	1.48	0.73	68.1	**0.99**	**1.98**
M&P	**A**		**m**	**Φ_{crit}**	**R^2**	**RSS**	**A**		**m**	**Φ_{crit}**	**R^2**	**RSS**
150	4.72		0.59	65.7	**0.99**	**2.66**	6.41		0.18	65.1	**0.96**	**2.42**
160	0.95		1.17	69.4	**0.99**	**6.01**	1.40		0.60	67.8	**1.00**	**0.64**
170	0.95		1.22	69.6	**0.99**	**9.32**	1.18		0.75	68.1	**0.99**	**1.97**

Corrections of the apparent shear stress and viscosity values

One important assumption made in the derivation of the equations for a capillary rheometer is that a stable laminar flow is achieved along the capillary. This is not necessarily true for the entire pathway through the capillary and will depend on the fluid tested. An L/D ratio above 30 is typically accepted as a sufficiently high value for the complete development of a laminar steady state flow along the major part of the capillary. Before knowing the real viscous behaviour of a feedstock, Newtonian behaviour is assumed to calculate an apparent value for the shear rate ($\dot{\gamma}_{app}$), shear stress (τ_{app}) and, by extension, the shear viscosity (η_{app}) variables following equations Eq.A1.1 to Eq.A1.3:

$$\dot{\gamma}_{app} = \frac{4 \cdot Q}{\pi \cdot R^3} \qquad \text{Eq.A1.1}$$

$$\boldsymbol{\tau}_{app} = \frac{R \cdot \Delta P_{tot}}{2 \cdot L} \qquad \text{Eq.A1.2}$$

$$\boldsymbol{\eta}_{app} = \frac{\tau_{app}}{\dot{\gamma}_{app}} \qquad \text{Eq.A1.3}$$

where R is the capillary radius. The variable Q represents the volumetric caudal or flow rate through the capillary. Unfortunately, the melted feedstocks usually present more complex non-Newtonian behaviours; thus, the above $\dot{\gamma}_{app}$ expression is not entirely valid. Furthermore, a drawback arises while measuring ΔP_{tot}. As a consequence of the capillary size limitations, ΔP_{tot} is obtained by a sole pressure transducer situated not along the capillary to measure real pressure drop at the capillary but at the entrance of the capillary. Thereby, ΔP_{tot} is not only caused by the resistance of the melt against the forced flow through the capillary but also to a large extent by other factors. One commonly dominant factor occurs at the capillary entrance where feedstock flow is forced to pass through. The elastic properties of the viscoelastic melt temporally absorb and elastically store some of the energy of the extrusion pressure exerted by the piston. This energy is recovered at the capillary exit without having participated in the activation of the flow. Thus, an overpressure is registered at the transducer. However, this drawback may also be an advantage; if this elongational contribution to the pressure (ΔP_e) could be isolated and separated from the capillary shear contribution (ΔP_s), it would allow not only the correction of shear stresses but also the determination of extensional (or elongational) viscosity (η_e). In fact, a capillary rheometer is commonly used as an indirect method to measure η_e in polymers [1]. One simple way of proceeding with the shear rate and shear stress corrections consists of first correcting τ_{app} with Bagley's method and then correcting $\dot{\gamma}_{app}$ with the Weissenberg-Rabinowitsch correction. Bagley's method consists of measuring ΔP_{tot} with several capillaries of different L/D ratios with equal diameters. At least three different ratios per measuring condition are recommended because although the normal behaviour of ΔP_{tot} versus L/D is linear due to pressure effects, it does not necessarily always behave linearly. An acceptable linear approach can be made using only two capillaries if one of them has a ratio L/D<1, which is close to the idealised L/D=0[2]. For this ideal condition, the capillary contribution to the total measured pressure is inexistent and, thus, ΔP_e can be estimated. Then, the value of ΔP_s can be calculated from Eq.A1.4:

$$\Delta P_{tot} = \Delta P_e + \Delta P_s \qquad \text{Eq.A1.4}$$

After knowing ΔP_s and applying the Weissenberg-Rabinowitsch equations, the true shear rate, shear stress and, by extension, true shear viscosity can be calculated with Eq.A1.5 to Eq.A1.7:

$$\tau_s = \frac{R \cdot \Delta P_s}{2 \cdot L} \qquad \text{Eq.A1.5}$$

$$\dot{\gamma}_s = \frac{\dot{\gamma}_{app}}{4} \cdot \left(3 + \frac{\partial \lg \dot{\gamma}_{app}}{\partial \lg \tau_s}\right) \qquad \text{Eq.A1.6}$$

$$\eta_s = \frac{\tau_s}{\dot{\gamma}_s} \qquad \text{Eq.A1.7}$$

Although this work demonstrates that the experimental data can be adjusted to different mathematical models that are not excessively complex, when the Weissenberg-Rabinowitsch correction is applied Eq.A1.6 to simplify the assessment of the derivative term, a polynomial regression is made for the representing points curve lg $\dot{\gamma}_{app}$ versus lg τ_s, with a third-order polynomial selected.

Some examples of the real viscosity vs. real shear rate and real shear stress vs. real shear rate after applying Bagley and Weissenberg-Rabinowitsch are shown in Figure A1. 2.

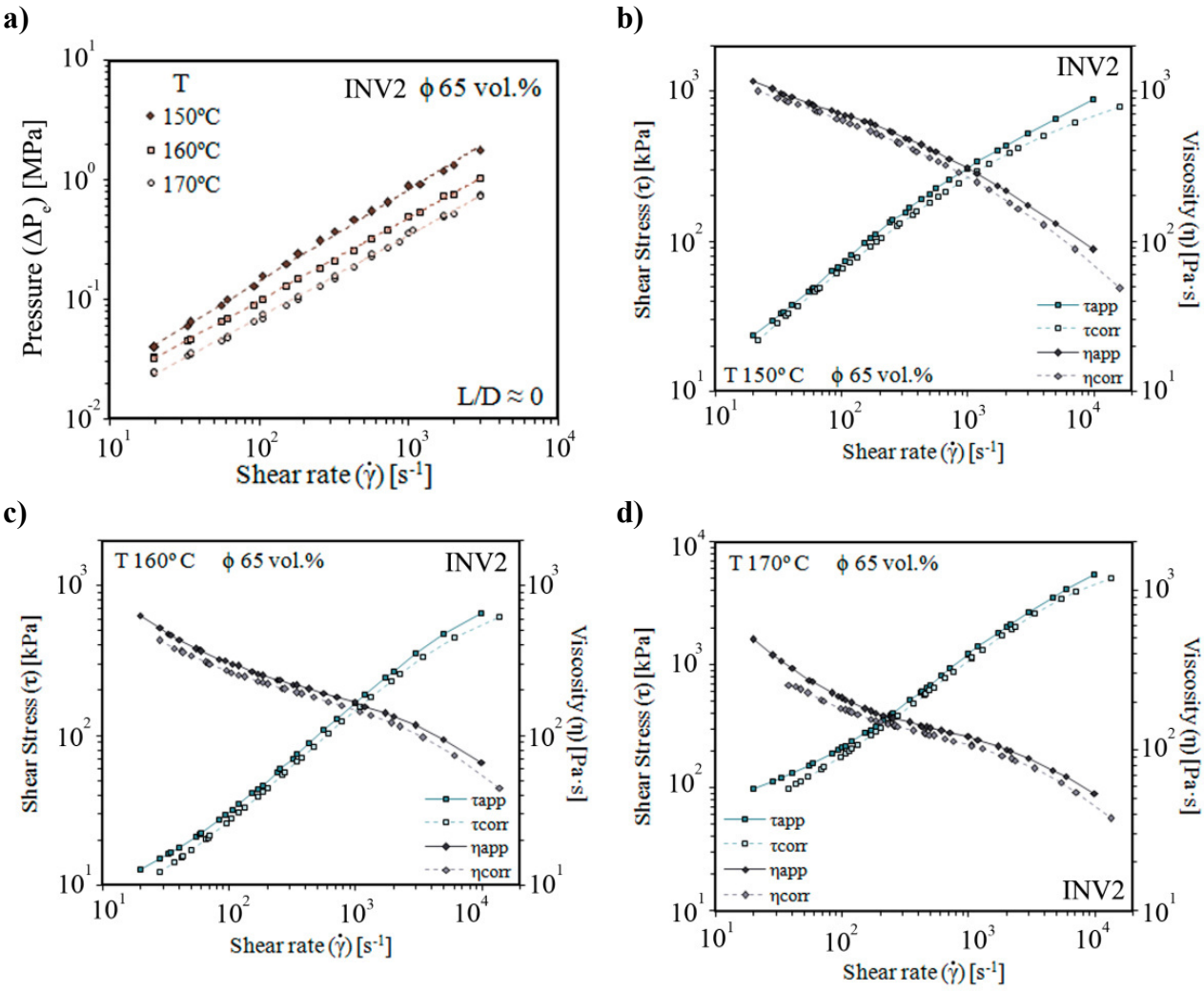

Figure A1. 2 Different plots showing the Bagley and Weissenberg-Rabinowitsch corrections of the viscous behaviour experimental data of an INV2 65 vol.% feedstock: a) Pressure vs. shear rate plot of L/D≈0 capillary measurement for Bagley corrections, b) apparent and real viscosity and shear stress curves at 150 ºC, c) apparent and real viscosity and shear stress curves at 160 ºC, d) apparent and real viscosity and shear stress curves at 170 ºC.

References

1. Gotsis, A.D. and A. Odriozola, *The relevance of entry flow measurements for the estimation of extensional viscosity of polymer melts.* Rheologica Acta, 1998. **37**(5): p. 430-437.
2. Aho, J. and S. Syrjala, *Evaluation of different methods for determining the entrance pressure drop in capillary rheometry.* Applied Rheology, 2008. **18**(6): p. 63258 (5 pp.)-63258 (5 pp.).

Paper 1

P1

E. Bernardo, J. Hidalgo, A. Jiménez-Morales and J.M. Torralba

Feedstock development for Powder Injection Molding of Zirconium Silicate

This work was orally presented at Euro PM11 Conference celebrated in Barcelona and included in the proceedings of this congress (Vol.4, p. 111-116). The manuscript was refereed by Dr Gemma Herranz from Castilla la Mancha University.

Later, it was published in the journal Powder Injection Molding International (Vol. 6, No.1, p. 75-78, March 2012) by courtesy of EPMA.

Feedstock development for powder injection moulding of zirconium silicate

Elena Bernardo (1), Javier Hidalgo (1), Antonia Jiménez-Morales (1) and José M. Torralba (1,2)

(1) Materials Science and Engineering Department, Universidad Carlos III Madrid
(2) Institute IMDEA Materials, Universidad Carlos III Madrid

ABSTRACT

The interest in Zirconium Silicate $ZrSiO_4$ (zircon) arises from its wide availability and excellent properties. Due to its hardness, good corrosion resistance, high melting point, low thermal expansion and chemical inertness, $ZrSiO_4$ can be used in many different applications. Powder Injection Molding is a suitable alternative for ceramic processing. In this paper, a whole PIM process has been developed for $ZrSiO_4$ using micrometer sized powders. Three different binders systems have been investigated: conventional LDPE-PW, HDPE-PEG and alternative CAB-PEG system. Process parameters for different feedstocks have been evaluated and compared. The behavior of binders using PEG as additive is comparable to those using PW, with the benefit of non harmful solvent. There is evidence of improved compatibility between binder components in the CAB-PEG system leading to higher sinter properties. It has been demonstrated that, for $ZrSiO_4$ contents up to 60 vol.%, injection molding can be accomplished at low debinding rates.

Keywords: feedstock, zirconium silicate, CAB-PEG binder system, HDPE-PW binder system

1. Introduction

Zirconium Silicate ($ZrSiO_4$), commonly known as zircon, is a ceramic material which could be found in form of natural sand mineral or be synthetically produced. Among its unique thermo-physical properties, zircon include very low and uniform thermal expansion coefficient compared with typical structural ceramics ($4.1 \cdot 10^{-6}$/ºC from room temperature to 1400ºC) and low thermal conductivity (5.1 W/m·ºC at room temperature and 3.5 W/m·ºC at 1000ºC) [1]. Both properties derive in an outstanding thermal shock resistance. The zircon strength retention at high temperatures is significant and its mechanical properties remain good up to 1400ºC for fully densified zircon. Moreover, Zircon exhibits excellent chemical and corrosion resistance against acids, glass melts, molten metal alloys and slag [2].

All these properties mentioned above make zircon a very suitable candidate for refractory applications and make this material a potential candidate for structural applications as well. It is extensively used in a wide range of applications such as construction material in glass tanks, in iron and steel production, in energy technology, as moulds and cores in precision investment casting or as protective coatings of steel-moulding tools.

Most of the processes for zircon powder consolidation found on literature are based on press and sintering, being of relevance the works concerning hot isostatic pressure technique (HIP) [1, 3]. However, there are scarce works which describe conformation of zircon by powder injection moulding. N. Schlechtriemen et al. describe a process for consolidate synthetic zircon by reaction sintering of silica and zirconia powder mixtures [4]. To the best of the authors' knowledge, there are no publications using PIM technique applied to natural zircon powders from raw treated sand. Anyhow, the unique characteristics of PIM technique may lead to interesting advantages of as-prepared pieces and consolidate zircon as a competitive material for structural purposes.

The present work carries out a study of the application of different binder systems commonly used in PIM to mineral zircon powder. The study particularly focuses on the advantages of using PEG based binder compared to conventional polyolefin based binder systems. Despite possessing exceptional characteristics for PIM and being one of the most economic alternatives, polyolefin based binder systems are controversial since they use toxic and hazardous solvents during one stage of the debinding. Recently harmless PEG based binders exhibit good binder properties and an environmental and economic solvent debinding in water [5]. However, PEG blends commonly combine with a polyolefin polymer seems to be less compatible causing poorer homogeneity and green properties. The use of the natural derived CAB studied in this work, presents better compatibility with PEG [6] and it is proposed as a potential alternative to polyolefin binder systems.

2. Experimental procedure

2.1 Materials and feedstock development

Zircon powder used in this study (average size of 1.604 μm) was gently supplied by GUZMAN GLOBAL S.L (Spain). Its chemical composition and powder characterization are given in Table 1 and Table 2 respectively. The particle size distribution curve obtained by laser diffraction (Malvern 2000E equipment) and a micrograph of the zircon powder are shown in Figure 1.

Table 1 Chemical composition (wt.%) of ZrSiO4 powders

	ZrO_2	SiO_2	Al_2O_3	TiO_2	Fe_2O_3
Composition (wt.%)	66	33.59	0.25	0.11	0.05

Table 2 Properties of ZrSiO4 powders

Properties	Zircon
Morphology	angular
Density ($g \cdot cm^{-3}$)	4.58
Tap density (%real)	32.45%
Apparent density (%real)	21.07%

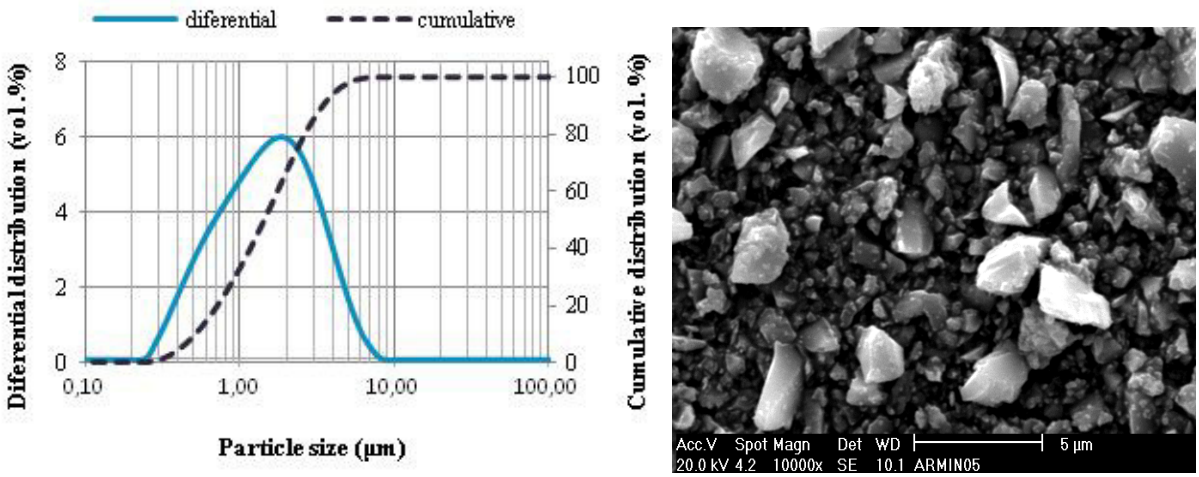

Figure 1 Particle size distribution obtained by laser diffraction (left) and SEM image of zircon powder (right).

Three different binder systems were studied. Two conventional polyolefin based binders LDPE-PW and HDPE-PEG were selected in order to evaluate advantages of using a binder based on acetate-butyrate of cellulose (CAB) and PEG. Table 3 resumes the selected systems.

Table 3 Feedstocks' composition

Feedstock	Solid loading	Binder	Supplier	Tag
Feedstock 1	55 vol.%	47% LDPE 48%PW 5% SA	Dow Panreac Sigma Aldrich	F1
Feedstock 2	60 vol.%	30% CAB 551 60% PEG20k 5% PEG10k 5% PEG4k	Eastman Sigma Aldrich Sigma Aldrich Sigma Aldrich	F2
Feedstock 3	55 vol.%	55% HDPE 40% PEG 5% SA	Dow Sigma Aldrich Sigma Aldrich	F3

Blends were prepared in a torque rheometer ThermoHaake, model Haake Rheocord 252p, with varying solid loadings from 50% to 60% in volume of the powder for each feedstock. The details of the selected feedstock compositions are presented in Table 3. In the case of feedstock 1 (F1) and feedstock 3 (F3), a solid loading of 55 vol.% was chosen as the optimum solid loading, whereas 60 vol.% of powder was selected for feedstock 2 (F2). The mixing process was carried out at a temperature of 160ºC and a rotors speed of 40rpm for 60 min, since at this time homogeneity of the feedstock was observed. After granulation, injection step was performed in a transfer injection moulding machine AB. Maximum pressure was set at 1 MPa and hold pressures were 11 sec. Mould temperature varied from 40ºC, in case of CAB-PEG feedstock to 100ºC for polyolefin based binders.

2.2 Debinding and sintering

Two-step debinding process is carried out in this study. First, solvent debinding was performed at 60ºC for 6h by immersion of F1 samples in hexane. The feedstocks F2 and F3

were subjected to a water-solvent debinding at the same temperature and time than F1. The selected heating profile during thermal debinding in air followed three different stages at 300, 475 and 550 ºC with holding times of 1h at each temperature. Debinding rate was set at $2ºC \cdot min^{-1}$ for the entire process.

After complete binder removal, samples were sintered at 1500ºC for 1h and 3h in air in order to evaluate the influence of sintering time on final properties. Heating and cooling rate was 10ºC/min during sintering cycle.

2.3 Characterization

Thermogravimetric analysis (TGA) is performed in a Perkin-Elmer equipment, model STA6000, at a heating rate of $10ºC \cdot min^{-1}$ in air in order to determine the decomposition temperatures of the binder components. After debinding, the carbon content is evaluated using conventional LECO CS-200 equipment.

The as-sintered samples were tested on a three-point bending machine; model Microtest, equipped with a 1kN load cell. A crosshead speed of 0.5 $mm \cdot s^{-1}$ was applied. Scanning electron microscopy (SEM Philips XL30) was used in order to investigate moulded and solvent-debound samples as well as fracture surfaces.

3. Results and discussion

3.1 Feedstock characterization

The main concern during feedstock production is to obtain a homogenous feedstock. Uniformity of the feedstock can be measured by means of torque reometry [7]. Figure 2.a shows torque values measured at the steady state versus solid loading for each feedstock. Critical solid loading was achieved at 60 vol.% in the case of F1 and F3. However, F2, based on CAB-PEG mixture, allowed higher volume fraction of powder (65 vol.%) due to lower viscosity of the mixture. This could reveal a better compatibility of the feedstock components.

It was previously determined that a good moulding injection process usually requires a torque value below 4Nm for the model of injection machine used in this study [8]. Therefore, powder fraction was limited to 55 vol.% for F1 and F3, whereas F2 contained 60 vol.% of solid loading. For these solid loadings, torque values versus time are given in Figure 2.b for each feedstock at 160ºC. Homogeneity of the feedstocks was achieved after 40 min for all cases.

After injection, feedstock homogeneity was also study through density measurements and SEM characterization. An inhomogeneous feedstock may result in density gradients and lead to distortion during consequent steps of the PIM process. Table 4 shows green density values of each feedstock. For F2, experimental values are consistent with theoretical ones calculated with the rule of the mixes indicating uniform particle-binder distribution for F2. Nevertheless, F1 and F3 experimental values partly differ from theoretical ones.

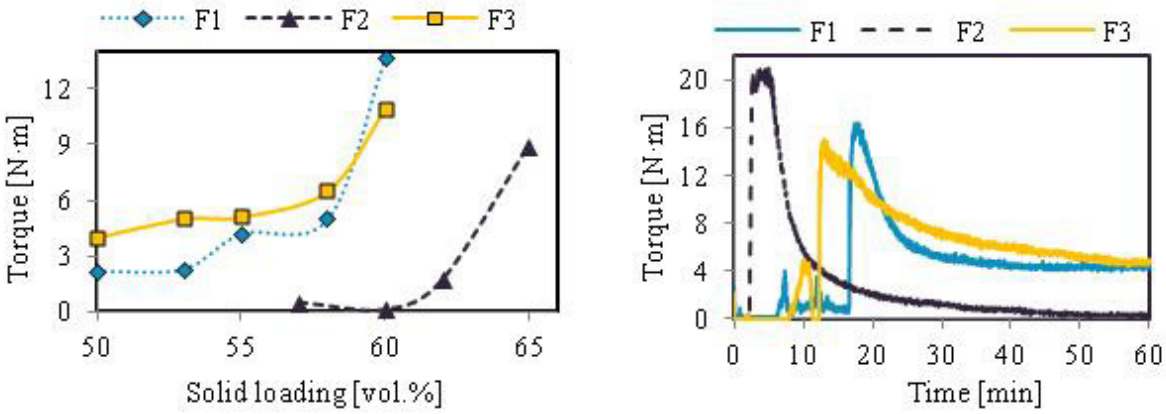

Figure 2 Left) Torque value at the steady state versus powder volume fraction and right) torque curves for the three studied feedstocks obtained through torque reometry at 160ºC for 60 min.

SEM micrographs of the feedstocks illustrate these differences. Figure 3.b shows as-moulded sample of F2 where binder is evenly distributed throughout the sample, and higher magnifications do not show any density segregation. However, density gradients are more noticeable for F1 and F3 which explains higher deviation in green density measurements. In this case, binder separation is most probably promoted by either lower compatibility or worse wetting behavior between the powder and binder.

Table 4 Comparison of experimental and theoretical green densities values for each feedstock

Green density ($g \cdot cm^{-3}$)	F1	F2	F3
Picnometer value	3.01	3.23	3.11
Theoretical value	2.93	3.23	2.99

It is important to point out that even though powder did not have ideal characteristics for its implementation in MIM technology (shape and tap density), as-moulded parts presented perfect shape retention. In the case of F2, the presence of PEG with low molecular weight and better powder-binder compatibility significantly reduce viscosity of the feedstock and make it more suitable for injection at higher solid loadings.

3.2 Debinding

During solvent debinding, more than 75% of soluble component (PW and PEG) was successfully removed after 6 hours for all cases without formation of cracks or swelling. More efficient elimination was achieved in the case of F2, from which 95% of the PEG was extracted even though higher powder loading is present. SEM characterization showed homogenous elimination at both regions close to the edge and the core of the specimen indicating good accessibility of the solvent as well as efficient diffusion of soluble component.

Applying a heating rate of $2ºC \cdot min^{-1}$ during thermal debinding did not result in any dimensional distortion or defect. Figure 4 shows carbon content results of samples after debinding. There is not any remarkable difference among them, although F3 shows the highest levels. This result confirms complete CAB removal after debinding.

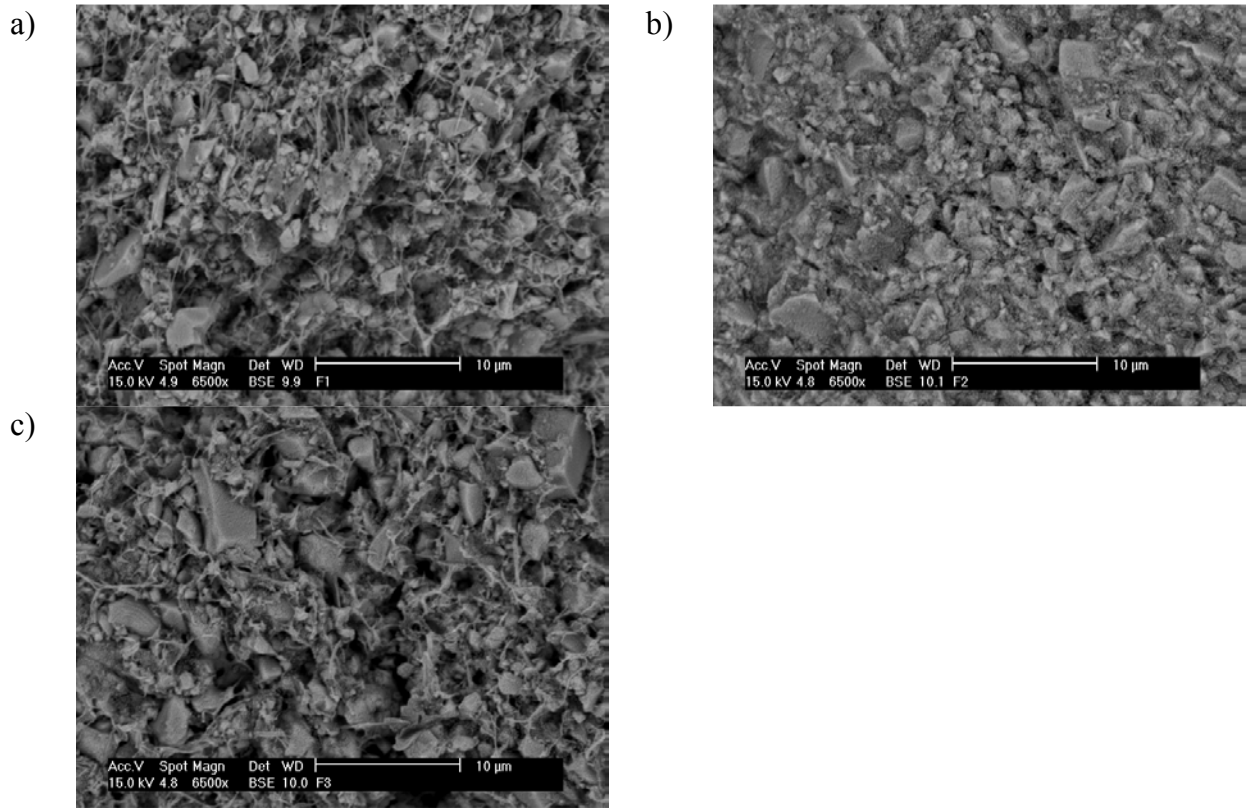

Figure 3 SEM micrographs of specimens after injection at scale 10 µm and 6500x: (a) F1 based on LDPE and PW, (b) F2 based on PEG and CAB and (c) F3 based on HDPE and PEG.

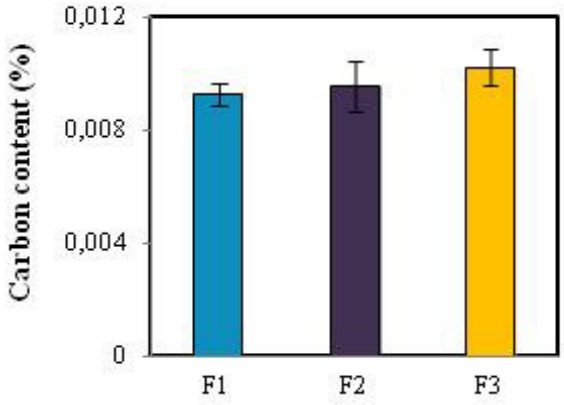

Figure 4 Carbon content (%) after debinding at 2ºC/min

3.3 Mechanical properties

The results from bending experiment of the as-sintered samples are given in Figure 5.a. It can be observed that flexural strength increases with increasing sintering time in all cases. There is evidence of improved flexural strength of F2 compared to conventional polyolefin based binders. This fact is especially true when compared to F3. Observed density gradients and higher viscosity of the feedstock may explain the detrimental effect on final properties of this sample. Besides, higher solid loadings in F2 also favor densification of the compact. Maximum value is achieved after 3h of sintering.

Maximum flexural strength (F2) is comparable to hot-pressed zircon samples at 1500ºC from the literature. Increasing sintering temperature up to 1600ºC leads to flexural strength enhancement from 150 MPa to 320 MPa for pure zircon, although impurities may decrease these value [3, 9].

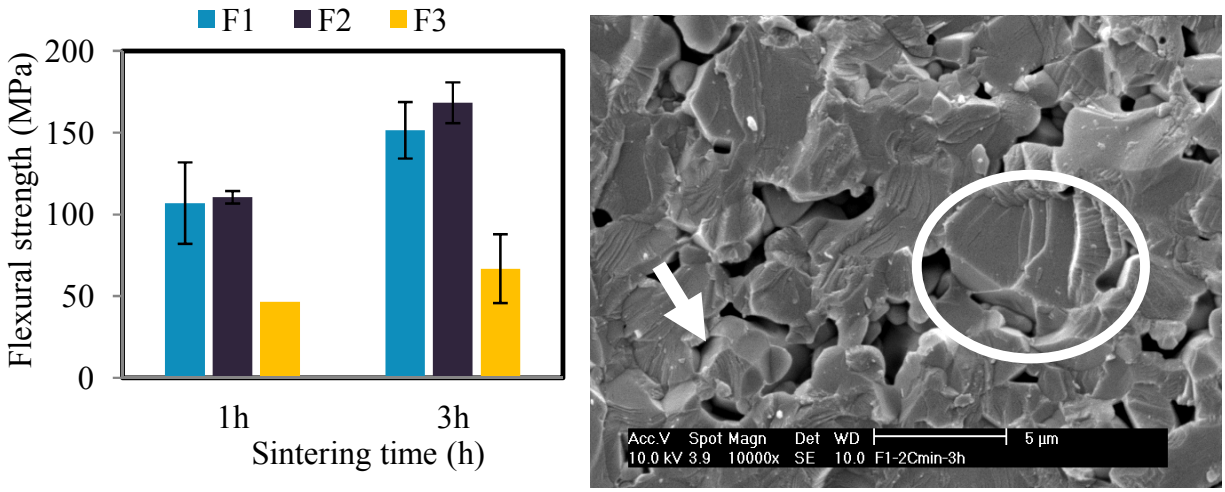

Figure 5 (Left) Comparison of flexural strength values of the as-sintered samples of each feedstock after 1h and 3h of sintering and (Right) SEM micrograph of F1-3h sintering specimen showing main failure mechanisms

The microstructural evolution of fracture surfaces at different sintering times are shown in Figure 6. After 1h of sintering at 1500ºC, F2 specimen exhibited the greatest sinter neck growth. F1 and F3 seem to have less developed inter-particle connections and higher residual porosity, whereas F2 shows smaller rounded pores.

Increasing sintering time results in better developed inter-particle connections and, therefore, higher densification in all cases which is in agreement with flexural strength results shown above. F2 exhibits almost full density which is consistent with maximum flexural strength value. Observed lower flexural strength of F3 is related to higher residual porosity even after 3h of sintering. Cleavage facets and intergranular fracture are predominantly the main failure mechanisms for all specimens (Figure 5.b).

4. Conclusions

The present study carries out the optimization of a PIM process for mineral zircon powder. Alternatively to conventional polyolefin binder, this study has focused on the development of an economic and efficient binder based on water-soluble PEG and natural derived CAB. This combination resulted in rapid homogenization of the feedstock in the presence of higher solid loading compared to prevailing polyolefin based binder. There is evidence of better compatibility between feedstock components that improves rheological behavior of the mix. Despite characteristics of zircon powder, which are considerate inappropriate for PIM, the low viscosity of the feedstock favored zircon particle motions and facilitated injection of the feedstock at 60 vol.% of solid loading. Combination of solvent and thermal debinding resulted

in gradual binder removal and comparable elimination efficiencies to conventional binders. Moreover, F2 provides with the highest flexural strength after 3h of sintering in air at 1500ºC. Thereafter, improvement in final sinter density was achieved when CAB and PEG compose the binder system.

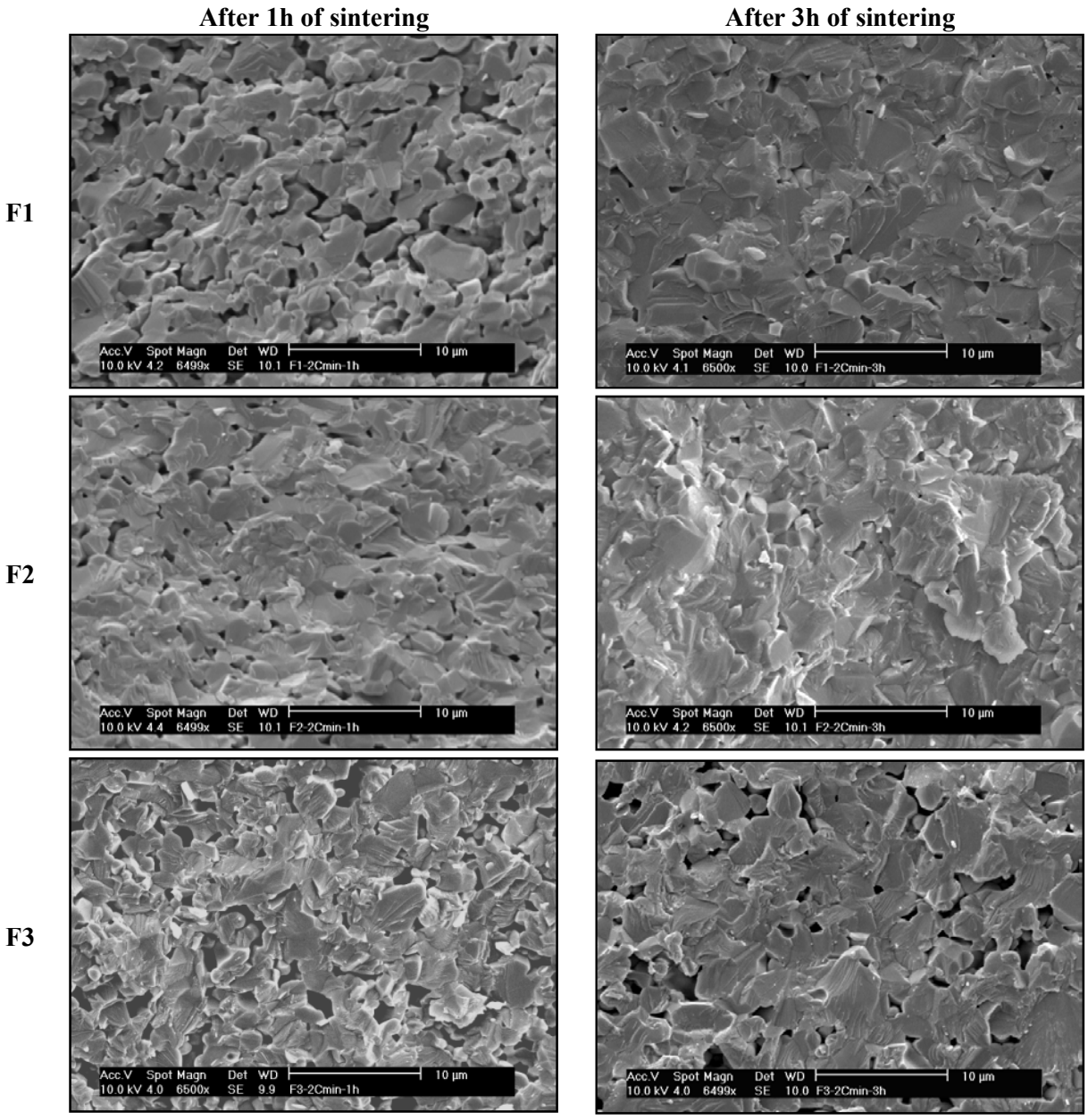

Figure 6 SEM micrographs of the fracture surfaces of as-sintered specimens after 1h or 3h sintering

Acknowledgements

This paper was first presented at Euro PM11 Conference, Barcelona, Spain, and is published courtesy of the EPMA. The authors thank GUZMAN GLOBAL S.L (Spain) for supplying the powder.

REFERENCES

1. Shi, Y., et al., *TEM and HREM characterization of hot-pressed zircon ceramics.* Materials Letters, 1995. **23**(4-6): p. 247-252.
2. Kaiser, A., M. Lobert, and R. Telle, *Thermal stability of zircon (ZrSiO4).* Journal of the European Ceramic Society, 2008. **28**(11): p. 2199-2211.
3. Shi, Y., X. Huang, and D. Yan, *Fabrication of hot-pressed zircon ceramics: Mechanical properties and microstructure.* Ceramics International, 1997. **23**(5): p. 457-462.
4. Schlechtriemen, N., et al., *Optimization of feedstock properties for reaction-bonded net-shape zircon ceramics by design of experiments.* Ceramics International, 2010. **36**(1): p. 223-229.
5. Krauss, V.A., et al., *A model for PEG removal from alumina injection moulded parts by solvent debinding.* Journal of Materials Processing Technology, 2007. **182**(1-3): p. 268-273.
6. Song, M., Park, M.S., Ki,m, J.K., *Water-soluble binder with high flexural modulus for powder injection molding.* Journal of Materials Science, 2005. **40**: p. 1105 – 1109.
7. German, R.M., *Injection molding of metals and ceramics*, ed. M.P.I. Federation. 1997, New Jersey.
8. Hidalgo, J., Contreras, J.M., González,S., Jiménez-Morales, A., Torralba, J.M. *Rheological Behaviour of Powder Injection Moulding (PIM) Feedstocks Fabricated with a Thermoplastic Binder System Based on Polysaccharides*. in *World PM Congress*. 2010. Florence.
9. Rendtorff, N.M., L.B. Garrido, and E.F. Aglietti, *Mechanical and fracture properties of zircon-mullite composites obtained by direct sintering.* Ceramics International, 2009. **35**(7): p. 2907-2913.

Paper 2

P2

J. Hidalgo, C. Abajo, A. Jiménez-Morales, J.M. Torralba

Effect of a binder system on the low-pressure powder injection moulding of water-soluble zircon feedstocks

This work was published in the Journal of the European Ceramic Society (vol.33, pp. 3185-3194, 2013) , DOI: 10.1016/j.jeurceramsoc.2013.06.027

Effect of a binder system on the low-pressure powder injection moulding of water-soluble zircon feedstocks

J. Hidalgo[1,a], C. Abajo[2,a], A. Jiménez-Morales[2,a], J.M. Torralba[2,a,b]

a Materials Science Department at Carlos III University of Madrid, Avd. Universidad 30, 28911 Leganés (Spain).
b IMDEA Materials Institute, Eric Kandel 2, 28906, Getafe (Spain)
1 Corresponding author: Materials Science Department at Carlos III University of Madrid, Avd. Universidad 30, 28911, Leganés (Spain), phone number: +34916249482 e-mail: jhidalgo@ing.uc3m.es
2 Co-authors contact information: C. Abajo: cabajo@pa.uc3m.es, A. Jiménez-Morales: toni@ing.uc3m.es, J.M. Torralba: josemanuel.torralba@imdea.org

ABSTRACT

Micronized natural zircon sand powders were used as a raw material to conduct low-pressure powder injection moulding (LPPIM) processes. PIM could lead to new technological applications for this mineral, which has very stable dimensional behaviour with changing temperature. Zircon powders that have unconventional attributes for PIM (in terms of size and morphology) were mixed with poly(ethylene glycol) (PEG) based binders. Combinations of this water-soluble substance with different polymers, including low-density polyethylene (LDPE) and several types of acetate butyrate celluloses (CAB), were investigated. The influence of acetyl, butyryl and hydroxyl groups on the behaviour of the created feedstocks at different process stages and on the final piece properties were studied. The higher affinity of CAB with PEG and zircon powders compared with LDPE could result in improved densification and properties, but the butyryl, acetyl and hydroxyls groups affect the processability of these feedstocks.

Keywords: zircon, powder injection moulding, poly(ethylene glycol), cellulose acetate butyrate

1. Introduction

The present work is based on the use of water-soluble binder systems in the low-pressure injection moulding (LPPIM) processing of micronized, natural zircon ($ZrSiO_4$) powders. Most of the processes for zircon powder consolidation that are found in the literature are based on pressing and sintering, including relevant works concerning hot-pressed zircon parts [1, 2]. However, there are few works that describe the processing of zircon via injection moulding. N. Schlechtriemen et al. [3] described a process for the consolidation of synthetic zircon via the reaction sintering of silica and zirconia powder mixtures. Hidalgo et al. [4] successfully fabricated micronized zircon sand pieces using high-pressure powder injection moulding (HPPIM).

The LPPIM method includes the following main steps: mixing of a powder with a binder system, moulding, debinding and sintering. The use of a low pressure could be beneficial in terms of cost savings for equipment and tooling, compared with HPPIM [5-7]. This process has other advantages besides the economic aspects. The shear forces in the tool walls and cavities are reduced, which is especially beneficial when using highly abrasive hard ceramics. This phenomenon would avoid the pernicious contamination of the powders with other elements and enable the use of inexpensive moulds. Furthermore, lower internal pressures are generated in the green body after injection. Nevertheless, LPPIM implies the use of a lower viscosity feedstock, compared with HPPIM, and may lead to the development of some intrinsic defects during injection, such as trapped air voids.

Zircon is a ceramic material that can be found in natural mineral sand form, which normally has other compound traces, or can be synthetically produced in an impurities-free form. Zircon exhibits excellent, stable thermophysical properties over a wide range of temperatures. Zircon has no phase transformation up to approximately 1500-1550ºC, at which it dissociates into silica and zirconia [8]. This temperature varies depending on the impurities that are present in the raw material as well as its processability and properties [9]. The high melting point of zircon reaches up to 2200ºC. Zircon has a very low and uniform thermal expansion coefficient compared with typical ceramics (4.1·10-6/ºC from room temperature to 1400ºC) and a low thermal conductivity (5.1 W/m·ºC at room temperature and 3.5 W/m·ºC at 1000ºC). All of these properties lead to a remarkable thermal shock resistance and refractory properties. The strength retention of zircon at high temperatures is significant, and its mechanical properties are good up to 1400ºC for fully densified zircon [2]. Moreover, zircon exhibits excellent chemical and corrosion resistance against acids, glass melts, molten metal alloys and slag. All of these properties make zircon a very suitable candidate for refractory applications and also make this material a potential candidate for structural applications. The unique characteristics of PIM technology may lead to interesting advantages for zircon as a competitive material for structural purposes, thus increasing the number of applications for zircon.

Nevertheless, the above zircon properties complicate the sinterability and densification of zircon powders. Producing defect-free, fully dense specimens with good mechanical properties is the main challenge for introducing zircon as a competitive ceramic material into complex shape parts that are produced by LPPIM. In this respect, the choice of a suitable binder system could lead to different final piece properties. In this work, two types of water-soluble binder systems are studied. The first type consists of low-density polyethylene (LDPE) as a holder component, and the second type consist of cellulose acetate (CAB). All binder compositions are based on poly(ethylene glycol) (PEG)'s being the water-removable part of the binder. In addition to the advantages of cost reduction and the non-harmful use of water as the solvent, CAB-based binders have net zero CO_2 emissions due to the thermal degradation of this cellulose derivative polymer. However, the main attraction in using CAB comes from the possible better interactions with PEG and zircon powder particles, which would result in an improved homogenisation of all feedstock components and, therefore, the final piece properties. The physicochemical properties of CAB depend on the grade of substituent acetyl,

butyryl and hydroxyl groups in the main chain. Three different CABs with variable percentages of these substituents were selected to study the influence of the type of CAB on the processability characteristics of zircon feedstocks.

2. Experimental

2.1 Materials

Micronised mineral zirconium silicate sand was used for this study. The powders were supplied by GUZMAN GLOBAL S.L (Nules, Spain). The chemical composition of the powders is listed in Table 1. These powders exhibit an irregularly shaped morphology, as shown in Figure1, which also shows the particle size distribution curve for the zircon powder. A Malvern 2000 laser-scattering particle size analyser was used to measure the particle size distribution. The irregular morphology of these powders contrasts with the spherical or round powders that are conventionally used for PIM. The particle sizes parameters , the D_{50} and D_{90}, of the powders are 1.604 and 4.650 µm, respectively, which are relatively low values for PIM. The powders have a specific surface area of 5.0363 m²/g, which was determined by a Micrometrics Gemini VII BET measurement device. The low tap and apparent densities, 32.45% and 21.07% of the material density (4.58 g·cm^{-3}), respectively, reflect the low-packing capacity of the powders and their tendency to form agglomerates, which are both direct consequences of the shape and particle size of the powder.

Table 1 Chemical composition of the zircon powders

	ZrO_2	SiO_2	Al_2O_3	TiO_2	Fe_2O_3
wt.%	66	36.59	0.25	0.11	0.05

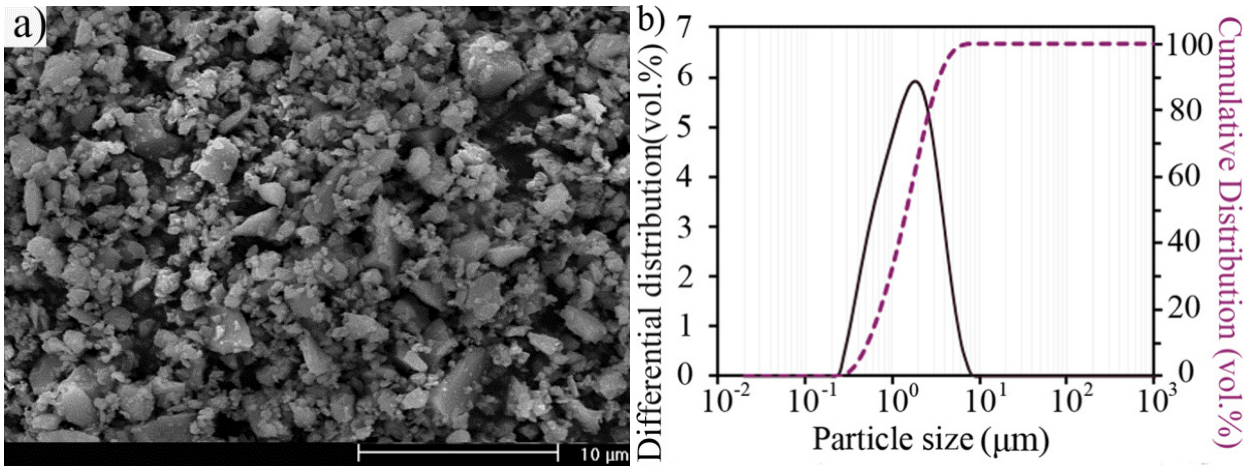

Figure 1 a) Secondary electron scan SEM image of the zircon particles; b) particle size distribution of the zircon powders.

Four types of binder systems were selected. All of these systems are shown in Table 2. The B130, B230 and B330 compositions are based on CAB and PEG binders, but the percentages of acetyl, butyryl and hydroxyl groups in each composition vary. The remaining B430 is based

on LDPE and PEG. This last composition was selected as a typical combination of a polymer in water-soluble PEG-based binders for comparison. The volume percentage of PEG (the water-soluble part) is kept constant in all cases to best compare the influences of the other components on the process conditions and final properties of the zircon samples.

Table 2 Binder system compositions

	B130	**B230**	**B330**	**B430**	
Commercial name	CAB381-0.1	CAB551-0.01	CAB553-0.4	LDPE 780E	PEG20k
Supplier	Eastman	Eastman	Eastman	Dow	Fluka
Butyryl [wt.%]	37	53	46	-	-
Acetyl [wt.%]	13	2	2	-	-
Hydroxyl [wt.%]	1.5	1.5	4.8	-	-
Content [vol.%]	30	30	30	30	Balanced

By*xx: y=1,2,3 or 4(type of binder), xx= content of y in vol.%.*

2.2 Methods

The binders and zircon powders were mixed in a Rheomix 600 Haake rheometer coupled with a Haake Rheocord 252p module. Roller blade-type rotors were used for the mixing experiments. A temperature of 150ºC and a rotor speed of 50 rpm were used in all experiments, and the mixing chamber was filled with feedstock up to 72% of its volume (the total chamber volume is 69 cm^3). The feedstock temperature and torque were monitored as the output parameters. The equipment is self-calibrating when it reloads at the start of every new measurement. A thermocouple is placed at the confluence of the rotor flow, at which the feedstock is well mixed, to monitor the temperature of the feedstock.

Capillary rheology measurements were conducted in a Reoflixer Haake capillary rheometer to determine the apparent viscosity of the different fabricated powder-binder blends by varying the shear rates from 10 to 10000 s^{-1}. The capillary that was used in this work has a length-to-diameter ratio, L/D, of 30. Because no abrupt variations between the apparent and real viscosities were expected and the experimental conditions were the same in all cases, corrections to the apparent viscosity were not considered for feedstock comparison. For low-pressure injection moulding, a Bimba AB transfer injection machine was used. A pressure of 0.8 MPa was employed in all cases, and the injection and mould temperatures were modified for each composition. A bending test part mould was used to fabricate green parts 60x8x4 mm.

Two different ways of debinding the organic components of the feedstock were evaluated: a whole thermal debinding and a combination of a first step, in which PEG was extracted via solvent elimination in distilled water, followed by a thermal elimination of the remaining CABs or LDPE. The debinding conditions can be found in Figure 2. To evaluate the thermal degradation, thermogravimetric analyses were performed in a Perkin Elmer STA6000 simultaneous thermal analyser. The weight loss ratio was evaluated with changing temperature from 50 to 600ºC at a heating rate of 10ºC/min in both air and nitrogen atmospheres. The

percentage of PEG elimination with time during solvent debinding was evaluated by simply weighing the parts after immersion in water and drying at 70ºC for 12 hours.

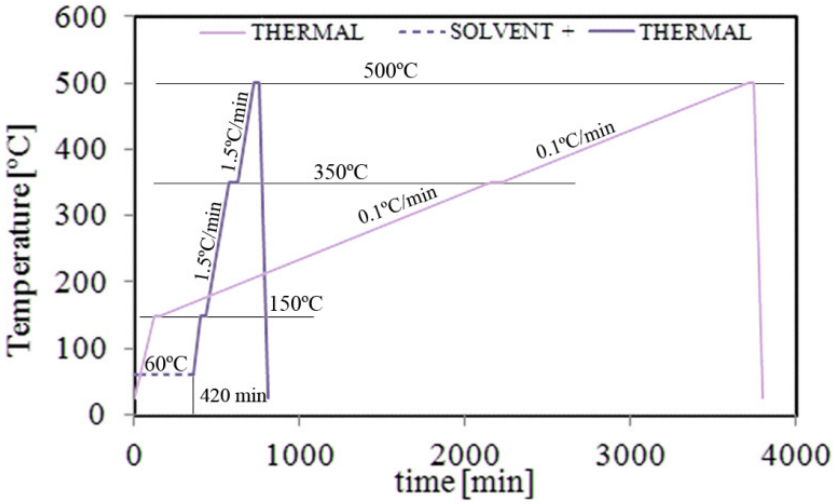

Figure 2 Debinding cycle conditions: the short cycle corresponds to solvent (300 min immersed in distilled water + 120 min dried in air) plus thermal debinding, and the long cycle corresponds to a whole thermal debinding cycle with very low heating rates to avoid defects.

After debinding, the parts were sintered in a vacuum atmosphere (pressure < 2·10-5 bar) at 1450ºC for one hour with heating and cooling rates of 5ºC/min. A Shimadzu AG-1 1kN mechanical testing machine was used to conduct three-point bending tests to determine both the green strength of the as-injected parts and the bending strength of the sintered parts. A crosshead speed of 1 mm/min was chosen for the tests. For scanning electron microscopy (SEM), a Philips XL-30 microscope was used.

3. Results and discussion

3.1 Rheological study

3.1.1 Torque Rheology

In Figure 3a the evolution of the torque with time is shown for the mixing process with different feedstocks; in all cases, the solid loading contents were kept constant at 57.5 vol.%. Figure 3b shows the average torque values after 40 minutes of mixing for different solid loading contents and formulations. It could be observed that B230 has the minimum stabilised torque value of all the evaluated solid loadings. The torque measurements of B230 could be directly related to the lowest viscosity at the shear rate intervals that are developed due to the mixer screws. This formulation also stabilises the monitored torque values in a shorter period of time than the other formulations. At the opposite extreme is B430, which has the maximum torque value after 60 minutes. The stabilisation of the average torque values, $\bar{M}$, indicates that the components of the mixture are effectively dispersed and homogenised.

The gap between the maximum and minimum torque values of the stabilised region, $\overline{\Delta M_{est}}$, indicates the homogenisation extent. If there are regions with different component concentrations, the torque values will fluctuate depending on the sizes of these regions. Large fluctuations could reveal incompatibilities with binder components that will not homogeneously mix but could also indicate that a critical solid loading is achieved, which would mean that there is not enough binder to embed all of the powder particles [10]. Table 3 lists the different parameters that were measured during mixing. The totalised torque (TTQ) parameter has been shown to be effective for evaluating the mixing behaviour of PIM feedstock [4]. The TTQ values are related to the total mechanical energy that is required to move the feedstock bulk during mixing up to a certain point. These values are proportional to the areas under the torque curves.

Table 3 Torque experiment measured parameters after 60 minutes of mixing. The averaged values correspond to the last two minutes of collected data for three batches per composition.

$\Phi = 57{,}5$vol.%	$\bar{M}$ [N·m]	$\overline{\Delta M_{est}}$[N·m]	$\overline{TTQ}$[J·min]	T [ºC]
B130	4.04±0,45	0.13±0,03	527±17	160.7
B230	2.40±0,25	0.12±0,03	193±4	155.2
B330	3.53±0,75	0.16±0,02	343±22	158.9
B430	5.64±0,85	0.17±0,03	860±116	164.2

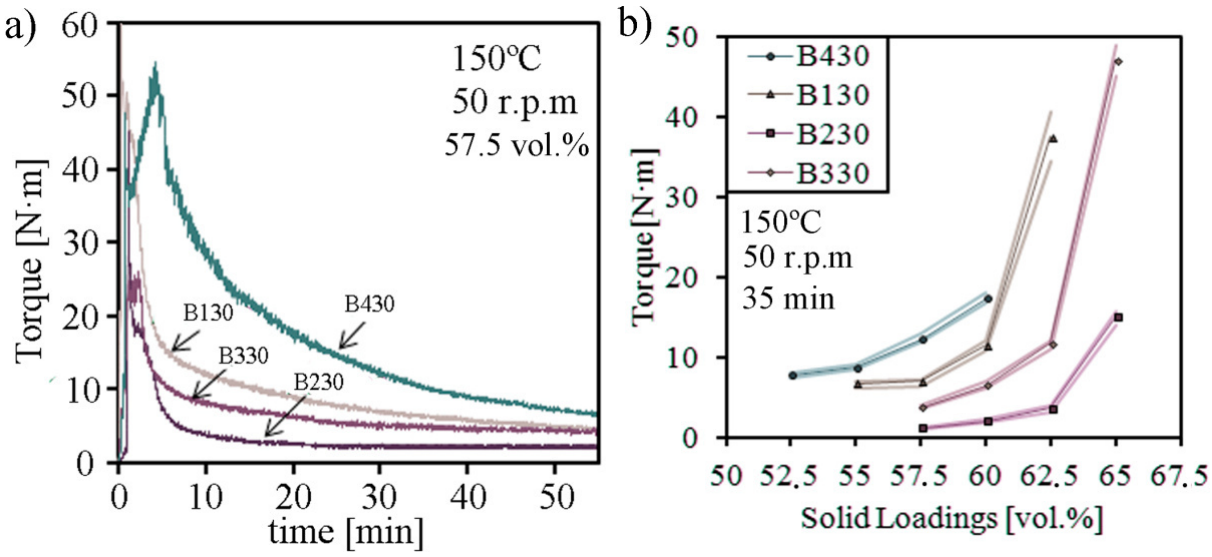

Figure 3 a) Torque evolution with time for different formulations and 57.5 vol.%. b) Average torque values at minute 35 of mixing for different solid loading contents and formulations; three measurements are represented for each condition, with the medians represented by the points.

From these results, it could be stated that B430 needs a higher mechanical energy to disperse all of the components at a certain temperature and rotor speed. This result could be partially due to the binder viscosity but is mostly due to the binder capacity to incorporate powder particles. Table 3 also presents the temperatures of the mixtures after 60 minutes of mixing. All of the feedstocks exhibit an increase in the mixture temperature compared with the

expected 150ºC of the heating plates. These increments could be explained by particle-particle friction. Because the binder contributes to particle lubrication, thus reducing friction forces, the binders that most successfully disperse and embed powder particles will reduce the particle friction. This phenomenon would be reflected by reductions in the mixture temperature and the TTQ values. In this respect, it could be stated that the best formulation in terms of the miscibility between the different components is B230, which has CAB with a high content of butyryl groups and with low contents of acetyl and hydroxyl. Conversely, the worst mixing capabilities corresponds to B430, which has LDPE.

3.1.2 Capillary Rheology

The feedstocks exhibit well-differentiated capillary rheological behaviours depending on the formulation. This fact is reflected in Figure 4, in which the viscosity versus shear rate curves for the different feedstock are plotted. Single points represent measured values, while dashed lines correspond to the curve fitting of a mathematical model. A modified Cross model (Eq. 1) was used to try to describe the flow behaviour of the feedstock. This model has been shown to properly fit rheological data from PIM feedstocks and to efficiently predict the flow behaviour of these feedstocks [11]. This modified Cross model generalises the typical PIM feedstock apparent viscosity (η) dependence on the shear rate ($\dot{\gamma}$), including the possible occurrences of a threshold shear stress (τ_y) and a zero viscosity (η_0), which represents the value of the viscosity during the Newtonian plateau that normally occurs at very low shear rates. The m and C parameters are related to the shift from Newtonian to pseudoplastic behaviour, in which the viscosity decreases with increasing shear rate.

$$\eta = \frac{\tau_y}{\dot{\gamma}} + \frac{\eta_0}{1+(C\cdot\dot{\gamma})^m} \qquad (1)$$

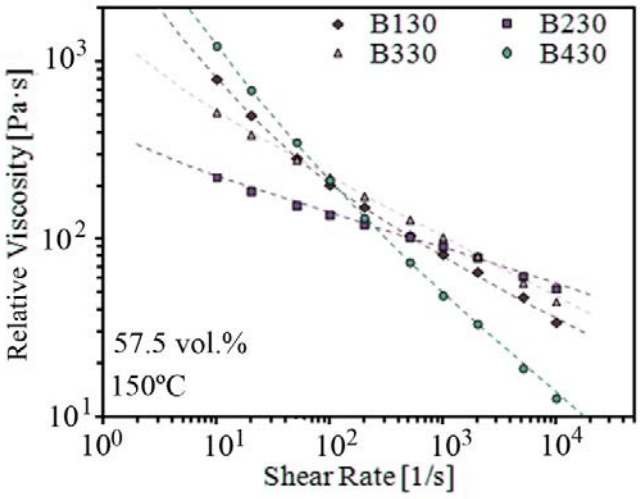

Figure 4 Viscosity measurements of different feedstock compositions.

When the m parameter in the Cross modified model approaches zero, the viscosity behaviour is more Newtonian, i.e., the viscosity is less dependent on the shear rate. Conversely, the higher the m parameter, the more pseudoplastic the behaviour, i.e., the viscosity decreases

more abruptly with increasing shear rate. In this respect, B230 behaves more like a Newtonian fluid and B430 behaves more like a pseudoplastic. Table 4 shows the resulting modified Cross model parameters after the fit to experimental data.

Table 4 Modified Cross parameters that resulted from experimental data fitting.

	τ_y [Pa]	η_0 [Pa·s]	C [1/s]	m []	R^2
B130	4765	12643	6197	0.33	0.99992
B230	114	1582	655	0.21	0.99842
B330	795	3707	34	0.34	0.99985
B430	8201	8086	29	0.51	0.99996

Generally, a pseudoplastic behaviour is more desirable because the flow behaviour will improve with increasing shear force during mould filling. However, a Newtonian behaviour would be perfectly acceptable if the viscosity values remain acceptable for moulding over the whole shear rate range. The use of feedstocks in a melted or fluidic state that have viscosities between 1.5 and 4.0 Pa·s enables transfer inside the mould using compressed air with a pressure on the order of 0.8 MPa [6]. Thus, none of the feedstocks would have enough flow capacity to be injected at 150ºC considering the expected low shear rates that are produced during mould filling under low pressures. Therefore, the optimisation of the injection temperature should be performed by increasing the temperature to lower the feedstock viscosity until the mould is successfully filled at this temperature. The capillary rheology results are consistent with the torque measurements in the range of 10 to 100 s^{-1} and most likely represent the typical shear rate interval in the mixing chamber for the selected rotation speed [12].

3.2 Injection and green strength

The injection process was optimised for the four feedstocks by modifying the injection and mould temperatures and keeping the pressure at 0.8 MPa. After injection, green bending test parts were subjected to a bending test, and the maximum stress before breakage was evaluated and compared to determine the green strength. All of these results are shown in Table 5, where T_{inj} represent the injection temperature, T_{mould} represents the mould temperature and $\bar{\sigma}_{green}$ represents the average value of the green strength after eleven measurements with the corresponding standard deviation.

Table 5 Injection parameters after optimisation and the green strength values.

	T_{inj} [ºC]	T_{mould} [ºC]	$\bar{\sigma}_{green}$[MPa]
B130	180	80	13.15±1.17
B230	180	40	10.23±4.07
B330	190	60	8.74±2.32
B430	190	70	10.49±1.67

It should be noted that, apart from the differences in the injection conditions, there were other issues that arose during the injection stage. The CAB-based binders had a tendency to swell during cooling. Furthermore, the time that was needed to rigidify the injection-softened state was much longer than that for the LDPE-based composition. In the case of CABs, if the part was extracted before complete solidification, it frequently stuck and plastically deformed. These difficulties were more pronounced in the case of the B330 composition, which had a higher cooling time and a tendency to deform during extraction. The B330 composition had the CAB with the highest content of hydroxyl groups, which could be related to these problems. In this respect, the better CAB-based composition was B130, which had a cooling time close to that of the LDPE-based composition and less tendency to stick to the mould walls. This result coincides with a low level of butyryl and hydroxyl groups. On the other hand, the LDPE feedstock exhibited the best cooling times of all the compositions and parts and was thereof easily extracted from the mould. However, the LDPE-based feedstock tends to shrink, which creates shrink cavities in the surface. This type of defect was difficult to eliminate under the low pressure injection conditions. Another critical issue that was observed was the presence of trapped air voids. Some of the compositions exhibited this shortcoming to different extents. This problem arises from the capacity of the binders to evacuate or dissolve gases, which is enhanced by the fact that the feedstock is not previously mixed before injection and by the low pressure that is used. The feedstocks that are based on B130 and B430 rarely exhibited voids, and, if observed, these voids were isolated throughout the part volume. This isolated void occurrence was more frequent in the case of B330. Conversely, the B230 parts exhibited voids throughout all of the part volume, and this phenomenon occurred for all injections. The B230 composition has the highest percentage of butyryl groups, which lowers the melting point and the viscosity of the binder system. This phenomenon most likely leads to the feedstock pellets coalescing before air evacuation. It can be conclude that, although the B130 and B430 feedstocks exhibited higher viscosities, they still have suitable characteristics for injection at low pressures, if the proper injection conditions are selected.

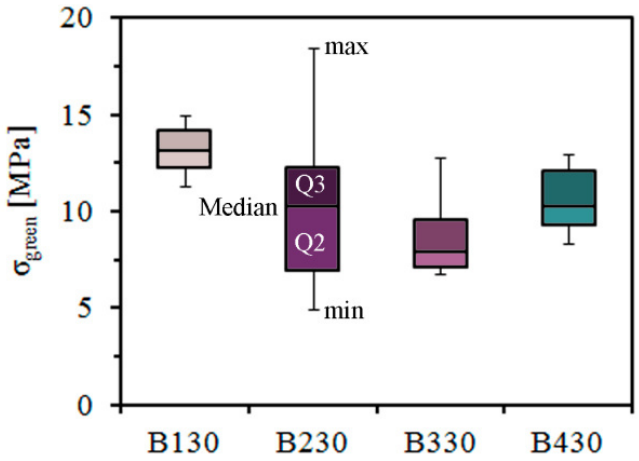

Figure 5 Whisker plot of the green strength results after 11 trials per feedstock composition.

Regarding the green strength measurements, this property will depend on the intrinsic mechanical properties of the binder system components, the interaction between the organic compounds and the powder particles, the dispersion and homogenisation of the components, the presence of internal defects, such as trapped air voids, the residual stresses after injection, etc. This fact makes it difficult to isolate the specific factors that affect the green strength. Figure 5 shows a whisker plot of the green strength results for the different compositions after eleven trials. The B130 composition exhibited the highest average green strength and the lowest dispersion of results. The B230 composition exhibited the highest green strength individual value, but the variability of the results was the highest of all the feedstocks. This result could be explained by the presence of voids, which act as stress concentrators. The lowest green strength results were observed in B330.

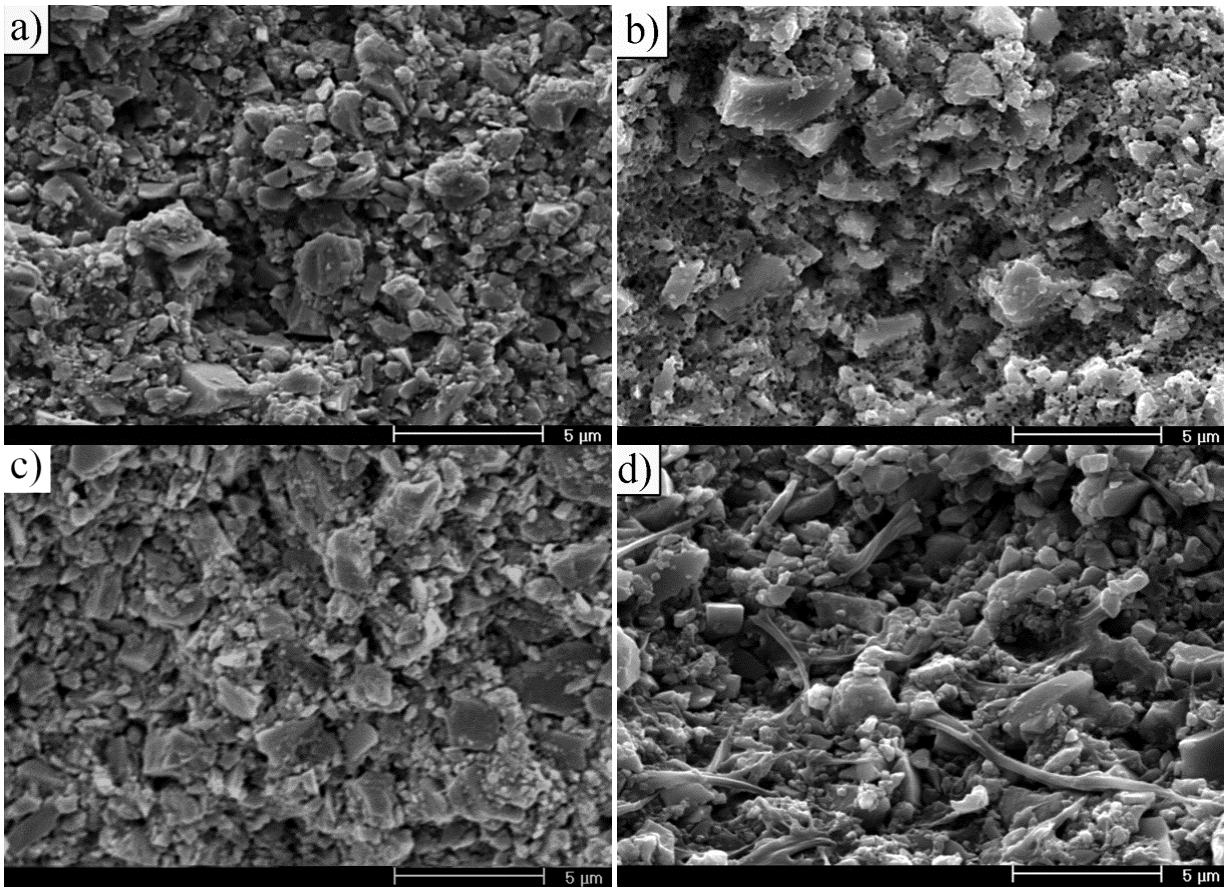

Figure 6 SEM images of the green part fracture surfaces after 10 min of etching in distilled water to remove PEG: a) B130, b) B230, c) B330 and d) B430. A secondary electron detector and the same magnification were used to take the pictures.

Images of the fracture surfaces of the green parts, which were observed by scanning electron microscopy (SEM), are shown in Figure 6. All of these samples were etched with distilled water for 10 min to remove PEG. All of the compositions exhibited homogeneity in the dispersion of the feedstock components, as expected from the torque measurements. Nevertheless, significant differences could be observed by comparing the CAB-based and LDPE-based feedstocks. In the case of the CAB-based feedstocks (Figure 6a-c) it appears that

PEG and CAB were more effectively mixed, as deduced from the smaller porosity that was left after PEG removal. Furthermore it appears that there is more affinity between CAB and the zircon particles because this compound apparently embeds the particles in a better way than the compound with LDPE. In Figure 6d, LDPE fibres can be easily distinguished, which is not the case for CAB fibres in the CAB feedstocks. These LDPE fibres will most likely leave a greater free volume than the CAB fibres after thermal debinding, which may lead to a bigger porosity after sintering, thus deteriorating the mechanical properties. Moreover, the patterns in the LDPE fibre distributions have been reported to be linked to macro-defects, such as bending of the sintered part, because of heterogeneities [13].

3.3 Debinding

3.3.1 Thermal Debinding

Thermal debinding studies were performed using thermogravimetry analyses (TGA) by measuring the feedstock organic content degradation in terms of weight loss with changing temperature. Two different atmospheres, inert nitrogen and oxidative oxygen, were used. The samples were heated from 50ºC to 600ºC. The resulting TGA curves for different feedstocks with 57.5 vol.% solid loadings and different atmospheres are plotted in Figure 7. Some degradation parameters, such as the onset (T_{ONSET}), final (T_{END}) and maximum weight loss rate (T_{MAX}) temperatures, are compiled in Table 6. In all of the feedstocks, the onset temperatures in the air atmosphere are lowered than the ones that were measured in the nitrogen atmosphere. This result is due to the oxidative effect of oxygen both for CAB and PEG.

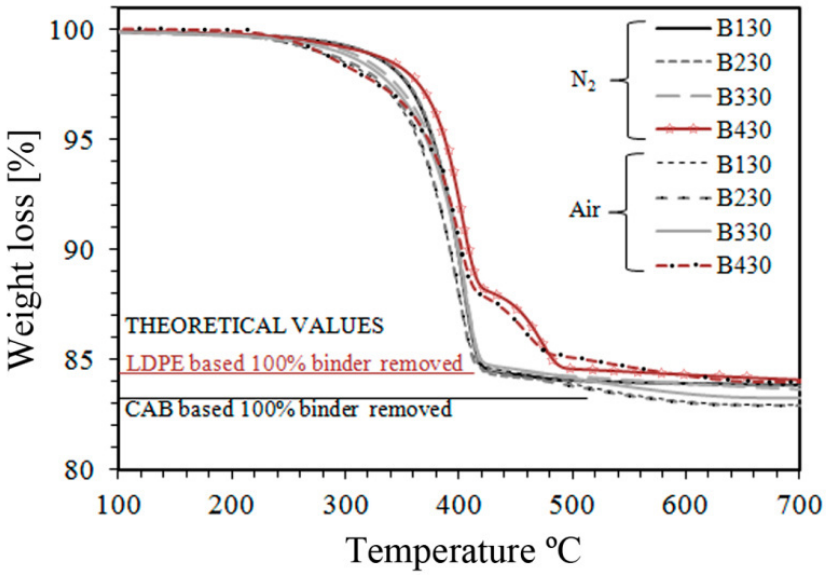

Figure 7 TGA results of the thermal elimination of the organic components in an N_2 protective atmosphere and in an air oxidising atmosphere. Bottom left legend: the grey and red lines indicate the theoretical weight loss values considering 100% binder removal for the CAB-based and LDPE-based binders, respectively.

The feedstock that was based on LDPE degrades in two subsequent steps according to the degradation temperature ranges of PEG first and LDPE second. The feedstocks that contained various types of CAB behave similarly, with the decomposition of the binder components occurring in a single stage. This contrast with the two well-defined decomposition steps that are observed in the sole binder TGA curves (not presented in this work) corresponds to the volatilisation of CAB and PEG. The occurrence of a single step could be associated with a juggling effect between CAB and the zircon powder, which, in principal, is beneficial for the homogenisation of all the feedstock components. However, the degradation temperature intervals for the CAB-based feedstock is narrow and, combined with the concurrent degradation of the CAB and PEG molecules, leads to a risk of defect formation, most likely blisters, when a single thermal debinding step and high heating rates are used. This phenomenon requires a drastically reduced heating rate of 0.1ºC/min to avoid blister formation, which still occurs when heating at 0.5ºC/min during the thermal debinding of the injected bending test green pieces. However, even for 0.1ºC/min, internal pressures were generated in the case of the thermal degradation of B130 and B330 that produced part deformation. This phenomenon was not observed in the B230 and B430 parts.

Table 6 Different temperatures of the degradation intervals for the different feedstock compositions. Because B430 degrades in two subsequent steps, the table contains the temperatures intervals of both steps.

Atmosphere	Air				Nitrogen			
Binder	**B1**	**B2**	**B3**	**B4**	**B1**	**B2**	**B3**	**B4**
$\mathbf{T_{onset1}}$ **[ºC]**	250.6	253.0	257.5	232.8	349.6	347.9	318.4	259.5
$\mathbf{T_{max1}}$ **[ºC]**	401.2	400.0	404.2	399.6	402.9	403.5	404.3	401.8
$\mathbf{T_{end1}}$ **[ºC]**	411.1	410.2	416.5	430.7	413.6	413.1	416.3	433.8
$\mathbf{T_{onset2}}$**[ºC]**	-	-	-	430.7	-	-	-	433.8
$\mathbf{T_{max2}}$ **[ºC]**	-	-	-	460.9	-	-	-	473.8
$\mathbf{T_{end2}}$ **[ºC]**	-	-	-	479.2	-	-	-	492.8

It could be observed from the Figure 7 that all of the binder systems are completely removed from the bulk part at 500ºC in the case of an air atmosphere. However, when using a nitrogen atmosphere, all of the CAB-based binders leave a residue that is not eliminated even when the feedstocks are heated up to 700ºC. This residue, which is presumably mainly composed of carbon, is undesirable because it could contaminate zircon during sintering and weaken the zircon properties. Therefore, an air atmosphere is preferred for debinding zircon feedstocks because oxygen would not affect zircon at the chosen thermal debinding temperatures and would completely remove any carbon source before the sintering stage.

3.3.2 Solvent Debinding

The solvent debinding of one of the binder components is normally performed prior to the thermal debinding of the other binder components because several advantages are achieved. Thermal debinding occurs at the same time in the whole volume of the green part. The generated volatiles are evacuated via diffusion through the melted components, which could

build up pressure inside the part core and generate defects, thus distorting the part geometry. When some of the binder components are removed by a solvent, the process evolves from the part surface to the inner core, thus creating interconnected pore channels that will facilitate subsequent volatile removal during thermal debinding. Thus, not only are distortion defects avoided, but higher heating rates are possible, thus considerably reducing the PIM time cycle.

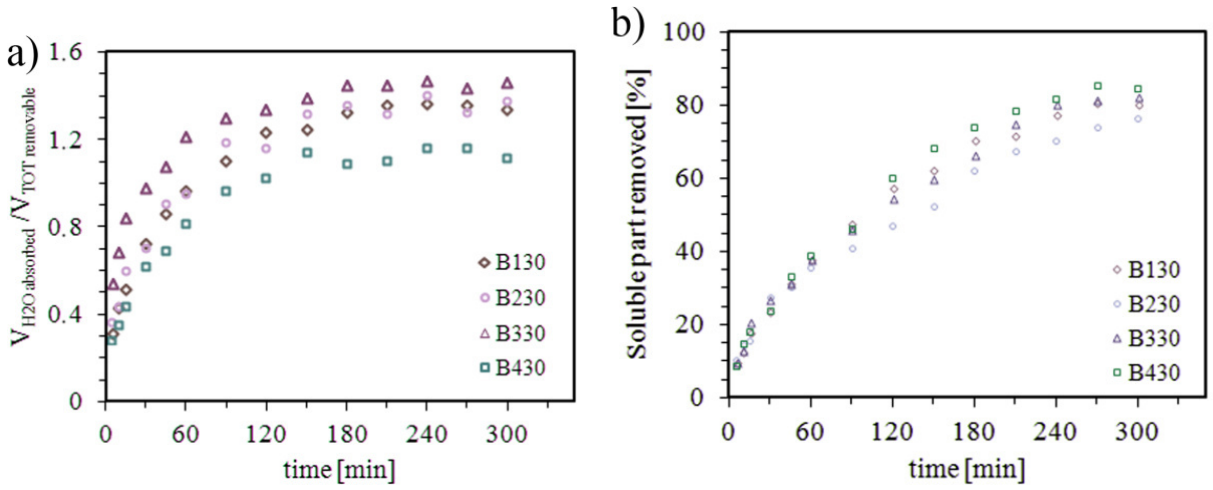

Figure 8 Solvent debinding in distilled water at 60ºC: a) ratio between the absorbed volume of water divided by the total eliminable volume of PEG with time; b) percentage of PEG eliminated with time.

In this work, PEG was chosen as the water-soluble binder component. To study the evolution of PEG elimination in a water solvent, several green parts of different feedstocks were immersed in distilled water at 60ºC and extracted after certain times up to 300 minutes. The part weights before immersion, just after extraction and after drying in a furnace at 70ºC overnight were measured. The water absorption and removed PEG percentages with time were assessed using these weights. Figure 8a represents the volume of water that was absorbed with time normalised to the total eliminable volume of PEG. All of the parts have approximately the same cross-section. From the graph, it could be deduced that, independent of the feedstock type, water takes approximately one hour to completely diffuse in the part bulk. This result coincides with the stabilisation of the water absorption value. Differences are observed in the percentages of the water that is absorbed for each feedstock type, which could be explained by the differences in the swelling levels. If undesired swelling is produced, the volume of the part is altered and the capacity to absorb water is modified. The more the part swells, the more water that is admitted. A volume ratio between the water absorbed and the total volume of eliminable PEG of greater than one indicates swelling. This fact was corroborated by the measurements of the parts before and after immersion. One possible reason why B330 exhibited a higher water absorption level than the other binders is the high hydroxyl group percentage in the CAB chains compared with those of B130 and B230, which both have the same amount of hydroxyl groups and behave similarly. This fact also would explain the behaviour of the B430 parts. B430 contains LDPE with no hydroxyl groups, so this composition has the least water absorption.

Figure 8b represents the soluble part of the binder that is removed with time. It could be observed that three different kinetics occur: first, water starts diffusing before PEG removal, then, the PEG elimination rate increases, most likely because the part begins to swell, and, finally, when the water absorption reaches a maximum, the PEG elimination then decelerates as the pathway to reach the part surface lengthens. In the order B430, B130, B330 and B230, PEG is eliminated more rapidly and more efficiently. Because the binder components are more compatible, it would be more difficult to separate them and to extract one of the components from the others. This phenomenon could occur with B330 and B230, which already demonstrated good affinity between these types of CAB and PEG. Conversely, B430, which exhibited the worst affinity between LDPE and PEG, resulted in a system with a better PEG elimination.

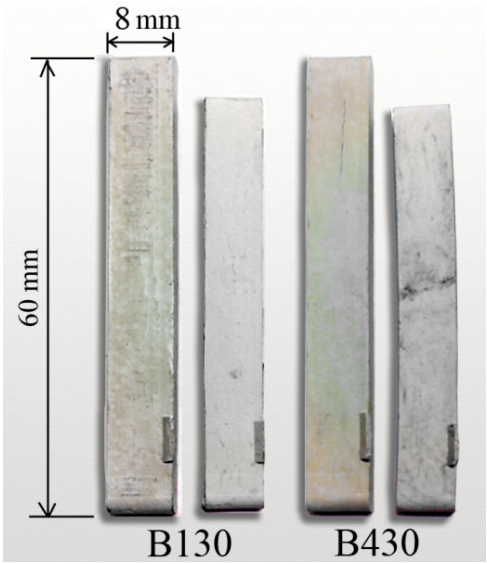

Figure 9 Comparison between the green parts (left) and the sintered parts (right) for compositions B130 and B430. Both sintered parts were subjected to a solvent debinding step. The curved shape in the case of B430 is caused by heterogeneities in the part. In all of the parts, near the bottom right corner, the injection point could be observed.

3.4 Densification after sintering and bending strength

After debinding, the parts were sintered in a vacuum atmosphere at 1450ºC for one hour. Heating up to 1450ºC was conducted with a heating rate of 5ºC/min. These conditions were selected not to obtain a fully dense part but to initiate the sintering mechanisms and to maintain some porosity to determine if the LDPE fibres in the B430 feedstocks influence densification during sintering. Furthermore, two different debinding processes were used, as reflected in Figure 2. The first process consisted of solvent debinding for six hours, followed by thermal debinding, and the second process consisted of full thermal debinding. A comparison between the green parts and the sintered parts for the B130 and B430 compositions are shown in Figure 9. The main differences between the CAB and LDPE compositions are evidenced on the macroscopic scale by the curved shape after sintering of B430 in contrast with the straight shapes of the CAB-based sintered parts. This phenomenon is

a direct result of the distribution of the binder components on the microscopic scale, with a more homogeneous distribution occurring for all of the components in the case of the CAB-based feedstocks, as discussed in previous paragraphs.

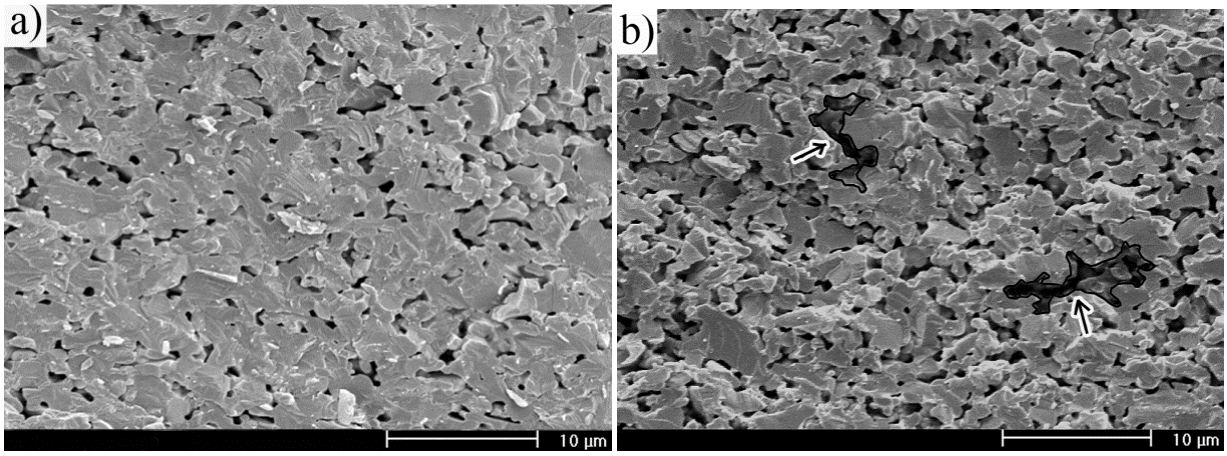

Figure 10 Fracture surfaces of the sintered parts after the bending test: a) the B330 sintered part and b) the B430 sintered part; the porosity that is most likely derived from the LDPE elimination is indicated by the arrows.

On the microscopic scale, Figure 10 shows some examples of the magnified fracture surfaces after bending test of the sintered parts. Differences in the residual porosity densities and the porosity types could be observed between the CAB- and LDPE-based binders. The B330 parts exhibited the best densification of all the compositions (Figure 10a) with small round pores. The rest of the compositions produced similar densification results, as exemplified by B430 in Figure 10b. However, in the case of B430, some areas with larger-than-average pores could be observed (as indicated by the arrows). These pores appear to have inherited the morphology and volume that was left by the LDPE fibres (Figure 6d) after debinding.

The bending strength results for the different compositions and the debinding conditions are reflected in Figure 11, along with the fracture surface typology and defects. In the case of the solvent debinding methodology, the best results were obtained for the B130 and B330 compositions. High bending strength values were obtained for composition B330, even though the parts exhibited pronounced cracks in the fracture surface, which are most likely caused by swelling after solvent debinding. The compositions B230 and B430 exhibited lower bending strength values, with B230 having a higher variability in the measurements. This variability for B230 was observed in the green strength measurements and is most likely a consequence of macro-defects, such as voids or little delaminating layers, that are due to solvent debinding. Generally, the fracture surfaces of the CAB-based parts that were subjected to solvent debinding exhibited a well-defined typology of two trapezoidal surfaces converging in the middle of the fracture surface. This typology is not exhibited in the case of thermal debinding, which may indicate that it is a consequence of solvent debinding.

In the case of the thermal debinding parts, B130 and B330 exhibited a large blister in the middle of the fracture surface that extends all along the part length. This phenomenon may be

the reason for the lower bending strength values compared with B430 and the increased variability in the results. However, in this case, B230 behaves better with no blistering effect observed, which leads to an improved bending strength in comparison with B430, although some other macro-defects were observed, such as internal voids. This result reveals the importance of the porosity that is generated on the microscopic level.

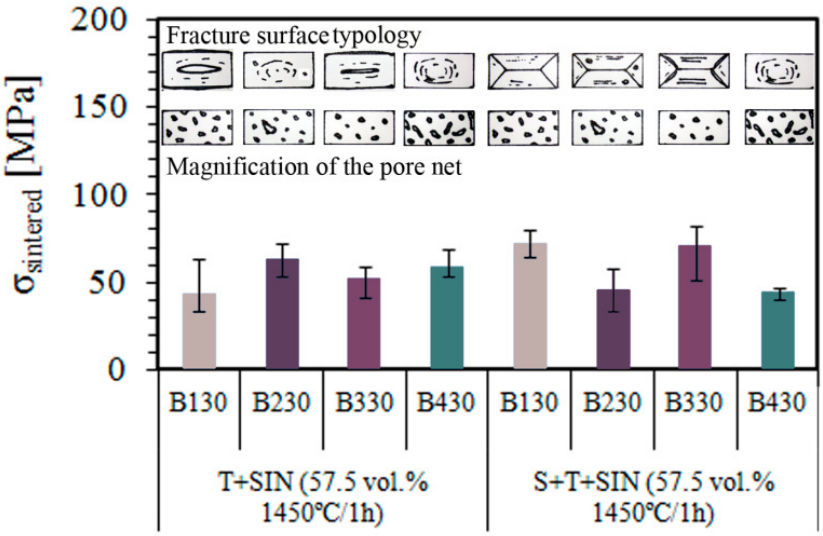

Figure 11 Bending test results of the sintered parts with sketches of the fracture surface typologies and pore nets for the different cases.

The obtained bending strength results were low for all of the cases compared with other processing methods or conditions. Bernardo et al. [14] obtained bending strength values of higher than 150 MPa in PIM sintered zircon parts, but a solid loading of 60 vol.%, a sintering temperature of 1500ºC and a sintering time of 3 hours were used, which favour densification. Shi et al. [2] obtained flexural strength values of approximately 160 MPa in hot-pressed parts that were sintered at 1500ºC for 1 h using a crosshead speed of 0.5 mm/min. It should be noted that, in this work, the sintering conditions were chosen not to fully densify the parts but to study the remaining porosity dependence on the binder system composition. In this respect, the CAB-based compositions were shown to produce denser pieces than LDPE-based feedstocks, not considering the defects that were generated. Moreover, these binder systems have a higher solid loading and better homogenise all of the components in a way that would improve the mechanical properties if the sintering conditions are also improved.

4. Conclusions

The influence and suitability of different binders for developing zirconium silicate feedstock for LPPIM were studied. This work focused on the influence of different CABs with variable contents of butyryl, acetyl and hydroxyl groups in the main polymeric chain. A conventional LDPE binder formulation was also selected for this study.

In principal, the binder composition severely influenced the behaviour of the as-created feedstock at all stages of the LPPIM process. The CAB-based formulations exhibited better miscibility with the PEG water-soluble part and, possibly, improved affinity with the zircon powder particles as more homogeneous distributions were observed for all components. This phenomenon generally leads to better shape retention after sintering and avoids curved parts, which occurred with LDPE feedstocks. The CAB formulations exhibited generally better mechanical properties for both the green strength and the bending strength in comparison with the LDPE formulation. The higher strength after sintering was associated with the morphology and size of some pores, which were most likely inherited from the sites that were occupied by the LDPE fibres as opposed to the small round pores that were left by CABs.

Of the CAB feedstocks, B130 exhibited the most equilibrated features at all the LPPIM stages and produced pieces with less defects and superior properties. This composition has CAB with low contents of hydroxyl and butyryl groups. Several macro-defects and possible internal stresses arise in the CAB-based compositions during the injection and debinding stages. For these feedstocks, it is difficult to solely use thermal debinding due to the coincidence of the PEG and CAB degradation ranges. This phenomenon most likely occurs due to a good affinity between both substances and with zircon powders because, separately from the powders, the binder degrades in several different temperatures ranges that coincide with the elimination of the organic components. Higher swelling and higher water absorption were observed for the CAB compositions during solvent debinding. These phenomena may be consequences of the hydroxyl groups that are present in the CAB polymeric chain.

Acknowledgments

The authors wish to thank GUZMÁN GLOBAL S.L. and MIMTECH ALFA for their collaboration on the ECOPIM project (ref. IPT-2011-0931-20000), which was funded by the Spanish Ministry of the Economy and Competitiveness. Furthermore, the authors would like to acknowledge the strong support from the ESTRUMAT projects (ref. S2009/MAT-1585), which were funded by the CAM-Consejería Educación Dir. Gral. Universidades e Investigación, and from the COMETAS project (ref. MAT2009/14448-C02-02), which was funded by the Spanish Ministry of the Economy and Competitiveness.

REFERENCES

1. Rendtorff, N.M., S. Grasso, C. Hu, G. Suarez, E.F. Aglietti, and Y. Sakka, *Dense zircon (ZrSiO4) ceramics by high energy ball milling and spark plasma sintering.* Ceramics International, 2012. **38**(3): p. 1793-1799.

2. Shi, Y., X.X. Huang, and D.S. Yen, *Fabrication of hot-pressed zircon ceramics: Mechanical properties and microstructure.* Ceramics International, 1997. **23**(5): p. 457-462.

3. Schlechtriemen, N., J.R. Binder, R. Knitter, and J. Hausselt, *Optimization of feedstock properties for reaction-bonded net-shape zircon ceramics by design of experiments.* Ceramics International, 2010. **36**(1): p. 223-229.

4. Hidalgo, J., A. Jimenez-Morales, and J.M. Torralba, *Torque rheology of zircon feedstocks for powder injection moulding.* Journal of the European Ceramic Society, 2012. **32**(16): p. 4063-4072.

5. Medvedovski, E. and M. Peltsman, *Low pressure injection moulding mass production technology of complex shape advanced ceramic components.* Advances in Applied Ceramics, 2012. **111**(5-6): p. 333-344.

6. Gorjan, L., A. Dakskobler, and T. Kosmac, *Partial wick-debinding of low-pressure powder injection-moulded ceramic parts.* Journal of the European Ceramic Society, 2010. **30**(15): p. 3013-3021.

7. Krindges, I., R. Andreola, C.A. Perottoni, and J.E. Zorzi, *Low-pressure injection molding of ceramic springs.* International Journal of Applied Ceramic Technology, 2008. **5**(3): p. 243-248.

8. Kaiser, A., M. Lobert, and R. Telle, *Thermal stability of zircon (ZrSiO4).* Journal of the European Ceramic Society, 2008. **28**(11): p. 2199-2211.

9. Awaad, M. and S.H. Kenawy, *Sintering of zircon: the role of additives.* British Ceramic Transactions, 2003. **102**(2): p. 69-72.

10. Enneti, R.K., V.P. Onbattuvelli, and S.V. Atre, *Powder binder formulation and compound manufacture in metal injection molding (MIM)*, in *Handbook of metal injection molding*, D.F. Heaney, Editor. 2012, Woodhead Publishing Limited: Cambridge. p. 64-92.

11. Hidalgo, J., A. Jimenez-Morales, and J.M. Torralba, *Rheological characterization of zirconium silicate feedstcoks based on water soluble binder*, in *Proceedings EuroPM 2012*, EPMA, Editor. 2012: Basel.

12. Schramm, G., *A practical approach to Rheology and Rheometry*. 2nd ed. 2004, Karlsruhe: Thermo Electron GmbH.

13. Quinard, C., T. Barriere, and J.C. Gelin, *Development and property identification of 316L stainless steel feedstock for PIM and mu PIM.* Powder Technology, 2009. **190**(1-2): p. 123-128.

14. Bernardo, E., J. Hidalgo, A. Jimenez-Morales, and J.M. Torralba, *Feedstock development for Powder Injection Moulding of zirconium silicate.* Powder Injection Moulding International, 2012. **6**(1): p. 4.

Paper 3

P3

J. Hidalgo, A. Jiménez-Morales, J.M. Torralba

Torque rheology of zircon feedstocks for powder injection moulding

This work was published at the Journal of the European Ceramic Society (Vol.32 (16), pp. 4063-4072, December 2012)

Torque rheology of zircon feedstocks for powder injection moulding

J. Hidalgo[*,a], A. Jiménez-Morales*[,a], J.M. Torralba*[,a,b]

[a] Powder Technology Group of Department of Materials Science and Engineering of Carlos III University of Madrid, Leganés, 28911 (Spain)
[b] IMDEA Materials Institute, Madrid (Spain)
*Corresponding authors. Tel. : +34 916249482. E-mail: jhidalgo@ing.uc3m.es (J.Hidalgo), toni@ing.uc3m.es (A. Jiménez Morales), torralba@ing.uc3m.es (J.M. Torralba)

Abstract

In this work, a cellulose acetate butyrate (CAB) and polyethylene glycol (PEG) blend is used as the binder system in a zirconium silicate mineral powder feedstock for Powder Injection Moulding. These irregular zircon powders make the mixing process and the selection of an optimal solid loading level a difficult task. Torque rheology methodologies combined with other techniques are used for evaluation of the parameters affecting the mixing process and determination of the critical powder volume concentration (CPVC). Temperature variations during the mixing process are monitored and used as an indicator of the friction energy of the system and thus for the optimal solid loading selection. There have thus far been limited amounts of work conducted on torque rheology of highly loaded feedstocks that incorporate a study of the system's temperature evolution. A detailed study could be a key factor for understanding the mixing behaviour of highly loaded feedstocks.

Keywords: Powder injection moulding, torque rheology, zircon, cellulose acetate butyrate

1. Introduction

Powder Injection Moulding (PIM) has become a competitive manufacturing technology that can be applied to nearly any ceramic or metallic material processed as fine powder. PIM is suitable for applications which require a large production series of complex geometries, even to the point of occasionally being the only viable method for producing a particular part or product.

The solid loading level and mixing methods are two factors that determine many characteristics of the feedstock. Feedstock homogeneity during the mixing stage is crucial to achieving good results throughout the PIM process and consistent products [1, 2]. Careful choice of mixing method and parameters is the key for achieving a homogeneous mixture that is free of agglomerates and has an optimal powder and binder content [3]. Solid loading is defined as the ratio of powder volume to the total volume of solids and binder. Determination of the optimal solid loading admitted by the binder system is also important. After binder removal, much empty space is left between powder particles, which should be filled by atomic diffusion during the sintering stage. This mass transfer during sintering causes shrinkage and

densification in the piece. Minimising the binder content without compromising the rheology and the integrity of the feedstock assists in increasing process tolerances and reducing cycle time.

Torque rheometers are used extensively as tools for characterising the evolution of the feedstock component mixing process and for evaluating the mixture homogeneity. They have also been demonstrated to be quite useful for determining the optimal and critical solid loadings for a feedstock [4, 5]. In a torque rheometer, the torque exerted by gyratory rotors to displace a bulk of a fluidised mass is measured as a function of the time to create a plot of torque versus time, called a rheogram. The torque is related to the fluid viscosity and can thus serve as a measure of the resistance of a fluid to deformation by either shear or tensile stress [6].

In this work, torque rheology was used to characterise some important aspects of the mixing behaviour of micron-size zircon powders with water soluble binder systems based on PEG and CAB. Variations in mixing torque and feedstock temperature over time at several different solid loading levels has been studied. Zircon powders have non-conventional attributes for a PIM process which requires special consideration for the interpretation of results. Several authors have noted atypical behaviour in torque-based evaluations of the critical powder volume concentration (CPVC) of non-conventional PIM powders. Aggarwal et al. [7] describe abnormal rheological behaviour in torque experiments to determine the critical solid loading of irregularly shaped niobium powders. The CPVC value could not be clarified with this method due to absence of instabilities for solid loading values in the CPVC region. Barreiros et al. [8] also note the problem and further present a new methodology for the determination of critical solid loading by torque rheology for unconventional PIM powders, based on the intersection of different linear trends in plots of torque versus solid loading.

These non-classical torque behaviours make it difficult to determine the feedstock's critical solid loading. Feedstock temperature will be monitored during mixing, which will reveal some important aspects to consider when the critical solid loading is assessed. Although it is well known that temperature influences rheology, its variation during the mixing process is not often [9] considered in torque rheology. For supporting torque rheology measurements, capillary rheology and density measurements of the resulting feedstock have been carried out. A complete PIM process has been also carried out for a feedstock composition optimized with the above methodologies proposed.

2. Materials

Micronised mineral zirconium silicate sand was used for the study. The powders were supplied by GUZMAN GLOBAL S.L (Nules, Spain). They present an irregularly shaped morphology as shown in Figure 1, which also shows the particle size distribution curves for the zircon powder. A Malvern 2000 laser scattering particle size analyzer was used to measure particle size distribution. The irregular morphology of these powders contrasts with the spherical or round-shaped powders conventionally used for PIM.

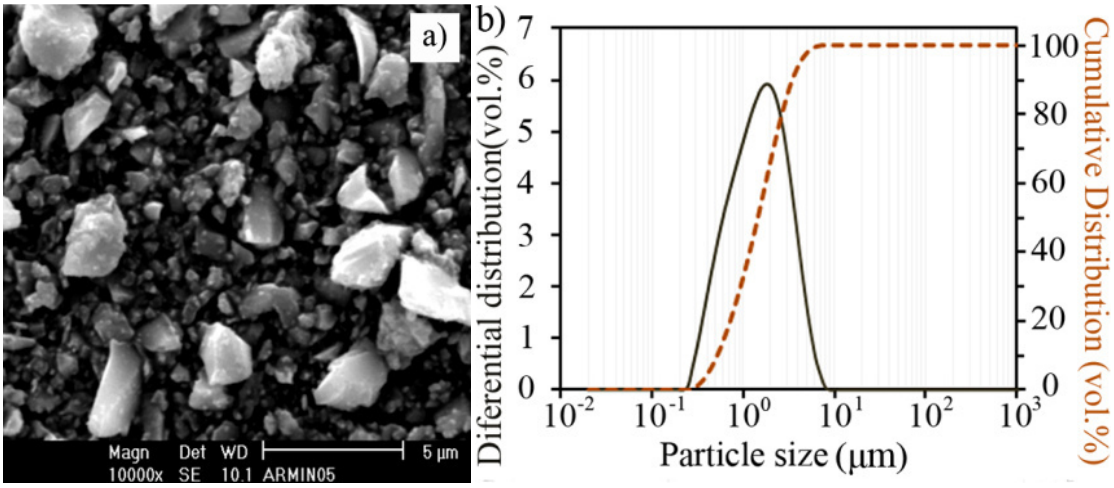

Figure 1 a) An SEM micrograph of zircon powders and b) their particle size distribution curves by laser scattering.

The particle size of the D_{50} and D_{90}powders are1.604 and 4.65 µm, respectively, which corresponds to values extremely low for PIM. The powders have a specific surface area of 5.0363 m²/g, which was measured using a Micrometrics Gemini VII BET measurement device. The low tap and apparent densities, 32.45 % and 21.07% of the material density (4.58 $g \cdot cm^{-3}$), respectively, reflect the low packing capacity of the powders and their tendency to form agglomerates, both of which are a direct consequence of the unconventional shape of the powder. These unattractive characteristics would normally make the powder unsuitable for a PIM process [2]. PIM has generally been limited to high performance and dimensionally precise components, associated with the use of expensive raw materials with tailored characteristics. The use of non-conventional PIM powders such as natural raw materials or waste products from other processes has been investigated and shown to be possible [10, 11]. This previous work leads us to consider the use of as-supplied natural zircon mineral sand as a possible raw material for PIM purposes.

Table 1 Composition of the binder.

	CAB381-0.1	**CAB551-0.01**	**PEG20K**	**PEG4K**
VOL.%	10	30	58	2
T_{MELT} [ºC]	155-165	127-142	63-66	58-61
T_{GLASS} [ºC]	123	85	< 0	< 0
M_W	20000	16000	20000	4000
Supplier	Eastman	Eastman	Aldrich	Aldrich

A binder system based on polyethylene glycol (PEG) and cellulose acetate butyrate (CAB) was selected. This type of binder has been demonstrated to be effective for zircon PIM, providing improved properties compared with other binder systems [12]. Two types of CAB, CAB381-0.1 and CAB551-0.01, with different percentages of butyryl, acetyl and hydroxyl groups were blended with two types of PEG, PEG20K and PEG4K, with different average

molecular weights. The composition of the binder system and the characteristics of the components are summarised in Table 1.

3 Experimental procedure

A Rheomix 600 Haake rheometer coupled with a Haake Rheocord 252p module equipped with roller blade-type rotors was used to perform the mixing experiments. A temperature of 150ºC and a rotor speed of 50 r.p.m were used in all experiments and the mixing chamber was filled up with feedstock to 72 % of its volume (the total chamber volume is 69 cm^3). Feedstock temperature and torque were monitored as the output parameters. The equipment is self-calibrating as it reloads at a start of every new measurement. A thermocouple is placed at the confluence of the rotors' flow, where the feedstock is well-mixed, to monitor the temperature of the feedstock. A value for the critical solid loading or critical powder volume concentration (CPVC) will be determined by experiments varying the solid loadings. The CPVC is the ratio at which powder particles are tightly packed and binder fills all the voids between particles. In previous experiments, results have been demonstrated to be highly sensitive to the way in which components are added as well as the percentage of the mixing chamber occupied by the feedstock. Zircon powders, CAB powders and PEG flakes are first mixed and homogenised with a Turbula mixer at room temperature for one hour, and then poured into the rheometer together. The as-prepared solidified feedstocks were grinded in a blade mill to create pellets for further experiments of density measurements and capillary rheology.

To complement torque results, capillary rheology was carried out in a Bohlin Instruments RH2000 Capillary Rheometer. The study comprises the investigation of the relationships between the viscosity and: 1) the shear rate (in a range from 10 to 10000 1/s), 2) temperature (trials from 140 to 170ºC each 10ºC) and 3) solid loading. Several dies and transducer pressure sensors were used to allow a wide shear rate range (3 magnitude orders) and pressure range with the maximum accuracy possible and attending the interval of solid loading proposed. The relation between the die diameter and its length was kept constant in a value of 30, which is the minimum recommended to achieve a laminar flow along the die. In all the cases the apparent shear viscosity was calculated.

4. Results

4.1 Critical solid loading by torque rheology

In Figure 2, torque versus time rheographs and temperature versus time curves are presented for different solid loadings ranging from 52.5 to 65 vol.%. The mixing time was fixed at approximately 50 minutes. For low solid loading contents (52.5, 55 and 57.5 vol.%), the torque value stabilises relatively quickly, in less than 30 minutes from closure of the internal mixing chamber (this corresponds approximately to the maximum torque value registered for each experiment). For the remainder of the higher solid loading content samples, stabilisation of the torque is not completely achieved within 50 minutes. The feedstock temperatures measured during the experiments also follow this trend.

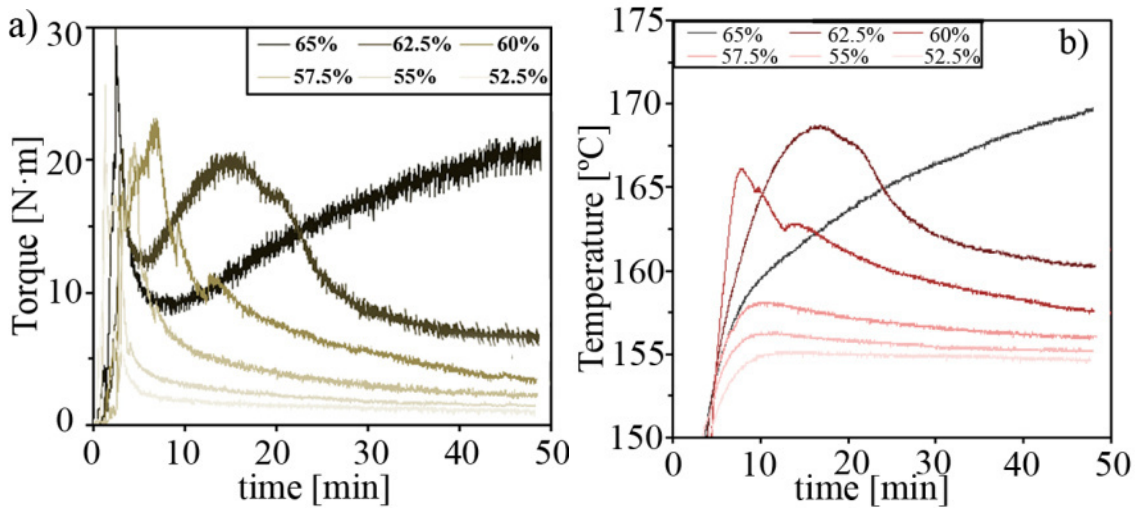

Figure 2 a) Torque vs. time and b) temperature vs. time curves for several solid loading expressed vol.%.

The temperature vs. time curves appear to follow similar trends as those of torque vs. time. The evolution of both parameters, in the case of high polymer loading, can be explained mainly as a direct consequence of the interparticle friction. Thus, both parameters evolve similarly as the particles come closer together with increased solid loading. The only deviation from this trend occurs during the first stage of mixing, but can most likely be attributed to increased temperature from the heating plates rather than particle friction.

Monitoring the temperature can be a helpful complementary tool to find the optimal and critical solid loadings. The critical solid loading could be determined as 65 vol.% because torque and temperature do not stabilise even after a long period of time. The temperature exceeds 170ºC, which is 20ºC above the programmed mixing temperature. However, the 62.5 vol.% sample also shows severe difficulty in achieving equilibrium and high temperatures during the mixing process, indicating high inter-particle friction. Furthermore, for both solid loading values, the average difference between consecutive registered torque values is higher than for the rest of the solid loadings, an indicator of composition heterogeneities and a solid loading over the critical value. This controversy highlights the necessity of employing complementary characterisation techniques to come to a clear conclusion.

The area under the torque vs. time curve at a given time is commonly referred as totalised torque (TTQ)[13]. This value, which represents the energy being put into the system during that given time, is also representative of the total energy dissipation rate in a suspension or likewise, in loaded polymeric blends. TTQ can be used to estimate the relative network strength in suspensions [14], or the processability of polymer-filler composites [15]. In this work, TTQ is proposed as an estimate of friction energy because binders are highly loaded and friction forces predominate over cohesion forces. The TTQ values could also be converted to work energy by equations found in the literature [14, 16]. The work energy supplied to the system by the rotors (E_t) represents a force (F) multiplied by a distance (d). In a torque

rheometer, the distance covered by the blade is equal to the angular speed (*N*) expressed in rpm, multiplied by the average blade radius (*r*) and by two times pi. Considering that torque (*M*) is a function of force, $M = F \cdot r$, the work energy as a function of TTQ is reflected in expression (1):

$$E_t = F \cdot d = 2 \cdot \pi \cdot r \cdot N \cdot \int_{t1}^{t2} \left(\frac{M(t)}{r}\right) \cdot dt = 2 \cdot \pi \cdot N \cdot TTQ \qquad (1)$$

The specific energy of processing (E_{sp}) is obtained from E_t as a function of the material mass inside the mixing chamber (equation (2)),

$$E_{sp} = E_t \cdot m_{feed}^{-1}. \qquad (2)$$

The percentage of specific energy dissipated by friction can be assessed considering the overheating of the feedstock together with the specific heat of the feedstock (equation (3)),

$$E_{frict} = c_{feed} \cdot \Delta T_{oh} \qquad (3)$$

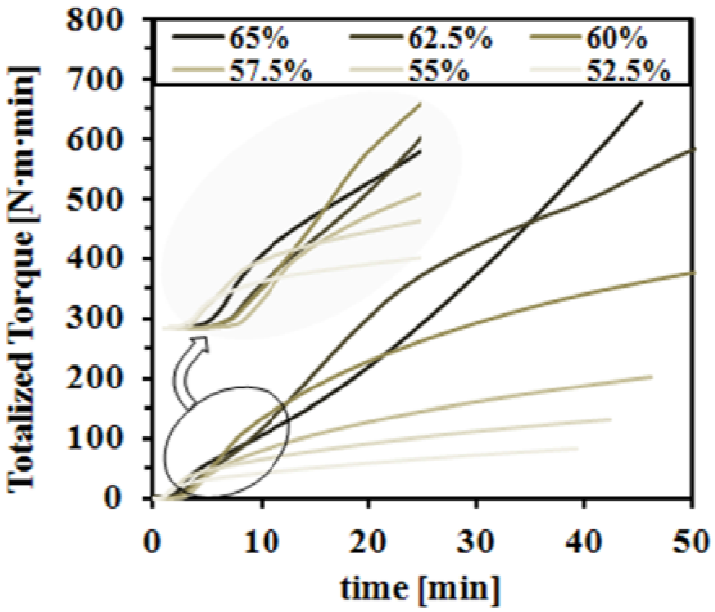

Figure 3 Totalised torque curves for different solid loadings in vol.%.

To better interpret the torque results, totalised torque curves are presented for the different solid loading levels in Figure 3. Processability parameters are summarised in Table 2. The value M represents the average torque value across the torque stabilization region. Then the ΔM parameter represents the average deviation of the torque values from the average value for this region and is a rough indicative of the feedstock homogenization; the lower the ΔM the better the homogenization.

It should be noted that all totalised torque curves have approximately the same slope at the first stages of the experiment. This indicates that in all cases, approximately the same amount of energy is dissipated per unit of time during this period. This result is consistent if it is

considered that at the very beginning, all mixtures are in a similar situation in which interparticle friction is predominant before complete particle dispersion in the binder. This slope is maintained for a period of time depending on the solid loading level, and then it changes to a less pronounced slope which is maintained for the rest of the experiment.

Table 2 Processability parameters after 50 min of mixing.

POWDER VOL.%	**M** [N·m]	**ΔM** [N·m]	**T** [ºC]	**TTQ** [J·min]	**E_t** [17]	**E_{sp}** [J/g]
52.5	1.06	0.18	154.8	99.7	31.3	213.0
55	1.44	0.14	155.2	129.7	40.7	269.5
57.5	2.20	0.30	156.0	202.1	63.5	408.9
60	3.18	0.26	157.4	376.7	118.3	742.4
62.5	6.15	0.48	160.8	579.9	182.2	1114.1
65	20.20	0.98	169.3	738.3	231.9	1383.6

The period in which the initial slope is maintained depends on the ability of the system to incorporate the binder and coat the particles. The ability of the system to accomplish it decreases as the solid content increases. The final slope also rises as the solid loading increases, which indicates the increasing dissipation of energy and is also consistent with the increased temperature behaviour. As the solid loading increases, less binder is available to lubricate the particles, decreasing inter-particle distance and increasing the probability of contact. Friction work is converted into heat. As the friction work increases, the system is less able to dissipate heat and thus, the temperature rises. All the materials behave following curves that, after an initial period of strong growing, trend to reach a steady state regime with the time, except those curves for 62.5 and 65 %. In these former cases, the curve for 62.5% seems to be capable to reach the steady state regime after much higher times, but the curve related 65% it cannot be occur. This behaviour could be an indicator that the CPVC has been reached or overcome.

4.2 Feedstock density measurements

Determination of the CPVC was also accomplished with a density technique. The density of the resulting solidified feedstock was measured with a Micrometrics AccuPyc 1330 helium pycnometer. For compositions above the critical solid loading, the amount of binder is insufficient to cover the particles and fill the remaining free volume. This results in the formation of voids inside the feedstock bulk; considering that no material is lost during the mixing process, this means that the density will be lower than the theoretical density. Determination of the CPVC by measurement of the feedstock density takes this fact into account. For solid loadings near 100 vol.%, voids begin to interconnect creating an open porosity and the density values begin to approach the theoretical ones once again.

The density values for the different feedstocks are shown in Figure 4. It can be appreciated that for all the different solid loading levels, the measured value is very close to the theoretical

value. Moreover, the deviation of the measured density values from a mean density calculated from three different batches is almost negligible. The only exception is the 65 vol.% solid loading sample; the pronounced divergence from the theoretical density indicates excess powder content and the resulting formation of voids. This observation, taken together with the torque experimental results, indicates that the critical solid loading value is approximately 62.5 vol.%. The formation of voids can be observed in Figure 5, which shows scanning electron microscope (SEM) images of as-prepared 52.5and 65 vol.% solid loading feedstocks. In the 52.5 vol.% solid loading sample, shown in Figure 5a, it can be observed that the binder completely covers all powder particles, representing an excess of binder. For the 65 vol.% solid loading feedstock shown in Figure 5b there are heterogeneous regions indicating a lack of binder and voids are clearly visible.

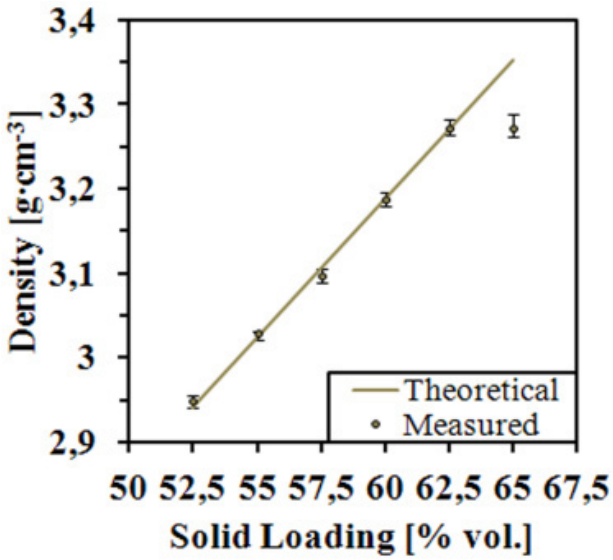

Figure 4 Density(theoretical and measured) of the feedstocks for different solid loadings.

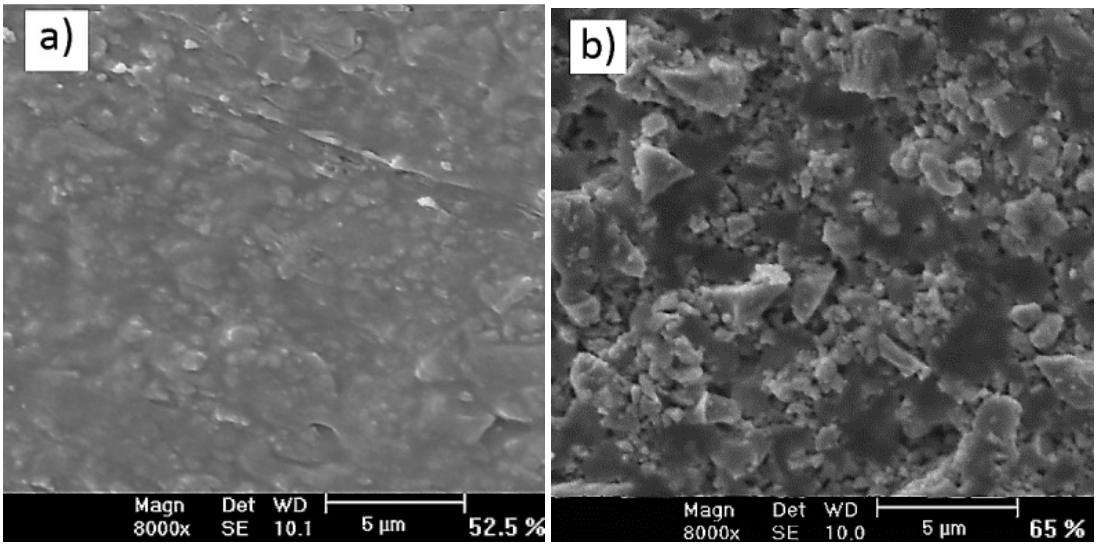

Figure 5 SEM images of as-prepared feedstocks: a) 52.5 vol.% of zircon, b) 65 vol.% of zircon.

4.3 Capillary Rheology

Capillary rheology was used both to determine the rheological behaviour of the feedstocks and to assess the CPVC value. This kind of rheology allows studying the viscosity and its dependence with different affecting variables. The main influencing variables on the viscosity of PIM feedstocks, shear rate ($\dot{\gamma}$), temperature (T) and solid loadings (ϕ), were analysed.

4.3.1 Shear rate and solid loading viscosity dependence

Regarding the shear rate viscosity dependence, PIM feedstocks normally behave as pseudoplastic materials along the entire shear rate ranges typical for PIM (10^1 to 10^4 s^{-1}) ; their viscosity decreases with an increment of shear rate. This behaviour can be approximately described by the power law (4):

$$\eta = k \cdot \dot{\gamma}^{n-1} \qquad (4)$$

where n is the so-called flow index and represents the shear rate sensitivity. Values of n<1 corresponds to the mentioned pseudoplastic behaviour. As the value approaches n=1 the feedstocks viscosity becomes less sensitive to shear rate until the value 1 is reached; in that case viscosity does not depend on shear rate. This kind of behaviour is referred as Newtonian. For values higher than 1, viscosity increase with an increment of shear rate which is referred as dilatant behaviour. Powder law is effective for its straightforwardness, but fails in predicting viscosity when shear rate trends to cero or infinite. It requires materials with infinite viscosity at shear rates near zero and zero viscosity as the shear rate take values near infinite which is not the common case. There are a number of other models that could better describe the whole flow behaviour of shear-dependent fluids, but they do so at the cost of simplicity.

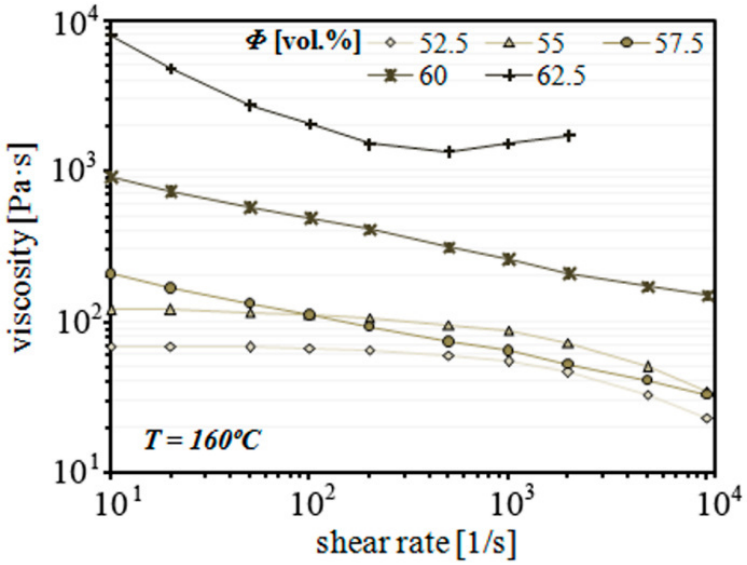

Figure 6 Experimental results of the shear viscosity dependence with shear rate for different percentages of solid loadings for 160º C.

Figure 6 shows the variations of the shear viscosity value for different shear rates in the range from 10^1 to 10^4 s^{-1} and for the temperature of 160º C. In low solid loading feedstocks (52.5 and 55 vol.%) a Newtonian behaviour is distinguished for low shear rates, which turns into pseudoplastic for higher values. This fact happens for all the temperatures studied (from 140º C to 170º C), being markedly more clear at higher temperatures. The turning point for the behaviour change is displaced to lower shear rate values as the temperature decreases. For 57.5 and 60 vol.%, the behaviour is completely pseudoplastic. In case of 57.5 it can be seen at Figure 6 that the curve overlaps the 55 vol.% one. This is an uncommon behaviour as it is a generally accepted statement that viscosity of compounds at all concentrations is higher than of the preceding lower concentration.

An explanation is unclear, but it could be justified considering the presence of agglomerates. Torque rheometer could be limited for exerting enough shear stresses to agglomerate breakage [3]. If the binder is not able to provide with enough shear stress too, high binder contents could also limit agglomerate breakage [18]. However during mixing process of high solid loadings concentrations at torque rheometer, agglomerates interactions increase. Thereby erosive effects become notorious and thus it does agglomerate rupture. It is well established that presence of agglomerates affects feedstock viscosity; the greater the number of particles in the agglomerate, the lower the packing density and the higher viscosity [1, 2]. This should also be reflected accordingly in the torque values, but stabilized torque values increase with the solid loading. Nevertheless, the shear rates in torque rheometer are in the order of 10-100 s^{-1} [6].

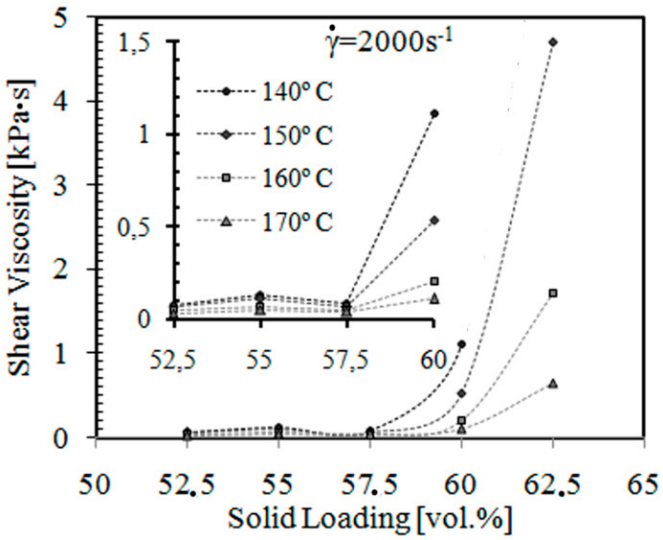

Figure 7 Dependence of shear viscosity with solid loading for different temperatures and for the shear rate of 2000 s^{-1}.

For such values, capillary rheology results are consistent with torque measurements. In contrast, shear stresses produced by the capillary could be high enough for develop hydrodynamic or erosive agglomerates destruction at high shear rates. It is widely accepted that the change from Newtonian plateau to non-Newtonian flow arises from the disruption of

agglomerates [19] among other possible factors, which would explain the behaviour observed. As the experiment temperature is increased, viscosity of binder decreases as well as the viscous forces imposed by the binder on the particles making the agglomerated structure to prevail for a wider shear rate interval.

In the case of 62.5 vol.% feedstock, a dilatant behaviour is observed for high shear rates. This is an indicative that a solid loading percentage is within the region near the CPVC and the feedstock is not suitable to be injected. Moreover, pressures registered for values above 2000 s^{-1} exceed the maximum of the permitted by the pressure transducer used. The same occurs with 65 vol.% of solid loading in which no viscosity value could be registered for any temperature value, being imprecise if this happened because of flow restriction or equipment limits.

The solid loading dependence of viscosity for different temperatures at 2000 s^{-1} is shown in Figure 7. There it could be appreciated more clearly the viscosity fall from 55 to 57.5 vol.% that come about for all temperatures and then the abrupt rising for higher solid loadings. At critical solids loading the feedstock has a very high viscosity therefore slight excess binder is used to provide lubricity for molding, thereby, solid loadings of 60 and 62.5 vol.% seems to approach or meet the CPVC condition. It looks like the mixing process of 57.5 vol.% was more effective in the rupture of agglomerates and getting all the components together, therefore, the viscosity descend due to a better packing. However, excepting 62.5 vol.%, all the feedstocks present viscosities under 10^3 Pa·s for all the shear rates and for temperatures above 150º C. These values are considered quite reasonable in PIM processes for making possible proper mould filling.

4.3.2 Temperature viscosity dependence

The study of the dependence of feedstock viscosity with the temperature is also important. If the viscosity is very sensitive to the temperature variation, any small fluctuation of temperature during moulding will produce viscosity changes, producing stress concentration in the moulded part, resulting in cracking and distortion. The influence of temperature on viscosity can be expressed by the Arrhenius type equation (5):

$$\eta = B \cdot exp\left(\frac{E_a}{R \cdot T}\right) \qquad (5)$$

where E_a represents the activation energy, R is the gas constant and B is the viscosity at the reference temperature T_0.

Figure **8** shows the temperature dependence of viscosity results for 57.5 vol.% at different shear rates. The activation energy at a certain shear rate and the reference parameter may be estimated by plotting the neperian logarithmic of viscosity of feedstock against the inverse of temperature. The E/R coefficient represents the slope of the resulting linearization curve.

Table 3 collects values of activation energies for different solid loadings and shear rates. Allaire et al. [20] proposed the activation energy value of 40 kJ/mol as the level above which the probability of defects occurring during injection moulding becomes unacceptable for sub-micrometer zirconia blends. All the activation energies, except for the 57.5 vol.% of solid loadings, fairly exceeds this value in almost all the shear rates. These deviations are more pronounced at high solid loadings. In that cases, activation energy increase with the shear rate. For lower solid loading this tendency is the inverse. The reduction of viscosity owing to the pseudoplastic behaviour of these feedstocks at high shear rates appears to dominate the changes in viscosity related to temperature.

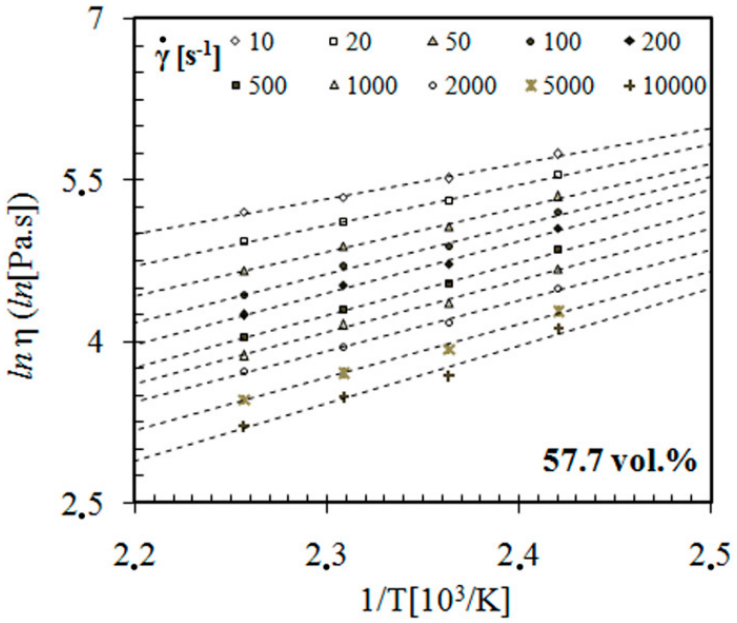

Figure 8 Dependence of shear viscosity with temperature for solid loading of 57.5 vol.%.

Table 3 Values of the activation energy for different solid loadings and shear rates.

	$\dot{\gamma}$ [s^{-1}]		
Φ [vol.%]	**20**	**200**	**2000**
52.5	79.49	64.24	52.32
55	76.40	59.84	46.61
57.5	44.54	40.02	35.90
60	106.66	119.55	119.65
62.5	97.75	252.18	153.72

E_a [kJ/mol]

4.3.3 CPVC determination

The graph presented in Figure 9 shows the evolution of n, B and E rheology parameters with variations of solid loadings for the reference conditions of 160ºC and 2000 s^{-1}. A region of pronounced sudden variation of all rheological parameters (n. E. and B) occurs at 57.5–60 vol% solids loading. This region can be considered as critical solids loading region. A

minimum activation energy is obtained for the 57.5 vol.% , being this solid loading the less sensitive to temperature variations. This minimum matches with a maximum of the B parameter and an inflection point in the value of the flow index. These indicators have been used in several works to give clues of the CPVC values [4, 7].

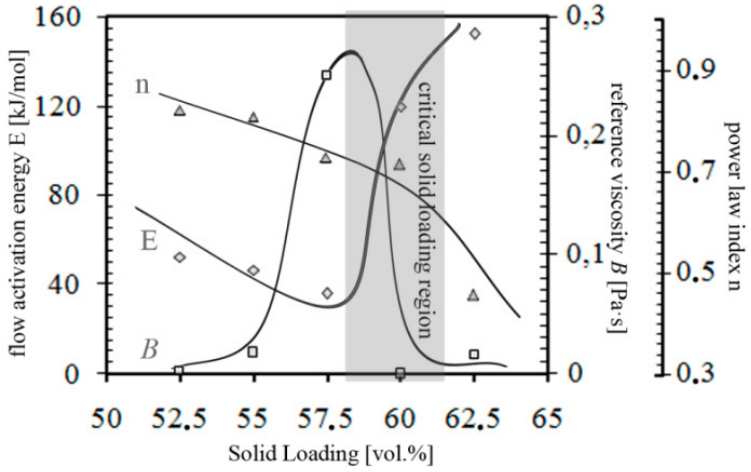

Figure 9 Determination of the critical solid loading region.

4.3.4 General moldability parameter

In the above paragraphs rheology parameters were separately studied and plotted in different axes giving unclear or incomplete insights for optimal solid loading value determination. A general moldability index α_{stv} is proposed to summarize and globally describe the rheological behaviour of a feedstock taking into account all the parameters. This index was developed to compare the moulding capacity of plastics [21], but its utility for other different systems like PIM feedstocks has being also contrasted [22]. The subscripts s, t, v represents the shear sensitivity, temperature sensitivity and viscosity respectively. The general moldability index is defined as (6):

$$\alpha_{stv} = \frac{1}{\eta_0} \cdot \frac{\left|\frac{\partial log\eta}{\partial log\dot{\gamma}}\right|}{\frac{\partial ln\eta}{\partial(1/T)}} = \frac{1}{\eta_0} \cdot \frac{1-n}{E/R} \qquad (6)$$

where η_0 in this work was taken as the reference viscosity at 160º C and shear rate of 2000 s^{-1}. The n parameter is the power law flow index and it was calculated by linearization of power law at the pseudoplastic region of the curves. Linearization was carried out by taking logarithms in both sides of the equation (4).

The higher the moldability index is the better the general rheological properties are. In that respect it can be stated that 57.5 vol.% feedstock presents the most favourable rheological characteristics, therefore, it can be considered as the optimal solid loading. This solid loading presents the higher value of the moldability index resulting from balanced values of the parameters $1/\eta_0$, 1-n and E/R which evolve differently with solid loadings.

4.4 PIM of optimal solid loading feedstock

A whole PIM process was carried out for 57.5 vol.% feedstock. Bending test specimens with dimensions, 25.2 mm large, 5.61 mm wide, 0.94 mm thick, were injected in an ARBURG injection moulding machine. Temperature of 150º C and pressures of 1800 bar produces best densified green parts out of flaws. Two steps binder removal was carried out. First, a solvent debinding in water was performed to remove PEG and create open channel to facilitate further CAB thermal elimination without defects formation. At 60º C, 86.76 vol.% of PEG was removed in two hours. A thermal debinding in air up to 550ºC allowed burning out completely all the remaining CAB as registered in thermo-gravimetrical analysis measurements with a Perkin Elmer STA6000. The sintering process consisted on a two step sintering cycle in air. Brown specimens were heated up to 1400º C holding this temperature for 15 minutes. Then they were cooled until reach 1100ºC; this temperature was maintained during 120 minutes before cooling to room temperature.

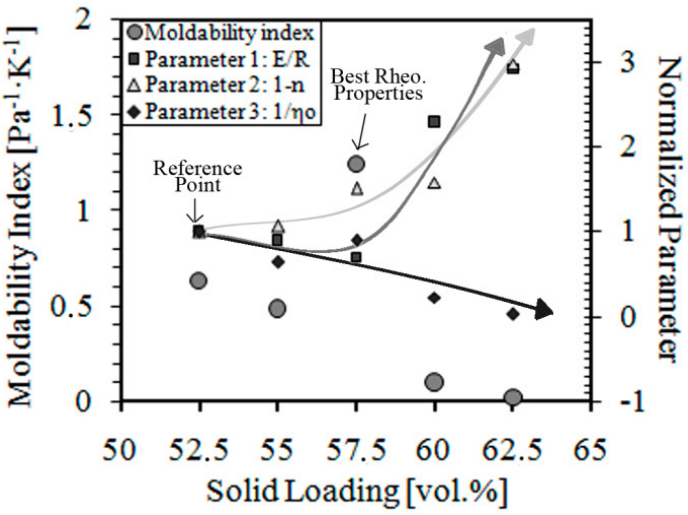

Figure 10 General moldability index versus solid loading vol.%.

In Figure 11 pieces after different stages of the PIM process are presented. The evolution of the specimens' dimensions could be observed. Globally, after sintering, a volumetric shrinkage of 24.82 vol.% was achieved. Pieces keep their shape with no deformation signals and apparently they have no defects. This is a good indicative of feedstock homogenization, good injection and proper further binder elimination stages.

5. Discussion

Classical mixing theory attempts to explain how the torque required to mix a sample is affected by increased solid loading. A model with spherical particles is commonly used to describe the different situations that can occur during mixing of the feedstock components. As the solid loading increases, the particles are more closely packed and there is less inter-particle space occupied by the binder. This normally leads to an increased mixing torque. For PIM feedstocks with spherical or round-shaped powders, the critical powder volume content means

that particles are tightly packed touching ones each other by contact points. The binder fills all voids between particles but it does not form a coating separating particles.

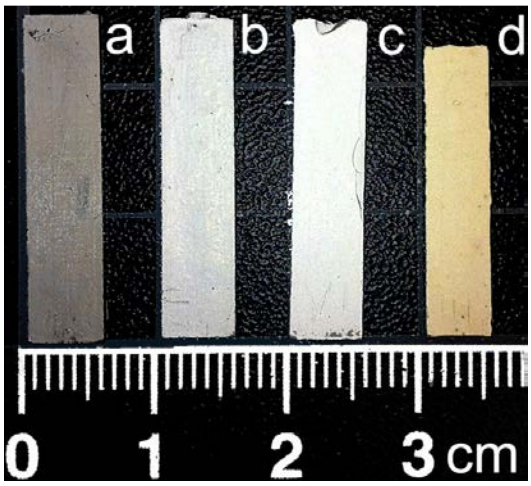

Figure 11 Evolution of specimens during the different stages of the PIM process: a) injected green part b) brown part after solvent debinding c) brown part after thermal debinding d) sintered part.

At the critical solid loading, under classical torque behaviour, the mixing torque increases significantly and becomes erratic due to inter-particle friction. Once the critical point is surpassed, there is no longer enough binder to cover the particles and the capacity of the binder to trap the powder particles diminishes resulting in a reduction of the mixing torque. The feedstock density is also reduced due to void formation in regions that the binder is unable to fill. An optimal solid loading is defined as the ratio of powder to binder near the critical solid loading level in which the particles are tightly packed but there is still sufficient binder to coat them.

For irregularly shaped particles an equivalent particle diameter could be assessed. However, the ability of classical theory to describe non-conventional PIM powders is limited. Increased surface contact is possible with irregularly shaped particles potentially increasing the interparticle friction drastically. A critical situation can also arise without actual particle contact if the particle movement is blocked by severe packing. This can take place even when the particles have a fine coating of binder, which usually acts as a lubricant, if the powder geometry does not allow proper powder flow.

Figure 12 attempts to visually explain this issue. Figure 12A describes a typical situation in which there is an excess of binder. Particles can move with relative freedom, even with enough space for rotation. The opposite situation, in which there is an excess of powder, is shown in Figure 12D with voids coloured black. Figure 12B represents a high particle packing situation in which binder covers all particles and the particles do not touch; this can be considered optimal solid loading, though the freedom of movement seems to be reduced sufficiently to possibly disallow rotation. The situation presented in Figure 12C is even more tightly packed than Figure 12B in which there is evidence of some point contacts, but there is

still enough binder to coat the majority of the particles, a critical loading. Situations B and C would presumably result in high mixing torque values, making it difficult to ascertain which of the situations corresponds to the critical. Although particle movement seems to be prohibited, if it happens, it could be explained by the presence of continuous regions with high binder content along a specific direction.

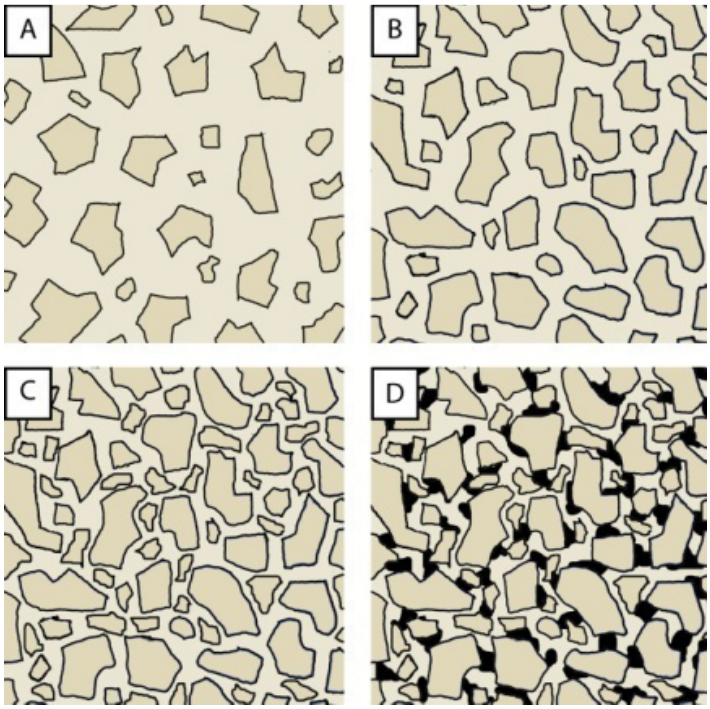

Figure 12 Models of different situations in loaded binders: B) excess of binder. B) optimal load. C) critical load. D) excess of powder with black areas representing voids.

Torque experiments carried out with zircon feedstocks show that a critical situation can occur for solid loadings in which mixing torque stabilises over time. These findings are compared with density measurements and capillary rheology and are reflected in high increases in mixture temperatures and specific processing energies. The melted feedstock flow could be explained by the existence of continuous binder-rich regions which allow movement in certain directions without particle friction, which would lead to torque values lower than expected and stabilisation of the mixing torque at the CPVC. This idea has been proposed by others previously [23] and is known as the slip band theory.

This theory could be consistent with Aggarwal et al. [7] findings. In their work the noticed abnormal torque behaviour with an increase in the torque observed when the solid loading was increased in the feedstock; however, the torque unexpectedly stabilised rather than become erratic for solid loadings corresponding to the CPVC value. This was attributed to a lack of point contacts between particles or what could be related with the slip bands. Nevertheless, the number of particle contacts increase with an increase of the solid loading and is evinced by the rise in feedstock temperature during torque measurements.

6. Conclusions

Facing the task of evaluating the feedstock mixing behaviour of unconventional PIM powders requires special care in the interpretation of results. A combination of different techniques becomes necessary to make a reliable evaluation. Torque rheology experiments provide evidence of the physical changes in the feedstocks during the mixing process.

Monitoring of feedstock temperature can be a powerful tool for interpretation of the mixing mechanism and for determining the optimal mixing parameters. A direct relation between torque and feedstock temperature was revealed by taking into account the level of particle friction, which causes these parameters to rise or fall together. The use of totalised torque curves allows evaluation of energy dissipation during processing that is consistent with the temperature results. The level of temperature rise could be abrupt for loadings near the CPVC composition, which was determined to be between 60 and 62.5 vol.%. These results were contrasted with capillary rheology and density measurements. The optimum solid loading resulted to be 57.5 vol.% which presents the best rheological conditions and an absence of agglomerates due to effective mixing. A complete PIM process was successfully carried out for an optimum solid loading feedstock.

Acknowledgments

The authors would like to acknowledge the companies GUZMÁN GLOBAL S.L and ALFA MIMTech for their support and partnership in the project IPT-2011-0931-020000 granted from the Spanish Ministry of the Economy and Competitiveness and the European Funds for Regional Development (FEDER). They would also kindly thank the Applied Mechanics Department of FEMTO-ST Institute and the ENSMM (Besançon, France) where some of the experimental works were performed. The suggestions and technical support of T. Barriere and G. Michele were much appreciated.

References

1. German, R.M. and A. Bose, *Injection Molding of Metal and Ceramics*. 1997: Metal Powder Industries Federation.
2. Mutsuddy, B.C. and R.G. Ford, *Ceramic Injection Molding*. 1995, UK: Chapman and Hall.
3. Suri, P., et al., *Effect of mixing on the rheology and particle characteristics of tungsten-based powder injection molding feedstock.* Materials Science and Engineering a-Structural Materials Properties Microstructure and Processing, 2003. **356**(1-2): p. 337-344.
4. Contreras, J.M., A. Jimenez-Morales, and J.M. Torralba, *Experimental and theoretical methods for optimal solids loading calculation in MIM feedstocks fabricated from powders with different particle characteristics.* Powder Metallurgy, 2010. **53**(1): p. 34-40.
5. Supati, R., et al., *Mixing and characterization of feedstock for powder injection molding.* Materials Letters, 2000. **46**(2-3): p. 109-114.

6. Schramm, G., *A practical approach to Rheology and Rheometry*. 2nd ed. 2004, Karlsruhe: Thermo electron.
7. Smid, I., G. Aggarwal, and P. Seong Jin, *Development of niobium powder injection molding: Part I. Feedstock and injection molding.* International Journal of Refractory Metals & Hard Materials, 2006. **24**(3): p. 253-62.
8. Vieira, M.T. and F.M. Barreiros, *PIM of non-conventional particles.* Ceramics International, 2006. **32**(3): p. 297-302.
9. Checot-Moinard, D., C. Rigollet, and P. Lourdin, *Powder injection moulding PIM of feedstock based on hydrosoluble binder and submicronic powder to manufacture parts having micro-details.* Powder Technology, 2011. **208**(2): p. 472-479.
10. Agote, I., et al., *Rheological study of waste porcelain feedstocks for injection moulding.* Journal of the European Ceramic Society, 2001. **21**(16): p. 2843-2853.
11. Vieira, M.T., et al., *Optimization of the sintering process of raw material wastes.* Journal of Materials Processing Technology, 1999. **93**: p. 97-101.
12. Bernardo, E., et al., *Feedstock development for Powder Injection Moulding of zirconium silicate.* Powder Injection Moulding International, 2012. **6**(1): p. 4.
13. Cheremisinoff, N., *Product design and testing of polymeric materials*. 1990, USA: Marcel Dekker.
14. Abu-Orf, M. and B. Örmeci, *A new tool for measuring biosolids floc strength*. 2004, USA: IWA, Publishing.
15. Escocio, V.A., et al., *Thermal and Dynamic Mechanical Characterization of TPU/Mica Composites Prepared by Torque Rheometer.* Polimeros-Ciencia E Tecnologia, 2011. **21**(3): p. 240-245.
16. Lapa, V.L.D., et al., *Aluminum hydroxide and carbon black filled NBR/PVC composites-vulcanization and processability studies.* Polymer Testing, 2002. **21**(4): p. 443-447.
17. Salomon, A. and K. Fielder, *Practical use of differential calorimetry for plastics*, in *Hadbook of Plastics Analysis*, H. Lobo and J. Bonilla, Editors. 2003, Marcel Dekker: New York. p. 79-109.
18. Hausnerova, B., *Rheological characterization of powder injection molding compounds.* Polimery, 2010. **55**(1): p. 3-11.
19. Kurzbeck, S., J. Kaschta, and H. Munstedt, *Rheological behaviour of a filled wax system.* Rheologica Acta, 1996. **35**(5): p. 446-457.
20. Allaire, F., B.R. Marple, and J. Boulanger, *Injection-molding of submicrometer zirconia - Blend formulation and rheology.* Ceramics International, 1994. **20**(5): p. 319-325.
21. Weir, F.E., *Moldability of plastic based on melt rheology - 1: Theoretical development.* Spe Transactions, 1963. **3**(1): p. 32-36.
22. Li, Y., B. Huang, and X. Qu, *Viscosity and melt rheology of metal injection moulding feedstocks.* Powder Metallurgy, 1999. **42**(1): p. 86-90.
23. Chuankrerkkul, N., P.F. Messer, and H.A. Davies, *Flow and void formation in powder injection moulding feedstocks made with PEG/PMMA binders Part 2 - Slip band model.* Powder Metallurgy, 2008. **51**(1): p. 72-77.

Paper 4

P4

J. Hidalgo, A. Jiménez-Morales, T. Barriere, J.C. Gelin and J.M. Torralba

Water soluble Invar 36 feedstock development for µ-PIM

This work was published in Journal of Materials Processing Technology (Vol.214 (2), pp. 436-444, 2014).

Water soluble Invar 36 feedstock development for μ-PIM

J. Hidalgo[a], A. Jiménez-Morales[a], T. Barriere[b], JC. Gelin[b], J.M. Torralba[a,c]*

a Materials Science Department at Carlos III University of Madrid, Leganés (Spain)
b Applied Mechanics Department at FEMTO-ST Institute, Besançon (France)
c IMDEA Materials Institute, Getafe (Spain)
* Corresponding author: Avd. Universidad 30, 28911, Leganés (Spain), e-mail: jhidalgo@ing.uc3m.es

Abstract

A water soluble binder system based on cellulose acetate butyrate (CAB) and polyethylene glycol (PEG) is proposed and investigated to carry out a micro powder injection moulding (μPIM) process with an INVAR 36 alloy powders. The overall process was optimised with an emphasis on the determination of the optimal solid loading. Several methodologies were evaluated and compared to determine this parameter. A full μPIM was performed with different powder content feedstocks. Dog bone-type micro test parts were fabricated thereof and their mechanical properties were evaluated. Solid loadings up to 65 vol.% resulted to have the most equilibrated properties to successfully fabricate Invar 36 micro parts with the selected powder and binder system.

Keywords: micro powder injection moulding, INVAR 36, solid loading optimisation

1. Introduction

Micro Powder Injection Moulding (μPIM) is a leading manufacturing method for the production of complex, net-shaped and high performance micro components at competitive costs. As remarked by Heaney [1] and many other authors, this promising technology has experienced rapid growth due to the rising demand for the application of micro components. Attia and Alcock [2] compiled a thorough revision of μPIM. Micro components are classified into the three categories, namely: micro parts, micro-structured components and micro-precision parts. Micro-precision parts are employed for different application, includding micro moulds, micro-mechanics, micro-fluidics, micro-sensors, micro-scale medical devices and other micro systems. Ruh et al. [3] performed studies regarding size accuracy of microgear wheels. They stated that this kind of parts require high dimensional stability and should have tolerances in the micron range. Dimensional changes with temperature can be minimised by employing materials with low coefficients of thermal expansion (CTE). In that respect, Maslyuk [4] et al. reported that iron-nickel based Invar alloys are a potential alternative when an application demands similar characteristics to austenitic stainless steel and also a thermal stability up to around 250 ºC. Within the Fe_x-Ni_{x-1} invar alloy family, INVAR 36 (Fe_{64}-Ni_{36} according to DIN 1.3912) is a suitable material for precision components and utilities, such as clockworks, motor valves and physical or topographical devices. At a 0–100°C temperature range, the CTE of the Fe_{64}–Ni_{36} invar is about $(1–2)\cdot10^{-6}K^{-1}$. Khomenko [5] studied the origin

and specific features of invar anomalies of physical properties of Fe-Ni alloys with FCC lattice. The low thermal expansion coefficient of the alloy is assumed to be due to the competition of magnetic and lattice contributions below the Curie temperature and is associated with the development of an austenitic FCC Fe-Ni lattice.

In μPIM, a powder is mixed with a binder to obtain homogeneous feedstocks with features that allow for the injection of a part with the desired geometry. Once the part is moulded, the binder is removed and the powders are consolidated by sintering. Kong et al. [6] employed different methodologies to the determination of critical and optimal powder loadings for 316L fine stainless steel feedstocks for μPIM. They concluded that the optimal powder content in the powder/binder feedstock and a suitable mixing technique are the keys to achieve a homogeneous feedstock with the best properties after the injection, debinding and sintering steps. The literature includes several examples of the processing of low CTE invar type parts by PIM. Chi et al. [7] performed PIM of complex invar alloy parts by combining Fe carbonyl and Ni carbonyl powders. Do Nascimento [8] investigated different combinations of Iron-Nickel-Cobalt invar type powders for developing PIM parts.

Fabrication of micro parts via μPIM deals with issues that do not occur in conventional PIM processes. One important concern is the need of very fine powders with particle sizes in the micron range. This entail several problems. Suri et al. [9] studied the influence of agglomerates in sinter parts. They concluded that to obtain a homogeneous and high quality feedstock for μPIM, powder agglomeration in the feedstock should be avoided as it leads to defects in the final products. Particle sizes from 0.1 μm to 15 μm are typically affected by agglomeration in PIM. Rajabi et al. (2012) reviewed works that use nanosized powder particles in PIM. Very fine particles and thus agglomeration-prone particles complicate the mixing and rheological behaviour of the as-prepared feedstocks. The micron size of the parts and the reduced diameters of the runners require a better flow behaviour than in conventional PIM. However, one benefit of small powders may be the decrease in the CTE with decreasing grain size. Bitkulov et al. [10] reported a decrease in the CTE by a factor of two between an Invar 36 alloy with coarse and other with very fine grain sizes.

Another important issue to consider is the possible contamination with carbon and oxygen during the processing of micro-scale parts. Maslyuk et al. [4] reviewed different Fe-Ni powder compositions physical properties and their applications and Nadutov et al. [11] and [12] investigated the magnetic properties Fe-Ni-C invar alloys. Both works remarked that presence of C and other elements like N worsen the thermal stability of invar alloys. Hatate et al. [13] reported that the CTE is directly affected by the concentration of carbon and nickel in Fe-(27~40 wt.%) Ni Invar alloy. They also suggested that the CTE of the Fe-Ni-C Invar alloy is affected by Ni segregation in the primary austenite microstructure related to carbon content. However, Wittenauer et al. (1994) and (1996) realised that small amounts of carbon could be beneficial to improve mechanical properties while an acceptable low CTE is maintained. Carbon presumably affects mechanical properties by strengthening the interstitial solid solution.

This work analyses various conventional methodologies along with other techniques to determine the optimal solid loading of Invar 36 low CTE alloy feedstocks for μPIM. The microstructures and mechanical properties of as-produced parts were also investigated. A binder system based on cellulose acetate butyrate (CAB) and polyethylene glycol (PEG) was mixed with Invar 36 powders. The behaviour of this type of binder in PIM processes has received little study. Minseok el al. [14] developed a binder system based on CAB, poly (methyl methacrylate) and PEG. In previous works of Bernardo et al. [15] and Hidalgo et al. [16] have presented CAB as an alternative to conventional polyolefins in binder formulations with water soluble PEG. In Hidalgo et al. [17] this cellulose derivative polymeric substance has exhibited a better affinity with PEG than polyolefin compounds, which may lead to better feedstock homogenisation. They realised that the selected CAB-based feedstocks also generally exhibit better rheological behaviour than polyolefin formulations. This commonly led on to higher optimal solid loadings, which was beneficial for improving the tolerance and properties of the final part. Nevertheless, CAB-based formulations have never been employed in PIM or μPIM of INVAR 36 alloy. This study also demonstrates that this type of binder system is suitable for μPIM of an INVAR 36 alloy up to 65 vol.%.

2. Experimental

Gas atomised Invar 36 alloy powders were used. The INVAR 36 alloy consists of 36 wt% Ni, with the balance comprised of Fe except for some other trace elements. Table 1 presents the composition of the Invar 36 alloy. The powders were supplied by Sandvik Osprey Ltd. (UK). The powder has a particle size distribution with a D_{90} of 5.9 μm. Particle size distribution curves are presented in Figure 1 along with a scanning electron microscopy (SEM) image showing the spherical shape of the particles.

Table 1. Composition of the INVAR 36 alloy with some characteristic particle size parameters.

Composition	**Ni**	**Mn**	**Si**	**C**	**Fe**	**Particle Size Distribution**	**d_{10}**	**d_{50}**	**d_{90}**
[mass%]	36.50	0.20	0.02	0.01	Balance	[μm]	1.9	3.4	5.9

The Invar 36 powders were mixed with a binder system based on a combination of several thermoplastic polymers, including different molecular weights of poly (ethylene glycol) (PEG) (supplied by Sigma-Aldrich) and two types of cellulose acetate butyrate (CAB) (supplied by Eastman) with a variable content of acetyl, butyryl and hydroxyl groups. The binder component contents and component specifications are included in Table 2.

Several feedstocks with variable solid loadings ranging from 57.5 to 70 vol.% were prepared in a Haake Rheomex twin sigma rotor internal mixer, and the same mixing parameters were used for all feedstocks. The feedstocks were mixed at 150ºC and a rotor speed of 50 rpm for

one hour to ensure homogenisation. Capillary rheology measurements were conducted using a Rosand RH2000 capillary rheometer.

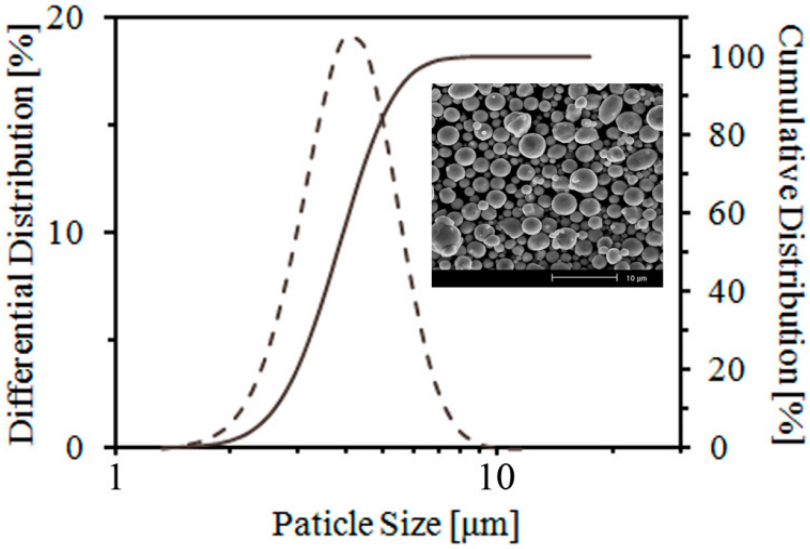

Figure 1. Particle size distribution curves of the INVAR 36 gas atomised powders together with an SEM image of the powder demonstrating the spherical particle shape.

Table 2. Binder composition.

Component	Acetyl*	Butyryl*	Hydroxyl*	%vol
CAB381-0.1	13	37	1.5	30
CAB551-0.01	2	53	1.5	10
PEG 20k	-	-	-	58
PEG 10k	-	-	-	2

** Percentage of side groups in chain*

The relationship between the length and the diameter of the capillary is 30/1 with capillary diameter of 1mm. The density of the resulting solidified and pelletised feedstock was measured with a Micrometrics AccuPyc 1330 helium pycnometer. The feedstocks were employed to perform an entire μPIM process. A Battenfeld microinjection moulding machine was used to inject micro parts for tensile and bending tests. A vacuum atmosphere was used for both the thermal debinding and sintering stages. Solvent debinding in water at 60 ºC for two hours was carried out prior to thermal debinding. A Kammrath and Weiss micro-mechanical testing stage with a load cell of 1 kN was used to perform micro tensile tests at room temperature. Scanning electron microscopy (SEM) was performed using a Philips XL-30 microscope.

3. Results

3.1 Torque measurements

Monitoring the evolution of torque values with mixing time is conventionally used as a simple method to evaluate critical and optimal solid loadings. For example, in the work of Contreras

et al. [18] this technique, in combination with other methods, was employed to study the effect of different particle sizes and geometries. The torque versus mixing time curves of Invar 36 feedstocks with different solid loadings (Figure 2 a) exhibited two different behaviours after the mixing chamber was closed with all the components inside:

i. An abrupt increase in the torque occurred followed by a gradual decrease until it stabilised. This behaviour was observed at solid loading below 67.5 vol.%

ii. For 70 vol.%, an abrupt increase in torque occurred followed by a rapid decrease and a progressive increase thereafter. The torque values varied more erratically during this progressive increase. All these findings are considered evidence of critical solid loading. However, after reaching a maximum, the torque values decreased again and then stabilised.

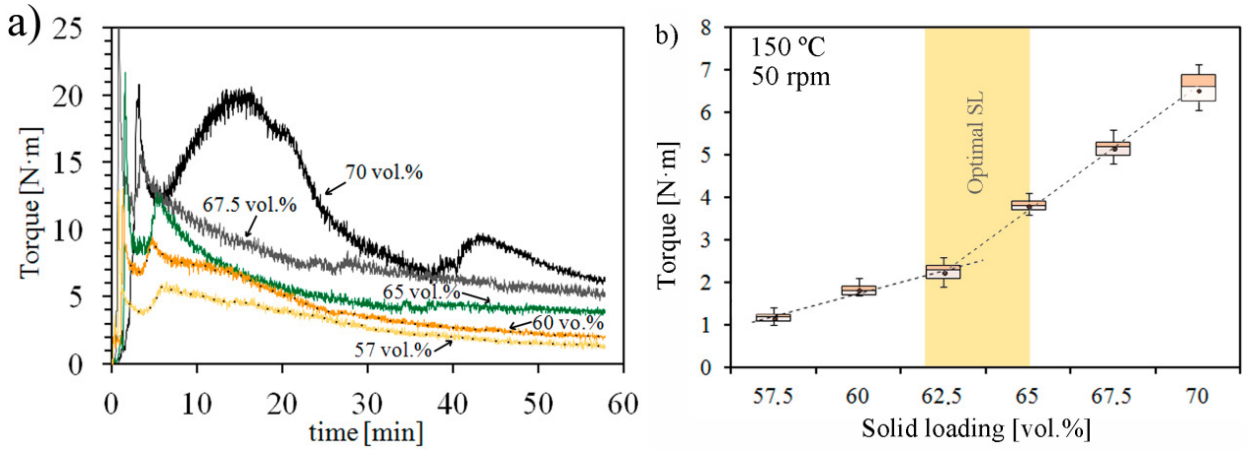

Figure 2. a) Mixing torque as a function of mixing time at 150 ºC and 50 rpm for different powder volume content feedstocks, b) mixing torque as a function of solid loading. The points represent the average torque values over 2 minutes (from minute 60 to minute 62) with values recorded each second. The upper and lower whiskers represent the maximum and minimum torque measured, respectively, the box represents the second and third quartiles, and the line represents the median.

This change in mixing behaviour is normally associated with solid loading near the critical powder volume content (CPVC), i.e., the minimum volume of binder necessary to completely embed powder particles.

As the powder content is increased, it becomes more difficult to incorporate powder into the binder and to achieve a homogeneous component distribution. If particle agglomeration occurs, mixing could also be hindered. Figure 2 b presents the average torque steady flow values after 60 minutes of mixing as a function of powder volume content. The box and whisker plots for each average value illustrate the variability of the results during the last 2 minutes and thus of the homogeneity of the mixtures. A disruption in the torque versus solid loading dependence was observed at 62.5 vol.% feedstock, as it can be seen from the change in the slopes of two straight lines fitting the experimental points. Barreiros and Vieira [19] linked this fact with CPVC. However, they noted that for a better determination of the optimal

solid loading the properties of sintered parts of compositions close to these points should be further evaluated.

In previous works, Hidalgo et al. [16] have monitored a ceramic-type feedstock temperatures during mixing and have noted that the mixture temperature is higher than the programmed temperature for all feedstocks studied. This temperature difference became more intense as the solid loading increased and approximately followed the torque behaviour. This behaviour was related to a particle friction effect and is in agreement with the principle of torque measurements. Temperature and torque parameters are related to the energy necessary to displace and mix all components together. Greater friction between particles leads to a greater restriction to the feedstock flow, increasing the energy needed. In Cheremisinoff [20] the totalised torque value (TTQ) calculated from torque rheology of different polymers is proposed as an useful parameter for several purposes. The energy employed during mixing can be summed up with TTQ, representing the area under the torque vs. time curve at a given time. This value, which represents the necessary mixing energy during a given period of time, is also representative of the total energy dissipation rate in a suspension or in loaded polymeric blends. Abu-Orf et al. [21] used TTQ to estimate the relative network strength in suspensions. Escocio et al. [22] evaluated the processability of polymer-filler composites with the TTQ parameter. In this work, TTQ is used to estimate of friction energy because binders are loaded in high concentrations and friction forces predominate over cohesion forces. The work energy supplied to the system by the rotors (E_t) represents a force (F) multiplied by a distance (d). In a torque rheometer, the distance covered by the blade is equal to the angular speed (N) expressed in rpm, multiplied by $2\pi r$, where the r is the average blade radius. Considering that torque (M) is a function of force, $M = F \cdot r$, the work energy as a function of TTQ is given by the expression (1):

$$E_t = F \cdot d = 2 \cdot \pi \cdot r \cdot N \cdot \int_{t1}^{t2} \left(\frac{M(t)}{r}\right) \cdot dt = 2 \cdot \pi \cdot N \cdot TTQ \qquad (1)$$

The specific energy of processing (E_{sp}) is obtained from E_t as a function of the material mass inside the mixing chamber (Eq. (2)),

$$E_{sp} = E_t \cdot m_{feed}^{-1}. \qquad (2)$$

The percentage of specific energy in terms of heat dissipated by friction can be assessed considering the overheating of the feedstock (ΔT_{oh}) together with the specific heat (c_{feed}) of the feedstock,

$$E_{frict} = c_{feed} \cdot \Delta T_{oh} \qquad (3)$$

Table 3 reports some of the mixing energy parameters assessed after 60 minutes along with the chamber temperatures. A progressive increase in the temperature and the energy necessary to mix feedstock's components was observed as the solid loading increased, with a remarkable increase between two consecutive solid loading values as the CPVC value was approached.

This could be linked with the decreasing capacity of the binder system to lubricate all the powder particles as the solid loading increases, leading to an increase in the friction energy involved in the system which is dissipated as the temperature increases and also affects the torque values.

Table 3. Torque rheology parameters after 60 minutes. From left to right, average torque values with standard deviation, temperature, totalised torque, energy supplied by the rotors, the specific energy for feedstocks with different solid loadings and the friction energy dissipated by heat.

POWDER %VOL.	$\bar{M} \pm SD$ [N·m]	T [ºC]	TTQ [J·min]	E_t [23]	E_{sp} [J/g]	C_{feed}* [J/g·ºC]	E_{frict} [J/g]
57.5	1.17±0.09	153.8	148.4	46.62	179.76	1.12	4.56
60	1.83±0.11	154.9	190.2	59.75	222.99	1.08	5.29
62.5	2.24±0.16	155.2	205.8	64.65	233.76	1.05	5.46
65	3.81±0.12	155.9	247.7	77.82	275.88	1.01	5.96
67.5	5.17±0.18	157.3	348.1	109.36	372.24	0.98	7.15
70	6.53±0.27	159.1	469.3	147.43	487.54	0.94	8.55

* Cp calculated by the mixing rule considering $C_{Invar36}$ = 0.515 J/g·ºC, C_{CAB} = 1.55 J/g·ºC and C_{PEG} = 2.2 J/g·ºC

3.2 Density measurements

The CPVC was also determined with a density technique. For compositions above the critical solid loading, the amount of binder is insufficient to cover the particles and fill the remaining free volume. This results in the formation of voids inside the feedstock bulk; considering that no material is lost during the mixing process, this means that the density would be lower than the theoretical density calculated by the mixing rule. CPVC determination by measurement of the feedstock density takes this fact into account.

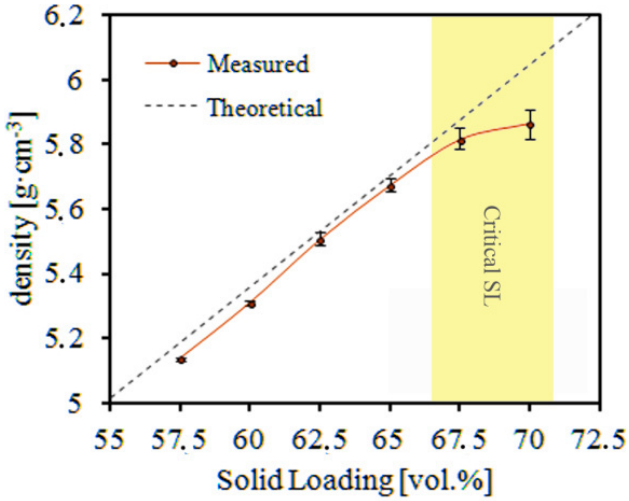

Figure 3. Feedstock density as a function of solid loading measured with a helium pycnometer. Points (with corresponding error bars) represent the average values after four measurements in different portions of each pelletised feedstock batch. Dashed lines represent theoretical values as predicted with the mixing rule.

The density values of the different feedstocks are shown in Figure 3. For all the different solid loadings up to 65 vol.%, the measured values were very close to the theoretical values.

Nevertheless, all the values were lower than the corresponding theoretical values which can be explained by the occurrence of agglomerates. The deviation of the measured density values from the mean density calculated from four different portions of each batch was almost negligible in this range of solid loadings. From that point on, for 67.5 vol.% and 70 vol.% feedstocks, the marked divergence from the theoretical density indicates excess powder content, resulting in void formation. The variability of the results also indicates heterogeneities in the batch composition derived from a less efficient mixture, which may be attributed to the CPVC. These observations, taken together with the torque experimental results, suggest that the critical solid loading value should be placed at 67.5 vol.%, although the torque measurements do not provide clear evidences of the CPVC.

3.3 Capillary rheology

The homogeneity of the feedstocks was also evaluated by measuring the variability of the feedstock viscosity over time. This was accomplished using a capillary rheometer, which forced the melted feedstock to pass through a fine capillary. Hausnerova [24] presented a very thorough work about capillary rheology in PIM. The feedstock viscosity, especially that of the highly charged PIM feedstocks, is sensitive to variations in composition. Although the torque rheometer also indicated heterogeneities, the capillary rheometer provides a more precise way to evaluate this characteristic. The torque rheometer evaluates the global feedstock's bulk at a given time, whereas the capillary rheometer measures finite portions of the feedstock's bulk. Figure 4 shows apparent viscosity values as a function of time for different binder compositions at 150 ºC and a shear rate of 1000 s^{-1}. Feedstocks up to 62.5 vol.% showed little variability in viscosity with time, with most values falling within the standard deviation interval. Slight heterogeneities were observed in the 65 vol.% feedstock, which maintains a highly constant viscosity over time, with some exceptions. Viscosity values became more erratic in the 67.5 vol.% feedstock, suggesting heterogeneity appropriate for the CPVC. Results could not be obtained at 70 vol.% because this feedstock exceeded the maximum viscosity detectable by the capillary rheometer under these conditions.

It is worth to note that this method could be sensitive to the experimental shear rates chosen. Hausnerova [24] reported that viscosity values could be erratic at certain shear rates due to flow instabilities caused by other factors than the mentioned compositional heterogeneity, e.g binder-powder segregations caused by shear. In Invar 36 feedstocks similar results were obtained after carrying out trials at 10 and 100 s^{-1}. Nevertheless, changes in the viscosity values with time for 67.5 vol.% under these conditions were smoother than those observed at 1000 s^{-1}. If other factors influencing severe flow instabilities at 1000 s^{-1} exist, they are likely driven by heterogeneities in the feedstock composition. This conclusion is supported by the heterogeneities observed after torque rheology and density measurements.

$$\log(\eta) = B + \frac{E_a}{R} \cdot \frac{1}{T} \qquad (4)$$

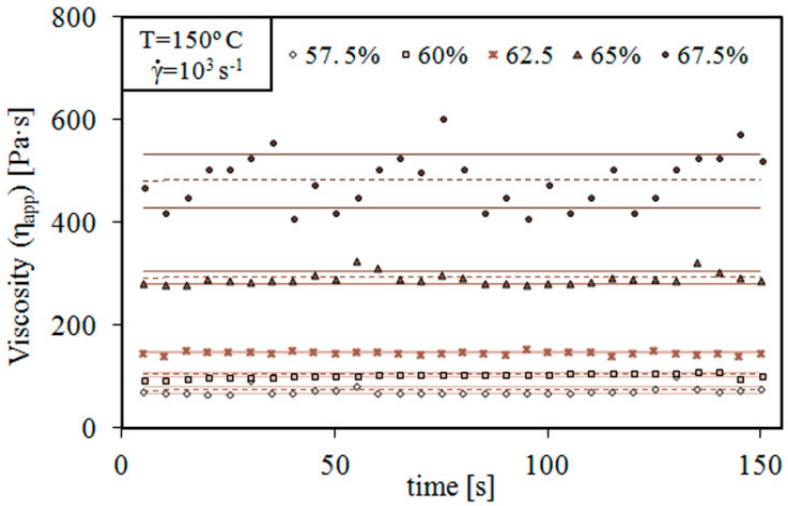

Figure 4. Apparent viscosity values as a function of time for different powder volume content feedstocks tested at a shear rate of 1000 s^{-1} and 150 ºC. Dashed lines represent the average value while straight lines enclose values within two standard deviations.

Another sophisticated way to determine optimal and critical solid loading to support capillary rheometer measurements is by calculating the apparent flow activation energy (E_a) according to Eq. (4). Viscosity values are needed for at least three different temperatures with the rest of the conditions kept constant (shear rate, solid loading, etc.). Flow activation energy can be calculated from the slope of the logarithm of viscosity (η) versus the inverse of temperature (T), which should be a straight line. R is the gas constant and B is the logarithm of a reference viscosity at certain T. Viscosity values were measured at 150 ºC, 160 ºC and 170 ºC and 5000 s^{-1}.

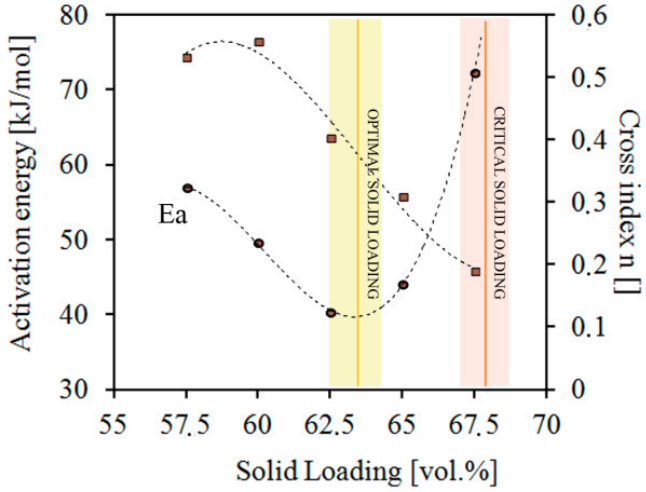

Figure 5. Apparent flow activation energy and Cross index m at 160 ºC as a function of solid loading. Activation energy was calculated from viscosity values at 5000 s^{-1} at three temperatures (150 ºC, 160 ºC and 170 ºC) according to the slope of the linear regression of the representation of the logarithm of viscosity versus the inverse of temperature

The results are shown in Figure 5, which plots the apparent flow activation energy as a function of solids loading. An increasing number of publications have reported the occurrence of a minimum in the flow activation energies and variations in other rheological parameters

(such as the power law or Cross exponents) for solid loadings correlated with the optimal powder content. Contreras et al. [18] registered this behaviour for feedstocks of superalloy powders with different particle sizes and particle distributions. Similar findings were reported by Kong et al. [6] in stainless steel feedstocks and by Hidalgo et al. [16] for a irregular shape ceramic powders feedstcoks. In the INVAR 36 feedstock, a reduction of the Cross exponent occurred at 62.5 vol.% feedstock (Figure 5), along with a minimum in the activation energy for this composition. Considering that result, the optimal solid loading for INVAR 36 feedstocks could be between 62.5 vol.% and 65 vol.%. According to German and Bose [25], the optimal solid loading should be around 5 % less than the critical solid loading. This recommendation is based on the experience in PIM field. In the case of Invar 36 feedstocks the optimal solid loading seemed to occur at compositions around 67.5 vol.% which coincides with German's recommendation.

3.4 µPIM of selected feedstocks

A complete µPIM process was carried out for 57.5 vol.%, 60 vol.%, 65 vol.% and 67.5 vol.% feedstocks. Micro tensile and bending test specimens were injected in a Battenfeld microinjection moulding machine. The dimensions of the green parts as replicated from the mould are shown in Figure 6 a. A nozzle temperature of 170 ºC was selected and the mould was heated at 30 ºC. Injection and post pressures of 1000-1200 bar and 500-600 bar (held during 5 s) respectively generally leaded to complete dense green parts without apparent flaws. The volume of dosage was also optimised. The presence of flaws as short shots, flash or warpage depended on the feedstock powder volume content thus injection conditions were varied around those values to minimise them.

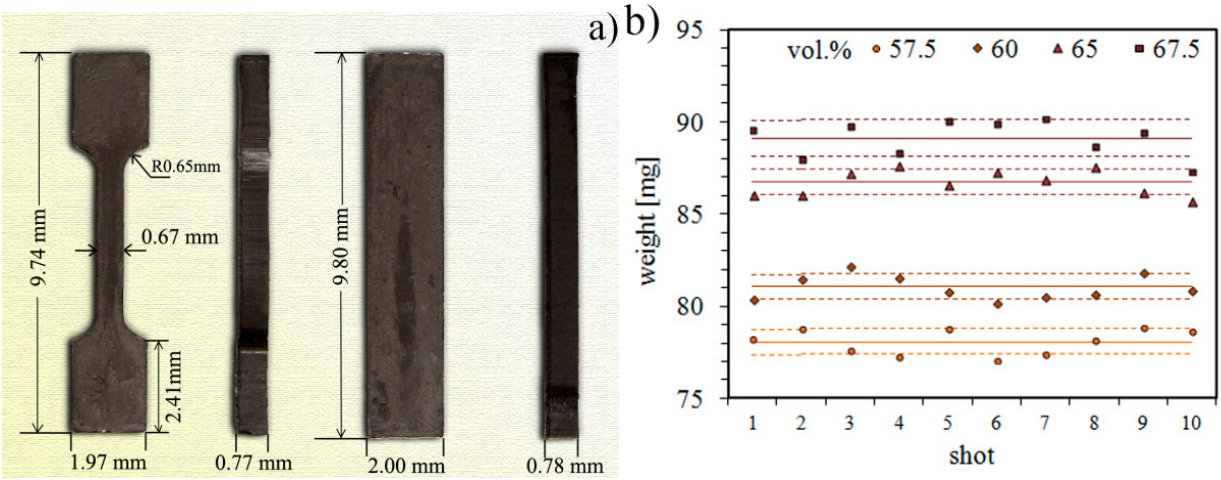

Figure 6. a) Green part dimensions as replicated from the mould cavity. The parts shown here correspond to 65 vol.% solid loading. b) Variations in the weight of the apparently flawless injected micro-parts for different solid loading feedstocks. Straight lines represent the average value while dashed lines represent the upper and lower standard deviations from the average values.

Although 67.5 vol.% feedstocks were able to be injected, in some cases short shoots occurred at pressures near the maximum allowed by the injection machine. That demonstrates that this

composition was almost at the limit, and that small differences in composition made the injection unfeasible. The weights of the apparently flawless injected micro-parts varied as shown in Figure 6 b. Straight lines represent the average value while dashed lines represent the upper and lower standard deviations from the average values. The most variable results corresponded to 67.5 vol.%, although any pieces that were not completely injected were discarded for the analysis.

Figure 7 shows the evolution of the mould filling during the injection optimisation process for a 60 vol.% feedstock and a 67.5 vol.% feedstock. The sequences were made varying the volume of dosage between 20 and 45 mm^3. Some differences were observed between the two processes. In the case of 60 vol.% feedstocks (Figure 7 a), the melted feedstock advanced evenly to fill the mould, expanding like a fan after reaching the end cavity of the part as it broadened after the tight channel. This behaviour could be linked with a viscoelastic fluid. However, the expansion after the broadening was not as evident in the 67.5 vol.% feedstock, and it seemed that the feedstock continued to move forward, retaining the shape of the tight channel like a typical plug flow. When this flow front reached the end of the part it was sent back and the end cavity was filled up with both a back flow and a forward flow, in this case from fresh melted feedstock coming through the tight channel. In a plug flow, the central part of the flow, enriched in powder particles, moves like a solid, while in the regions near the walls, the viscoelastic binder-rich feedstock facilitate the advance. A plug flow may form in CPVC situations because the binder system is not able to lubricate powder particles and their movements are restricted. The pressure may also be responsible for the rejection of some of the binder from the core to the surface, worsening the effect of low binder content in the core.

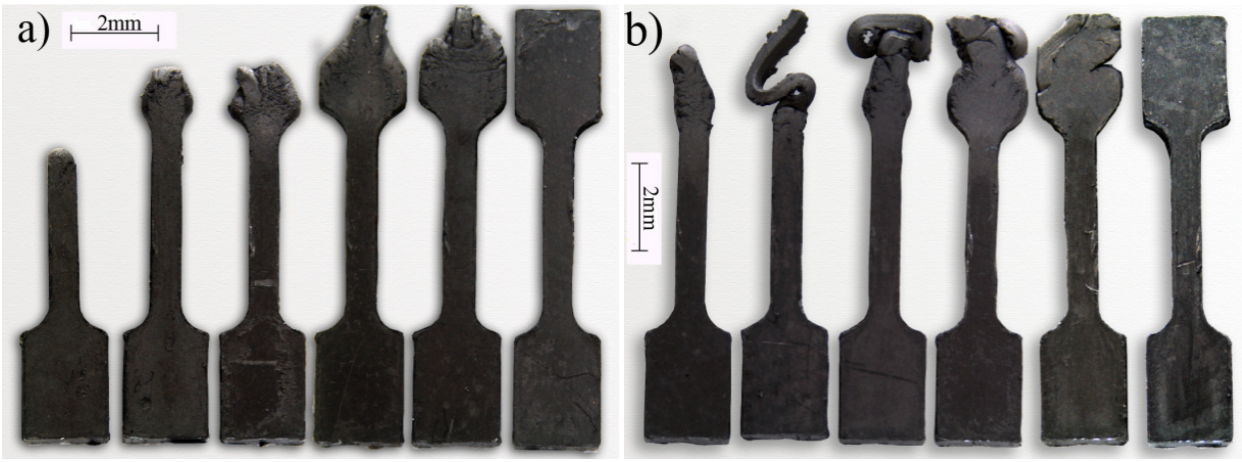

Figure 7. Evolution of the mould filling during the injection optimisation process: a) 60 vol.% feedstock, b) 67.5 vol.% feedstock.

Injection optimisation indicated that even though 67.5 vol.% solid loading showed signs of CPVC, it still had enough viscosity to be injected but also showed signs of undesirable plug flow. In that respect, 65 vol.% feedstocks showed good filling behaviour and good process reproducibility in terms of the micro part weight.

The occurrence of CPVC around 67.5 vol.% was also demonstrated by the analysis of SEM micrographs of the different compositions of injected micro parts shown in Figure 8. In case of 57.5 vol.% and 60 vol.% micro parts (Figure 8 a&b, respectively), low particle packing was observed with regions with high percentages of polymeric compounds indicating an excess of binder. Better packing of the powder particles was observed in 65 vol.% micro parts (Figure 8 c), with particles embedded more homogeneously in the binder system and without any regions with a high percentage of binder. At 67.5 vol.% solid loading (Figure 8 d), injected micro parts exhibited regions with a lack of binder surrounding powder particles, indicating that the critical solid loading was surpassed in some of the regions of the micro part.

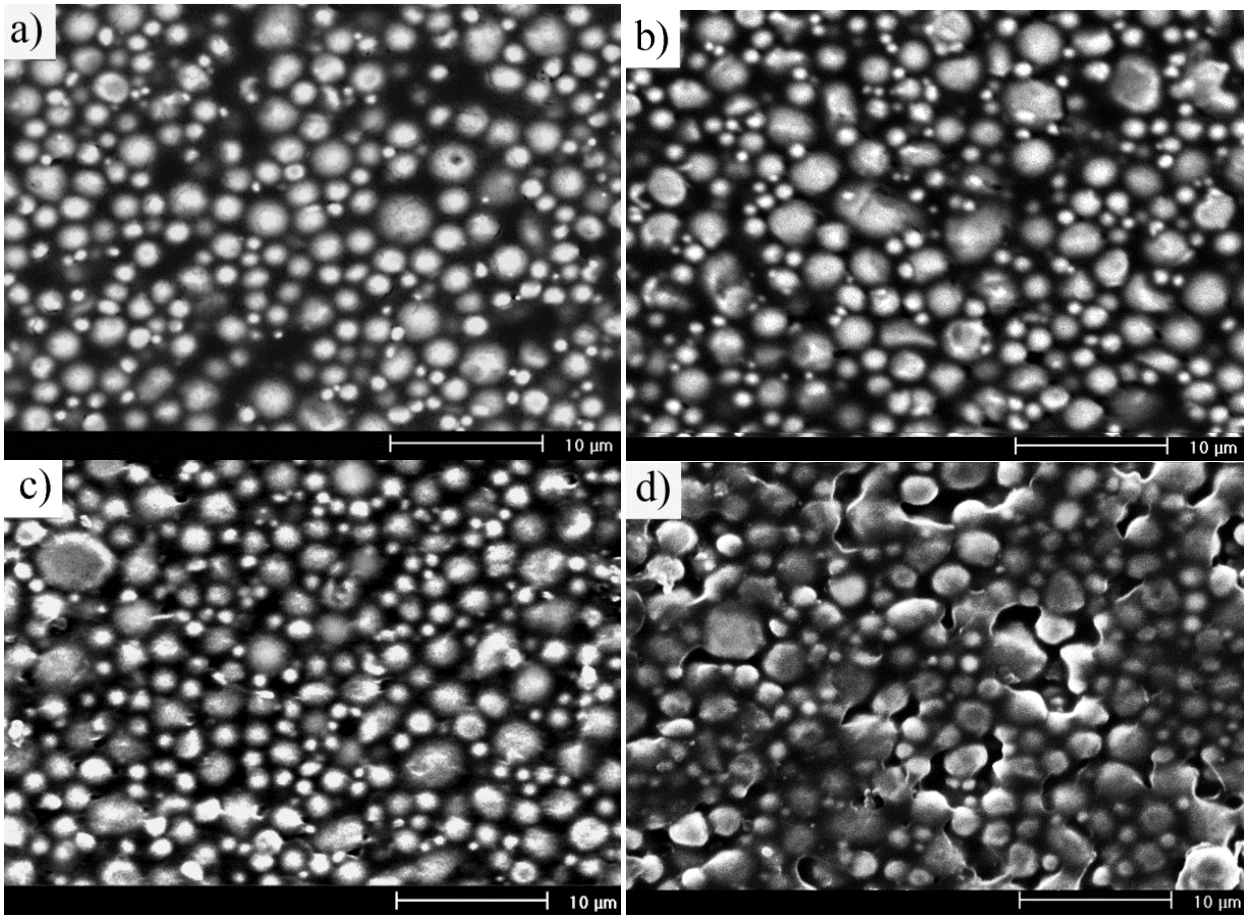

Figure 8. Back scattering electron SEM images of the surfaces of injected parts: a) 57.5 vol.%, b) 60 vol.%, c) 65 vol.%, d) 67.5 vol.%.

3.5 Debinding optimisation

A two step binder removal process was carried out after injection. First, a solvent debinding step was performed in water to remove PEG and create an open channel to facilitate further thermal elimination of CAB without defect formation. Figure 9 shows the evolution of the water solvent debinding over time for different solid loading feedstocks at 60 ºC. In 3 h, 91.4 vol.% of PEG was removed, in the worst case corresponding to 57.5 vol.% micro parts. Unlike what would be commonly expected, a worsening of the extraction with solid loading due to higher packing of the particles, increasing solid loading positively affected binder removal. The best results were obtained with 65 vol.% and 67.5 vol.% parts, with almost 100% of the

removable part eliminated after 3 hours. There were no clear differences in the elimination rates. When solid loading is increased the particle packing commonly increases, reducing the possibility that PEG evacuates channels during debinding and hindering the diffusion from the core to the surface. This normally would lead to a reduced rate of elimination and less effective removal of the soluble part. Nevertheless, the thinness of the pieces and the small amount of removable part probably resulted in only slight differences. In the case of the 57.5 vol.% part, the effectiveness of the solvent debinding could be reduced because there is also more CAB. CAB has exhibited a good affinity with PEG, potentially causing some degree of miscibility between the two compounds. If this has occurred, CAB could retain some PEG, complicating its elimination. Another possible fact is a segregation of PEG and CAB due to the high shear force caused by the small diameters of the runners and micro parts. Shear force increases as the solid loading increases. Hence, PEG could migrate predominantly to the part surfaces, promoting the plug flow observed during injection of higher solid loading. The subsequent solvent extraction would be facilitated in such a case.

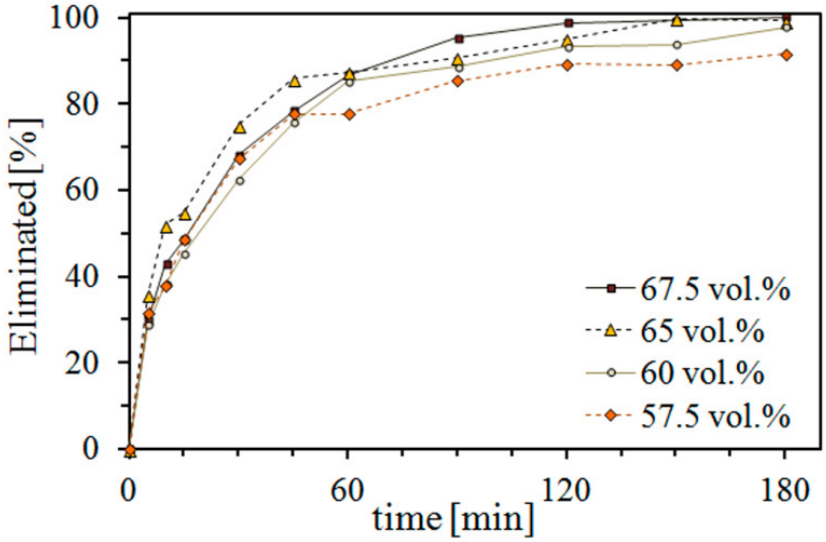

Figure 9. Evolution of solvent debinding over time determined by measuring the removal of the soluble part at 60 ºC using water as the solvent.

Thermal debinding in vacuum up to 500 ◦C for 1 h at a heating rate of 2 ºC/min allowed for almost all of the remaining CAB to be burned out. Although a small percentage of organic compounds remained after thermal elimination, they presumably would be removed at higher temperatures by pyrolysis.

3.6 Sintering and micro-tensile tests

During the sintering stage, brown specimens were heated at several heating rates (2 ºC/min or 5 ºC/min) up to different temperatures (1000 ºC or 1100 ºC) in a vacuum atmosphere and held at the target temperature for 15 min. In Figure 10 a, pieces after different stages of the PIM process are presented for the 57.5 vol.% feedstock heated at 2 ºC/min to 1100 ºC. The 57.5 vol.% parts had the largest contraction; hence the evolution of the parts' dimensions could be better observed. Due to the small size of the sintered parts, it was difficult to obtain reliable data on the densification of the parts by a helium pycnometry or by dilatometry. Therefore, the

densification of the pieces was evaluated by direct measurements of the micro part dimensions and by investigating the microstructure. Figure 10 b shows the part shrinkage during the sintering process for different sintering conditions and solid loading compositions. Note that as the solid loading increased, the shrinkage decreased because less free volume was present after binder removal. This is a positive outcome when dealing with tolerances. The general tendency of the shrinkage indicated a better densification as the temperature and the heating rate were increased. In some cases, the shrinkage almost corresponded to the theoretically full densification of the parts, which could give a rough idea of the extent of densification.

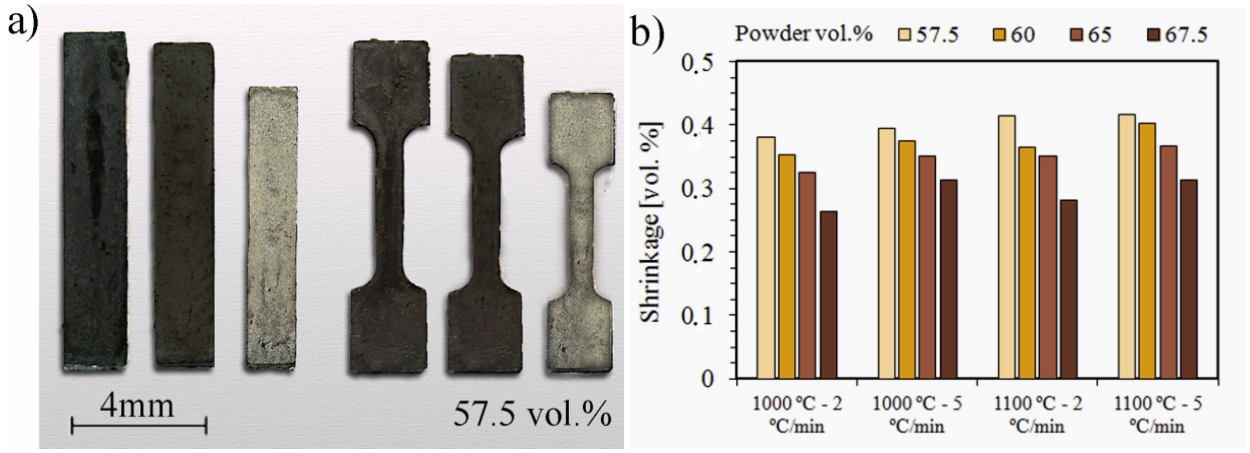

Figure 10. a) Examples of the variation in part dimensions during different stages of the μPIM process for the 57.5 vol.% feedstock. From left to right for each part geometry: green part, brown part after debinding and sintered part. b) Shrinkage of the sintered part at different sintering conditions and solid loadings.

Figure 11 presents back scattering electron images of sintered 57.5 vol.% and 65 vol.% parts at 1100 ºC and 5 ºC/min. An apparently full austenite microstructure was developed at all compositions with similar grain sizes of around 50 μm in their longest diameter. Carbon content was measured with a LECO device resulting in no more than 0.06 mass%, and with highly consistent results for all solid loadings. Graphite precipitation was not observed, which is consistent with the results of Wittenauer [26] which analysed Invar 36 compositions at these carbon contents. X-ray diffraction experiments confirmed the presence of typical Fe-36Ni austenite but also revealed a slight amount of ferrite formation that was not detected during microstructure inspection. The development of this austenitic microstructure suggests that the low CTE typical of INVAR 36 alloys can be achieved.

Significant differences were observed in the pore quantity and the pore net distribution. In the case of 57.5 vol.% (Figure 11 a), the pore density was high and heterogeneous with small pores in the range of the particle size or below, but large areas of bigger pores were also observed and were sometimes interconnected, forming clusters. In contrast, the 65 vol.% (Figure 11 b) parts exhibited less large pores than the 57 vol.% parts, they were more homogeneously distributed and no interconnected pore cluster areas were observed. These differences could be linked with the shrinkage results, giving an idea of the part densification. However, a similar quantity of small pores could be associated with residual porosity after the

sintering of small particles. Large pores may occur because of the low packing of powder particles and voids left by binder removal that could not be densified and closed by mass diffusion during sintering. After the sintering cycle, original particles and particle sintering necks were still observed in both the 57.5 vol.% and 65 vol.% microstructures. For all powder contents except 57.5 vol.%, a fine oxide layer was detected surrounding some ancient particles. In some cases, this layer was discontinuous and sintering necks were formed. Although a carbo-reductive process was expected between possible oxide layers and the residual organic binder after thermal degradation, differences in the internal pressures and CO/CO_2 ratios due to closer arrangement of particles may lead to differences in the effectiveness of oxide reduction or oxidation due to CO_2 during the sintering cycle.

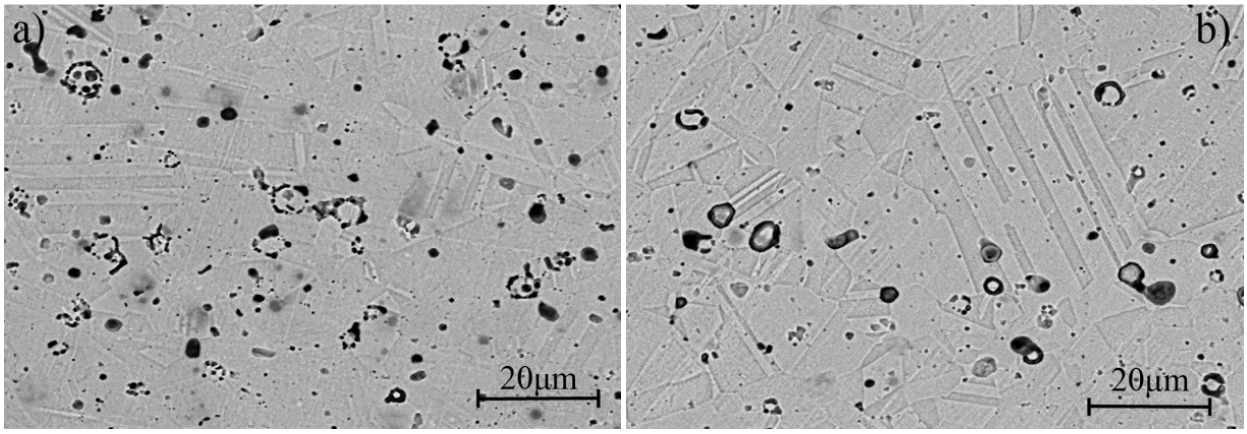

Figure 11. Back scattering electron SEM images for sintered micro parts at 1100 ºC and 5 ºC/min, a) 57.5 vol.% and b) 65 vol.%.

Finally, micro parts sintered under the optimal conditions (1100 ºC and 5 ºC/min) were subjected to micro-tensile experiments. Zhao et al. [27] discussed the limitations and issues in correctly interpreting micro tensile experiments. This work assumes errors in strain measurements as the data were collected directly from the cross head displacement without any extensometers, digital image correlation or laser interferometry. Thus, only engineering results are presented here. However, as the tests were performed on the same device, the results are valid for comparative purposes. Figure 12 shows stress and strain engineering curves for different solid loading sintered micro parts, and Table 4 collects some mechanical properties derived from these curves. The ASTM designation A658 covers 36 percent nickel-iron alloy and specifies a tensile strength of 448-552 MPa, a minimum yield strength (0.2% offset) of 241 MPa and a minimum elongation of 30% for a wrought material. The results derived from the micro-tests were consistent with these specifications despite the parts were fabricated by powder metallurgy. The value of Young's modulus (E) was similar regardless of solid loading with the exception of 65 vol%. The values of the offset yield strength and tensile strength varied with the solid loading, increasing with higher solid loading up to a maximum of 65 vol.%. This fact could be most likely correlated with the dependence of porosity on solid loading. As the porosity increases, less effective area is available to withstand applied forces.

Furthermore, pores could act as stress concentrators. However, despite the fact that elongation values are not completely reliable, better elongation results were obtained at 57.5 vol.%, with the greatest area fraction of voids and the lowest spatial separation between voids. Desrpés [28] analysed the factors influencing the ductile behaviour of porous nickel-based superalloys to perform simulations on the mechanical behaviour of these alloys. The result obtained with 57.5 vol,% Invar 36 feedstock, may contradict predictions of the most probable void coalescence, and thus most probable catastrophic failure, of materials with high porosity contents. Other factors could affect ductility such as the extent of dislocation generated after sintering. Nevertheless, a coherent explanation may be developed based on the fact that in the 57.5 vol.% micro part, there were not appreciable oxide layer embedding original particles. This fine oxide layer was observed at all other compositions, explaining the poorer elongational results of those samples. In the case of the 67.5 vol.% parts, the diminution of mechanical properties could be presumably explained by a deterioration of the green part characteristics due to a less effective injection. Although these parts contained less porosity and better microstructural features, macro defects arose in these parts.

Table 4. Different mechanical properties derived from engineering stress and strain curves for different solid loading sintered micro parts.

Solid loading [vol.%]	57.5	60	65	67.5
Tensile Strength [MPa]	478±20	499±28	510±23	471±25
Yield Strength (0.2 % offset) [MPa]	248±21	262±20	280±19	255±23
Young's Modulus [GPa]	57±1	57±1	52±3	57±1
Elongation [%]	30±3	26±2	27±2	25±3

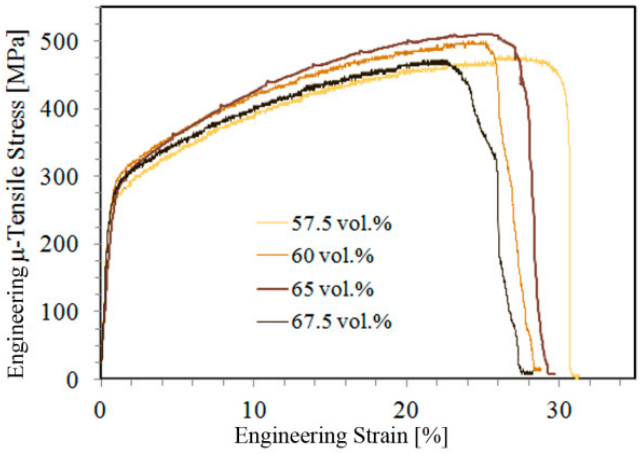

Figure 12. Engineering stress and strain curves for sintered tensile micro parts with different solid loadings.

Carefully taking into account the micro mechanical test results, the mechanical behaviour at different solid loadings indicated an optimal solid loading of around 65 vol.%. This

would confirm all the results for solid loading optimisation. These parts exhibited good particle packing, leading to better tolerances and mechanical properties without the macro defects that arise at 67.5 vol.%.

4. Conclusions

This work combined several techniques to determine the critical powder volume content of INVAR 36 feedstocks based on a CAB and PEG binder system. This type of feedstock was formulated and tested to carry out an entire μPIM process. The following conclusions were drawn:

- All the used techniques combined with the microinjection results and micro mechanical tests pointed to an optimal solid loading of 65 vol.%.
- The 67.5 vol.% feedstock still flows sufficiently well to be injected, but it was at the limit of the CPVC value; it presented compositional heterogeneities and other indications of proximity to the CPVC such as a deviation from the theoretical density value.
- The proposed binder system generally results in good flow behaviour and technical characteristics of the feedstock and sintered parts, enabling its use in μPIM of an INVAR 36 alloy.

5. Acknowledgments

The authors wish to thank GUZMÁN GLOBAL S.L. and MIMTECH ALFA for their collaboration on the ECOPIM project (ref. IPT-2011-0931-20000) that was funded by the Spanish Ministry of the Economy and Competitiveness. Furthermore, the authors would like to acknowledge the strong support from the ESTRUMAT projects (ref. S2009/MAT-1585), which were funded by the CAM-Consejería Educación Dir. Gral. Universidades e Investigación, and from the COMETAS project (ref. MAT2009/14448-C02-02), which was funded by the Spanish Ministry of the Economy and Competitiveness.

References

1. Cha, B., et al., *Micro powder injection molding process using TiH2 powder.* Journal of Ceramic Processing Research, 2012. **13**: p. S22-S25.
2. Attia, U.M. and J.R. Alcock, *A review of micro-powder injection moulding as a microfabrication technique.* Journal of Micromechanics and Microengineering, 2011. **21**(4).
3. Ruh, A., et al., *Studies on size accuracy of microgear wheels produced by powder injection molding of zirconia feedstocks.* International Journal of Advanced Manufacturing Technology, 2012. **58**(9-12): p. 1051-1059.
4. Maslyuk, V.A., O.A. Panasyuk, and O.V. Vlasova, *Physical, technological and magnetic properties of powder iron-nickel alloys.* Powder Metallurgy and Metal Ceramics, 2003. **42**(9-10): p. 536-539.

5. Khomenko, O.A., *Origin and specific features of invar anomalies of physical properties: Fe-Ni alloys with an FCC lattice.* Physics of Metals and Metallography, 2007. **104**(2): p. 146-156.
6. Kong, X., T. Barriere, and J.C. Gelin, *Determination of critical and optimal powder loadings for 316L fine stainless steel feedstocks for micro-powder injection molding.* Journal of Materials Processing Technology, 2012. **212**(11): p. 2173-2182.
7. Chi, Z., L. Jing, and X. Rong, *An Investigation on a New Type of Fe-Ni Alloy in MIM Process.* Advanced Materials Research, 2011. **311-313**: p. 653-6.
8. do Nascimento, R.M., et al., *Microstructure and dilatometric behavior of powder injection molded low-expansion alloys.* International Journal of Powder Metallurgy, 2006. **42**(6): p. 29-38.
9. Suri, P., R.M. German, and J.P. de Souza, *Influence of mixing and effect of agglomerates on the green and sintered properties of 97W-2.1Ni-0.9Fe heavy alloys.* International Journal of Refractory Metals & Hard Materials, 2009. **27**(4): p. 683-687.
10. Bitkulov, I.K., et al., *Effect of severe plastic deformation on the properties of the Fe-36% Ni invar alloy.* Physics of Metals and Metallography, 2006. **102**(1): p. 91-96.
11. Nadutov, V.M., et al., *Magnetic properties of alloyed invar alloys on the base of Fe-Ni-C.* Metallofizika I Noveishie Tekhnologii, 2006. **28**: p. 39-48.
12. Nadutov, V.M., et al., *Interatomic Interaction and Magnetostriction in Invar Fe-Ni-C-Based Alloys.* Metallofizika I Noveishie Tekhnologii, 2009. **31**(8): p. 1021-1034.
13. Hatate, M., H. Sumimoto, and K. Nakamura, *Influence of carbon and nickel on linear thermal-expansion coefficient in low thermal-expansion Fe-Ni-C alloys.* Journal of the Japan Institute of Metals, 1990. **54**(9): p. 1036-1040.
14. Minseok, S., et al., *Water-soluble binder with high flexural modulus for powder injection molding.* Journal of Materials Science, 2005. **40**(5): p. 1105-9.
15. Bernardo, E., et al., *Feedstock development for Powder Injection Moulding of zirconium silicate.* Powder Injection Moulding International, 2012. **6**(1): p. 4.
16. Hidalgo, J., A. Jimenez-Morales, and J.M. Torralba, *Torque rheology of zircon feedstocks for powder injection moulding.* Journal of the European Ceramic Society, 2012. **32**(16): p. 4063-4072.
17. Hidalgo, J., A. Jimenez-Morales, and J.M. Torralba, *Thermal stability and degradation kinetics of feedstocks for powder injection moulding – A new way to determine optimal solid loading?* Polymer Degradation and Stability, 2013. **98**(6): p. 8.
18. Contreras, J.M., A. Jimenez-Morales, and J.M. Torralba, *Experimental and theoretical methods for optimal solids loading calculation in MIM feedstocks fabricated from powders with different particle characteristics.* Powder Metallurgy, 2010. **53**(1): p. 34-40.
19. Vieira, M.T. and F.M. Barreiros, *PIM of non-conventional particles.* Ceramics International, 2006. **32**(3): p. 297-302.
20. Cheremisinoff, N., *Product design and testing of polymeric materials*. 1990, USA: Marcel Dekker.
21. Abu-Orf, M. and B. Örmeci, *A new tool for measuring biosolids floc strength*. 2004, USA: IWA, Publishing.
22. Escocio, V.A., et al., *Thermal and Dynamic Mechanical Characterization of TPU/Mica Composites Prepared by Torque Rheometer.* Polimeros-Ciencia E Tecnologia, 2011. **21**(3): p. 240-245.

23. Salomon, A. and K. Fielder, *Practical use of differential calorimetry for plastics*, in *Hadbook of Plastics Analysis*, H. Lobo and J. Bonilla, Editors. 2003, Marcel Dekker: New York. p. 79-109.
24. Hausnerova, B., *Rheological characterization of powder injection molding compounds.* Polimery, 2010. **55**(1): p. 3-11.
25. German, R.M. and A. Bose, eds. *Injection Molding of Metals and ceramics*. 1997, Metal Powders Industry Federation.
26. Wittenauer, J., *Factors affecting the mechanical strength of Fe-36Ni Invar*. Invar Effect: A Centennial Symposium, ed. J. Wittenauer. 1996. 231-238.
27. Zhao, Y.H., et al., *Influence of specimen dimensions and strain measurement methods on tensile stress-strain curves.* Materials Science and Engineering a-Structural Materials Properties Microstructure and Processing, 2009. **525**(1-2): p. 68-77.
28. Desrpés, M., *On the Evaluation of Ductile Behaviour of Porous Nickel-Based Superalloys Using Finite Element Method* in *Department of Mechanical Engineering* 2005, McGill University: Montreal.

Paper 5

P5

J. Hidalgo, A. Jiménez-Morales and J.M. Torralba

Rheological characterization of zirconium silicate feedstocks based on water soluble binders

This work was orally presented at Euro PM12 Conference celebrated in Basel and included in the CD of proceedings of this congress (Powder Injection Moulding – Special Materials 1. ISBN:978-1-899072-36-1). The manuscript was refereed by Dr Volker Piotter, Karlsruhe Institute of Technology.

Rheological characterization of zirconium silicate feedstocks based on water soluble binders

Javier Hidalgo (1), Antonia Jiménez-Morales (1) and José M. Torralba (1,2)

[1]*Unversidad Carlos III Madrid, Avd. Universidad 30 28911(Leganés).* jhidalgo@ing.uc3m.es, toni@ing.uc3m.es
[2]*IMDEAMaterialsInstitute, Profesor Aranguren s/n 28040 (Madrid).* josemanuel.torralba@imdea.org

ABSTRACT

Zirconium Silicate powders from crushed sand were investigated as raw material for Powder Injection Moulding (PIM). The powders, having unconventional characteristics for PIM, were mixed with a binder system based on Cellulose Acetate Butyrate (CAB) and poly-ethylene glycol (PEG). The rheological behavior of the as-prepared feedstock was studied with a capillary viscosimeter. The dependences of viscosity with variables such as temperature, shear rate or solid loading were determined and compared with different conventional models relating these variables. Model parameters were assessed and adjusted by an iterative computational method to best fit with experimental results. Errors of the different models were compared by box-plots diagrams to determine the best adjusting model.

Keywords: Zircon, CAB, PEG, rheology, PIM.

1.Introduction

Powder Injection Moulding (PIM) is one of the main manufacturing processes of parts with complex geometry, thin walls and for large production batches. This technology is being applied to a wide variety of ceramic or metallic materials, or combinations of both[1, 2]. The process consists on the mixture of a fine material powder with different polymer-like compounds, the so-called binder system. The binder system should provide enough fluidity to the feedstock in order to allow a correct mould filling during injection and it should be easily removed in subsequent stages. Thus, the binder system must be added in such a quantity to keep optimum process condition and time cycle.

In order to obtain reliable products by PIM technology, one of the main demands is understanding the rheological behavior of the feedstocks[3]. It comprises the study of the feedstock's capacity to flow and the way it does attending different factors. Viscosity (η) is commonly used as the physical property which best summarizes and characterizes the rheological behavior of a fluid. It could be defined as the resistance that a fluid offers to displace itself when a certain stress is applied to it. Particle size distributions and morphology are the most relevant factors affecting viscosity of PIM feedstocks[4].The own rheological behavior of the binder system also affects. Other parameter which influences appreciably the viscosity is the solid loadings content (Φ), normally expressed in vol.%. In most of the cases this value easily exceeds the 60 vol.%. Apart of the aforementioned factors, temperature (T), shear rate ($\dot{\gamma}$) and pressure (P) are other factors to take into account during a rheological study [5-7].

The several different parameters influencing viscosity make the rheological study a complex task. Generally, each parameter is studied separately, varying it and fixing the rest. There is an extensive literature which proposes relationships between viscosity and the mentioned parameters by using mathematical models [8, 9]; in such a manner, there are many equations which in some extent could be adjusted to follow empirical data trends. These equations try to reflect the individual or combined influence of the variables. The establishment of these mathematical models could become a very useful tool when optimizing process conditions. This is subordinated to an accurate matching of the models with real performance. Recently, computational simulation is gaining recognition to save time and costs during the process design [10, 11]. Computational simulation is coupled with these models and its efficacy depends on the reliability of the model.

In this work a systematic rheological study has been carried out for feedstocks comprising zirconium silicate (zircon) powders and a binder system based on poly-ethylene glycol (PEG) and cellulose acetate butyrate (CAB). This kind of binder systems seem to be highly compatible and thus adequate for zircon PIM. Furthermore they allow less harmful and more environmental friendly debinding processes [12].To the date, there are sporadic works about these binder systems and after an extensive review, none was found referring the rheological study of the proposed feedstocks.

2 Experimental procedures

2.1 Materials

For the feedstock preparation, natural crushed milled zircon sand powder was used. The powder was provided by GUZMÁN GLOBAL S.L. (Spain). The particles have irregular shape and the particle size distribution parameters D50 y D90 are 1.604 and 4.65 μm, respectively. Their specific surface was measured with a BET device and resulted to be 5.0363 m²/g. The small size of the powders is related with their tendency to form agglomerates. They are reflected on the low values of apparent density (21.07%) and tap density (35.45%).

The binder system is made by blending two different PEG formulations with M_n 20000 and 4000 with two different kinds of CAB formulations, CAB381-0.1 and CAB551-0.01. PEG samples were supplied by Sigma Aldrich while CAB samples were from Eastman. Each CAB has different percentages of acetyl, butyryl and hidroxyl side chain groups which are shown in Table 1 with the volumetric content of the different components of the binder system.

Table 1 Characteristics and volumetric content of the binder's components.

Component	Acetyl	Butyryl	Hydroxyl	%vol
CAB381-0.1	13	37	1,5	10
CAB551-0.01	2	53	1,5	30
PEG 20k	-	-	-	58
PEG 4k	-	-	-	2

2.2 Capillary Rheology

For the rheological study a Bohlin Instruments RH2000 Capillary Rheometer was used. Mixtures were prepared with different solid loading contents (52.5, 55, 57.5, 60 and 62.5 vol.%) by a Haake Rheomix twin roller blade mixer. The study comprises the investigation of the relationships between the viscosity and: 1) the shear rate (in a range from 10 to 10000 1/s), 2) temperature (trials from 120 to 170ºC each 10ºC) and 3) solid loading. Several dies and transducer pressure sensors were used to allow a wide shear rate range (3magnitude orders) and pressure range with the maximum accuracy possible and attending the interval of solid loading proposed. The relation between the die diameter and its length was kept constant in a value of 30, which is the minimum recommended to achieve a laminar flow along the die. In all the cases were calculated the apparent shear viscosity.

3 Results

3.1 Dependence of viscosity with shear rate

The rheological behaviour of PIM feedstocks in a fluid state in commonly pseudo-plastic[13, 14], and could be adequately adjusted by a power law (1):

$$\eta = k \cdot \dot{\gamma}^{n-1} \qquad (1)$$

where η is the feedstock viscosity, $\dot{\gamma}$ the shear rate and k a constant.The n parameter is denoted as the flow index. This equation can be linearized by applying logarithms in both terms (2):

$$\log \eta = \log k + (n-1) \cdot \log \dot{\gamma} \qquad (2)$$

where (n-1) represents the slope of a straight line. If n takes values near 1, the behaviour is considered as Newtonian and the viscosity does not depend on the shear rate. If n takes values lower than the unit, the slope turns negative and reflects a thinning behaviour so-called pseudo-plastic. For values higher than the unit, viscosity increases with shear rate.

Figure 1 shows the results of the viscosity dependence with shear rate for four different solid loading and for several temperatures. The dashed line represents the points adjusted by the power law curve. These kinds of feedstocks do not show and exclusive pseudo-plastic behaviour in the PIM typical shear rate intervals. First, at low shear rates, it could be observed a plateau in which viscosity remains constant independently of the shear rate; it can be assessed that we have a Newtonian flow. This first stage of the viscosity curve is clearer and more extended than as the solid loading is reduced and temperature is increased. As the shear rate increases, subsequently the viscosity begins to decrease with a pseudo-plastic behaviour. With solid loadings of 57.5 and over, the behaviour is exclusively pseudo-plastic for the entire shear rate interval. Lastly, depending on temperature and solid loading, it is possible to observe again a Newtonian behaviour at high shear rates (Figure 1b, 170º C).

For low shear rates near zero is common for PIM feedstocks to observe a yield stress, τ_y, which represents a minimum shear stress to flow occurs. However for these feedstocks and for

the conditions studied, the predicted τ_y was negligible or not observed which does not assure that it does exist at all.

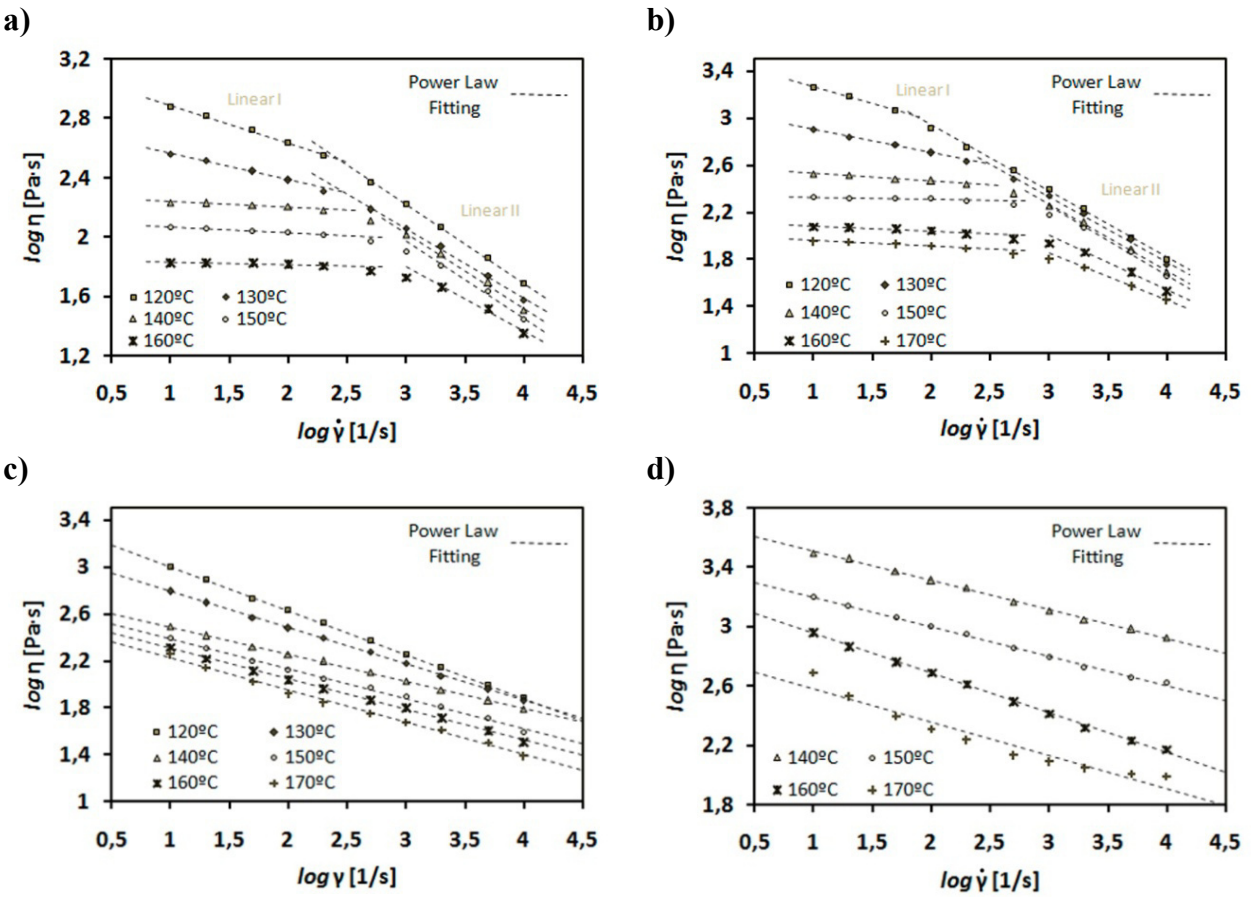

Figure 1 log η versus log $\dot{\gamma}$representation of the experimental data for different temperatures and the adjustment to the power law model a) 52,5 vol.% zircon powder, b) 55 vol.%, c) 57,5 vol.% d) 60 vol.%.

This kind of behaviour seems to match better with more complex models than the powder law. In this work the Williamson, Cross, Carreau and Carreau-Yasuda models have been selected as candidates for describing the viscosity behaviour. All the mathematical formulas are collected in Table 2.

Table 2 Different models selected for adjusting experimental points.

Model	Equation
Williamson[15]	$\eta = \eta_0 - k \cdot \dot{\gamma}^{n-1}$
Cross [16]	$\eta = \eta_0 + \frac{(\eta_0 - \eta_\infty)}{1 + (k \cdot \dot{\gamma})^n}$
Carreau[17]	$\eta = \eta_0 + \frac{(\eta_0 - \eta_\infty)}{(1 + (k \cdot \dot{\gamma})^2)^{\frac{n-1}{2}}}$
Carreau-Yasuda[18]	$\eta = \eta_0 + \frac{(\eta_0 - \eta_\infty)}{(1 + (k \cdot \dot{\gamma})^a)^{\frac{n-1}{a}}}$

These models have been validated in numerous occasions in other type of systems. Williamson model reproduces the first two stages, while the rest are designed to fit the whole curve in all the shear rate ranges from cero to infinite and reproduce the three common stages. All of them differ on the number of coefficients that can be modified to perform a non-linear regression for experimental point adjustment. The cero viscosity η_o, the asymptotic value of the viscosity for the Newtonian period at low shear rates, is a common coefficient in all the equations. The rest of parameters, k, n, a will determine the severity and the point in which viscosity turns from Newtonian to pseudo-plastic.

For the non-linear regression of the experimental set of points and adjustments of the models, software for solving and optimizing equations was used. This software employs optimization algorithms based on the generalized reduced gradient method GRG [19, 20] which also allows solving non-linear regression problems. For such purposes, a minimization problem is set out for the sum of squared residuals (RSS), being the residuals the difference between the model predicted value and the real value. The predicted model values depend on the variation of the model equation coefficients. The software varies them in and iterative process until the RSS value is minimized. In this work a minimization problem for an RSS modified (RSSp) was set out. The RSSp is an RSS value with the residuals pondered by dividing them by the measured value. The values of viscosity could differ in several magnitude orders with the variation of shear rate. The RSS by itself could cause that only the highest values of viscosity, the ones which might contribute more extensively to the sum of squares, were adjusted properly. The RSSp tries to make the adjustment process more equilibrated for all the points. The multiple regression coefficient (R^2) was also used to validate the model adjustments.

Table 3 collects all the different adjusted coefficients for the different models and conditions. The values for η_∞ were omitted because generally it takes values near cero. The only exceptions were the 60% vol. solid loading feedstock for the temperatures 160ºC y 170ºC. This coefficient represents the asymptotic value of the viscosity for high shear rates.

According with the values of R^2 (near to 1) and the RSS_P (as low as possible), the models which best fit with the experimental set points for all conditions are the Cross and the Carreau-Yasuda models. Williamson model has demonstrated to adjust the points worse than other models. Regarding the sensitivity of the method, studies were carried out to determine if the minimum RSS_p values approached were relative or absolute and the effect of the coefficients variation in RSS_p. For low solid loading contents (52.5 and 55 vol.%), in which the first Newtonian stage is well defined, the RSS_p value is very sensitive to the fluctuations of the model coefficients. Beginning from different random setting out coefficients values, they converge to the same unique solution. However, for higher solid loadings, as the η_o is not well defined by the experimental points, the algorithm could give back several optimum solutions. Although the adjustment of points still provide with a good R^2 and RSS_p values for certain models, the value of η_o obtained is imprecise and depends on the setting out chosen. That could be noticed in Table 3 which shows that higher values of η_o are predicted for higher temperatures, which is contrary to the normal and well experimentally contrasted fall of the

viscosity values when temperature is increased. To that respect, the model which behaves more coherently is the Carreau-Yasuda. The values for that model always trend to lower values when temperature is increased.

Table 3 Adjusted coefficients for different models and conditions and R^2 and RSS_P.

Williamson

	52.5 vol.%				55 vol.%			
T [°C]	η_0	k	n	R^2	RSS_P	η_0	k	n	R^2	RSS_P
140	229,1	29,42	1,208	0,943	4,869	538,8	134,70	1,142	0,985	8,275
150	1322,7	6,50	1,301	0,980	0,984	212,2	9,02	1,337	0,979	5,113
160	72,3	1,01	1,424	0,977	0,303	133,6	5,43	1,317	0,997	0,352
	57.5 vol.%					60 vol.%				
150	9744,0	9406,06	1,002	0,953	19,419	22223	20475	1,007	0,964	74,469
160	25215,5	25001,62	1,001	0,950	17,607	27633	26693	1,003	0,963	98,044
170	27084,3	27084,65	1,006	0,915	24,971	103383	102973	$3 \cdot 10^{-4}$	0,854	108,87

Carreau

	52.5 vol.%				55 vol.%			
T [°C]	η_0	k	n	R^2	RSS_P	η_0	k	n	R^2	RSS_P
140	166,4	$2,51 \cdot 10^{-4}$	0,510	0,9963	0,730	314,1	$2,95 \cdot 10^{-4}$	0,477	0,9872	4,714
150	111,3	$1,67 \cdot 10^{-4}$	0,533	0,9375	1,209	208,4	$1,40 \cdot 10^{-4}$	0,441	0,9970	0,778
160	66,5	$1,27 \cdot 10^{-4}$	0,598	0,9910	0,423	114,4	$1,83 \cdot 10^{-4}$	0,609	0,9764	1,8911
	57.5 vol.%					60 vol.%				
150	1232,0	58,38	0,746	0,9981	0,617	2085,7	0,387	0,800	0,9989	2,310
160	939,4	34,70	0,737	0,9984	0,365	3183,5	8,999	0,718	0,9989	1,391
170	932,3	15,72	0,860	0,9967	0,851	4987,1	10,72	0,458	0,9967	1,417

Carreau-Yasuda

	52.5 vol.%					55 vol.%				
T [°C]	η_0	k	n	a	R^2	RSS_P	η_0	$k \cdot 10^4$	n	a	R^2	RSS_P
140	171,2	$14,2 \cdot 10^{-4}$	1,513	1,12	0,9993	0,055	338,4	7,30	1,873	0,79	0,9964	0,513
150	117,3	$1,81 \cdot 10^{-4}$	2,146	0,75	0,9987	0,133	213,2	6,24	1,854	1,22	0,9989	0,755
160	68,6	$0,82 \cdot 10^{-4}$	2,500	0,31	0,9983	0,061	122,1	0,44	2,713	0,63	0,9959	0,098
	57.5 vol.%						60 vol.%					
150	900,0	16,99	1,754	8,00	0,9984	0,617	27268	$1,56 \cdot 10^{-5}$	7,98	1,20	0,9990	2,162
160	332,4	0,66	1,263	8,70	0,9978	0,365	22138	$0,89 \cdot 10^{-3}$	16,5	1,28	0,9985	1,390
170	319,9	0,63	1,339	17,37	0,9967	0,851	14991	83,41	17,4	1,54	0,9960	1,416

Cross

	52.5 vol.%					55 vol.%				
T [°C]	η_0	k	n	R^2	RSS_P	η_0	k	n	R^2	RSS_P
140	175,3	$5,19 \cdot 10^{-4}$	0,835	0,9987	0,289	336,6	$8,64 \cdot 10^{-4}$	0,826	0,9985	0,524
150	116,0	$3,75 \cdot 10^{-4}$	0,859	0,9981	0,161	214,5	$3,95 \cdot 10^{-4}$	0,979	0,9986	0,284
160	68,5	$2,26 \cdot 10^{-4}$	0,876	0,9997	0,021	119,9	$3,11 \cdot 10^{-4}$	0,782	0,9974	0,226
	57.5 vol.%					60 vol.%				
150	14285	$7,23 \cdot 10^{-3}$	0,257	0,9983	0,632	41090	$7,23 \cdot 10^{-4}$	0,204	0,9989	2,332
160	29966	$16,2 \cdot 10^{-3}$	0,264	0,9984	0,424	152250	$16,2 \cdot 10^{-3}$	0,271	0,9977	1,793
170	12427	$0,28 \cdot 10^{-3}$	0,344	0,9973	0,868	411498	$0,27 \cdot 10^{-3}$	0,557	0,9963	1,338

To make a better assessment and to compare different adjustments, the box plot for the square residuals divided by the experimental value were plotted for the different models and temperatures. With them the assessment is not only made by the global contribution of the residuals with RSSp, but moreover by the individual divergence between predicted values and experimental points. To take an example, Figure 2 is presented. It could be observed that Carreau-Yasuda and Cross models seem to produce pretty similar curves that fit with the points (Figure 2 left), moreover the RSSp values were also comparable. However, as it can be seen in the box-plot (Figure 2 right) the Carreau-Yasuda predicted individual points match

globally better with the correspondent experimental points. The dispersion of the residuals square by the experimental values is lower than for the Cross model, and more of them are within the first and second quartile (upper and bottom boundaries of the box) keeping more centered to the median (box division line).

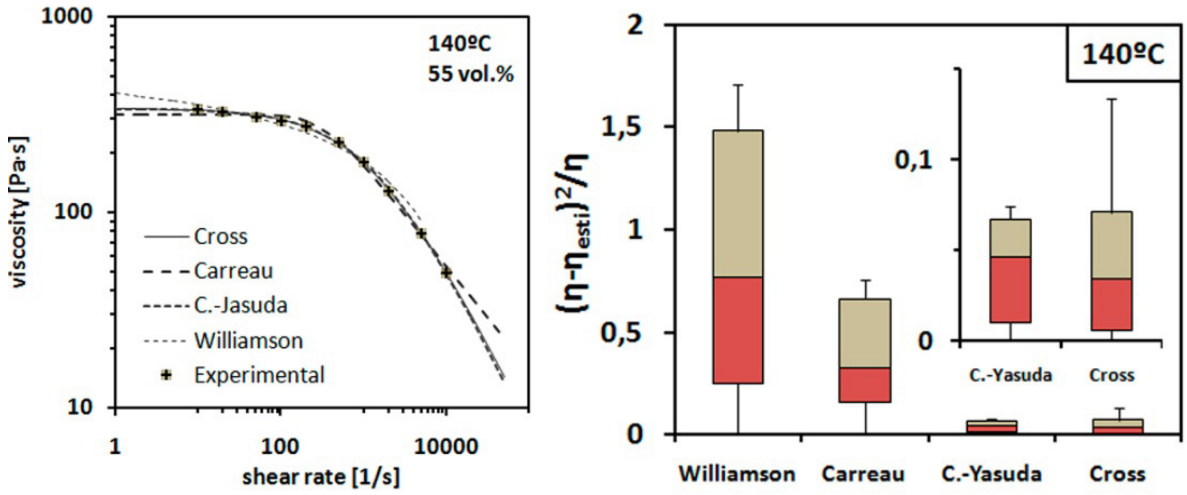

Figure 2 Adjustment of the different models to the experimental data for solid loading of 55 vol.% and 140ºC*: left* viscosity against shear rate curves, *right* box-plot of the square residuals divided by the experimental value.

This behaviour is generally repeated for the data adjustment for all the conditions proposed for Cross and Carreau-Yasuda models. Consequently, it could be concluded that the best curve regression is made by the adjustment of the Carreau-Yasuda coefficients. However, the Cross model gives also good results considering the values of R^2 and RSS_P employing less parameters.

4. Conclusions

Most commercial feedstocks used in PIM, have a pseudo-plastic behaviour in the shear rate range studied, and can be predicted according the power law. The rheological behavior of zircon feedstocks based on CAB and PEG binders proposed in this work, cannot be adjusted by the power law properly so we can conclude that it possess different pseudo-plastic behavior that should be analyses under different models. Trying to describe this different behaviour, several more complex models have been proposed and tested. Among them, the Carreau-Yasuda model seems to be the more accurate according the statistics used to validate it (RSSp and R^2). Furthermore, this model presents more coherent results when predicting η_o in situations in which experimental data follows exclusively a pseudo-plastic tendency. However, in that cases the estimation of η_o makes any sense for all the models for the uncertainty that comes from the possibility of obtaining multiple solutions. Powder law then becomes the best option, because of its simplicity and the possibility of linearization and thus a better assessing of equation coefficients. Carreau-Yasuda model implementation in simulation tools specially tailored for PIM would make sense only if a good characterization

of the low shear rate region is made, there is a Newtonian plateau and depreciable yield stress is observed.

ACKNOWLEDGEMENTS

The authors want to acknowledge GUZMÁN GLOBAL S.L. and MIMTECH ALFA for their collaboration in the project ECOPIM (ref. IPT-2011-0931-20000) funded by the Spanish Ministry of the Economy and Competitiveness. Furthermore they want to thank to the projects ESTRUMAT (ref. S2009/MAT-1585) funded by the CAM- Consejería Educación Dir. Gral. Universidades e Investigación and the project COMETAS (ref. MAT2009/14448-C02-02) funded by the Spanish Ministry of the Economy and Competitiveness. They would also thank to the FEMTO-ST institute at Besançon, and Dr. T. Barrier, and Prof. JC. Gellin.

BIBLIOGRAPHY

1. German, R.M., *Powder Injection Molding*, in *ASM Handbook*. 1998. p. 355-364.

2. German, R.M. and A. Bose, eds. *Injection Molding of Metals and ceramics*. 1997, Metal Powders Industry Federation.

3. Hausnerova, B., *Rheological characterization of powder injection molding compounds.* Polimery, 2010. **55**(1): p. 3-11.

4. Contreras, J.M., A. Jimenez-Morales, and J.M. Torralba, *Improvement of rheological properties of Inconel 718 MIM feedstock using tailored particle size distributions.* Powder Metallurgy, 2008. **51**(2): p. 103-106.

5. Hausnerova, B., et al., *The effect of powder characteristics on pressure sensitivity of powder injection moulding compounds.* Powder Technology, 2011. **206**(3): p. 209-213.

6. Hausnerova, B., et al., *Pressure-dependent viscosity of powder injection moulding compounds.* Rheologica Acta, 2006. **45**(3): p. 290-296.

7. Hausnerova, B., T. Sedlacek, and P. Vltavska, *Pressure-affected flow properties of powder injection moulding compounds.* Powder Technology, 2009. **194**(3): p. 192-196.

8. Lapointe, F., S. Turenne, and B. Julien, *Low viscosity feedstocks for powder injection moulding.* Powder Metallurgy, 2009. **52**(4): p. 338-344.

9. Honek, T., B. Hausnerova, and P. Saha, *Relative viscosity models and their application to capillary flow data of highly filled hard-metal carbide powder compounds.* Polymer Composites, 2005. **26**(1): p. 29-36.

10. Suri, P., et al., *Numerical analysis of filling stage during powder injection moulding: effects of feedstock rheology and mixing conditions.* Powder Metallurgy, 2004. **47**(2): p. 137-143.

11. Liang, S.-q., Y. Tang, and B.-y. Huang, *Rheology in metal powder injection molding.* Journal of Central South University of Technology, 2007. **14**: p. 372-377.

12. Bernardo, E., et al., *Feedstock Development for Powder Injection Moulding of Zirconium Silicate.* Powder Injection Moulding International, 2012. **6**(1): p. 75-78.

13. Edirisinghe, M.J. and J.R.G. Evans, *RHEOLOGY OF CERAMIC INJECTION-MOLDING FORMULATIONS.* British Ceramic Transactions and Journal, 1987. **86**(1): p. 18-22.

14. Huang, B.Y., S.Q. Liang, and X.H. Qu, *The rheology of metal injection molding.* Journal of Materials Processing Technology, 2003. **137**(1-3): p. 132-137.

15. Williamson, R.V., *The flow of pseudoplastic materials.* Industrial and Engineering Chemistry, 1929. **21**: p. 1108-1111.

16. Cross, M.M., *RHEOLOGY OF NON-NEWTONIAN FLUIDS - A NEW FLOW EQUATION FOR PSEUDOPLASTIC SYSTEMS.* Journal of Colloid Science, 1965. **20**(5): p. 417-&.

17. Carreau, P.J., *RHEOLOGICAL EQUATIONS FROM MOLECULAR NETWORK THEORIES.* Transactions of the Society of Rheology, 1972. **16**(1): p. 99-&.

18. Yasuda, K. 1979, Massachusetts. Institute of Technology: Cambridge, MA.

19. Lasdon, L.S., S.K. Mitter, and A.D. Waren, *CONJUGATE GRADIENT METHOD FOR OPTIMAL CONTROL PROBLEMS.* Ieee Transactions on Automatic Control, 1967. **AC12**(2): p. 132-&.

20. Waren, A.D., M.S. Hung, and L.S. Lasdon, *THE STATUS OF NONLINEAR-PROGRAMMING SOFTWARE - AN UPDATE.* Operations Research, 1987. **35**(4): p. 489-503.

Paper 6

P6

J. Hidalgo, A. Jiménez-Morales and J.M. Torralba

Thermal stability and degradation kinetics of feedstocks for powder injection moulding - A new way to determine optimal solid loading?

This work was published in Polymer Degradation and Stability (Vol. 98, pp. 1188-1195, 2013)

Thermal stability and degradation kinetics of feedstocks for powder injection moulding - A new way to determine optimal solid loading?

J. Hidalgo[a*], A. Jiménez-Morales[a] and JM. Torralba[a,b]

a. Materials Science Department at Carlos III University of Madrid. Avd. Universidad 30 28911, Leganés (Spain)
b. IMDEA Materials Institute (Getafe)
* Corresponding author: E-mail: jhidalgo@ing.uc3m.es, Telephone: +34916249482

Abstract

Degradation kinetics and the thermal stability of zircon powder injection moulding feedstocks (PIM) based on cellulose acetate butyrate (CAB) and polyethylene glycol (PEG) binders were investigated using simultaneous thermogravimetric analysis (STA). The initial decomposition temperature (IDT) and the integral procedure decomposition temperature (IPDT) were used to analyse the thermal stability of the binder system as a function of the solid loading content. The degradation kinetics were studied, and the degradation activation energy was assessed for varying zircon powder contents using isoconversional methods. All the methodologies revealed changes in the thermal degradation behaviours of the feedstocks for solid loadings that were previously determined to correspond to optimal solid loadings using other experimental procedures. These results may promote the proposal of thermodynamic degradation studies of feedstocks as an alternative or complementary technique to determine optimal solid loading contents in powder injection moulding (PIM). The studies in this paper also examined PIM process operation temperatures for zircon feedstocks.

Keywords: Powder Injection Moulding, Zircon, Cellulose Acetate Butyrate, Polyethylene Glycol, Thermal Degradation

1. Introduction

Powder injection moulding (PIM) is one of the main manufacturing processes used to produce small parts with complex geometries, thin walls and in large production batches [1, 2]. This technology is applied to a wide variety of ceramics, metals and combinations thereof [3]. The process consists of mixing a fine powder material with different polymer-like compounds, the so-called binder system. The binder system provides sufficient fluidity to the newly created feedstock to allow mould filling during injection and easy removal during the subsequent debinding process. The binder system must be added in such quantities so as to optimise the process conditions and time required. The volume occupied by the binder decreases during debinding, and the density of the powder particles increases during sintering to achieve the final part properties. Shrinkage occurs as consequence of sintering. To minimise shrinkage and increase part tolerances, the maximum powder volume fraction is desired. This powder particle fraction is limited by rheological factors and by technical considerations during debinding. The particle volume fraction ranges from 50 vol.% to approximately 70 vol.%,

depending on the powder and binder characteristics. At present, the optimal solid loading is determined by rheologic measurements and the final part properties.

Currently, there are various sophisticated methods of eliminating polymeric components of the feedstock, but debinding normally requires two consecutive stages. First, one of the binder components is removed by a physical solvent process that creates interconnected channels to facilitate the removal of volatiles during a second thermal debinding stage. This procedure not only prevents defects by relieving the internal pressure from any trapped volatiles but also allows a more rapid elimination of volatiles than a single thermal step process. Powder particles constitute a barrier for both polymer chains that are removed by solvent and volatile products resulting from thermal degradation, which limits the effectiveness of the debinding. Moreover, during thermal debinding, atmospheric and temperature conditions are important considerations. For typical polymer decomposition temperatures, the probability of material contamination with elements such as carbon or oxygen becomes especially important for metallic materials. Therefore, a thermal debinding process preferably uses an inert atmosphere whenever possible, although oxygen is more effective for organic component degradation.

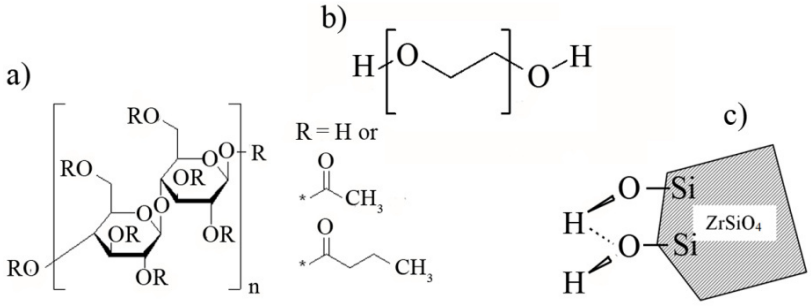

Figure 1. The chemical structures of the different feedstock components: a) the basic cellulose acetate butyrate monomer and possible substitution groups; b) poly(ethylene) glycol monomer and end chain hydroxyl groups; and c) a representation of the hydroxyl groups on the zirconium silicate particle surface.

Polymer decomposition mechanisms within the feedstock are very complex. The decomposition of a single binder component by itself is complex, as in PEG decomposition in an inert gas. Polyethylene glycol (Figure 1b) is a polyether compound formed by the polymerisation of ethylene oxide monomers with conforming linear chains. There is extensive literature describing the thermal degradation of PEG in terms of the decomposition of volatiles or the pyrolysis of by-products studied with chromatography, infrared spectroscopy or mass spectroscopy [4, 5]. The products obtained during PEG pyrolysis include various formaldehydes, acetaldehydes, ethylene glycol, ethylene oxide, water, low-carbon alkenes, carbon monoxide and dioxide and traces of other low molecular weight hydroxyl, carboxyl, carbonyl and ethereal compounds. The decomposition of CAB, an ester of cellulose that includes not only its main constituent monomers (beta-D-glucose chains) but also variable substitution of butyryl, acetyl and hydroxyl side groups, results in even more complex products (Figure 1a). Cellulose pyrolysis has been studied for more than six decades. Even so,

the molecular-level processes underlying the pyrolysis reactions remain poorly understood. Gongwer et al. detected carbon monoxide, carbon dioxide, methyl acetate and methyl butyrate among the volatile fractions derived from CAB pyrolysis with certain amounts of ketenes and ethyl ketenes, butyric and acetic acid [6]. That study showed the complexity of the products that presumably result from feedstock degradation. On the one hand, the findings indicate the probable influence of the different interactions among constituents on the global decomposition behaviour. Zirconium silicate surface and hydroxyl groups (Figure 1c) most likely interact with side or end groups present in the CAB and PEG chains. On the other hand, degradation compounds from the less thermally stable polymers may also affect the onset temperature of the most thermally stable polymer. Furthermore, particles act as a barrier to the removal of volatiles and, thus, affect the degradation rate.

In this work, simultaneous calorimetry and thermogravimetric analyses were performed to study the thermal decomposition of zirconium silicate feedstocks composed of cellulose acetate butyrate (CAB) and polyethylene glycol (PEG) binders in an inert nitrogen atmosphere. Binder and feedstock temperature stability and decomposition kinetics were investigated using integral procedure decomposition temperature (IPDT) and isoconversional methodologies, respectively. Several isoconversional methods were used, and their convenience is discussed. The FTIR technique was used to investigate possible interactions between feedstock components.

Several zirconium silicate feedstocks consisting of mixtures with different proportions of constituents were investigated; these variations allowed the effect of the effective powder surface on the chemisorption of CAB and PEG molecules and the channel volume used to remove volatiles to be elucidated. The degradation of the binder system was studied to evaluate the extent of the influence that particles exert on the decomposition of CAB and PEG. The results reveal changes in the thermal degradation behaviour with solid loading. Based on the findings, a method to determine the optimum solid loading conditions using thermogravimetric tools is proposed and discussed.

2. Experimental

Zirconium silicate powders were supplied by GUZMÁN GLOBAL S.L. (Nules,Spain) and exhibit an irregular, edged morphology. A Malvern 2000 laser scattering device was used to measure the particle distribution parameter. The particle size parameters (D_{50} and D_{90}) are 1,604 and 465 μm, respectively. The powders have a specific surface area of 5.0363 m²/g, as measured with a Micrometrics Gemini VII BET measurement device.

A binder system based on PEG and CAB was selected. These binders have been demonstrated to be effective for zircon PIM and provide improved properties when compared to other binder systems [7]. However, there are no published comprehensive studies on their thermal degradation. The binders consist of two types of CAB: CAB381-0.1 and CAB551-0.01. Each of these binders has different percentages of butyryl, acetyl and hydroxyl groups blended with

two types of PEG with different average molecular weights. The composition of the binder system and the characteristics of the components are shown in Table 1.

Table 1. Composition of the binder material.

	CAB381-0.1	**CAB551-0.01**	**PEG20K**	**PEG4K**
VOL.%	10	30	58	2
T_{MELT} [ºC]	155-165	127-142	63-66	58-61
T_{GLASS} [ºC]	123	85	< 0	< 0
M_W	20000	16000	20000	4000
Supplier	Eastman	Eastman	Aldrich	Aldrich

A Rheomix 600 Haake rheometer coupled with a Haake Rheocord 252p module was used for the mixing experiments. Different feedstock compositions, ranging from 0 vol.% zircon powder (single binder) to 52.5 vol.% (minimum solid loading tested) to 65 vol.%, were investigated in 2.5 vol.% increments. A temperature of 150º C was used for all the batches, and the mixing chamber was filled with feedstock to 72% of the total volume (the chamber volume is 69 cm^3). A rotor speed of 50 rpm was employed to mix the feedstock and the binder for 60 min to ensure complete homogenisation. In addition, a batch was produced by dissolving all of the binder components in an ethylene acetate solvent and placing it in a vacuum at 120ºC for eight hours to ensure maximum homogenisation of the polymer components.

A Perkin Elmer STA 6000 device was used to thermodynamically evaluate the decomposition of the binder and the feedstock. This device allows the simultaneous acquisition of the thermogravimetric TGA curves and the DTA/DSC curves. The examined temperature range was from 50ºC to 650ºC. Calcium oxalate was employed for thermogravimetric calibration, whereas elemental indium (99.999% pure) was used for heat and temperature calibration. An inert nitrogen atmosphere was employed with a flow rate of 40 ml/min. Feedstock pellets of approximately the same morphology and weight were used for the analysis. The net weight of the binder in the feedstock was constant for all experiments, with a minimum of 5 mg for all cases. For a thorough evaluation of the decomposition kinetics, four heating rates were evaluated: 10ºC/min, 15ºC/min, 20ºC/min and 25ºC/min.

A Philips XL 30 scanning electron microscope (SEM) and an Olympus GX71 light optical microscope (LM) with a polarised filter were used to determine the homogenisation. Fourier transform infrared spectroscopy (FTIR) measurements were recorded using a Perkin Elmer Spectrum GX device.

3. Results

3.1 Thermal degradation of binder in N_2

Figure 2 presents typical differential scanning calorimetry curves (DSC), thermogravimetry (TG) curves (or thermograms) and the derivative of the TG curves (DTG) for feedstocks in a

nitrogen atmosphere. The characteristic PEG melting peak can be observed between 50ºC and 70ºC in the DSC curve. The degradation temperature interval occurs between 350ºC and 440ºC and represents a single endothermic step.

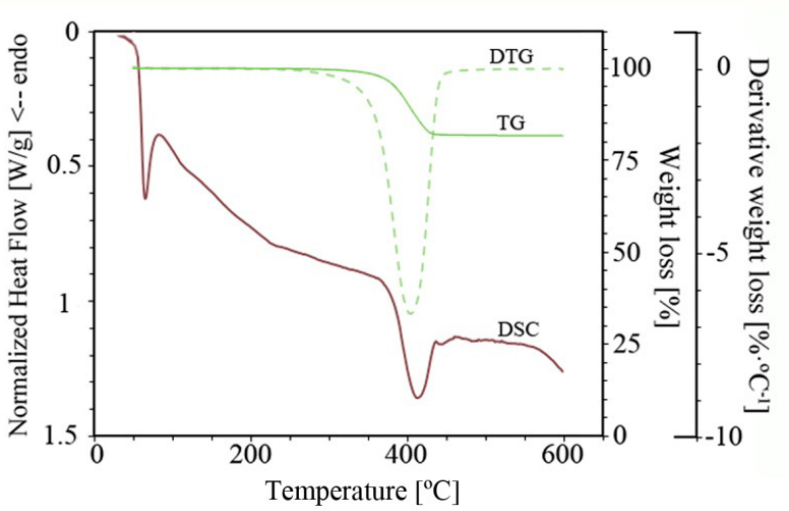

Figure 2. Typical simultaneous thermal analysis of the DSC, TG and DTG curves of the studied feedstocks. In this case, the curves correspond to a 52.5 vol.% feedstock subjected to a heating rate of 20 ºC/min.

The resulting TGA thermograms for different feedstock solid loadings at a heating rate of 20ºC/min are presented in Figure 3. The theoretical values of the maximum weight loss possible for these systems are represented by straight, dashed lines. None of the tests achieved complete thermal degradation of the polymer components, which suggests that for a nitrogen atmosphere, there is a residual portion of the binder component that does not degrade completely under these conditions up to 600ºC. Thus, this residue corresponds to incomplete CAB degradation.

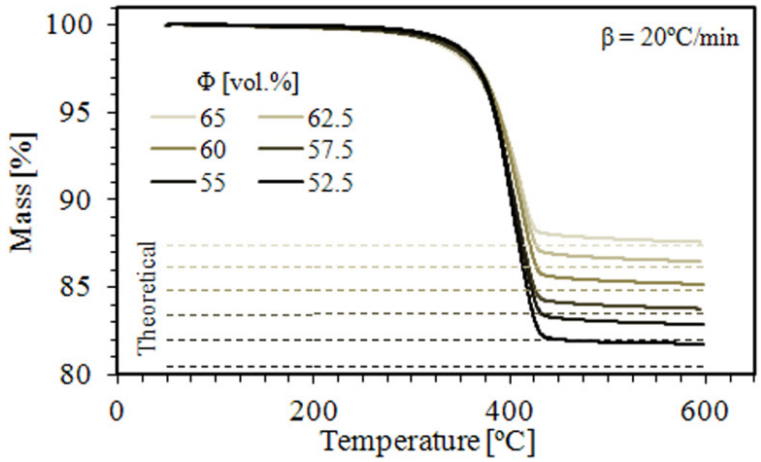

Figure 3. TGA weight loss results for different solid loadings.

The deviation from the theoretical value is considerably higher for feedstocks with lower solid loading content and diminishes as the solid loading increases. As the solid loading content

increases, the polymer weight that must be eliminated within the same time frame decreases; as a result, the deviation from the theoretical value will presumably decrease. Nevertheless, the deviations of the 52.5 vol.% and 55 vol.% feedstocks are high compared to those of the other feedstocks at higher solid loadings. A possible explanation could be a decrease in the organic compound molecular weight caused by mechanical scission of the chains. As the solid loading increases, the particles become arranged in a closer packing configuration, which increases the probability of particle contact despite the existence of a separating polymer gap. This arrangement increases the shear forces that support the binder components. Therefore, mechanical scission of the polymer chain may occur. As the polymer molecular weight decreases, the effectiveness of the thermal degradation in terms of the remaining residue increases.

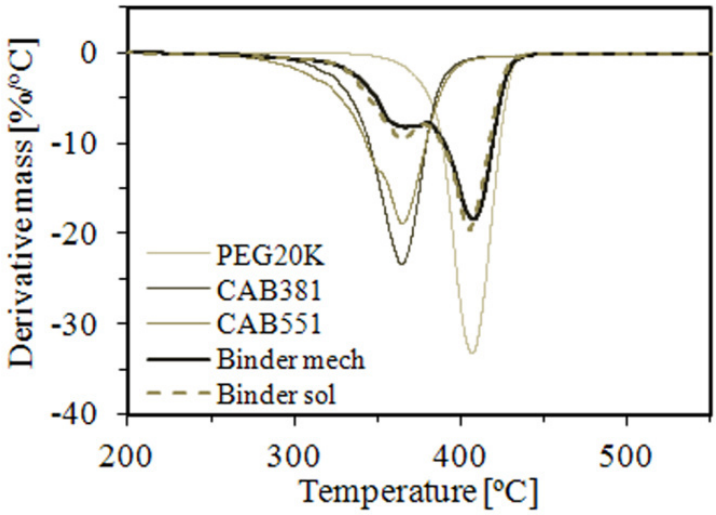

Figure 4. DTG curves of the mechanically mixed binder system (Binder mech), the ethylene acetate solvent mixture (Binder sol) and their individual components.

Nevertheless, the thermogram slope decreases as the solid loading increases. To some extent, this trend is contrary to the theoretical reduction in the binder molecular weight caused by increasing shear forces. The slope, which represents the weight loss ratio for different temperature increments, is an indicator of how the binder components are decomposed and removed from the system. The slope change has several interpretations, and its meaning remains controversial in high charged polymer systems. For high solid loading content, this trend may reveal increasing difficulty in removing decomposed volatiles because of the formation of a char layer or particle impediment as the solid loading increases for PIM feedstock. This issue has been extensively studied for systems in which the solid content is relatively low (up to 50 vol.%), especially in epoxy resins that are thermally stabilised with fillers [8, 9]. In such cases, many works attribute this decrease in the slope to the formation of a char layer, which contributes to the polymer thermal stability. In PIM systems, this behaviour is explained by the increasing packing of the powder particles because the solid load impedes the formation of evacuating channels or reduces their capacity by decreasing

their cross section; these effects are enhanced by the formation of a char layer around the particles.

As can be observed from Figure 2, for all of the feedstocks DTG curves, the decomposition of binder components in nitrogen, although it is a complex multi-component system, occurs in a single step via a dominant decomposition reaction or via concurrent decomposition reactions that occur within the same temperature range. This finding is in contrast to the two well-defined CAB and PEG degradation DTG peaks recorded for the binder system alone (Figure 4). The DTG peaks of each binder component without zircon powders (both separately and after mixing) are shown in Figure 4. The temperature for the maximum weight loss rate differs greatly between the CAB and PEG raw components. A small deviation is observed in the onset temperature, as well as a widening of the CAB degradation peak in the DTG curves for the binder system; these trends are observed when the binder components were mixed by mechanical and solvent methods, which may reveal a certain interaction between the PEG and CAB components. There is a single peak in the DTG curve of the feedstock, which shows that a certain type of interaction between the powders and the binder component may be occurring (i.e., chemisorptions of the OH or C=O carbonyl groups with zircon OH present on the particle surfaces). The degree of compatibility between CAB and PEG is directly related to the solubility or miscibility of these components, which could be such that, even after mixing by dissolution in a common solvent to promote maximum polymer chain entanglement, some rejection may occur between the components and lead to the formation of different phases. This effect is shown in Figure 5 where three phases are observed in the binder system without filler: a) a typical PEG micelle, b) an amorphous CAB region and c) a mixture of both CAB and PEG in a fibre structure.

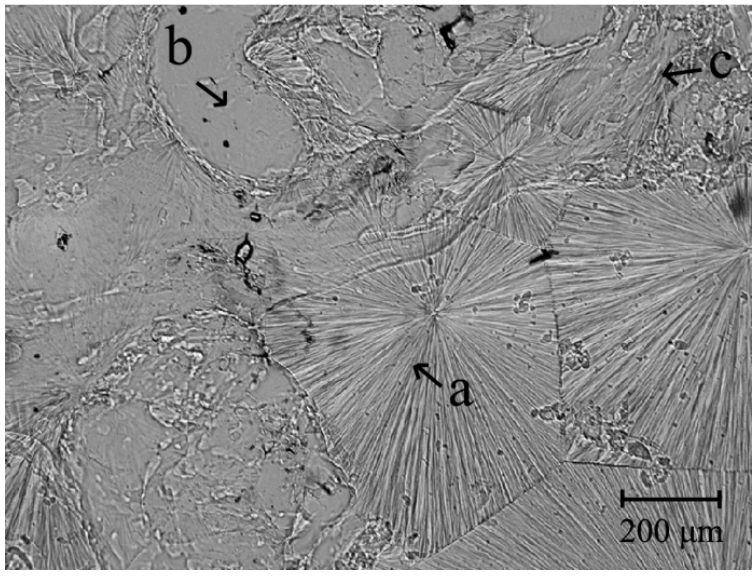

Figure 5. Polarised light optical microscopy image of the binder system: a) a typical PEG micelle; b) a region of pure CAB; and c) a region with a phase presumed to be a mixture of CAB and PEG.

If there is an interaction between the binder components and the particle surfaces, the points at which these interactions occur may act as anchor points to prevent component segregation and

promote the formation of smaller single component phases. This process is observed in Figure 6, which contains a scanning electron microscopy (SEM) image of the zircon feedstock. The zircon particles are homogeneously embedded in a homogenously mixed binder system. The CAB fibres interconnect the particles, and PEG surrounds both the CAB and zircon particles. This arrangement explains why the CAB and PEG degradation DTG peaks merge into a single peak.

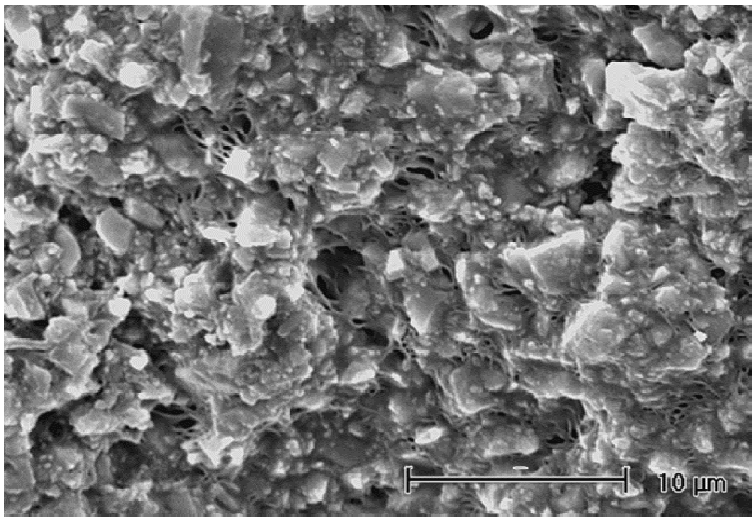

Figure 6. Scanning electron microscopy (SEM) image of the zircon feedstock. The zircon particles are homogeneously embedded in a homogenously mixed binder system.

To evaluate any possible interactions between the powder and binder components, FTIR experiments were performed for individual binder components, for the binder system itself and for the feedstock containing zircon powder. The resulting FTIR absorption spectra for the wave number range from 1600 to 4000 cm-1 are presented in Figure 7. The baselines were subtracted, and the curves were normalised to the maximum peak value. Additionally, there is a slight red shift (approximately 8 cm^{-1}) of the characteristic CAB peak (1757.6 cm-1) in the case of the feedstock but not in the binder system. This peak is related to the carbonyl group present in acetyl and butyryl substituents in CAB. There is also a slight red shift (approximately 10 cm-1) of the characteristic PEG peak (2884.8 cm-1) that is only observed in the feedstock. These peak displacements, along with the LOM and SEM images, are sufficient to dismiss possible experimental resolution error (1 cm^{-1}) and are evidence of certain interactions between the powder and binder components that explain the behaviour of the DTG curves. The specific nature of these interactions is not discussed in this work.

3.2 Thermal stability studies

The initial decomposition temperature (IDT) and the integral procedure decomposition temperature (IPDT) were used to analyse the thermal stability of the binder system as a function of the solid loading content. The IDT indicates the apparent thermal stability of binder system with regard to the maximum feedstock processing rate and moulding temperatures. The IDT is determined by the onset weight loss in the TGA curves of the different feedstocks.

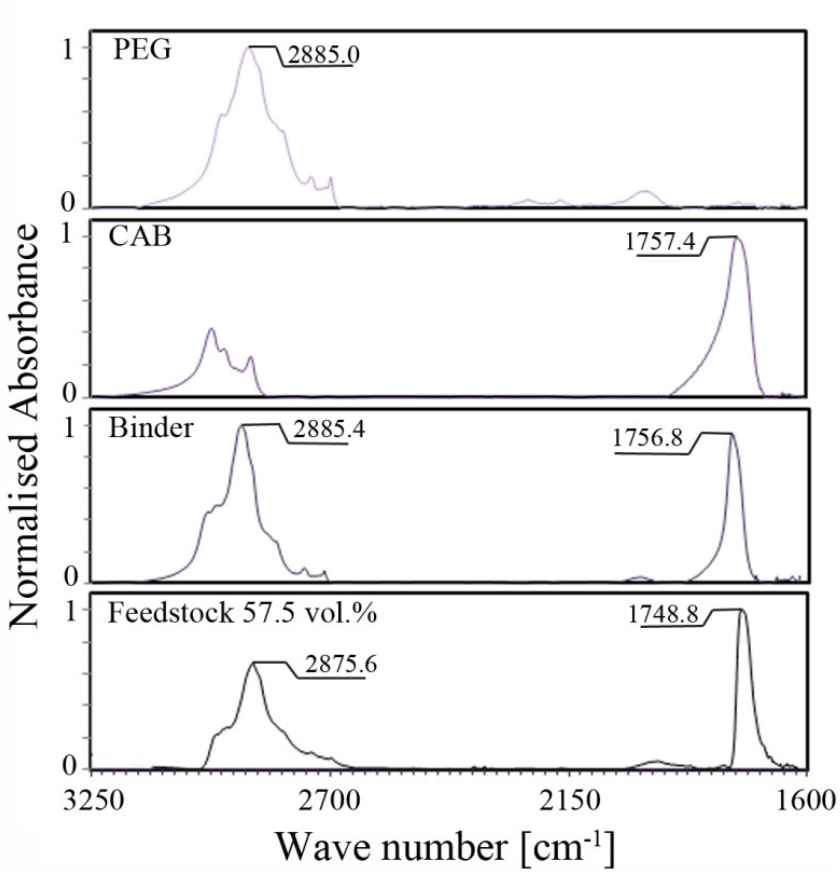

Figure 7. Fourier transform infrared (FTIR) spectra. From top to bottom: PEG20k, CAB 381, binder system and 57.5 vol.% feedstock. The curves were smoothed, base-line subtracted and normalised, but the peak values were determined from the original curves to avoid correction distortions.

Table 2. Thermal parameters deduced from the TG and DTG curves for different solid loadings.

Φ [vol.%]	IDT [ºC]	Tmax [ºC]	Tend [ºC]	ΔTpeak [ºC]	IPDT [ºC]
52.5	358.5	403.3	437.9	79.4	3846.8
55	359.0	404.4	437.8	78.8	4126.2
57.5	356.4	407.5	436.3	79.9	4398.4
60	356.3	411.2	436.9	80.6	4863.8
62.5	353.2	411.5	435.9	82.7	5376.3
65	351.4	410.9	433.6	82.2	5962.5

Table 2 presents the values of the degradation onset temperature (IDT), maximum thermogram derivative peak (T_{max}) corresponding to the temperature at the maximum degradation rate, degradation end temperature (T_{end}) and the wide thermogram derivative peak (ΔTpeak). The IDT and T_{end} values decrease when the solid loading increases; additionally, the peak widens, and T_{max} rises. The decrease in the onset and ending temperatures may indicate an incremental decrease in the binder molecular weights caused by the shear forces exerted by the powder particles on the binder components as the solid loading increases. However, the T_{max} increment suggests the weight loss decreased as the proportion of the zircon particles increases by an impediment of zircon particles.

The IPDT determined from the residual weight fraction in the TGA is a reproducible datum that can be consistently determined for diverse materials and represents both a truly comprehensive index of intrinsic thermal stability and a real temperature that has practical significance. The method for calculating the IPDT is proposed by Doyle [8, 10] and converts the area under the TGA curve into a value that approximately represents the characteristic end-of-volatilisation temperature, T_{a*} (Eq. 1):

$$T_{a*}[ºC] = A^* \cdot (T_f - T_i) + T_i \quad , \quad (1)$$

where A* is the area under the TGA curve within the evaluated temperature range (defined by initial temperature T_i and the final temperature T_f) and normalised with respect to both the residual weight and temperature. However, the IPDT takes into account the amount of refractory or non-volatile residues at T_f by means of the coefficient K^*. Therefore, the method to calculate the IPDT is described in Eq. 2:

$$IPDT[ºC] = A^* \cdot K^* \cdot (T_f - T_i) + T_i \; . \quad (2)$$

A representation of the areas S_1, S_2 and S_3 used to calculate A^* [$A^*=(S_1+S_2)/(S_1+S_2+S_3)$] and K^* [$K^*=(S_1+S_2)/S_1$] is shown in Figure 8. In these cases, the IPDT represents the inherent thermal stability of the binder system and describes the entire binder degradation process in terms of the decomposition and vaporisation of the different volatiles taking into account differences in the solid loading percentages. The higher the IPDT is, the more thermally stable the feedstock is. Thus, the binder components will resist higher temperatures until complete volatilisation occurs.

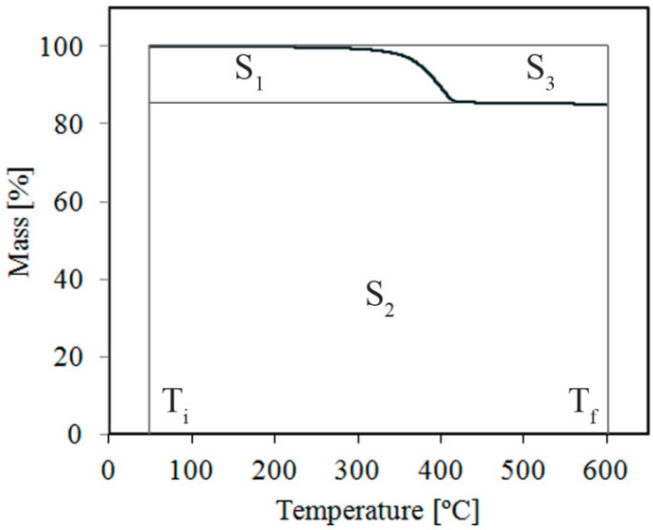

Figure 8. Schematic representation of S_1, S_2 and S_3 for the IPDT (60 vol.%, 10ºC/min and N_2)

IPDT values for different solid loading feedstocks and heating rates are presented in Figure 9. The value of the IPDT increases as the solid loading increases. Increasing the solid loading reduces the volatile fraction and the fraction of char formation that would reduce the release of

volatiles. Good thermal stability, heat-resistant properties and the high content of zirconium silicate powder particles reduce both the thermal degradation rate of the organic component of the feedstocks and the thermal stability. Two linear tendencies are observed in the plotted data. The first occurs below 57.5 vol.% solid loading and has a smoother slope than the second, which occurs for values greater than 57.5 vol.%. This change in the slope coincides with the optimum solid loading values determined for powder injection moulding in previous works with zirconium silicate feedstocks, as determined using rheological methods [11].

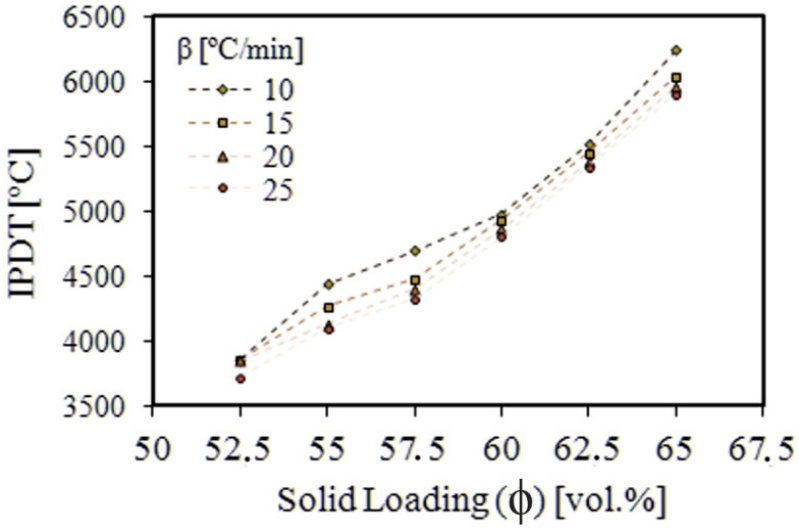

Figure 9. IPDT values for different solid loadings and heating rates.

3.3 Thermal degradation kinetics in nitrogen atmosphere

Non-isothermal isoconversional methods are chosen to study degradation kinetics of the selected PIM feedstocks. The main reason to select these methodologies instead of isothermal procedures is due to simplicity and to take in advance the conventional non-isothermal TGA curves that are employed in some steps optimization in PIM processes. Although non-isothermal approaches have several limitations in their use to ascertain kinetics parameters, they are frequently used to study the kinetics of charged polymers [12, 13].

These methods are based on studying the degree of conversion with respect to temperature at different heating rates. As an example, Figure 10 represents the typical conversion curves for zircon feedstocks at different heating rates; in this particular case, the loading is 60 vol.% feedstock. The degree of conversion for a certain temperature α is defined as the ratio of the actual weight loss m(T) to the total weight loss, as expressed in Eq. 3:

$$\alpha(T) = \frac{m_0 - m(T)}{m_0 - m_\infty}. \quad (3)$$

The variables m_o and m_∞ correspond to the initial and final masses, respectively. Unlike classical model-fitting methods, isoconversional methods do not assume a kinetic model $f(\alpha)$ to calculate the activation energy of a reaction. Instead, the apparent activation energy is calculated directly from the TGA curves. Consequently, the rate of degradation, dα/dt, is

assumed to depend on the temperature and weight of the sample. The main advantage of eliminating the necessity of a kinetic model, which for complicate reactions could result a complex task, is clouded by the influence of the sample mass and size in the apparent kinetics parameters calculated. Furthermore these parameters could be influenced by the thermal lag across the specimen [14].

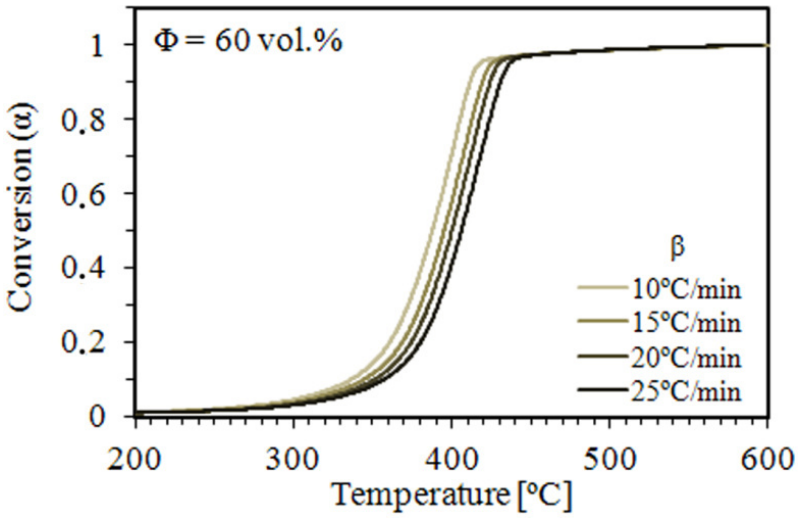

Figure 10. Typical conversion curves for zircon feedstocks at different heating rates (60 vol.% solid loading).

In literature a wide variety of non-isothermal models could be found. The lack of agreement among kinetic parameters calculated from the same set of experimental data using different methods of mathematical analysis is disturbing. In this work FWO and KAS integral methods are selected to estimate apparent activation energy values. They are based in the integral of the following expression (Equ.4):

$$\frac{d\alpha}{f(\alpha)} = \left(\frac{k_0 \cdot \exp(-Ea/R \cdot T)}{\beta}\right) \cdot dT, \qquad (4)$$

where k_0 represents the pre-exponential factor, or frequency factor; E_a is the apparent activation energy; R is the gas constant; T is the absolute temperature; and β is the heating rate (dT/dt).

The FWO [15, 16] method is based on the principle that a reaction rate at a constant conversion is only a function of temperature. Using Doyle's approximation [17] of the temperature integral $p(E_a/R \cdot T)$ and applying logarithms, the following expression is produced (Eq. 7):

$$\log(\beta_i) = \log\left[\frac{k_0 \cdot E_a}{R \cdot g(\alpha)}\right] - 2.315 - 0.4567 \cdot \left(\frac{E_a}{R \cdot T_{\alpha i}}\right), \qquad (5)$$

where g(α) represents the integral of $\frac{d\alpha}{f(\alpha)}$. Considering a constant conversion, the representation of logβ versus 1/T should be a straight line with a slope defined as

$d(\log\beta)/d(1/T)=-0.4567(E_a/R\cdot T)$. Therefore, the activation energy may be calculated from Eq. 8 as follows:

$$E_a = -\text{slope} \cdot \frac{R}{0.457}. \qquad (8)$$

The Kissinger-Akahira-Sunose method (KAS method) [18, 19] (Eq. 9) is based on the Coats-Redfern [20] approximation of the temperature integral $p(E_a/R\cdot T)$ as applied to Eq. 6 and considering that $2\cdot R\cdot T/Ea$ is much less than unity. The resulting relationships are expressed as:

$$\ln\left(\frac{\beta_i}{T_{\alpha i}^2}\right) = \ln\left(\frac{k_0 \cdot R}{E_a \cdot g(\alpha)}\right) - \frac{E_a}{R \cdot T_{\alpha i}}. \qquad (9)$$

Thus, the plot of $\ln(\beta/T^2)$ vs. $1/T^2$ for constant values of α and αi should be a straight line with a slope that can be used to calculate the apparent activation energy (Eq. 10):

$$E_a = -\text{slope} \cdot R. \qquad (10)$$

Some of the main shortcomings of both methods are using an approximation of the temperature integral and the selection of the integral limits, but the validity of the calculated apparent activation energies is assumed good enough for the general proposes of this work.

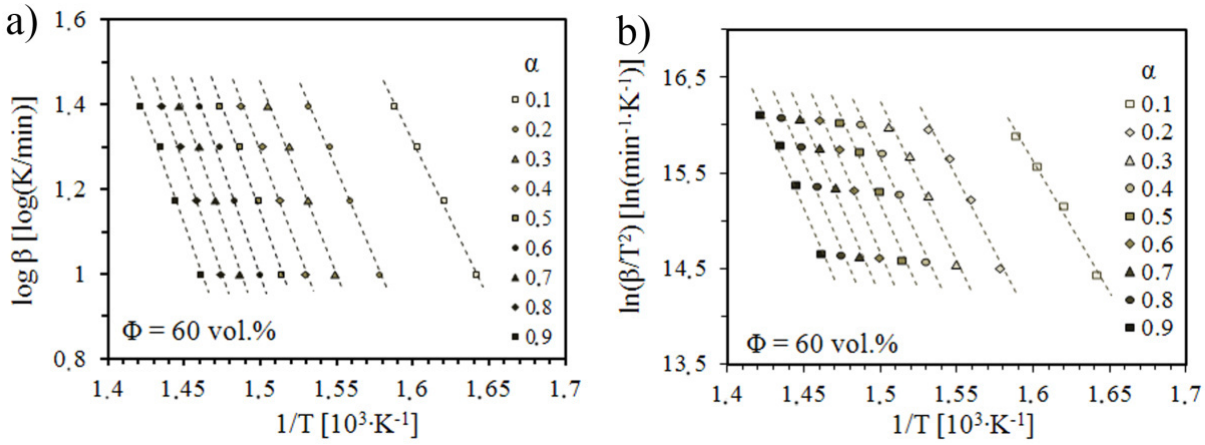

Figure 11. Isoconversional plots used to calculate the activation energy at the listed conversion α values by a) the FWO method and b) the KAS method for 60 vol.% zircon feedstock

Figure 11 shows the typical isoconversional curves of the FWO and KAS methods from which the apparent activation energy can be obtained. Both methodologies present a relatively good linear correlation with the experimental results, but the FWO method is more precise according to correlation coefficient. Table 3 presents some activation energy results and the corresponding correlation coefficient R^2 for each method. The KAS and FWO methods allow the calculation of the activation energy at different conversion values.

Table 3. Activation energies calculated by FWO and KAS methods.

60 vol.%	FWO		KAS	
α	**E_a [kJ/mol]**	**R^2**	**E_a [kJ/mol]**	**R^2**
0.3	165.7	0.993	252.5	0.983
0.4	172.9	0.993	263.8	0.983
0.5	179.1	0.987	272.6	0.971
0.6	186.3	0.993	285.1	0.983
0.7	186.9	0.991	285.5	0.980
Average	178.2		271.9	

Figure 12 shows the dependence on conversion of the apparent activation energy values, as assessed by the FWO and the KAS methods. Differences in the calculated values of the activation energies evidence the limitations of using non-isothermal approaches. Through α, the feedstocks seem to have an important influence on E_a that is independent of solid loading. Increasing dependence of the activation energy on the conversion is quite typical of polymer degradation [21]. This behaviour is considered to be an indicator of a complex reaction [22]. For the majority of the curve, E_a increases as the values of α increase up to a value at which E_a either stabilises or begins to decrease; this behaviour gives the curve a certain convexity. Vyazovkin and Lesnikovich [23, 24] noted that in non-isothermal experiments, patterns in the shape of the curve dependence of the apparent value of E_a on α could provide insights into the type of complex process taking place. An increasing dependence of E_a on α characterises concurrent, competitive reactions, whereas convexity indicates a change in the rate-determining step.

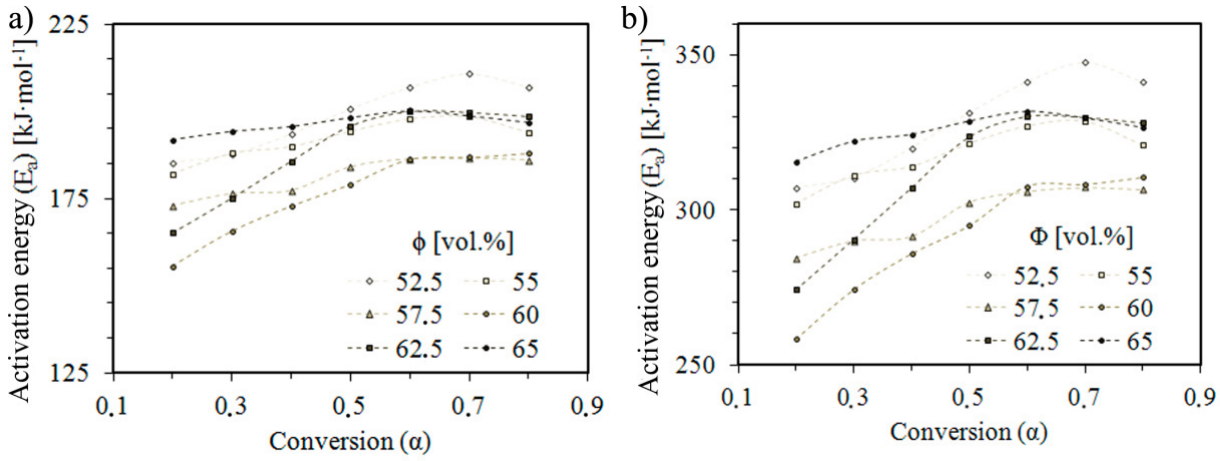

Figure 12. Dependence of the apparent activation energy on the conversion assessed using a) the FWO and b) the KAS methods.

The concurrent competitive reactions could be molecular degradation reactions of both CAB and PEG. The subsequent plateau at high conversion values may indicate the end of a reaction or the creation of open pathways that facilitate the removal of volatiles as the binder decomposes. Unfortunately non-isothermal methods without other supporting information

have generally a no-mechanistic value, but at least in this case could serve as a first rough approach to support the general analysis in combination with other methodologies presented.

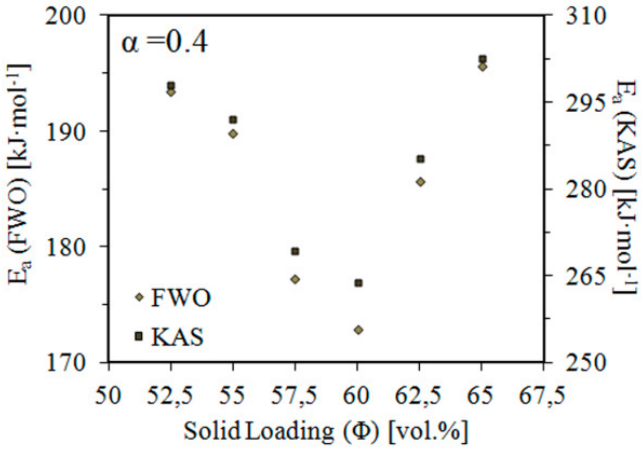

Figure 13. The activation energy dependence on the conversion.

Figure 13 represents the activation energies for a constant conversion of 0.4 for different feedstock solid loadings. A minimum activation energy is observed at 60 vol.%, which coincides with a minimum in the activation energy calculated by Hidalgo [11] using rheological methods for the same feedstocks.

This phenomenon may be explained by opposing effects. First, a reduction in the molecular weight of the polymer compound caused by shear forces as the solid loading increases reduces the activation energy. Simultaneously, a portion of the effective particle surface presumably interacts with the polymer compound and reduces the apparent activation energy of degradation. The opposite effect, an increase in the apparent activation energy, would occur as a consequence of particle packing as the solid loading increases, reducing the diameters of the volatiles-removal channels that may have been enhanced by the formation of a protective layer of char around the particles. All of these effects combine to minimise the apparent activation energy of degradation, reaffirming 60 vol.% as the optimum solid loading value with respect to both rheological concerns and thermal degradation of the binder. The direct relationship between the apparent activation energies, with respect to both rheological and thermal degradation concerns, is not clear. There are analogies in the possible explanations of the mechanisms that affect these factors, such as the change of the particle packing and the effective interaction surface between the organic compounds and the particles. Nevertheless, studying the thermal degradation by calculating activation energies for different solid loading conditions emerges as an alternative to the traditional rheological studies used to assess optimal solid loading in PIM feedstocks.

4. Conclusions

Thermal analyses via DSC and TG experiments in a nitrogen atmosphere were performed for different solid loading zircon feedstocks composed of CAB and PEG. Binder components

apparently thermally degrade by endothermic concurrent reactions in a single step between 350 ºC and 430 ºC. A possible interaction between the zircon particles and the binder components was revealed by this single peak and the infrared FTIR analysis. Thermal stability studies using the IPDT factor reveal a linear slope in the feedstock thermal stability as the solid loading increases. A change in the linear slope occurs at approximately 60 vol.% solid loading. This change coincides with the optimal solid loading calculated in previous studies using rheological methods. The kinetics of the thermal degradation of the binder components in terms of calculation apparent activations energies were also studied using the FWO and KAS methods. Variations in the apparent activation energies calculated using these methods suggest the occurrence of complex, concurrent and competitive reactions. A representation of the apparent activation energy at a constant conversion for different solid loadings shows that the activation energy is minimised at 60 vol.%. This value coincides with a minimum in the activation energy calculated using rheological methods in previous studies. All of these results emphasise the potential for using thermocalorimetric analysis instead of, or as a complement to, conventional rheological studies to determine the optimal solid loading of PIM feedstocks.

ACKNOWLEDGMENTS

The authors wish to acknowledge M. Crespo for her generously provided comments and discussion of the results. The authors also wish to thank GUZMÁN GLOBAL S.L. and MIMTECH ALFA for their collaboration on the ECOPIM project (ref. IPT-2011-0931-20000) that was funded by the Spanish Ministry of the Economy and Competitiveness. Furthermore, the authors would like to acknowledge the strong support from the ESTRUMAT projects (ref. S2009/MAT-1585), which were funded by the CAM-Consejería Educación Dir. Gral. Universidades e Investigación, and from the COMETAS project (ref. MAT2009/14448-C02-02), which was funded by the Spanish Ministry of the Economy and Competitiveness.

REFERENCES

1. German, R.M. and A. Bose, eds. *Injection Molding of Metals and ceramics*. 1997, Metal Powders Industry Federation.
2. German, R., *Metal powder injection molding (MIM): key trends and markets*, in *Handbook of Metal Injection Molding*, D. Heaney, Editor. 2012, Woodhead Publishing Limited.
3. Petzoldt, F., *Current Status and Future Perspectives of the MIM Technology.* Cfi-Ceramic Forum International, 2012. **89**(10): p. E11-E15.
4. Voorhees, K.J., S.F. Baugh, and D.N. Stevenson, *An investigation of the thermal-degradation of poly(ethylene glycol).* Journal of Analytical and Applied Pyrolysis, 1994. **30**(1): p. 47-57.
5. Arisawa, H. and T.B. Brill, *Flash pyrolysis of polyethyleneglycol .1. Chemometric resolution of FTIR spectra of the volatile products at 370-550 degrees C.* Combustion and Flame, 1997. **109**(1-2): p. 87-104.
6. Gongwer, P.E., H. Arisawa, and T.B. Brill, *Kinetics and products from flash pyrolysis of cellulose acetate butyrate (CAB) at 460-600 degrees C.* Combustion and Flame, 1997. **109**(3): p. 370-381.

7. Bernardo, E., et al., *Feedstock Development for Powder Injection Moulding of Zirconium Silicate.* Powder Injection Moulding International, 2012. **6**(1): p. 75-78.
8. Jin, F.-L. and S.-J. Park, *Thermal properties of epoxy resin/filler hybrid composites.* Polymer Degradation and Stability, 2012. **97**(11): p. 2148-2153.
9. Tarrio-Saaavedra, J., et al., *Effect of silica content on thermal stability of fumed silica/epoxy composites.* Polymer Degradation and Stability, 2008. **93**(12): p. 2133-2137.
10. Doyle, C.D., *Estimating thermal stability of experimental polymers by empirical thermogravimetric analysis.* Analytical Chemistry, 1961. **33**(1): p. 77-&.
11. Hidalgo, J., A. Jimenez-Morales, and J.M. Torralba, *Torque rheology of zircon feedstocks for powder injection moulding.* Journal of the European Ceramic Society, 2012. **32**(16): p. 4063-4072.
12. Jankovic, B., et al., *The comparative kinetic analysis of non-isothermal degradation process of acrylonitrile-butadiene/ethylene-propylene-diene rubber blends reinforced with carbon black/silica fillers. Part II.* Thermochimica Acta, 2012. **543**: p. 304-312.
13. Macan, J., et al., *Thermal degradation of epoxy-silica organic-inorganic hybrid materials.* Polymer Degradation and Stability, 2006. **91**(1): p. 122-127.
14. Holland, B.J. and J.N. Hay, *The value and limitations of non-isothermal kinetics in the study of polymer degradation.* Thermochimica Acta, 2002. **388**(1-2): p. 253-273.
15. Flynn, J.H. and L.A. Wall, *A quick direct method for determination of activation energy from thermogravimetric data.* Journal of Polymer Science Part B-Polymer Letters, 1966. **4**(5PB): p. 323-&.
16. Ozawa, T., *A new method of analyzing thermogravimetric data.* Bulletin of the Chemical Society of Japan, 1965. **38**(11): p. 1881-&.
17. Doyle, C.D., *Series Approximations to Equation of Thermogravimetric Data.* Nature, 1965. **207**(4994): p. 290-&.
18. Kissinger, H.E., *Reaction Kinetics in Differentical Thermal Analysis.* Analytical Chemistry, 1957. **29**(11): p. 1702-1706.
19. Akahira, T.S., T, *Joint convention of four electrical institutes*. 1971, Chiba Institute of Technology: Chiba. p. 22-31.
20. Coats, A.W. and J.P. Redfern, *Kinetic Parameters from Thermogravimetric Data.* Nature, 1964. **201**(491): p. 68-&.
21. Vyazovkin, S., N. Sbirrazzuoli, and I. Dranca, *Variation in activation energy of the glass transition for polymers of different dynamic fragility.* Macromolecular Chemistry and Physics, 2006. **207**(13): p. 1126-1130.
22. Elder, J.P., *Multiple reaction scheme modeling 3: Mutually independent nth order reactions.* Journal of Thermal Analysis, 1989. **35**(6): p. 1965-1984.
23. Vyazovkin, S.V. and A.I. Lesnikovich, *On the dependence of kinetic parameters and functions in non-isothermal kinetics.* Thermochimica Acta, 1987. **122**(2): p. 413-418.
24. Vyazovkin, S.V. and A.I. Lesnikovich, *An approach to the solution of the inverse kinetic problem in the case of complex processes.1. Methods employing a series of thermoanalytical curves.* Thermochimica Acta, 1990. **165**(2): p. 273-280.

Paper 7

P7

J. Hidalgo, J.P. Fernández-Blázquez, A. Jiménez-Morales, T. Barriere, J.C. Gelin and J.M. Torralba

Effect of the particle size and solids volume fraction on the thermal degradation behaviour of Invar 36 feedstocks

Polymer Degradation and Stability 98 (12) (2013) 2546-2555

Effect of the particle size and solids volume fraction on the thermal degradation behaviour of Invar 36 feedstocks

J. Hidalgo[a], J.P. Fernández-Blázquez[c], A. Jiménez-Morales[a], T. Barriere[b], JC. Gelin[b], J.M. Torralba[a,c]*

a Materials Science Department at Carlos III University of Madrid, Leganés (Spain)
b Applied Mechanics Department at FEMTO-ST Institute, Besançon (France)
c IMDEA Materials Institute, Getafe (Spain)
* Corresponding author: Avd. Universidad 30, 28911, Leganés (Spain), e-mail: jhidalgo@ing.uc3m.es

ABSTRACT

Degradation kinetics and the thermal stability of Invar 36 powder injection moulding feedstocks (PIM) based on cellulose acetate butyrate (CAB) and polyethylene glycol (PEG) binders were investigated using simultaneous thermogravimetric analysis (STA) and differential scanning calorimetry (DSC). The initial decomposition temperature (IDT) and the integral procedure decomposition temperature (IPDT) were used to analyse the thermal stability of the binder system as a function of the solid loading content and powder particle size. The degradation kinetics was studied, and the process apparent activation energies were assessed using isoconversional methods. All the methodologies revealed changes in the thermal degradation behaviours of the feedstocks for solid loadings that were previously determined to correspond to optimal solid loadings using other experimental procedures. The studies also contrast previous similar findings with a ceramic powder. Therefore these results strengthen the proposal of thermodynamic degradation studies of feedstocks as an alternative or complementary technique to determine optimal solid loading contents in metal injection moulding (MIM).

Keywords: Powder Injection Moulding, Invar 36, Cellulose Acetate Butyrate, Polyethylene Glycol, Thermal Degradation

1. Introduction

Powder injection moulding (PIM) is one of the main manufacturing processes used to produce small parts with complex geometries, thin walls and in large production batches [1]. This technology is applied to a wide variety of ceramics (commonly referred as ceramic injection moulding, CIM), metals (also referred as metal injection moulding, MIM) and combinations thereof [2]. The process consists of mixing a fine powder material with different polymer-like compounds, the so-called binder system. The binder system provides sufficient fluidity to the newly created feedstock to allow mould filling during injection. However, it will be removed during the subsequent debinding process, thus it has to allow an easy extraction. The binder system must be added in such quantities so as to optimise the process conditions and time required.

Elimination of the binder system out of the green body is the bottle neck in MIM processes and a critical and delicate step. It requires tailored optimisation of the time-temperature cycle in order to be economical and effective while avoiding faults like undesirable blistering [3]. For multi-component binders obtaining optimal thermal cycles is a difficult task that conventionally has been performed by "trial and error". However recent works propose to investigate the binder decomposition kinetics in order to identify points of rapid weight loss to avoid green parts damage, to speed up the debinding process and lower the overall cost [4-6].

The thermal burn out of organic components during debinding processes of MIM feedstock is intricate. There are several decomposition mechanism involved which are also dependant on several factors. Transport and elementary reactions steps could be rate limiting during debinding. Transport mechanisms would become more influential with increasing sample thickness, whereas in thin specimens such as in micro pieces, polymer decomposition kinetics would play a predominant role [7].

In previous works [8] we have proposed thermogravimetric analysis as an alternative to determine optimal solid loading for ceramic feedstocks while studying their thermal stability and decomposition kinetics. In this work same methods are contrasted with metallic powders. Calorimetric and thermogravimetric analyses were performed to study the thermal decomposition of an Invar 36 alloy ($Fe_{0.64}Ni_{0.36}$) feedstocks composed of cellulose acetate butyrate (CAB) and polyethylene glycol (PEG) binders in an inert nitrogen atmosphere. Binder and feedstock temperature stability and decomposition kinetics were investigated using integral procedure decomposition temperature (IPDT) and isoconversional methodologies, respectively. A number of isoconversional methods were used, and their convenience discussed.

Several Invar 36 feedstocks consisting of mixtures with different proportions of constituents were investigated. The volume fractions of metallic powders as well as the powder particle sizes were varied in this study. These variations allowed the effect of the effective powder surface on the interactions of CAB and PEG molecules with Invar 36 particles and the channel volume used to remove volatiles to be elucidated. The degradation of the binder system was studied to evaluate the extent of the influence that particles exert on the decomposition of CAB and PEG. The results reveal changes in the thermal degradation behaviour with solid loading and particle size. Based on these findings, we have contrasted the suitability to determine the optimum solid loading conditions using thermogravimetric tools.

2 Thermal Stability studies

The initial decomposition temperature (IDT) and the integral procedure decomposition temperature (IPDT) were used to analyse the thermal stability of the binder system as a function of the solid loading content and particle size. The IDT indicates the apparent thermal stability of binder system with regard to the maximum feedstock processing rate and moulding temperatures. The IDT is determined by the onset weight loss in the TGA curves of the different feedstocks. In this work IDT corresponds to the temperature at which the 2 % in

mass of the organic compounds was lost. The IPDT determined from the residual weight fraction in the TGA is a reproducible datum that can be consistently determined for diverse materials and represents both a truly comprehensive index of intrinsic thermal stability and a real temperature that has practical significance. The method for calculating the IPDT is proposed by Doyle [9, 10] and converts the area under the TGA curve into a value that approximately represents the characteristic end-of-volatilisation temperature, T_{a*} (Eq. 1):

$$T_{a*}[ºC] = A^* \cdot (T_f - T_i) + T_i \quad , \quad (1)$$

where A* is the area under the TGA curve within the evaluated temperature range (defined by initial temperature T_i and the final temperature T_f) and normalised with respect to both the residual weight and temperature. However, the IPDT takes into account the amount of refractory or non-volatile residues at T_f by means of the coefficient K^*. Therefore, the method to calculate the IPDT is described in Eq. 2:

$$IPDT[ºC] = A^* \cdot K^* \cdot (T_f - T_i) + T_i \, . \quad (2)$$

A representation of the areas S_1, S_2 and S_3 used to calculate A^* [$A^*=(S_1+S_2)/(S_1+S_2+S_3)$] and K^* [$K^*=(S_1+S_2)/S_1$] is shown in Figure 1. In these cases, the IPDT represents the inherent thermal stability of the binder system and describes the entire binder degradation process in terms of the decomposition and vaporisation of the different volatiles taking into account differences in the solid loading percentages. The higher the IPDT is, the more thermally stable the feedstock is. Thus, the binder components will resist higher temperatures until complete volatilisation occurs.

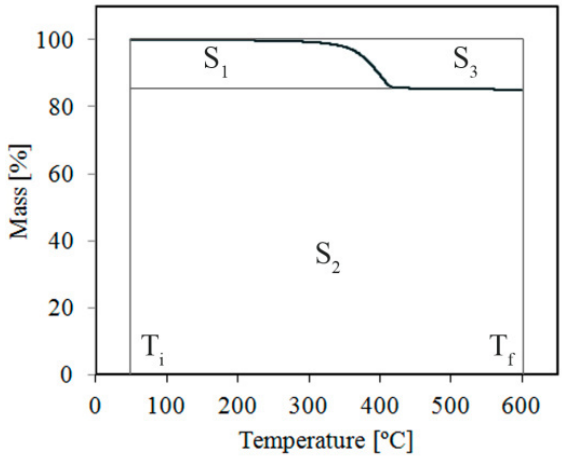

Figure 1 Scheme of the areas S1, S2 and S3 for the IPDT assessment

From the IPDT definition, it is clear that this value will be influenced by the selection of initial and final temperatures. To the best of the authors knowledge there is not a standard that defines where to set these temperatures. Hence, there is a limitation of using IPDT value when different systems are compared. In this work initial temperature was selected approximately considering the 20% below the IDT, which resulted to be 50 ºC. For the final temperature,

approximately the 20% above the end of degradation temperature was selected, which resulted to be 600 ºC. For comparison purposes this limits were maintained when determining the IPDT of different feedstocks and binder system components.

3 Degradation kinetic studies

A thorough discussion about the convenience of using model-free isoconversional methods to analyse thermal decomposition of MIM feedstocks could be found in the work of Salehi [7]. Model-free methods turn out to be the most reliable way to determine kinetic parameters of thermally activated complex processes, because the prior knowledge of the reaction mechanism is not necessary [11]. These methods are based on studying the degree of conversion with respect to temperature at different heating rates. The degree of conversion for a certain temperature α is defined as the ratio of the actual weight loss m(T) to the total weight loss, as expressed in Eq. 3:

$$\alpha(T) = \frac{m_0 - m(T)}{m_0 - m_\infty}. \quad (3)$$

The variables m_o and m_∞ correspond to the initial and final masses, respectively. In the model free methods apparent activation energy is calculated directly from the TGA curves. The term apparent activation energy comes for the uncertainty of the physical process associated to this activation energy. Activation energy most likely takes into account several different processes occurring at the same time. The rate of degradation, dα/dt, is assumed to depend on the temperature and weight of the sample. Therefore, the main advantage of eliminating the necessity of a kinetic model is clouded by the influence of the sample mass and size in the apparent kinetics parameters calculated. Furthermore these parameters could be influenced by the thermal lag across the specimen [12]. To reduce possible errors regarding size and mass, samples of similar dimensions and masses were employed. It is assumed for the thin disks employed that the binder removal rate is predominantly determined by decomposition rates of organics and not by transport processes.

In literature a wide variety of non-isothermal models could be found. The lack of agreement among kinetic parameters calculated from the same set of experimental data using different methods of mathematical analysis is disturbing. It has been shown that the causes for these differences are due to the intrinsic nature of the methods. In this work Flynn-Wall-Ozawa (FWO) and Kissinger-Akahira-Sunose (KAS) integral methods are selected to estimate apparent activation energy values. They are based in the integral of the following expression (Eq. 4):

$$\frac{d\alpha}{f(\alpha)} = \left(\frac{k_0 \cdot \exp(-Ea/R \cdot T)}{\beta}\right) \cdot dT, \quad (4)$$

where k_0 represents the pre-exponential factor, or frequency factor; E_a is the apparent activation energy; R is the gas constant; T is the absolute temperature; and β is the heating rate (dT/dt).

The FWO [13, 14] method is based on the principle that a reaction rate at a constant conversion is only a function of temperature. Using Doyle's approximation [15] of the temperature integral $p(E_a/R \cdot T)$ and applying logarithms, the following expression is produced (Eq. 5):

$$\log(\beta_i) = \log\left[\frac{k_0 \cdot E_a}{R \cdot g(\alpha)}\right] - 2.315 - 0.4567 \cdot \left(\frac{E_a}{R \cdot T_\alpha}\right), \qquad (5)$$

where $g(\alpha)$ represents the integral of $\frac{d\alpha}{f(\alpha)}$. Considering a constant conversion, the representation of $\log\beta$ versus $1/T$ should be a straight line with a slope defined as $d(\log\beta)/d(1/T)=-0.4567(E_a/R \cdot T)$. Therefore, the activation energy may be calculated from Eq. 6 as follows:

$$E_a = -\text{slope} \cdot \frac{R}{0.457}. \qquad (6)$$

The KAS method [16, 17] (Eq. 7) is based on the Coats-Redfern [18] approximation of the temperature integral $p(E_a/R \cdot T)$ and considering that $2 \cdot R \cdot T/Ea$ is much less than unity. The resulting relationships are expressed as:

$$\ln\left(\frac{\beta_i}{T_\alpha^2}\right) = \ln\left(\frac{k_0 \cdot R}{E_a \cdot g(\alpha)}\right) - \frac{E_a}{R \cdot T_\alpha}. \qquad (7)$$

Thus, the plot of $\ln(\beta/T^2)$ vs. $1/T^2$ for constant values of α and αi should be a straight line with a slope that can be used to calculate the apparent activation energy (Eq. 8):

$$E_a = -\text{slope} \cdot R. \qquad (8)$$

Some of the main shortcomings of both methods are using an approximation of the temperature integral and the selection of the integral limits, but the validity of the calculated apparent activation energies is assumed good enough for the general proposes of this work.

4. Experimental procedure

4.1 Materials

Gas atomised spherical Invar 36 powders were supplied by Sandvik Osprey Ltd. (UK). Two powders with different particle sizes were selected in this study. The coarsest powder was denoted as INV1 whereas the finest powder was denoted as INV2. A Malvern 2000 laser scattering device was used to measure the particle size distribution parameters. The powders specific surface areas were measured with a Micrometrics Gemini VII BET measurement device. All the particles parameters for both INV1 and INV2 are collected in Table 1.

A binder system based on PEG and CAB was selected. These binders have been demonstrated to be effective for PIM and provide improved properties when compared to other binder systems [19, 20]. However, there are no published comprehensive studies on their thermal degradation when Invar 36 particles are added.

Table 1 Particles parameters for INV and INV2

	Particle size Distribution				Specific area
	d_{10} [µm]	d_{50} [µm]	d_{90} [µm]	S_w	BET [m^2/g]
INV1	5.0	7.7	11.4	7.2	0.14
INV2	1.9	3.4	5.9	8.3	0.24

The binders consist of two types of CAB: CAB381-0.1 and CAB551-0.01 (Eastman). Each of these binder components has different percentages of butyryl, acetyl and hydroxyl groups. They were blended with two types of PEG (Sigma Aldrich) with different average molecular weights. The composition of the binder system and the characteristics of the components are shown in Table 2.

Table 2 Binder composition

Component	Acetyl*	Butyryl*	Hydroxyl*	%vol
CAB381-0.1	13	37	1,5	30
CAB551-0.01	2	53	1,5	10
PEG 20k	-	-	-	58
PEG 10k	-	-	-	2

** Percentage of side groups in chain*

4.2 Preparation of the samples

A Rheomix 600 Haake rheometer coupled with a Haake Rheocord 252p module was used for the mixing all feedstock components. Different feedstock compositions, ranging from 57.5 vol.% (minimum solid loading tested) to 72.5 vol.% (maximum solid loading tested), were investigated in 2.5 vol.% increments. A temperature of 150º C was used for all the batches, and the mixing chamber was filled with feedstock to 72% of the total volume (the chamber volume is 69 cm^3). A rotor speed of 50 rpm was employed to mix the feedstock and the binder for 60 min to ensure complete homogenisation. Thin samples of around the same size and weight were prepared by warm pressing of the as-prepared feedstocks to perform thermogravimetric and calorimetric analysis.

4.3 Termogravimetric and calorimetric analyses (STA and DSC)

A Perkin Elmer STA 6000 device was used to thermodynamically evaluate the decomposition of the binder and the feedstock. This device allows the simultaneous acquisition of the thermogravimetric TGA curves and the DTA/DSC curves. The examined temperature range was from 50ºC to 650ºC. Calcium oxalate was employed for thermogravimetric calibration, whereas elemental indium (99.999% pure) was used for heat and temperature calibration. An inert nitrogen atmosphere was employed with a flow rate of 40 ml/min. Feedstock pellets of approximately the same morphology and weight were used for the analysis. The net weight of the binder in the feedstock was constant for all experiments, with a minimum of 5 mg for all cases. An open aluminium oxide crucible was used to perform the experiments. For a thorough evaluation of the decomposition kinetics, four heating rates were evaluated:

10ºC/min, 15ºC/min, 20ºC/min and 25ºC/min. The buoyancy effect in TGA has been taken into account by carrying out empty crucible runs and subtracting the resulting weight differences from the subsequent sample mass loss data [21].

A TA Instruments Q200 differential scanning calorimeter (DSC) equipped with a refrigerated cooling system was also employed to contrast STA results. The base line was calibrated in scanning the temperature domain with an empty pan. The temperature and the enthalpy were calibrated using indium as a standard. All the experiments were carried out with an aluminum pan with 8-12 mg of sample. These experiments allow data acquisition at lower temperatures ranges with a better resolution than with combined STA technique. Typical heating-cooling-heating cycles were programmed to delete the thermal history of the feedstocks and to evaluate the melting and crystallization temperatures. The experimental temperature range varies from -20 to 190ºC to avoid any possible degradation of the components and to allow complete crystallization. Heating rates of 10 ºC/min were selected.

4.4 Polarised light microscopy

Investigation of PEG crystallisation in different systems was performed by an Olympus GX71 light microscope with light polarising filters. A thin layer on around 0.5 mm was created by facing two microscope slides and pressing the sample in its melting state. Samples were melted at 160º C during 30 minutes. Then they were air quenched at same cooling rates for comparison purposes.

5 Results and discussion

5.1 DSC investigations

Characteristic melting and crystallization PEG peaks as well as CAB transition temperatures were investigated by DSC measurements. This study was done for the single binder components, the binder and the different feedstocks. Changes in the peaks features in terms of temperature displacements and specifics enthalpies increment may reveal the occurrence of interactions between binder components and between binder components and powder particles. These interactions may affect the decomposition behaviour of the feedstocks. Salehi et al. [7] demonstrated that the kneading effect and the presence of powder particles in PS promote the formation of weak links between polymer chains. This was related with a lowering of the degradation activation energy which enables the weak links to act as initiation points for PS degradation.

In Figure 2 the DSC curves of the binder system and the binder components are plotted. Table 3 collects characteristic events during the heating and the cooling along the DSC curves. The value for the second heating and cooling cycles are presented. During the first heating cycle a melting peak was observed for CAB381 and CAB551 occurring at 147.7 ºC and 125.5ºC respectively. No peak appears during subsequent cooling and heating cycles, therefore crystallization did not take place at the cycle conditions as it occurred with the PEG.

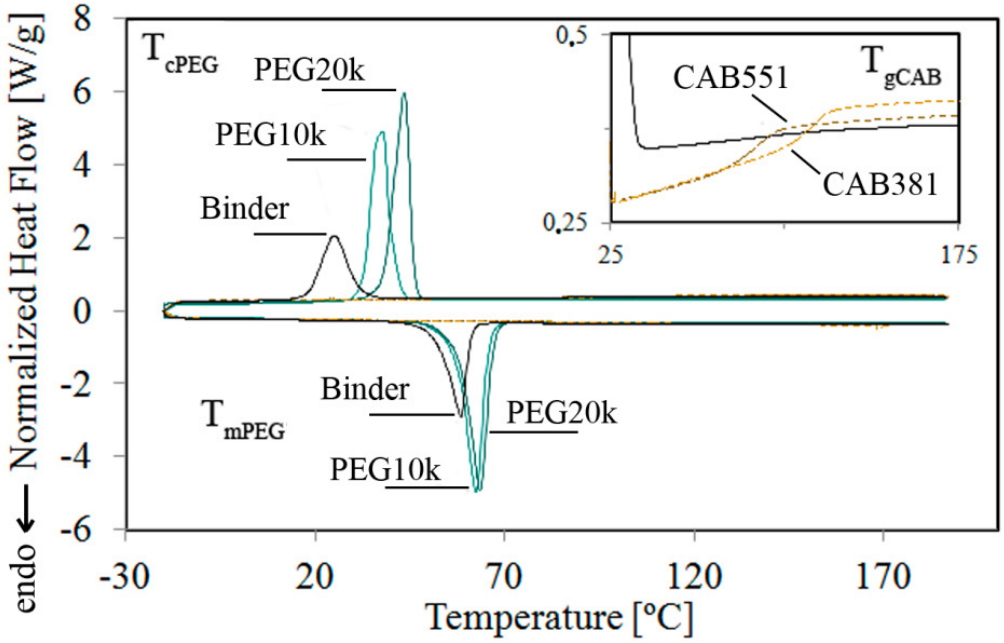

Figure 2 Normalized heat flow vs. temperature DSC curves for the binder system and the single binder components

Table 3 Characteristic events during the heating and cooling processes of the single binder components and the binder system. T_{mPEG}: PEG melting temperatures; T_{cPEG}: PEG crystallization temperatures; T_{gCAB}: glass transition of CAB; ΔH_{mPEG}: specific enthalpy of melting relative to the PEG mass; ΔH_{cPEG}: specific enthalpy of crystallization relative to the PEG mass

	PEG 10K	PEG 20K	CAB 381	CAB 551	BINDER
T_{mPEG} [°C]	62.5	63.4	-	-	58.5
ΔH_{mPEG} [J/g_{PEG}]	175.6	181.7	-	-	240.6
T_{cPEG} [°C]	37.7	43.4	-	-	25.0
ΔH_{cPEG} [J/g_{PEG}]	172.1	177.5	-	-	218.4
T_{gCAB} [°C]	-	-	104.1	89.3	No detected

Comparing different binder components and binder system, differences in the melting and crystallising of PEG10K and PEG20K are comprehensible due to the differences in their molecular weights. Differences in the glass transitions of the CAB are also predictable due to differences in the side groups' composition. The PEG20k and PEG10k melting points are very similar in contrast with the differences observed in their crystallization peaks. The melting point is less sensitive to variations of the molecular weight but this feature or others affect on the crystallization kinetics of the PEGs. Actually, differences in the crystallization behaviour were observed by controlled temperature polarized light microscopy experiments during cooling. The PEG20k began to crystallise at higher temperatures and a higher density of nucleation points was observed. Contrary, the PEG10k began to crystallise at lower temperatures and less nucleating points were observed. These results are consistent with the DSC measurements. As result big spherulites are observed for PEG10k compared with those for PEG20k as shown in the POM images presented in Figure 3.

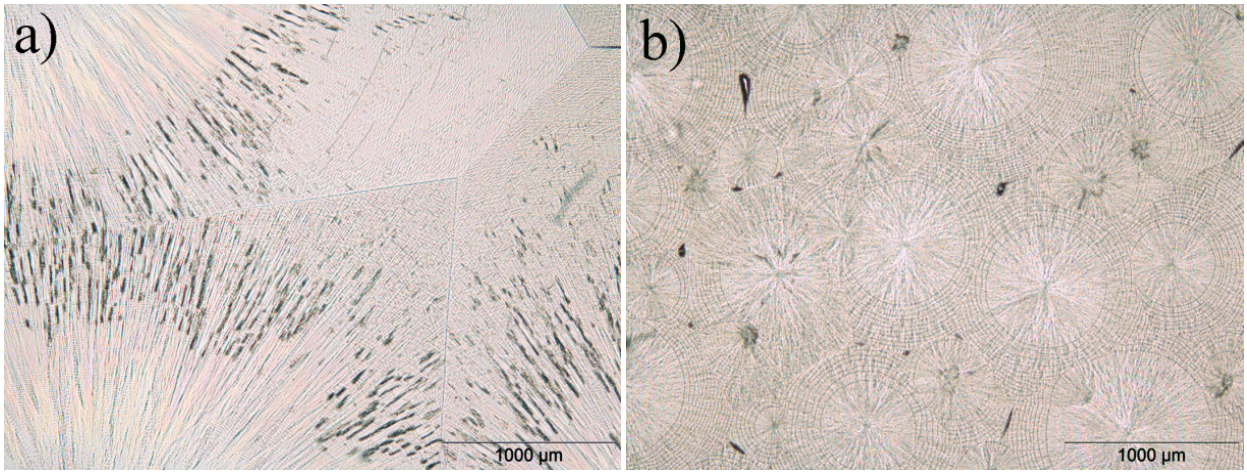

Figure 3 POM images of PEG spherulites for a) PEG10k and b) PEG20k

The melting and crystallisation peaks associated to the PEG components in the binder system fell drastically to temperatures far below those of the single components, however, the enthalpy related to PEG mass increased. These facts can be explained by a certain miscibility of CAB and PEG polymer chains, which is supported by two observations: a) Both CAB381 and CAB551 presented a glass transition which was not detected in the binder system; b) The increase of melting enthalpy related to PEG mass suggests that CAB takes part in the formation of PEG crystals. It would be explained by a widening of glass transition temperature range for the CABs and a displacement of this glass transition to lower temperatures. This would be agreed with and strengthen the assumption of the interactions between the CABs and PEGs binder components. In addition to DSC measurements, controlled temperature polarized light microscopy experiments during cooling were carried out. Onset of crystallisation of PEG spherulites in the binder system occurred at lower temperatures than those for single PEGs which is coherent with DSC results.

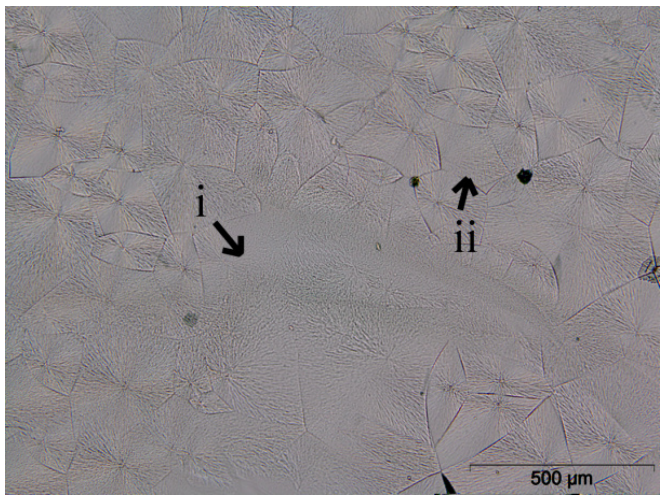

Figure 4 POM image of the binder system: i) zone with blurred PEG spherulites most likely as consequence of high concentration of CAB and certain interactions between both substances, ii) More common PEG spherulite typology most likely with less or no content of CAB.

However a higher density of nucleation points were observed compared with single PEGs. This also emphasises interactions between components; the CABs molecules most likely act as a nucleation agent but also retard the crystallization during cooling. A polarised optic microscope (POM) image of the binder system is shown in Figure 4. A decrease of the spherulites size in comparison with Figure 3a-b, which represents the single PEGs, could be observed. This image also shows a zone that presents a variation in the spherulite morphology. The spherulites borders are blurred most likely as consequence of high concentration of CAB and certain interactions between both substances.

Table 4 shows the influence of the solid loading and particle size on the melting and crystallization peaks associated with the PEGs. One remarkable finding is the general observation of these peaks at temperatures between those for the PEGs and the binder system. A reasonable explanation of this fact could be given considering interactions between the binder components and the metallic powders. Most probably PEG chains interact with the powder which is evidenced by the feedstocks PEGs' peak displacement to higher temperatures than the PEGs' peak corresponding to the binder system. Invar 36 particle surfaces are covered by a natural occurring oxide layer. Namely, hydroxyl groups are well reported to be present on metal oxide surfaces [22]. Several works studied the interactions between PEG and silica or alumina powders by infrared spectroscopy [23, 24]. They state that hydrogen bonds are formed between the PEG etheric oxygen group and the metal surface hydroxyl group. PEGs' chains, if thermally or mechanically driven, may possibly have a higher interaction with oxide surface. In the same way, CABs interactions with metallic powders are not discarded but they could not be proven, neither experimentally nor by literature. Further studies should be carried out to ascertain the nature of possible bondings.

Table 4 Characteristic events during the heating and cooling processes of the different feedstocks. T_{mPEG}: PEG melting temperature; T_{cPEG}: PEG crystallization temperature; ΔH_{mPEG}: specific enthalpy of fusion relative to the PEG mass; ΔH_{cPEG}: specific enthalpy of crystallization relative to the PEG mass

	INV1				INV2			
Φ [vol.%]	**T_{mPEG} [ºC]**	**ΔH_{mPEG} [J/g_{PEG}]**	**T_{cPEG} [ºC]**	**ΔH_{cPEG} [J/g_{PEG}]**	**T_{mPEG} [ºC]**	**ΔH_{mPEG} [J/g_{PEG}]**	**T_{cPEG} [ºC]**	**ΔH_{cPEG} [J/g_{PEG}]**
57.5	-	-	-	-	60.9	165.8	35.5	159.2
60	59.1	148.9	38.4	143.8	60.6	153.0	35.9	151.3
62.5	59.6	146.2	39.6	142.5	59.9	155.3	33.2	147.0
65	59.0	150.1	39.0	145.3	56.8	154.0	31.0	147.0
67.5	58.7	150.7	38.3	149.8	-	-	-	-
70	57.5	128.9	35.3	128.3	-	-	-	-

The melting and crystallization temperatures are not very influenced by the solid loading up to certain points that depend on the particle size. In INV1 feedstock a pronounced melting and crystallization temperature fall occurs at 70 vol.% solid loading whereas the similar behaviour is observed for INV2 at 65 vol.% solid loadings. These compositions were associated with critical powder volume content (CPVC) situations in previous studies. The enthalpy values also show similar behaviours but the drop on the enthalpy values occurred at 60 vol.% in the case of INV2. As long as there is enough inter-particle gap to allow the formation of PEG's crystalline regions, the phase transitions will not be critically altered. In such cases the effect

of high free volume for crystallization prevails over the effect of the particle surface increment and reduction of inter particle distances. Since the particles packing is increased, the confinement of the organics is increased reducing the effective volumes that will allow a free growth of crystalline lamellas. Comparing both powder-types, there is a significant crystallization temperature reduction in case of INV2 feedstock while these variations are less obvious but also occurs with the melting points.

5.2 Thermal stability studies

The Figure 7a shows typical simultaneous thermal analysis curves for Invar 36 feedstocks; in this case curves for an INV2 feedstock with 60 vol.% and a heating rate of 10 ºC/min are plotted. The normalized DSC curve can be plotted simultaneously with the TGA curve and its derivative, the DTG curve (or the weight loss ratio). Figure 7b focuses on a comparative of the TGA curves between INV2 feedstocks with different solid fractions. Similar tendencies are observed for INV1 feedstocks.

Table 5 collects some decomposition parameters at 10 ºC/min of the different feedstock compositions and Table 6 does for the binder and the binder's components. The initial decomposition temperature (IDT) represents the temperature at which the 2 mass% of the total binder mass was eliminated. The α_{max} and the T_{max} represent respectively the conversion and temperature at the maximum weight loss ratio point. The T^0_{max} represents the extrapolated temperature at the maximum weight loss ratio considering a 0 ºC/min heating rate. The Res refers to the organic residual mass at 600 ºC pondered to the total binder weight and the IPDT to the integral procedure decomposition temperature.

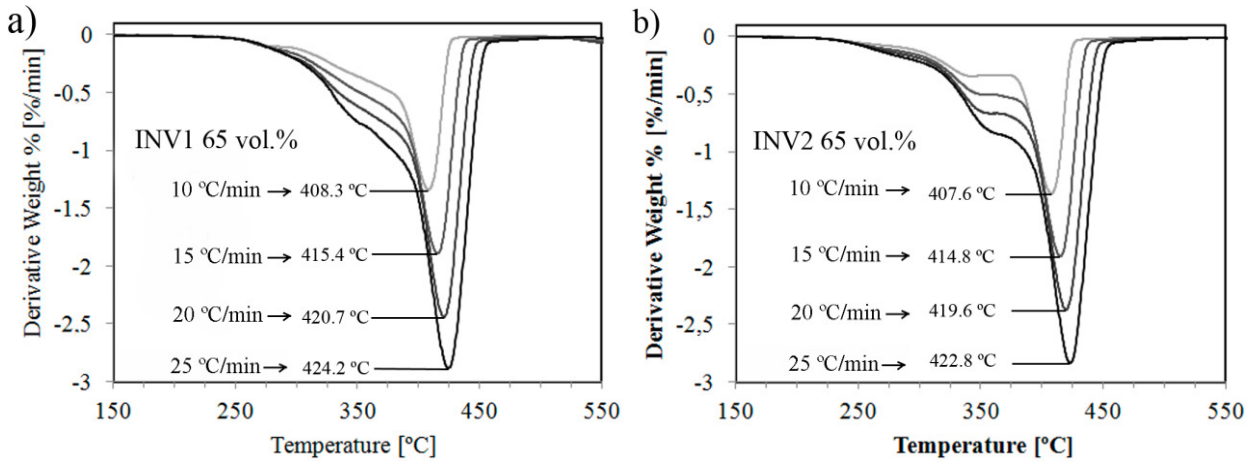

Figure 5 DTG curves at different heating rates for a) INV1 65 vol.% feedstock and b) INV2 65 vol.% feedstock

The feedstock organic components decomposition in nitrogen atmosphere occurs in three consecutive overlapped steps as it is deduced from feedstocks DTG curves (Figure 7a and Figure 5a-b). The highest decomposition rates occur at high temperatures and correspond to the volatilizations of compounds resulting from the degradation of PEG which is the principal component of the binder. The two previous decomposition steps could be linked with the

decomposition of CAB. The feedstocks' decomposition behavior contrasts with a two step binder decomposition process as could be seen in the DTG curves for the single components and the binder system in Figure 6. The first step occurring in the feedstocks' DTG curves is not registered in the decomposition of the binder system (Figure 6). The idea that the first decomposition step occurring at low temperatures is associated with an interactive or catalytic effect of the powders over the polymeric compounds is not discarded.

The PEG seems to have a stabilizing effect in the decomposition of the CAB as deduced from the displaced DTG peak associated with the CAB in the binder system to higher temperatures. This effect could be revealing some interactions between the CAB and the PEG which is in consonance with DSC results. Furthermore CABs and PEGs decomposition peaks tend to overlap in the feedstocks DTG curves. Although certain compatibility is assumed between CABs and PEGs, their miscibility is not complete as it was contrasted with well differentiated CAB rich and PEG rich regions in the binder system (Figure 4). The kneading effect that the powder particles exerts over the binder components may cause a smaller and closer PEG rich and CAB rich regions or increase the miscibility between the molecules in case there is any. The CAB and PEG polymer chains may be more effectively entangled and the formation of weak links could be promoted. This would explain the displacement and overlapping of these substances decomposition peaks, presumably because of a hindering of the elimination of the CABs' decomposition components entrapped in these smaller domains.

Table 5 Comparative of different degradation parameter for different INV1 and INV2 feedstock at different solid loadings

	INV1						INV2					
Φ [vol.%]	IDT [ºC]	α_{max} [%]	T_{max} [ºC]	T^0_{max} [ºC]	Res [%]	IPDT [ºC]	IDT [ºC]	α_{max} [%]	T_{max} [ºC]	T^0_{max} [ºC]	Res [%]	IPDT [ºC]
57.5	-	-	-	-	-	-	261.2	72.5	407.5	276.7	5.4	8714
60	265.7	73.0	408.1	278.1	3.0	9260	259.9	75.5	407.2	285.2	5.7	9839
62.5	261.4	74.2	408.3	279.6	3.4	10388	257.8	75.8	407.1	290.2	6.4	10955
65	259.3	75.4	408.3	280.3	3.7	11513	256.3	75.6	407.8	285.8	6.8	12263
67.5	257.9	74.5	407.8	281.3	3.5	12655	248.1	75.7	407.7	284.1	6.3	13527
70	243.4	75.6	407.7	284.3	4.7	14776	241.1	75.5	407.1	282.3	7.0	14774
72.5	246.0	75.3	407.2	273.2	4.6	16689	-	-	-	-	-	-

The IDT of the binder system coincides with the minimum IDT of its components that corresponds to CAB551. However, there is a considerable reduction of the IDT values registered in the feedstocks and there is a clear dependence on the powder type and the solid loading. The lowest IDT values correspond to the INV2 feedstocks with high solid loadings. There is a direct relation of the total powder surface area with the IDT value. The main idea is that the mixing process favours the creation of weak links between polymers or between polymers and particles. These weak links are preferential points for the polymer chain scission during thermal degradation. It is well established that PEG thermal degradation proceeds by the random chain scission of C-O bonds [25]. Thermally promoted hydrogen abstraction reactions of hydroxyl radicals with C-O is one possible mechanism of chain scission. This reaction is kinetically more favorable than the own homolytic cleavage of C-O [26]. As the

solid fraction increases or the powder particle size is reduced, there is more available surface area for the creation of hydrogen bond or weak links favouring a subsequent catalytic effect at higher temperatures.

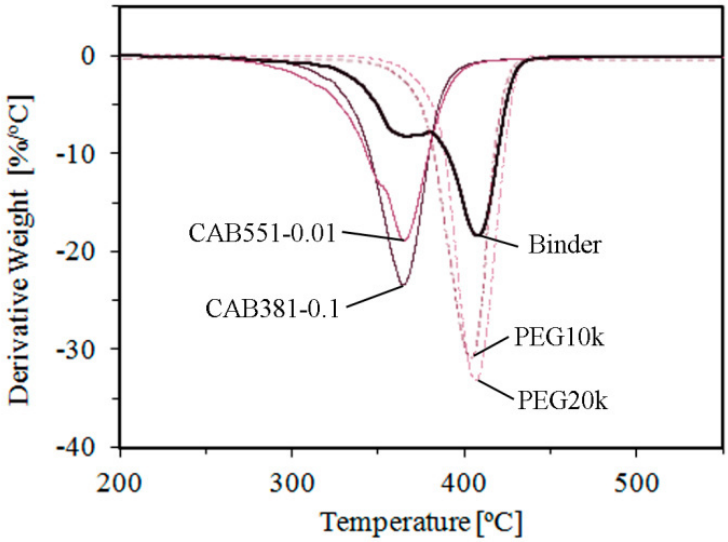

Figure 6 Comparative of DTG curves of the binder system and the binder components

The CABs do not completely volatilize at 600 ºC in nitrogen atmosphere and leave a solid organic residue. The proportion of this organic residue with respect to the total binder is reduced in INV1 feedstocks in comparison with the INV2 feedstocks and the sole binder, both having similar values. As the solid loading increases, the residue increases. Although the powder surface may be having a catalytic effect on the polymers decomposition, it could be also a site for the formation of a thermally stable char layer. As the powder surface increases there are more sites for a char layer formation. There is also the effect of the powder particle packing increment with the solid loading which complicates the evacuation of volatiles. In Figure 7b a reduction of the weight loss rate and the displacement of the TGA curve to higher temperatures as the solid loadings increases is observed. This behavior is in consonance with the possible hindering effect of the char layer formation around particles and the reduction of the evacuation pore-net channels sizes.

The variation of the IPDT values with the solid loading for INV1 and INV2 is shown in Figure 8. The IPDT increases with solid loading which is predictable by the variation of the S_2 area because of the increment of the metallic part. The typical linear tendency is observed, but the slope and the IPDT values for the same solid loading vary with the heating rates and particle type. A change in the slope takes place at 62.5 vol.% and 67.5 vol.% for the INV2 and INV1 respectively. This change in the slope coincides with the values of optimal solid loading around these compositions that were determined using several different methodologies in previous investigations with Invar 36 feedstocks. These results also support previous works that proposed this methodology as an alternative or a complement to conventional methodologies for assessing optimal solid loadings in ceramic powders [8].

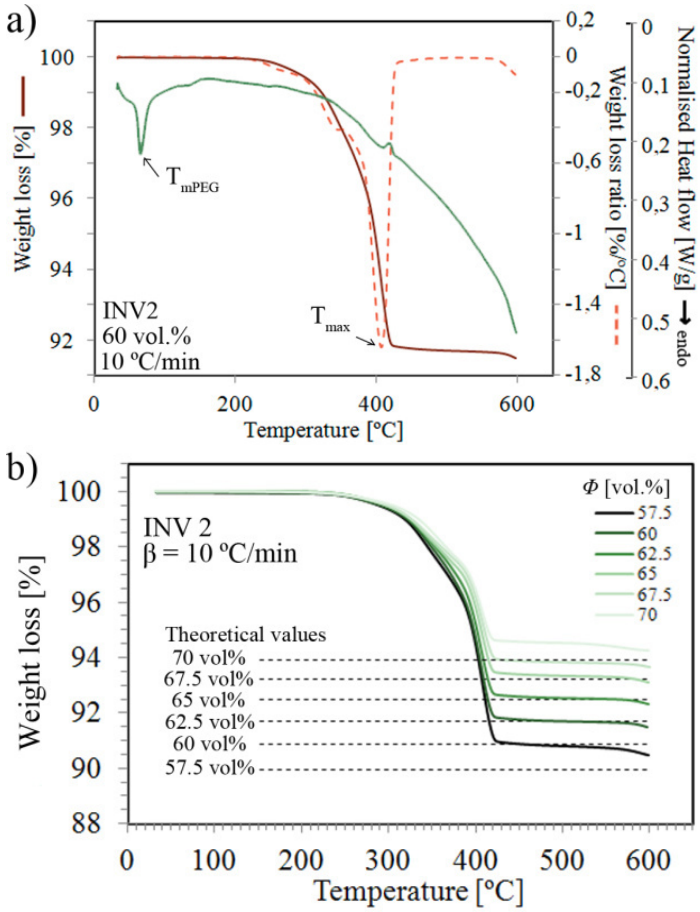

Figure 7 a) Typical STA curves (DSC, TGA and DTG) of the Invar 36 feedstocks exemplified by INV2 at 60 vol.% and 10 ºC/min b) Comparative of the TGA at different solid loadings of INV2 feedstocks as 10 ºC/min

Table 6 Comparative of different degradation parameter for binder system and binder components. The maximum degradation rate temperature is 404.5 ºC for the binder, but the peak corresponding to CABs' degradation is also presented.

	PEG 10K	PEG 20K	CAB 381	CAB 551	BINDER
IDT [ºC]	351.4	366.3	301.4	285.7	283.9
IPDT [ºC]	412.5	413.3	442.9	447.1	432.2
Res [%]	0.1	0.1	7.9	8.6	6.4
T_{max} [ºC]	401.2	406.8	364.6	363.6	366.7 404.5

This change in the slope may be explained assuming a char layer formation around the powder particles. The optimal solid loading is very near to the CPVC with the difference that in the first situation there is still a thin coating of polymers embedding the particles. This polymer coating enlarges as the solid loading is reduced. For low solid fractions, despite a char layer formation is most likely taking place, there could be still enough separation between particles to allow an effective removing of all the decomposition volatiles out of the green body. Nevertheless at optimal solid loading compositions the char layers of neighboring particles would collide hindering the volatiles evacuation causing the slope change. This slope change is telling that for subsequent solid loading increments the variation of the S_2 areas is

approximately constant while the values of the S_1 areas varies more abruptly (due to a reduction of the weight loss ratio and a displacement of the TGA curves to higher temperatures).

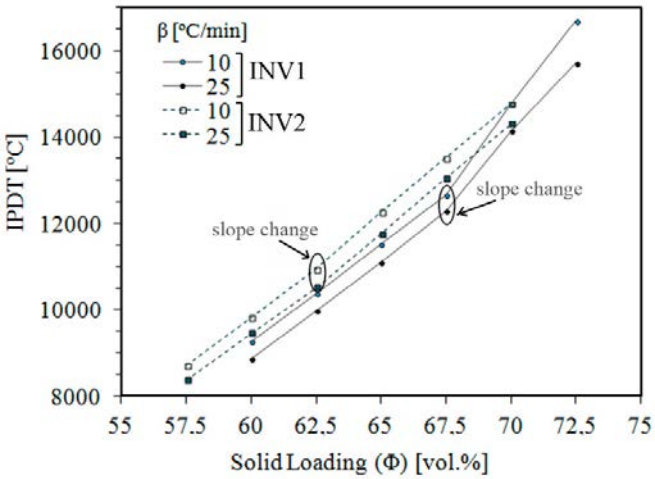

Figure 8 IPDT values evolution at different solid loadings, heating rates and for INV1 and INV2 feedstocks

5.3 Degradation kinetics

The KAS and FWO methods allow determining the activation energy at different conversion values. Figure 9 shows the dependence on the conversion of the apparent activation energy values, as assessed by the KAS method of the main binder components and the binder system while Figure 10 does it for the INV1 and INV2 feedstocks at different solid volumetric fractions. Similarities are found in the curves using the FWO method thus this graph was obviated. The KAS method uses a more accurate approximation of the integral temperature than FWO and it is considered to produce more reliable results of the activation energy [21].

The activation energies for the PEG20k maintain approximately constant with α variations, which likely indicates a single rate limiting decomposition step over the entire reaction duration. The averaged value of E_a using FWO method was 148 kJ/mol and in case of KAS method 144 kJ/mol. They properly suit with the typical PEGs activation energies interval (120-200 kJ/mol) reported in literature [25]. In the case of CAB there is a slight increment of the activation energy with α from 57 kJ/mol for α=0.2 to 97 kJ/mol for α=0.8 as determined with FWO and from 50 kJ/mol for α=0.2 to 91 kJ/mol for α=0.8 as determined with KAS. Increasing dependence of the activation energy on the conversion is not unusual in polymer degradation [27]. This behaviour is considered to be an indicator of a complex reaction [28]. Vyazovkin and Lesnikovich [29, 30] noted that in non-isothermal experiments, patterns in the shape of the curve dependence of the apparent value of E_a on α could provide insight into the type of complex process taking place. An increasing dependence of E_a on α characterises concurrent, competitive reactions, whereas convexity indicates a change in the rate-determining step. In the case of the binder system, the activation energies are higher than those for the single PEG and CAB.

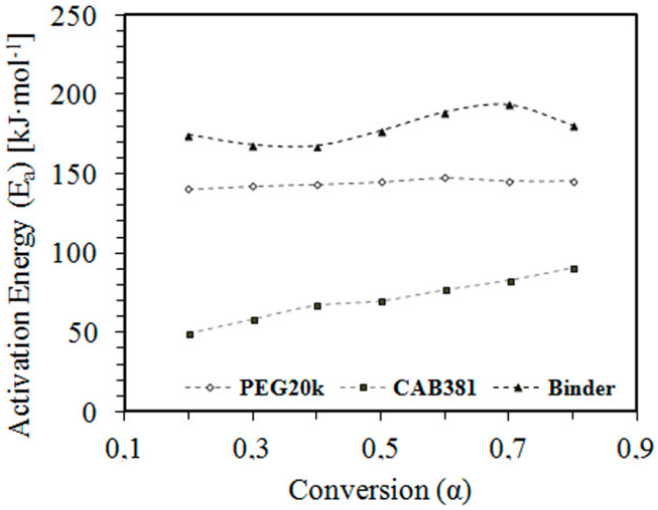

Figure 9 Evolution of the activation energies with the conversion calculated with the KAS method for the main binder components and for the own binder system

Several stages are observed. From conversion 0.2 to 0.4 a stable value of the Ea, with an average value of 172 kJ/mol calculated with FWO and170 kJ/mol in case of KAS, is observed. Then E_a increase up to 195 kJ/mol calculated with FWO and 194 kJ/mol in case of KAS for α=0.7. These results could agree with the suggested interactions between PEG and CAB observed by DSC. Grafting or cross-linking reactions between CAB and PEG functional groups presumably occurs creating more thermally stable reaction nucleus and thus increasing the activation energy. It is not the scope of this work to study the nature of those reactions which would be also very limited by the employed techniques.

Through α, the feedstocks seem to have an important influence on E_a that is independent of solid loading. Two stages are mainly observed. For the majority of the curve, E_a increases abruptly as the values of α increase up to a value at which E_a either stabilises or begins to decrease; this behaviour gives the curve a certain convexity. At low conversion rates the activation energy is lower than the binder's (taking α=0.3, Ea is less than 170 kJ/mol for almost all the feedstocks employing KAS method) which is suggesting that the degradation at this point is favoured by a catalytic effect of the powders. The concurrent reactions presumed from the E_a increment could be molecular degradation reactions of both CAB and PEG and other reactions that hinder the volatiles evacuation as well as the formation of a thermally stable layer around the particles (by recombination of degraded polymers forming crosslinks or formation of a char layer). The nature of this thermally stable layer and the reactions involving it are uncertain, but its formation is supported by the observation of an organic residue after TGA experiments. This residue is also observed in the thermal degradation of the studied CABs in nitrogen atmosphere. The subsequent plateau at high conversion values may indicate the end of a reaction or the creation of open pathways that facilitate the removal of volatiles as the binder decomposes. That last would suit with a slight progressive decrease of the activation energy at high temperatures. In many of the feedstocks, the value of the Ea in the plateau at high conversion rates is higher than 195 kJ/mol (KAS), which is higher activation energy than those for the binder. This evidences that the presence of the powder

influences negatively in the volatilisation of the break-down molecules at high conversion rates.

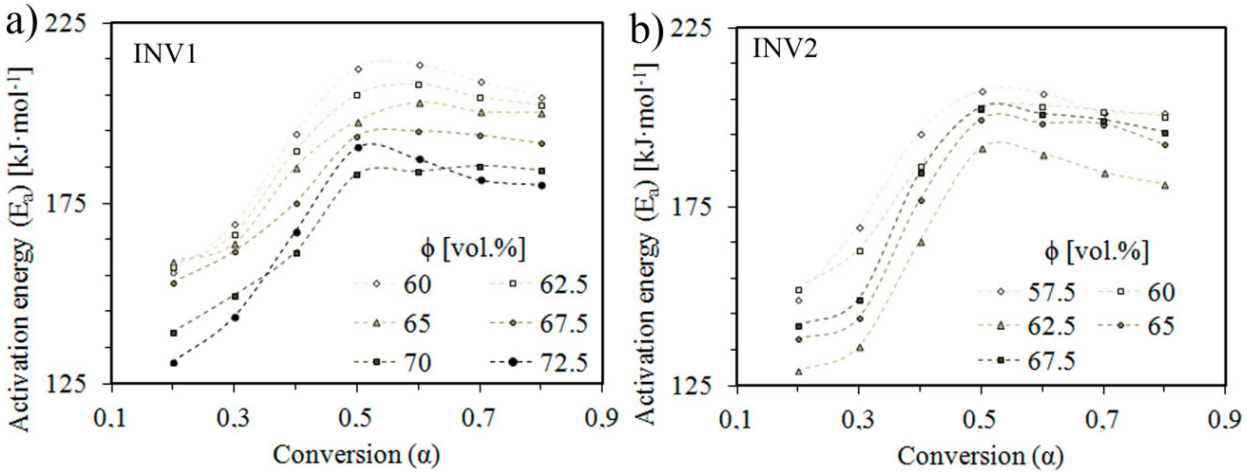

Figure 10 Evolution of the activation energies with the conversion calculated with the KAS method at different solids loading for a) INV1 feedstocks and b) INV2 feedstocks

Figure 11 represents the activation energies for a constant conversion of 0.5 and for different INV1 and INV2 feedstocks using KAS and FWO methods. In this case a minimum in the activation energy vs. the solid loading curves is observed at 62.5 vol.% and 70 vol.% for INV2 and INV1 respectively. It is worth to consider that the apparent activation energy summarises different effects involving the degradation of polymers, but at the end, as measured from TGA, E_a reflects how effective are the resulting break-down compounds volatilised. Degradation may begin at temperatures lower than the registered by TGA. However, a weight loss only would be appreciated when the decomposition species had a certain low molecular weight that allows for the volatilisation or for the mass transport trough different mediums, e.g. melted polymer, evacuating interparticle pathways, etc. In that respect, the occurrence of a minimum in the Ea vs. solid loading curve may be explained by opposing effects. First, an increment of the weak links as the solid loading increases, i. e. an increment of catalytic decomposition sites, may reduce the apparent degradations activation energy by favouring the fragmentation rate of the polymer chains. The opposite effect, an increase in the apparent activation energy, would occur as a consequence of a better particle packing as the solid loading increases, reducing the diameters of the volatiles-removal channels. This effect may have been enhanced by the formation of a thermally-stable layer of char around the particles. All of these effects combine to minimise the apparent activation energy of degradation.

Unfortunately non-isothermal methods without other supporting information have generally a no-mechanistic value, but at least in this case could serve as a first rough approach to support the general analysis in combination with other methodologies presented. The KAS and FWO methods may introduce errors because they are based on an approximation of the temperature integral [15, 18], but in any case it seems that the results are reaffirming 62.5 vol.% or 67.5

vol.% as the optimum solid loading value with respect to both rheological concerns and thermal stability studies of the feedstocks.

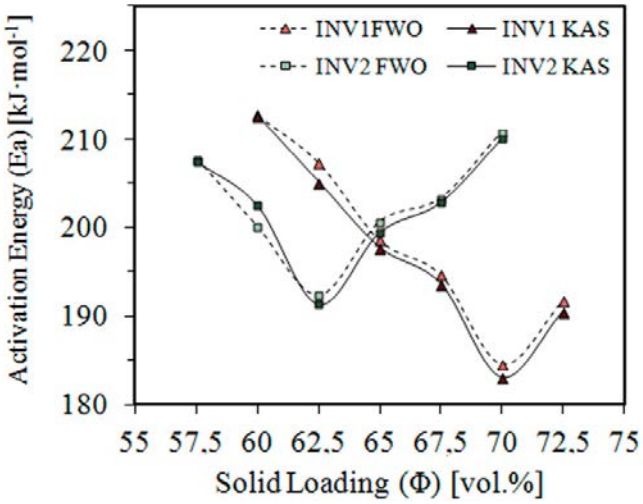

Figure 11 Activation energies evolution with solid loadings of INV1 and INV2 feedstocks calculated by FWO and KAS methods

The direct relationship between the apparent activation energies, with respect to both rheological and thermal degradation concerns, is not clear. There are analogies in the possible explanations of the mechanisms that affect these factors, such as the change of the particle packing and the effective interaction surface between the organic compounds and the particles. Nevertheless, studying the thermal degradation by calculating activation energies for different solid loading conditions emerges as an alternative to the traditional rheological studies used to assess optimal solid loading in PIM feedstocks.

6. Conclusions

Thermal analyses via DSC and TG experiments in a nitrogen atmosphere were performed for different solid loading Invar36 feedstocks composed of CAB and PEG. Two different powders sizes were selected. Binder components in presence of powder particles apparently thermally degrade by concurrent reactions in three steps between 250 ºC and 450 ºC. A possible interaction between the Invar 36 particles and the binder components was revealed by DSC analysis. Thermal stability studies using the IPDT factor reveal a linear slope in the feedstock thermal stability as the solid loading increases. A change in the linear slope occurs at approximately 62.5 vol.% solid loading for fine powder whereas this change occurs at 67.5 vol.% for the coarse powders. This change coincides with the optimal solid loading calculated in previous studies using rheological methods. The kinetics of the thermal degradation of the binder components in terms of calculated apparent activations energies were also studied using the FWO and KAS integral methods. Variations in the apparent activation energies calculated using these methods suggest the occurrence of complex, concurrent and competitive reactions. A representation of the apparent activation energy at a constant conversion for different solid loadings shows that the activation energy is minimised at 62.5

vol.% and 70 vol% for fine and coarse powders respectively. This value coincides with a minimum in the activation energy calculated using rheological methods in previous studies. The possible effects that lead on this minimum were discussed. It seems that the powder has a catalytic effect upon the binder decomposition but at the same time particles may be hindering the evacuation of volatiles. All of these results emphasise the potential for using thermocalorimetric analysis instead of, or as a complement to, conventional rheological studies to determine the optimal solid loading of MIM feedstocks.

ACKNOWLEDGMENTS

The authors a wish to thank GUZMÁN GLOBAL S.L. and MIMTECH ALFA for their collaboration on the ECOPIM project (ref. IPT-2011-0931-20000) that was funded by the Spanish Ministry of the Economy and Competitiveness. Furthermore, the authors would like to acknowledge the strong support from the ESTRUMAT projects (ref. S2009/MAT-1585), which were funded by the CAM-Consejería Educación Dir. Gral. Universidades e Investigación, and from the COMETAS project (ref. MAT2009/14448-C02-02), which was funded by the Spanish Ministry of the Economy and Competitiveness. J.P.F.-B. acknowledges support from "Marie Curie" Amarout Europe Program.

1. Petzoldt, F., *Current Status and Future Perspectives of the MIM Technology.* Cfi-Ceramic Forum International, 2012. **89**(10): p. E11-E15.
2. German, R., *Metal powder injection molding (MIM): key trends and markets*, in *Handbook of Metal Injection Molding*, D. Heaney, Editor. 2012, Woodhead Publishing Limited.
3. Yun, J.W., et al., *Effect of decomposition kinetics and failure criteria on binder-removal cycles from three-dimensional porous green bodies.* Journal of the American Ceramic Society, 2006. **89**(1): p. 176-183.
4. Liau, L.C.K. and C.C. Chiu, *Optimal heating strategies of polymer binder burnout process using dynamic optimization scheme.* Industrial & Engineering Chemistry Research, 2005. **44**(13): p. 4586-4593.
5. Aggarwal, G., et al., *Master decomposition curve for binders used in powder injection molding.* Metallurgical and Materials Transactions a-Physical Metallurgy and Materials Science, 2007. **38A**(3): p. 606-614.
6. Belgacem, M., B. Thierry, and G. Jean-Claude, *Investigations on thermal debinding process for fine 316L stainless steel feedstocks and identification of kinetic parameters from coupling experiments and finite element simulations.* Powder Technology, 2013. **235**: p. 192-202.
7. Salehi, M., et al., *Kinetic analysis of the polymer burnout in ceramic thermoplastic processing of the YSZ thin electrolyte structures using model free method.* Applied Energy, 2012. **95**: p. 147-155.
8. Hidalgo, J., A. Jiménez-Morales, and J.M. Torralba, *Thermal stability and degradation kinetics of feedstocks for powder injection moulding – A new way to determine optimal solid loading?* Polymer Degradation and Stability, 2013. **98**(6): p. 1188-1195.
9. Jin, F.-L. and S.-J. Park, *Thermal properties of epoxy resin/filler hybrid composites.* Polymer Degradation and Stability, 2012. **97**(11): p. 2148-2153.

10. Doyle, C.D., *Estimating thermal stability of experimental polymers by empirical thermogravimetric analysis.* Analytical Chemistry, 1961. **33**(1): p. 77-&.
11. Vyazovkin, S., *Model-free kinetics - Staying free of multiplying entities without necessity.* Journal of Thermal Analysis and Calorimetry, 2006. **83**(1): p. 45-51.
12. Holland, B.J. and J.N. Hay, *The value and limitations of non-isothermal kinetics in the study of polymer degradation.* Thermochimica Acta, 2002. **388**(1-2): p. 253-273.
13. Flynn, J.H. and L.A. Wall, *A quick direct method for determination of activation energy from thermogravimetric data.* Journal of Polymer Science Part B-Polymer Letters, 1966. **4**(5PB): p. 323-&.
14. Ozawa, T., *A new method of analyzing thermogravimetric data.* Bulletin of the Chemical Society of Japan, 1965. **38**(11): p. 1881-&.
15. Doyle, C.D., *Series Approximations to Equation of Thermogravimetric Data.* Nature, 1965. **207**(4994): p. 290-&.
16. Kissinger, H.E., *Reaction Kinetics in Differentical Thermal Analysis.* Analytical Chemistry, 1957. **29**(11): p. 1702-1706.
17. Akahira, T.S., T, *Joint convention of four electrical institutes*. 1971, Chiba Institute of Technology: Chiba. p. 22-31.
18. Coats, A.W. and J.P. Redfern, *Kinetic Parameters from Thermogravimetric Data.* Nature, 1964. **201**(491): p. 68-&.
19. Bernardo, E., et al., *Feedstock Development for Powder Injection Moulding of Zirconium Silicate.* Powder Injection Moulding International, 2012. **6**(1): p. 4.
20. Minseok, S., et al., *Water-soluble binder with high flexural modulus for powder injection molding.* Journal of Materials Science, 2005. **40**(5): p. 1105-9.
21. Vyazovkin, S., et al., *ICTAC Kinetics Committee recommendations for performing kinetic computations on thermal analysis data.* Thermochimica Acta, 2011. **520**(1-2): p. 1-19.
22. Tanaka, Y., et al., *Active hydroxyl groups on surface oxide film of titanium, 316L stainless steel, and cobalt-chromium-molybdenum alloy and its effect on the immobilization of poly(ethylene glycol).* Materials Transactions, 2008. **49**(4): p. 805-811.
23. Derosa, R.L. and J.A. Trapasso, *Poly(ethylene glycol) interactions with alumina and silica powders determined via DRIFT.* Journal of Materials Science, 2002. **37**(6): p. 1079-1082.
24. Rubio, J. and J.A. Kitchener, *Mechanism od adsorption of poly(ethylene oxide) flocculant on silica.* Journal of Colloid and Interface Science, 1976. **57**(1): p. 132-142.
25. de Sainte Claire, P., *Degradation of PEO in the Solid State: A Theoretical Kinetic Model.* Macromolecules, 2009. **42**(10): p. 3469-3482.
26. Vaghjiani, G.L. and A.R. Ravishankara, *Kinetics and mechanism of hydroxyl radical reaction with methyl hydroperoxide.* Journal of Physical Chemistry, 1989. **93**(5): p. 12.
27. Vyazovkin, S., N. Sbirrazzuoli, and I. Dranca, *Variation in activation energy of the glass transition for polymers of different dynamic fragility.* Macromolecular Chemistry and Physics, 2006. **207**(13): p. 1126-1130.
28. Elder, J.P., *Multiple reaction scheme modeling 3: Mutually independent nth order reactions.* Journal of Thermal Analysis, 1989. **35**(6): p. 1965-1984.
29. Vyazovkin, S.V. and A.I. Lesnikovich, *On the dependence of kinetic parameters and functions in non-isothermal kinetics.* Thermochimica Acta, 1987. **122**(2): p. 413-418.

30. Vyazovkin, S.V. and A.I. Lesnikovich, *An approach to the solution of the inverse kinetic problem in the case of complex processes.1. Methods employing a series of thermoanalytical curves.* Thermochimica Acta, 1990. **165**(2): p. 273-280.

Paper 8

P8

J. Hidalgo, A. Jiménez-Morales, T. Barriere, J.C. Gelin and J.M. Torralba

Mechanical and functional properties of an invar alloy for μ-MIM

This work has been accepted in Powder Metallurgy (2013)

Mechanical and functional properties of an invar alloy for μ-MIM

J. Hidalgo[1], A. Jiménez-Morales[1], T. Barriere[2], J.C. Gelin[2], J.M. Torralba[1,3]

1 Carlos III University of Madrid, Avd. Universidad 30, 28911 Leganés (Spain) jhidalgo@ing.uc3m.es, toni@ing.uc3m.es.
2 University of Franche-Comté, 26 rue l'Epitaphe, 25000 Besançon (France), thierry.barriere@univ-fcomte.fr
3 Institute IMDEA Materials, Eric Kandel 2, 28906 Getafe (Spain), josemanuel.torralba@imdea.org

Abstract

Micro metal injection moulding (μMIM) is a promising alternative for fabricating micro parts. Low coefficient of thermal expansion (CTE) Fe_x-Ni_{1-x} alloys are suitable to meet high dimensional stability with temperature keeping acceptable mechanical properties. However these alloys are sensible of elements contamination during the debinding and sintering stages and their dimensional stability and mechanical properties could be affected. The present work studies the effect of using combinations of debinding and sintering atmospheres in the μPIM of Invar 36 feedstocks based on cellulose acetate butyrate (CAB) binders. Micro-tensile specimens were successfully injected. Densification and microstructure at different conditions were linked with mechanical and physical properties of the parts. The processing conditions and thus the residual C, O and especially H influence severely these properties.

Keywords: Invar 36, cellulose acetate butyrate, polyethylene glycol, micro-MIM, sintering atmospheres.

1. Introduction

Powder metallurgy (PM) of Fe_x-Ni_{1-x} of low coefficient of thermal expansion (LCTE) alloys presents several processing advantages with respect casting. Energy and cost savings and a reduction of elements segregation risk could be achieved, thus increasing alloy properties [1]. Furthermore, PM can reduce tedious and time consuming machining steps that are specially complicated for Fe_x-Ni_{1-x} LCTE alloys due to their high ductility and low thermal conductivity. It is also greatly complicated to maintain Invar properties when joining by fusion welding. Such welding results in solidification cracking, porosity and reheating cracking when a matching CTE filler metal is used [2]. Metal injection moulding (MIM) design versatility may also eliminate the needs of joints by welding. To that respect MIM emerges as a cost-effective solution for near net-shape fabrication of complex geometry small pieces [3]. Examples of potential MIM application of LCTE alloys are wide in the field of high precision devices like in optoelectronic or light wave communication systems, housing or structural components [4]. Currently, there is an increasing demand of miniaturised components for micro devices like micro gears or micro actuators [5-8] in which micro metal injection moulding (μ-MIM) of low CTE alloys could be an interesting alternative.

The abnormal LCTE behaviour within metals, which normally considerably expand with heat and contract with cold, is consequence of the so-called Invar (volume INVARiance) effect. The physical mechanism explaining Invar effect still remains uncertain, but from general standpoint low expansion occurs due to two opposing effects over a specific temperature range. During heating, the alloy naturally expands while simultaneously a ferromagnetic-to-paramagnetic transformation imposes a magnetostriction that counteracts the expansion [9, 10]. The minimum CTE in the binary iron-nickel alloying system occurs in the composition $Fe_{0.65}$-$Ni_{0.35}$, the commercial Invar 36, which also has one of the lowest CTE of any alloy from room temperature to about 230ºC (the 4.5% cobalt modification has almost zero expansion over that range). Microstructure of Fe_x-Ni_{1-x} LCTE alloys commonly consists of a substitutional solid solution of nickel in iron creating an austenitic face centred cubic lattice. The austenitic γ phase, that is present at all temperatures, shows a high ferromagnetism at temperatures below the Currie temperature, and a paramagnetic behaviour above this temperature. Heterogeneities in the cast alloy and the presence of other elements like carbon introduce the possibility of formation of Ni segregation regions within the γ lattice [11-14]. Therefore low moment (LM) paramagnetic Fe-rich phases could coexist with clusters of Ni-rich high moment (HM) ferromagnetic order phase negatively affecting CTE. Furthermore a martensitic phase could be formed for quenched alloys which also degrade low expansion properties. However, elements like C and Ni act as a γ phase stabilizers diminishing the martensitic temperature (Ms). Concentrations below about 33 at.% Ni lead on structural transitions from γ to a body centred cubic phase α which does not show the Invar effect. Carbon presence could stabilize γ phase for concentrations below 33 at.% Ni.

Table 1 Mechanical properties of different Invar 36 materials.

Material	YS [MPa]	UTS [Mpa]	Strain to breakage [%]	H_v [Gpa]
Wrought Invar 36 (ASTM A658)	> 241	448-552	> 30	N/A
Wrought Invar 36[15]	275	490	40	1.30
High purity PM Invar 36 extruded[16]	271	468	70	N/A
Invar 36 (0.06 C)	310	N/A	N/A	1.5-1.6
Invar 36 ECAP 2 passes[17]	570	732	47	2.42
Invar 36 ECAP 12 passes[17]	835	912	52	2.60

Dimensional stability has to be accompanied with good mechanical properties. Table 1 shows some typical mechanical properties of Invar 36 alloys processed under different conditions. Invar 36 ordinary wrought alloy [15] and high purity powder-metallurgy-route processed alloy [18] have relatively low strength, but high ductility. Age hardening by some by addition of elements (Ti, Al, Sn, etc) is an alternative to enhance Invar 36 properties. Nonetheless the CTE, which is the property of primary importance in these alloys, increases with both aging and concentration of additions [19]. Small amounts of carbon could be beneficial to improve mechanical properties while an acceptable low CTE is maintained [14, 20]. Carbon presumably affects mechanical properties by strengthening the interstitial solid solution.

Moreover, creating ultra-fine grain structures by e.g. severe plastic deformation using equal-channel angular pressing (ECAP) has demonstrate to significantly increase mechanical properties without scarifying low CTE[17].

The present work studies the effect of debinding and sintering atmospheres in the mechanical and physical properties of Invar 36 micro parts. A binder composed of cellulose acetate butyrate (CAB) and water soluble polyethylene glycol (PEG) was used in the μMIM process. CAB thermoplastic polymers have been successfully employed for PIM proposes in several references [21, 22]. Nevertheless CAB does not degrade completely during thermal elimination step if a protective atmosphere is employed during debinding [23]. The residual carbon could be introduced in alloying system in further steps altering alloy properties. Air atmosphere is able to completely degrade CAB due to organic compounds oxidative reactions with oxygen but also oxidises metallic powders at typical debinding temperatures. Residual carbon introduced by CAB during debinding might be eliminated in presence of hydrogen, oxides or vacuum during sintering. However there is the concern of possible carbon contamination that would affect the part properties as well as interstitial hydrogen if this atmosphere is used. Taking into account all these facts, different debinding and sintering atmospheres have been used to study their effect in the sinterability, microstructure and elements contamination of Invar 36 micro parts. These results were linked with mechanical and physical properties. Micro tensile and hardness test were conducted and the coefficient of thermal expansion and Curie's temperature evaluated depending on the processing conditions.

2 Experimental processes

Gas atomized spherical INVAR 36 alloy powders were used in this study. The INVAR 36 alloy consists of 36 wt% of Ni and Fe balanced except some other elements traces. The composition of the INVAR 36 alloy is shown in Table 2 along with the particle size parameters. The powders were supplied by Sandvik Osprey Ltd. (UK). The powder has a particle size distribution with a D90 of 5.9 μm. The small size of the powders will allow a good reproducibility of the shape with smooth surfaces and a minimum part section of about 60 μm.

Table 2 Composition and particle size distribution parameters for Invar 36 powders

Composition	**Ni**	**Mn**	**Si**	**C**	**O**	**Fe**	**Particle Size Distribution**	**d_{10}**	**d_{50}**	**d_{90}**
[mass%]	36.50	0.20	0.02	0.01	0.13	Balanced	[μm]	1.9	3.4	5.9

Each powder was mixed with a binder system based on a combination of several thermoplastic polymers, employing poly (ethylene glycol) (PEG) (supplied by Sigma-Aldrich) of different molecular weights and two types of cellulose acetate butyrates (CAB) (supplied by Estman) with a variable content of acetyl, butyryl and hydroxyl groups. The binder component content and component specifications are included in Table 3.

Table 3 Binder composition

Component	Acetyl*	Butyryl*	Hydroxyl*	%vol
CAB381-0.1	13	37	1,5	30
CAB551-0.01	2	53	1,5	10
PEG 20k	-	-	-	58
PEG 4k	-	-	-	2

** Percentage of side groups in chain*

A feedstock with a powder solid loading fraction of 65 vol.% was prepared in a Haake Rheomex twin sigma rotor internal mixer. The feedstock was mixed at a temperature of 150ºC and a rotor speed of 50 rpm for one hour to ensure the homogenisation of all components. The feedstock was employed to perform a full μPIM process. Injection of tensile and bending test micro parts was carried out by a Battenfeld Microsystem 50 microinjection moulding machine. Green micro parts were subjected to a two steps debinding process. First a solvent debinding in water media at 30 ºC was carried out previous to a thermal debinding. Then, two types of atmospheres were used during thermal debinding, air or vacuum, trying to achieve different levels of residual carbon and oxides. During thermal debinding, specimens were heated up to 400 ºC with a heating rate of 2 ºC/min and this temperature was held during 30 minutes.

Brown parts were sintered at 1100 ºC and with a heating rate of 5 ºC/min in vacuum or hydrogen atmospheres. Sintering temperatures were held during 60 minutes. Therefore four types of sintered parts were obtained: debinding in vacuum – sintering in vacuum (V-V), debinding in vacuum – sintering in hydrogen (V-H), debinding in air – sintering in vacuum (A-V) and debinding in air – sintering in hydrogen (A-H). Examples of different green, brown and sintered parts are shown in Figure 1. The narrowest section of the parts corresponds to the tensile test sample with 0.7mm x 0.7 mm. However the runners of both parts have a diameter of 0.3 mm.

Sintered parts were characterised in terms of microstructure investigation with a Philips XL-30 scanning electron microscope (SEM) and a Philips X'Pert X-ray diffractometer. Sinterablity was assessed by three methodologies: relative density measurement by Archimedes immersion method, determination of porosity by image analysis and shrinkage by comparing green and sintered part dimensions. For the image analysis, light optical microscope (LOM) images of ten different regions within the polished part cross section were evaluated and an averaged value with the standard deviation presented. The specimens preparation, the brightness and contrast parameters used to discriminates features, the number of fields examined, the total surface examined and the magnification of the objective lenses were optimised to obtain the most reliable and comparable results possible. In this case the magnification was settled at x2000.

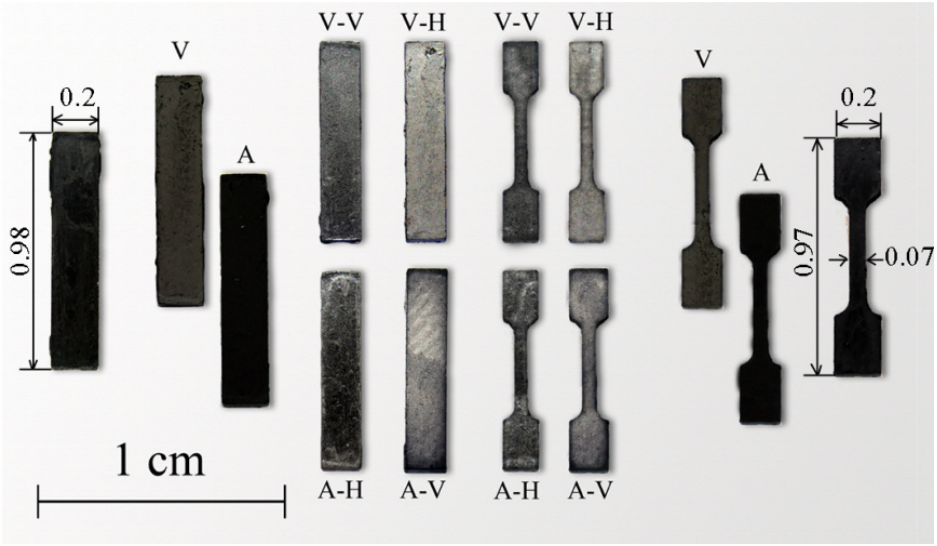

Figure 1 Green, Brown and sintered parts after different processing conditions: A: air, V:vacuum, H:hydrogen.

Residual carbon and oxygen content was measured by ThermoFischer Scientific Flash 2000 CHNS/O elementary analyser. Curie temperature that determines the end of the almost constant low thermal expansion temperature range in invar alloys was evaluated with a TA Instruments Q50 thermogravimeter coupled with a magnet placed always at the same distance to the sample. The ferromagnetic to paramagnetic transition is determined with a suddenly drop in the registered sample weight. The linear coefficient of thermal expansion was evaluated from room to 350 ºC at 5 ºC/min in a TA Instruments TMA. It uses a simple rod, hence the data presented are not absolute CTE but they still provide valuable information when the CTE's of the processes were compared. A Kammrath and Weiss micro-mechanical testing stage with a load cell of 1 kN was used to perform micro tensile tests at room temperature. This was coupled with a Zeiss EVOMA 15 SEM to perform in situ micro mechanical tests. A fractography analysis was carried out after the tests. Finally, the specimens' microhardness was obtained by a Time Technology Europe digital microhardness tester HVS-1000.

3 Results

3.1 Densification and elements analysis after sintering

After sintering in different atmospheres and at different heating rates the sinterability of the resulting parts was evaluated by different methodologies. Figure 2 shows the highly illuminated and contrasted LOM images of the cross section of the parts. In Figure 3, the relative density by Archimedes immersion method, the densification assessed by the ratio between the pore area to total area and the shrinkage values are presented. There were differences between the relative densification measured by Archimedes method and image analysis. This could be attributable to the presence of macro porosity in some areas of the parts or to the parameters chosen by image analysis. Nevertheless, the tendency was the same

in both cases. The residual carbon and oxygen content were also determined and the results were collected in Table 4.

Table 4 Carbon and oxygen contents for different processing conditions

	Powder	Debinding		Sintering			
		A	**V**	**A-V**	**A-H**	**V-V**	**V-H**
C [mass%]	0.01	0.12	0.73	0.06	0.06	0.06	0.05
O [mass%]	0.12	0.57	0.15	0.38	0.07	0.13	0.10

Labrador [24] studied the oxidation kinetics of a wrought Invar 36 alloy in air. The oxidation in terms of mass gains begins to be appreciable above 580 ºC, with the exclusive formation of porous iron oxides specially Fe_2O_3 but also Fe_3O_4 and FeO. Metallic oxide layers in the powder surface inhibit the atom diffusions and thus the sintering mechanism being this fact detrimental for densification of the sintered parts. Reductive conditions (hydrogen, vacuum or CO atmospheres) during sintering could act in the oxide layer enhancing sintering mechanisms. The thermodynamic data calculated using thermodynamic modelling software (HSC Chemistry 7.1) reveal that at 1100 ºC oxygen partial pressures of approximately 10^{-13} bar are needed to decompose the different iron oxides. Below this temperature, partial pressures have to be lowered to achieve the same effect. Carbon may also participate in the oxide reduction essentially in two stages [25, 26]. The first involves the reduction of surface oxides which are in contact with residual binder organic compounds during the heating stage. This reaction is the so called direct carbothermal reduction. The produced carbon monoxide can further react with the existing oxides towards the formation of carbon dioxide. This reaction in turn is called indirect carbothermal reduction. Direct and indirect carbothermal reductive reactions become more important above 720 ºC since then the equilibrium in the Boudouard reaction is shifted towards the formation of carbon monoxide which is the more stable product from this temperature and above. Regarding hydrogen as a reductive atmosphere, the reductive effect will depend on the water vapour partial pressure, the heating rates, the velocity and concentration of hydrogen. Jozwiak et al. [27] evaluates these parameters influence on the reduction of different iron oxides by hydrogen and concluded that the complete reduction of these oxides into metallic iron phase can be accomplished at a relatively low temperature, below 380 ºC. However this temperature shifted to higher temperatures as the heating rates are increases (around 750 ºC at 10 ºC/min). More over the effectiveness of the reduction was is strongly influenced by their size and crystallinity and presence of other metals.

The A-V turned out to be the most unfavourable condition in terms of densification and shrinkage due to the presence of oxide layers surrounding powder particles formed most likely during debinding. This was coherent with the high oxygen content measured in this condition in both brown and sintered parts compared to the original oxygen content of the powder. Although the vacuum condition may cause a reductive effect, the oxides layers were probably stable at sintering conditions and hindered the diffusion of the metallic atoms. However it is

worth to note that there was a considerable reduction of the oxygen content comparing the brown and sintered parts. This would be explained by a direct or indirect carbo-reductive effect of the remaining carbon after debinding aided by the low pressures.

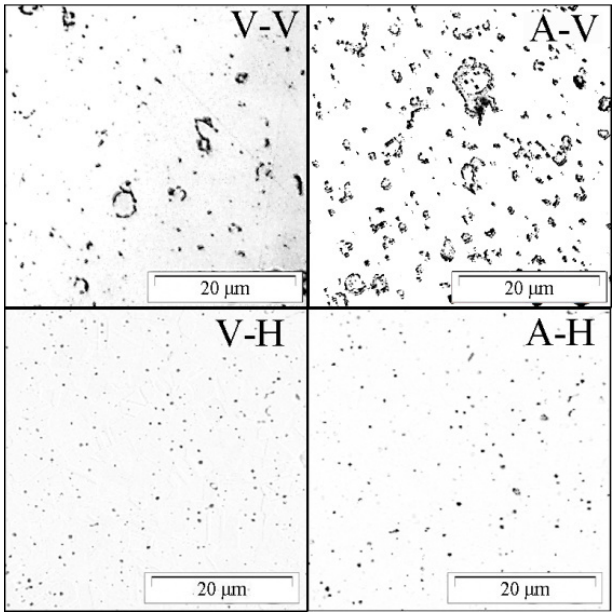

Figure 2. Highly contrasted LOM images of different grinded and polished Invar 36 micro parts at the same magnification for the evaluation of the densification and the remaining porosity. The specimens were not etched in this case.

In the V-V condition parts, some original powder particles were still observed as it occurred in A-V parts. The number of these original powder particles was considerably lower than in the A-V conditions as well as the proportion and size of pores observed. The oxygen measured in the V-V parts was lower than the A-V part but comparable to the corresponding brown part measured after debinding. These brown parts has slightly higher oxygen content than the original particles, thus it can be concluded that vacuum debinding atmosphere was effective to preserve particles from oxidation.

The parts sintered in hydrogen, independently of the debinding atmosphere, demonstrated to have a higher volumetric shrinkage factor and thus a better densification. They showed a homogeneous porosity distribution and the absence of original powder particles. These results were consistent with the low oxygen contents of these parts which demonstrated an efficiently reduction of the oxides by the hydrogen.

The measured carbon content was comparable in all conditions and was higher than the original powder particles. This denoted that there is a carbon contamination that cannot be avoided by any of the selected processing conditions. The carbon contents were still low but this contamination might affect the Invar properties.

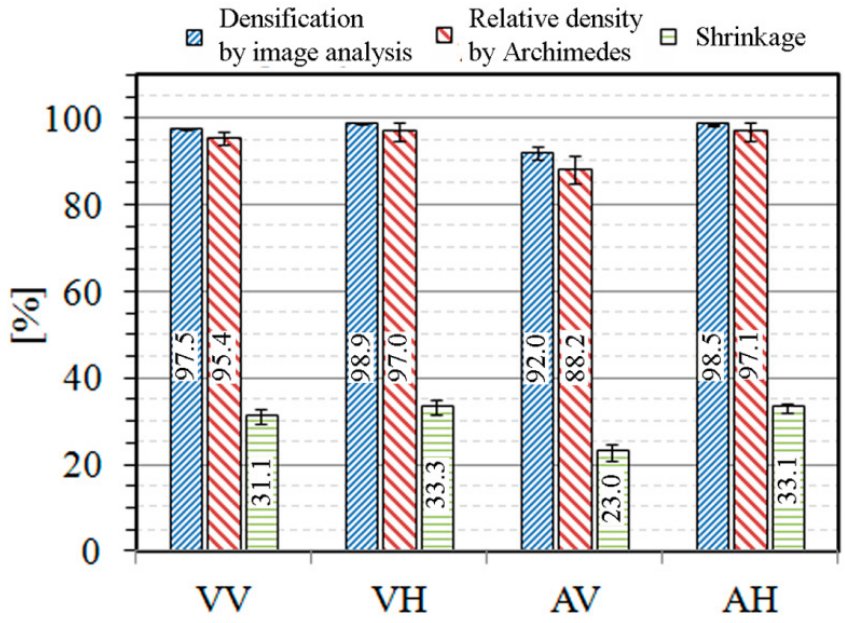

Figure 3.Sinterability study of the micro parts by different methodologies. The percentage of porosity was assessed by image analysis software. The relative density was measured comparing Archimedes method density with respect to the Invar 36 powders density. The shrinkage of the part was evaluated by direct measurement of the sintered part dimensions and comparing them with green part dimensions.

3.2 Microstructure analysis and phases determination by XRD

Figure 4 shows back scattering electron detector SEM images of INVAR 36 micro-parts cross sections representing different debinding and sintering conditions. With the exception of A-V parts (Figure 4 b) the rest of conditions developed a clear austenitic microstructure with typical austenite twin bands. The presence of a γ' Ni rich phase is not discarded but was not detected by SEM inspections. Sometimes γ' precipitates are in the order of nm which is out of the SEM range. In the same way graphite precipitates were not detected. The grain size of the austenite varied depending on the processing condition with apparently the bigger grains detected for the V-H condition (Figure 4 c). The big austenite grains of V-H made thinking on a prompter initiation of the elements diffusion mechanisms compared with other conditions. This would be explained by a rapid reduction of the particle surface oxide at earlier stages of the sintering. Comparing V-V and A-H conditions, the last seemed to have lower grain sizes. Finally, A-V condition had the smallest grain sizes in the order of powder particle size.

The pore sizes seemed to be higher than those observed in LOM by image analysis, but the proportion of porosity was similar and more coherent with the Archimedes measurements. However, in these cases the samples were etched and the porosity may be broadened. It is worth to note the roundness and the small sizes of the pores which were related to the ending stages of the sintering. The effectiveness of the sintering at 1100 ºC may be explained by the small powder particle size that is well established to promote sintering; as powders become finer, sintering activity increases and full density can be achieved at lower temperatures.

Imbaby et al. [28] reported that 99% density is obtained from 90%-4μm 316L powder at 1200 ºC.

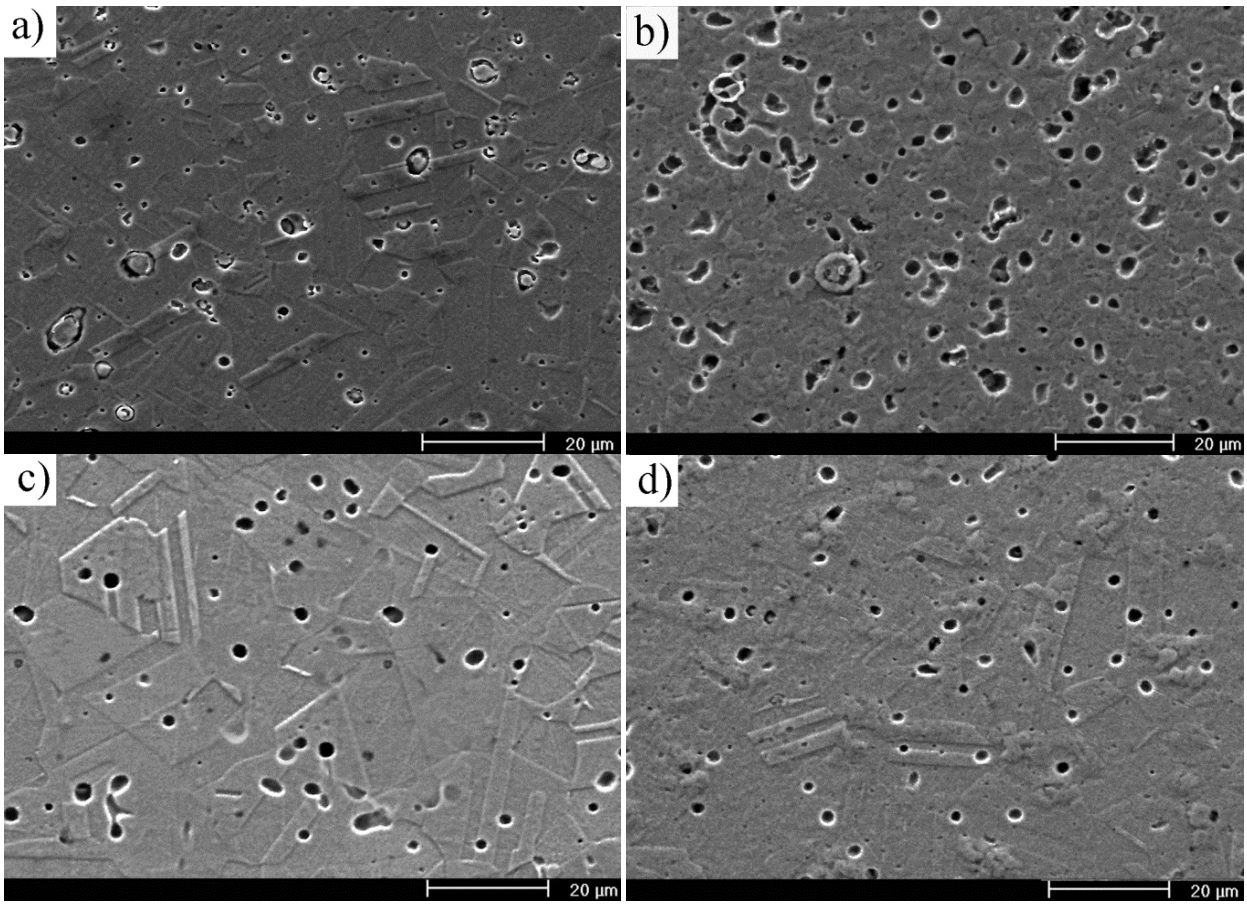

Figure 4 Secondary scattered electron detector SEM images of cross sections of different processing conditions INVAR 36 micro-parts: a) Vacuum-vacuum, b) air-vacuum, c) vacuum-hydrogen, d) air-hydrogen. The parts were etched with *aqua regia* a solution of concentrate nitric acid and concentrate hydrochloric acid in a volume ratio of 1:3.

As it was already observed by LOM, in case of sintering in vacuum conditions, some original powder particles that apparently had not take part of the sintering mass transfer mechanism were observed. However, some differences could be appreciated when comparing V-V or A-V. The main difference was the thickness of the oxide layer around particles. A thick dense oxide layer without fissures surrounded powder particles in case of A-V parts (Figure 5a) whereas a thin oxide layer with some discontinuities embedded powder particles in case of V-V parts (Figure 5b); in these discontinuities sintering necks had began to be formed. The residual carbon in V-V combined with a vacuum atmosphere had a reductive effect but it was not enough to reduce all the oxides. In the A-V and V-V SEM images the number of original particles was similar. This seems to contradict Figure 2 results were more original particles were observed in A-V condition. This may be explained by a combined effect of an etching media with ultrasound bath surface cleaning that made some particles to be removed from the surface of A-V condition. The fracture surfaces in Figure 11 again showed a higher density of original particles in the case of A-V condition.

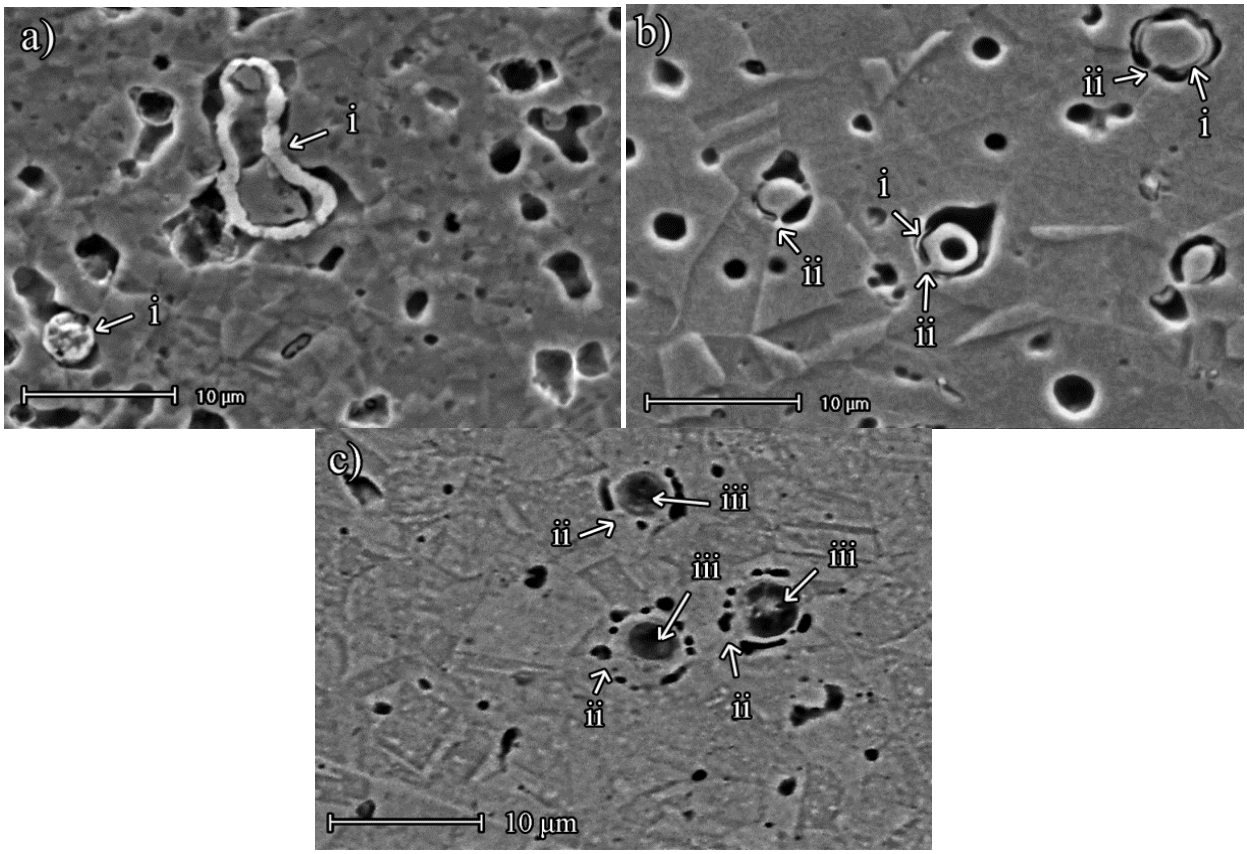

Figure 5 Secondary electrons detector SEM micrographs of cross sections of INVAR 36 sintered micro-part: a) A-V, b) V-V c) A-H. (i. oxide layer, ii. sintering neck, iii. micro void formed due to elements diffusion)

The absence of oxides in hydrogen sintered parts evidenced the efficacy of the reductive effect of a hydrogen atmosphere. However, some original particles were sporadically observed in A-H conditions (see Figure 5c). They were in a very advanced sintering stage with the entire surrounding oxide layer reduced and with lot of sintering necks. This was not observed in V-H parts. The oxide layer generated during debinding in air most likely was thicker than debinding in vacuum as it could deduced from A-V micrographs. Hence the A-H parts would need more time to end with the oxide layer reduction than V-H parts, and thus some particles are still at the end stages of the sintering. This also would explain the differences in grain sizes.

During SEM inspections SiO_2 and other complex oxides inclusions were found. Silica particles are often observed sintered materials because a small amount of silicon, <0.8%, is usually added into the melt to facilitate atomization. Silica particles are difficult to reduce, even though using hydrogen atmospheres, especially at 1100 ºC.

When XRD analyses were conducted to determine the phases formed during the different consolidating processes, similarities were observed in the resulting diffractograms. In all cases, as could be observed in Figure 6, austenitic γ(FCC) phase characteristic of $Fe_{0.64}$-$Ni_{0.36}$ was clearly identified and almost perfectly indexed by comparing peaks positions with XDR patterns. Nevertheless there were divergences in the relative peaks intensities patterns and

occurrence of double peaks. The double peaks at high angles was associated to Cu-$K_{\alpha 2}$ radiation as the second peak is displaced to higher angles and had almost the half of the intensity of the most intensive first peak. However at lower angles these double peaks of similar intensities could be associated with heterogeneities in the composition due to Ni segregations and lattice distortions caused by interstitial elements. For the original powders and for the A-V condition, small intensity peaks associated with a α BCC phase were detected. This fact was predictable since the non reduced oxide layer likely would have impeded the elements homogenisation by diffusion mechanisms, in case of having heterogeneous particle compositions and α particles.

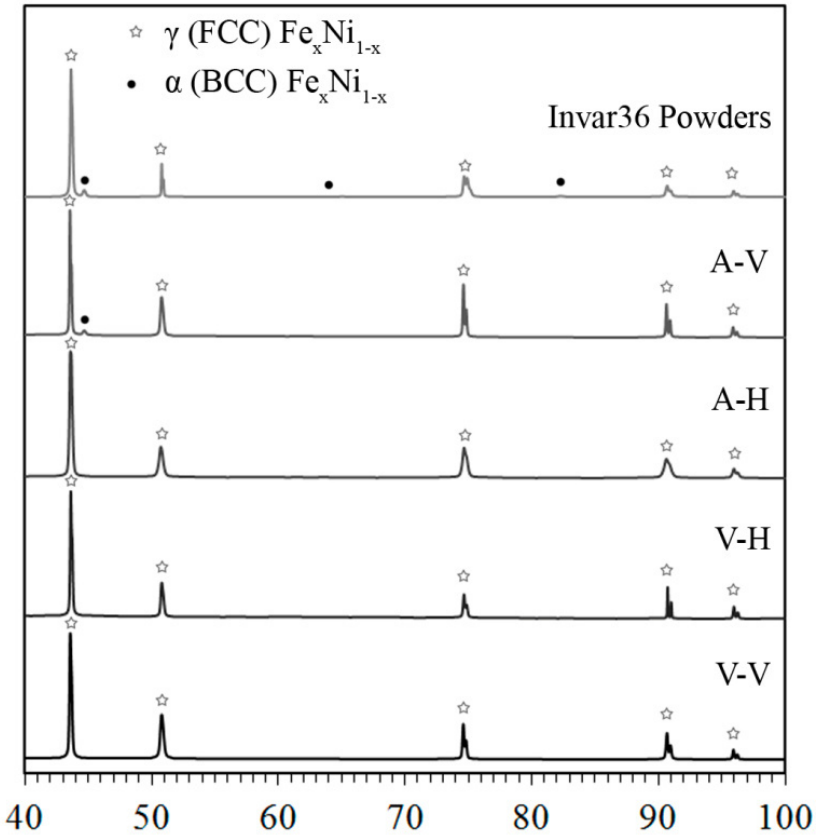

Figure 6 XRD diffractograms and phases identification of sintered parts subjected to different debinding and sintering conditions: a) vacuum-vacuum, b) air-hydrogen, c) vacuum-hydrogen, d) air-vacuum.

3.3 Coefficient of thermal expansion and Curie temperatures

Figure 7 shows a TGA weight loss (dashed line) associated with the Invar 36 ferromagnetic to paramagnetic transition, i.e. the Curie temperature. During this transition, a magnet positioned close to the sample stopped attracting it when the paramagnetic state occurred. The derivative of the curve represents the characteristic Curie temperature peak defined by its maximum, the offset and the width. Table 5 collects the results of the different processing conditions micro parts and of the original powders. Comparing the values, there was a reduction of the Curie temperatures in the sintered parts compared with the original powders. This could be

associated with the presence of interstitial elements (C or H) or Ni segregations. This variation was more severe in the sintered in hydrogen parts which remarked the negative effect of the hydrogen in this property. The wide peak registered for the powder particles may be associated with heterogeneities in the composition of different powders and/or the particle size distribution. The Curie's temperature has demonstrated to be influenced by composition and by the austenite grain size. This would also explain the double peak detected in the A-V condition which apparently showed the lowest grain size and also original powder particles.

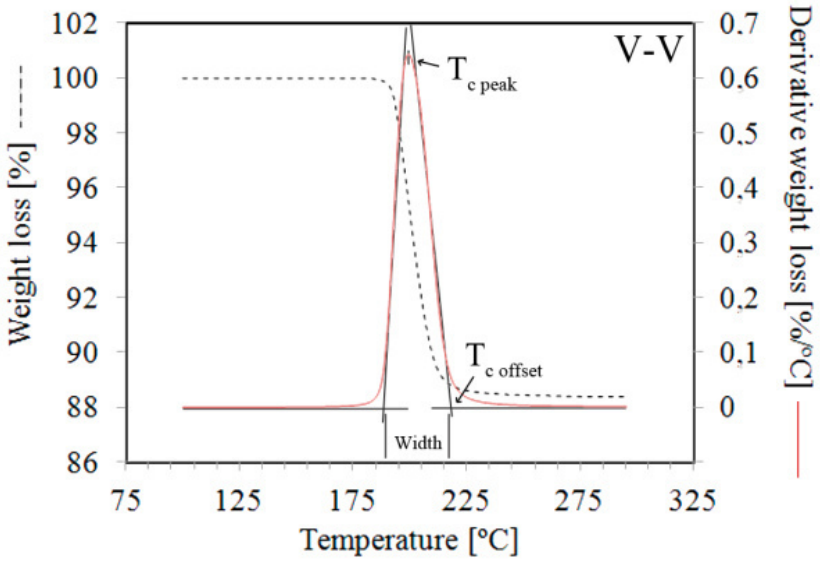

Figure 7 TGA weight loss (dashed line) associated with the Invar 36 ferromagnetic to paramagnetic transition. The derivative of the curve represents the characteristic Curie's temperature peak defined by its maximum, the offset and the width.

Table 5 Curie temperatures for different parts processed with different atmospheres

Tc [ºC]	INVAR Powder	V-V	V-H	A-V		A-H
Peak	221.2	199.4	185.7	213.7	236.7	186.7
Offset	282.2	216.0	196.4	245.4		201.6
Width	89.1	27.3	20.4	42.4		25.8

Figure 8 plots the linear coefficient of thermal expansion (CTE) at different temperatures of different debinding and sintering conditions. The small dimensions of the samples caused noise in the measurements of the expansion with temperature curves, thus smoothing had to be carried out to determine the linear CTE by the following expression:

$$CTE_{linear} = \frac{1}{L_0} \cdot \frac{\Delta L}{\Delta T} \qquad (1)$$

where L_0 is the initial length of the sample and ΔL represents the variation of length at a certain increment of temperature ΔT. Smoothing and the use of a simple rod dilatometer may produce some errors in the assessment of the linear CTE. Therefore the data presented are not absolute CTE but they still provide valuable information when the CTE's of the four processes

were compared. The values obtained and the behaviour with temperature and processing conditions seemed to be consistent with the Curies' temperature results and with the intrinsic behaviour of an Invar 36 alloy. At temperatures below the T_c, the CTE was low (in the order of 1.3 $10^{-6}\cdot ºC^{-1}$to 3 $10^{-6}\cdot ºC^{-1}$) and relatively steady. Near the T_c this tendency changed and the CTE values began to raise with temperature up to values were the curve seemed to stabilise again at temperatures above the T_c. The CTE at high temperatures was in the order of those for stainless steels. As it occurred with the T_c there was a clear effect of the sintering in hydrogen conditions in the CTE values. These conditions showed the worst values of CTE at all the temperature range.

A-V condition resulted to give the best CTE results. The reason explaining this fact was unclear, especially considering that some alpha phase was developed in these parts (as reflected in XRD analysis). A combined effect of Invar 36 low CTE until around 200 ºC and the low CTE of non-reduced oxides at higher temperature may be a plausible explanation. Moreover, the small grain size may be also influencing the results.

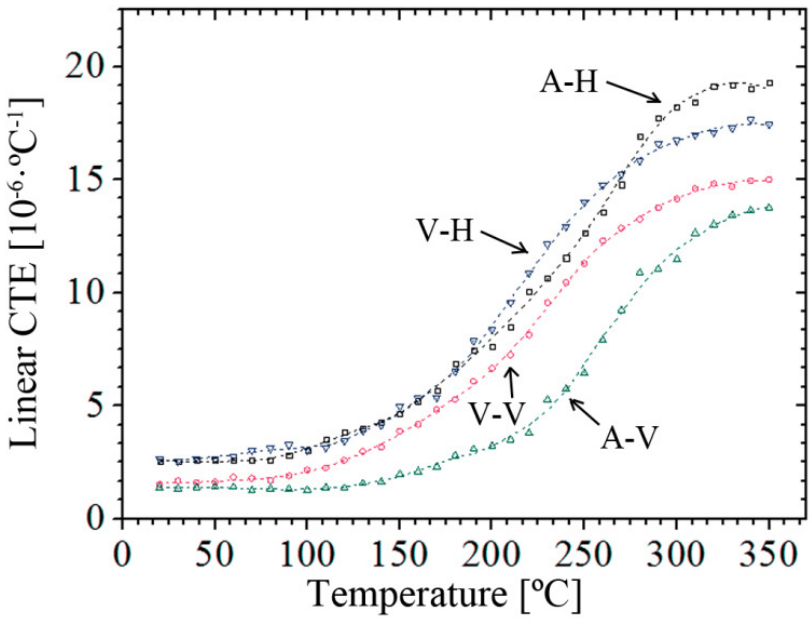

Figure 8 Linear coefficient of thermal expansion at different temperatures of different debinding and sintering conditions.

3.4 In situ tensile and hardness micro mechanical test

Figure 9 shows the representative strain-stress curves of different processing conditions. Table 6 collects some characteristic mechanical parameters according to these curves. Zhao et al. [29] discussed the limitations and issues in correctly interpreting micro tensile experiments. The micro test experimental studies assume errors in the strain measurements as the data were collected directly from the cross head displacement without any extensometers, digital image correlation or laser interferometry. Thus, only engineering results are presented in this work.

However, as the tests were performed on the same device, the results are considered valid for comparative purposes.

The ASTM Designation A658 covers 36 percent nickel-iron alloy and specifies a tensile strength of 448-552 MPa, a minimum yield strength (0.2% offset) of 241 MPa and a minimum elongation of 30%. Although these values are representative of the wrought Invar 36, the results derived from the micro-tests of powder consolidated specimens were consistent with these specifications and the values collected in Table 1. However there was a great diminution of the strain and thus of the ductility in the sintered in hydrogen parts. This coincided with the highest yield strength values registered.

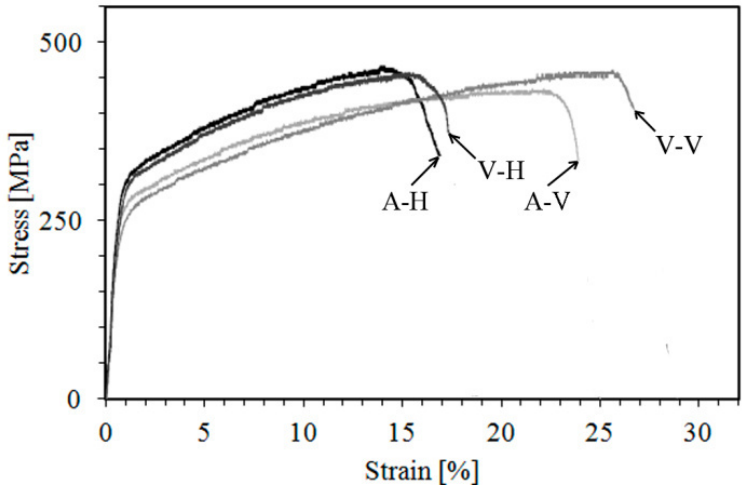

Figure 9 Representative stress-strain curves of different processing conditions.

Considering that the porosity values in V-V, V-H and A-H conditions were similar as well as the carbon content, it could be stated that hydrogen was the responsible of this embrittlement effect. However, the ultimate tensile stress (UTS) values were similar for those conditions. The lowest UTS was registered by the A-V condition and it is probably associated with the high porosity of these parts. The presence of oxides also limits the elongation values in comparison with the V-V condition. These results were consistent with the microhardness results. The highest HV corresponded to the sintered in hydrogen part evidencing the low ductility results. The lowest value corresponded to the A-V condition, most likely due to the high porosity. The micro hardness values were also in the range of the Invar 36 materials (see Table 1).

Table 6 Micro-mechanical properties of different processing conditions

	A-H	A-V	V-H	V-V
UTS [MPa]	466±15	436±22	458±15	462±19
Strain to fracture [%]	17±1	22±2	18±1	28±2
Yield strength (0.2% offset) [MPa]	290±12	252±21	267±15	212±19
H_V/9.8N [GPa]	1.70±0.021	1.2±0.023	1.69±0.020	1.63±0.021

A representative behaviour of the microstructure evolution with the applied stress in Invar 36 micro parts is shown in Figure 10, corresponding to V-V condition. No significant differences were observed for the rest of the conditions. At stresses near the yield point, a small deformation of the austenitic grain was observed but no other differences were observed in the microstructure comparing the images with the uncharged condition. Above the yield point the austenitic grain deformation became appreciable as well as the formation of slip bands. The deformation and the density of the slip bands were considerable near the UTS. The round pores were elongated in the strain direction and some of them begin to coalesce. At fracture, slip bands moving from different sliding directions were observed crossing over.

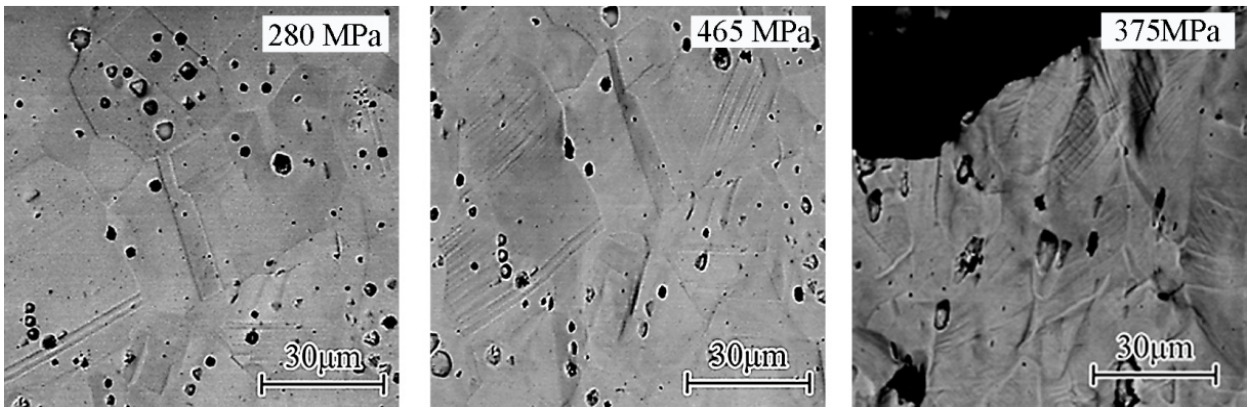

Figure 10 From left to right: evolution of the V-V parts microstructure with strain at approximately the yield point, the ultimate tensile stress and the rupture strength.

The fracture surfaces of all the tensile tested specimens were examined by SEM. Resultant fractography images are shown in Figure 11. In principal, the sintered in vacuum samples exhibited a typical ductile fracture by microvoids coalescence (MVC) based on the presence of dimples initiated at inclusions. These inclusions were sometimes original powder particles that were not sintered due to the presence of an oxide coat that was not reduced with the sintering conditions. This was more evident in the A-V condition (Figure 11b) with dimple sizes around 5μm. Spherical particles were clearly observed in the middle of the rounded dimple with the same size of powder particles. Deformation slip bands were observed in many dimples. Figure 12 shows a magnified image of A-V fracture surface with EDX semi-quantitative elemental analysis at different regions. The element estimation may fall in errors since the surface is rough. However, spherical Invar 36 particles were identified in the middle of the dimple (Figure 12(1)) with a broken oxide shell surrounding the particles (Figure 12(2)). Some silica inclusions were also identified in some dimples (Figure 12(3)).

By contrast the sintered in hydrogen specimen exhibited two modes of fracture: a predominant MVC and a second less ductile mode with some transgranular facets sometimes roughened by slip steps. The dimple sizes in those cases were smaller than sintered in vacuum specimens (around 1μm) most likely they were initiated by sub-micrometer inclusions. Moreover, there were less clear slip bands in the dimples or directly they were not observed. The presence of transgranular facets may be linked with the embrittlement observed in the stress-strain curves

of these conditions. Winding regions of apparently dimples clusters were observed in all specimens independently of the sintering atmosphere.

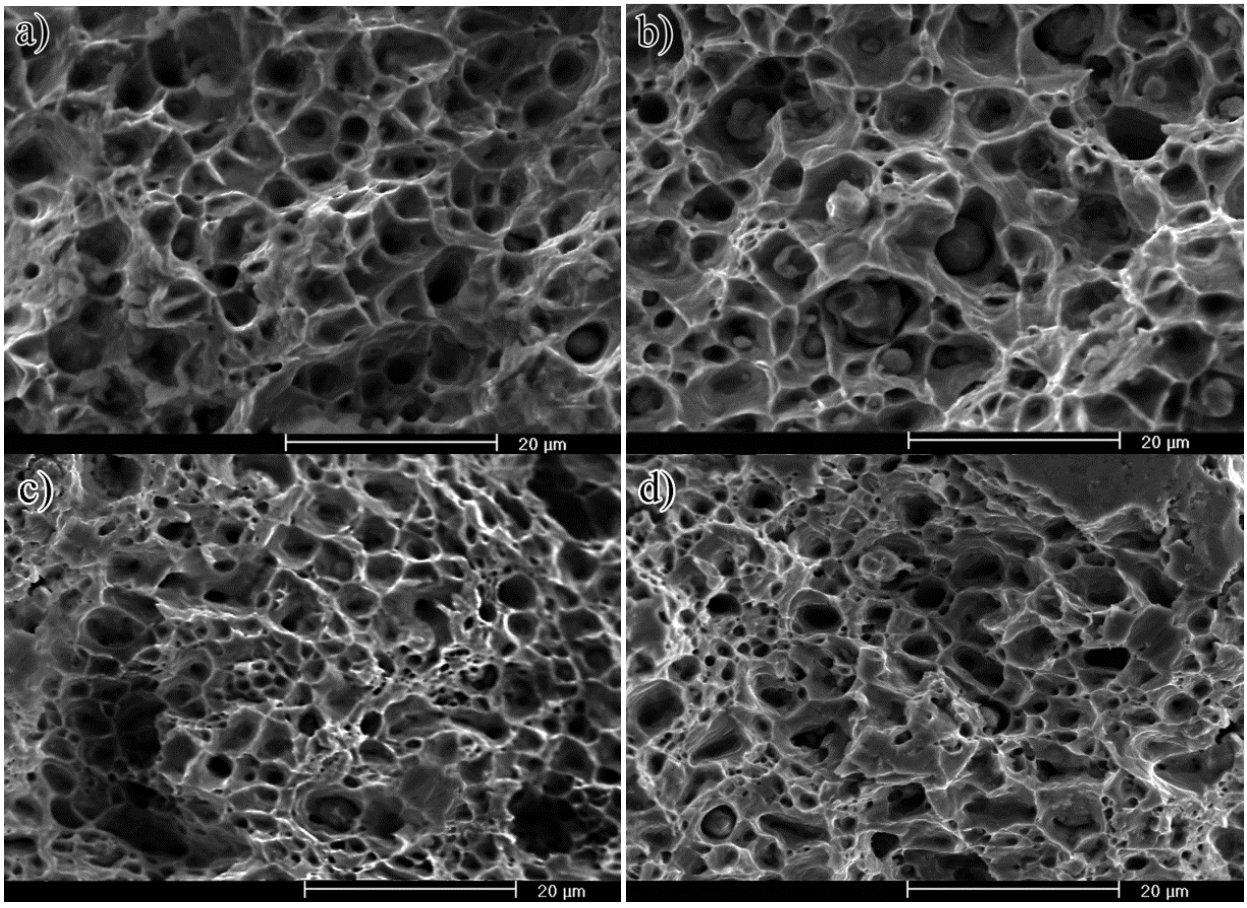

Figure 11 Fracture surfaces of different tensile specimens after micro tensile test: a) V-V, b) A-V, c) V-H and d) A-H.

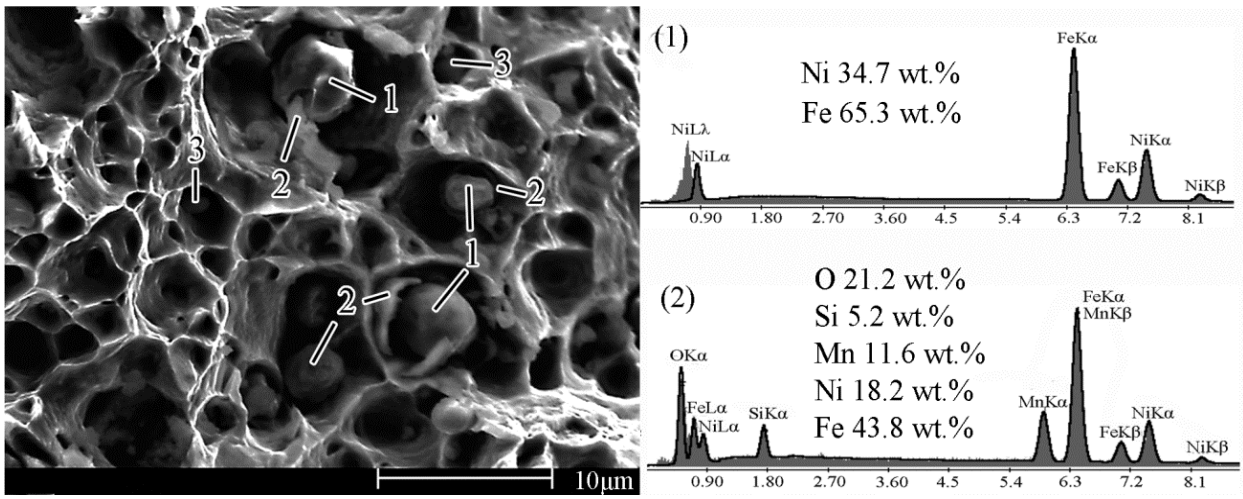

Figure 12 Magnified image of A-V fracture surface accompanied of EDX analysis at different points. (1) Original Invar 36 particle, (2) Possible complex FeNiSiMn oxide shell sourronding original Invar 36 particle, (3) Silica inclusions with a small amount of Mn according to EDX.

4 Conclusions

The effect of debinding and sintering atmospheres of INVAR 36 micro parts was investigated. The following conclusions were drawn:

- Air degraded more effectively CAB during sintering but is responsible of metallic particles oxidation. However these oxides could be reduced employing reductive hydrogen or vacuum atmospheres also aided by carboreductive effect of remaining carbon after debinding.
- The debinding in vacuum atmosphere leaved a high percentage of contaminating carbon source. Residual carbon could be eliminated by pyrolysis with vacuum media or by reductive hydrogen during sintering.
- All combined processing condition leaded to the formation of desirable austenitic microstructure responsible of the low CTE of INVAR 36 and produces similar levels of carbon contamination. This was contrasted by microstructure investigations by SEM, by XRD and element analysis.
- To some extent, resulting mechanical properties meet the standards of an Invar 36 alloy. Presence of none reduced oxides influenced the densification of the micro parts and leaded on a detriment of the mechanical properties.
- The hydrogen atmosphere have demonstrated to be effective for the reduction of oxides and the part densification, but this element has been easily introduced as an interstitial element worsening the ductility, the Curie's temperature and the coefficient of thermal expansion.
- The debinding and sintering in vacuum produced the most equilibrated physical and mechanical properties.

5 Acknowledgements

The authors wish to thank GUZMÁN GLOBAL S.L. and MIMTECH ALFA for their collaboration on the ECOPIM project (ref. IPT-2011-0931-20000) that was funded by the Spanish Ministry of the Economy and Competitiveness. Furthermore, the authors would like to acknowledge the funding provided by CAM-Consejeria de Educación Dir. Gral. Universidades e Investigación in the project ESTRUMAT (ref. S2009/MAT-1585) and the Nacional Project (MAT2012/38650-C02-01).

References

1. Maslyuk, V.A., O.A. Panasyuk, and O.V. Vlasova, *Physical, technological and magnetic properties of powder iron-nickel alloys.* Powder Metallurgy and Metal Ceramics, 2003. **42**(9-10): p. 536-539.
2. Jasthi, B.K., W.J. Arbegast, and S.M. Howard, *Thermal Expansion Coefficient and Mechanical Properties of Friction Stir Welded Invar (Fe-36%Ni).* Journal of Materials Engineering and Performance, 2009. **18**(7): p. 925-934.
3. Cha, B., et al., *Micro powder injection molding process using TiH2 powder.* Journal of Ceramic Processing Research, 2012. **13**: p. S22-S25.

4. Chun-Ting, L., C. Bi-Shiou, and S. Chi, *Cost-effective optoelectronic packages using powder metallurgy.* IEEE Journal of Selected Topics in Quantum Electronics, 2006. **12**(5): p. 970-82.
5. Attia, U.M. and J.R. Alcock, *A review of micro-powder injection moulding as a microfabrication technique.* Journal of Micromechanics and Microengineering, 2011. **21**(4).
6. Piotter, V., et al., *Powder injection moulding of metallic and ceramic micro parts.* Microsystem Technologies-Micro-and Nanosystems-Information Storage and Processing Systems, 2011. **17**(2): p. 251-263.
7. Kong, X., T. Barriere, and J.C. Gelin, *Determination of critical and optimal powder loadings for 316L fine stainless steel feedstocks for micro-powder injection molding.* Journal of Materials Processing Technology, 2012. **212**(11): p. 2173-2182.
8. Quinard, C., et al., *Elaboration of PIM feedstocks with 316L fine stainless steel powders for the processing of micro-components.* Powder Technology, 2011. **208**(2): p. 383-389.
9. Ruban, A.V., et al., *Magnetic state, magnetovolume effects, and atomic order in Fe65Ni35 Invar alloy: A first principles study.* Physical Review B, 2007. **76**(1).
10. Khomenko, O.A., *Origin and specific features of invar anomalies of physical properties: Fe-Ni alloys with an FCC lattice.* Physics of Metals and Metallography, 2007. **104**(2): p. 146-156.
11. Nadutov, V.M., et al., *Interatomic Interaction and Magnetostriction in Invar Fe-Ni-C-Based Alloys.* Metallofizika I Noveishie Tekhnologii, 2009. **31**(8): p. 1021-1034.
12. Nadutov, V.M., et al., *Magnetic properties of alloyed invar alloys on the base of Fe-Ni-C.* Metallofizika I Noveishie Tekhnologii, 2006. **28**: p. 39-48.
13. Kim, B.S., et al., *Effect of carbon on the coefficient of thermal expansion of As-cast Fe-30wt.%Ni-12.5wt.%Co-xC invar alloys.* Metals and Materials International, 2002. **8**(3): p. 247-252.
14. Wittenauer, J., *Factors affecting the mechanical strength of Fe-36Ni Invar*, in *Invar Effect: A Centennial Symposium*, J. Wittenauer, Editor. 1996. p. 231-238.
15. ASM, *Metals Hadbook:Properties and Selection - Nonferrous Alloys and Pure Metals*, ed. M. Park. Vol. 2. 1979, OH, USA.
16. Sokolowski, W., C. Hsieh, and T. O'Donnell, *New HP (high purity) Invar 36*. Invar Effect: A Centennial Symposium, ed. J. Wittenauer. 1996. 147-156.
17. Vinogradov, A., S. Hashimoto, and V.I. Kopylov, *Enhanced strength and fatigue life of ultra-fine grain Fe-36Ni invar alloy.* Materials Science and Engineering a-Structural Materials Properties Microstructure and Processing, 2003. **355**(1-2): p. 277-285.
18. Sokolowski, W., C. Hsieh, and T. O'Donnell. *New HP (high purity) Invar 36*. in *Invar Effect: A Centennial Symposium*. 1996.
19. Gulyaev, A.A. and E.L. Svistunova, *PRECIPITATION PROCESS AND AGE-HARDENABILITY OF FE-NI-BE INVAR-ALLOYS.* Scripta Metallurgica Et Materialia, 1995. **33**(9): p. 1497-1503.
20. Wittenauer, J., D.L. Yaney, and R.E. Lewis, *Microyielding in Fe-36Ni: Role of Carbon and Thermal Processing.* Scripta Metallurgica Et Materialia, 1994. **31**(11): p. 1531-1536.
21. Hidalgo, J., A. Jimenez-Morales, and J.M. Torralba, *Torque rheology of zircon feedstocks for powder injection moulding.* Journal of the European Ceramic Society, 2012. **32**(16): p. 4063-4072.

22. Minseok, S., et al., *Water-soluble binder with high flexural modulus for powder injection molding.* Journal of Materials Science, 2005. **40**(5): p. 1105-9.
23. Hidalgo, J., A. Jimenez-Morales, and J.M. Torralba, *Thermal stability and degradation kinetics of feedstocks for powder injection moulding – A new way to determine optimal solid loading?* Polymer Degradation and Stability, 2013. **98**(6): p. 8.
24. Labrador, N. and P. Lefort, *Invar alloy oxidation in air.* Journal De Chimie Physique Et De Physico-Chimie Biologique, 1999. **96**(5): p. 810-829.
25. Momeni, M., C. Gierl, and H. Danninger, *Study of the oxide reduction and interstitial contents during sintering of different plain carbon steels by in situ mass spectrometry in nitrogen atmosphere.* Materials Chemistry and Physics, 2011. **129**(1-2): p. 209-216.
26. Chasoglou, D., E. Hryha, and L. Nyborg, *Effect of process parameters on surface oxides on chromium-alloyed steel powder during sintering.* Materials Chemistry and Physics, 2013. **138**(1): p. 405-415.
27. Jozwiak, W.K., et al., *Reduction behavior of iron oxides in hydrogen and carbon monoxide atmospheres.* Applied Catalysis a-General, 2007. **326**(1): p. 17-27.
28. Imbaby, M. and K. Jiang, *Fabrication process of 3D micro components from stainless steel aqueous slurry.* World Congress on Engineering, WCE 2009, 2009: p. 536-40.
29. Zhao, Y.H., et al., *Influence of specimen dimensions and strain measurement methods on tensile stress-strain curves.* Materials Science and Engineering a-Structural Materials Properties Microstructure and Processing, 2009. **525**(1-2): p. 68-77.